From Permanent Deformation to Earthquake Mechanics Habilitation à diriger des recherches

Nadaya Cubas

UFR 918, Terre, Environnement, Biodiversité

From Permanent Deformation to Earthquake Mechanics

Habilitation à diriger des recherches

Nadaya Cubas

Institut des Sciences de la Terre de Paris
-
Sorbonne Université

Présentée le 29 Juin 2023 devant le jury composé de :

Serge Lallemand Directeur de recherche, CNRS, Géosciences, Université de Montpellier	**Rapporteur**
Matthias Rosenau Senior Researcher, GFZ, Postdam, Germany	**Rapporteur**
Laurence Audin Directrice de recherche, IRD, ISTERRE, Université de Grenoble	**Rapporteure**
Mireille Laigle Directrice de recherche, CNRS, Géoazur, Université de Nice	**Examinatrice**
Sylvie Leroy Directrice de recherche, CNRS, ISTeP, Sorbonne université	**Examinatrice**
Rodolphe Cattin Professeur, Géosciences, Université de Montpellier	**Examinateur**
Harsha Bhat Chargé de recherche, CNRS, Laboratoire de Géologie, ENS Paris	**Invité**

.

AVANT-PROPOS

Cette habilitation à diriger des recherches est tout d'abord composée d'un CV étendu, suivi d'une courte présentation de mes enseignements et des responsabilités attenantes.
Le mémoire se concentre ensuite sur les relations entre la déformation court- et long-terme des avant-arcs de subduction. Le mémoire commence par une brève introduction sur les avant-arcs de subduction, leur comportement sismogénique, et l'impact potentiel de ce comportement sur la construction à plus long-terme des avant-arcs. Cette introduction est suivie d'une description synthétique de l'ensemble des modèles pouvant être utilisés pour étudier les relations entre comportement mécanique et déformation, avec leur avantages et inconvénients.
La partie suivante est un résumé de mes travaux réalisés sur cette thématique. Dans une première partie, je présente comment la déformation et la morphologie de l'avant-arc peuvent donner accès aux propriétés mécaniques du mega-chevauchement. L'étude du Chili Central m'a permis de mettre en évidence des différences significatives de propriétés frictionnelles entre zones asismiques et sismiques. Ces différences sont suffisantes pour induire des variations dans la morphologie et dans la distribution de la déformation. Elles impliquent aussi une corrélation entre la distance fosse - côte et la quantité de couplage. Ces différences peuvent également mener à la formation de splay faults, et pourraient être à l'origine de l'activation d'une large faille normale par le séisme de Tohoku-Oki en 2011. Une fois les propriétés frictionnelles contraintes, il est possible ensuite de les intégrer à des modèles dynamiques de cycle sismique pour comprendre le comportement sismogénique d'une zone de subduction sur des échelles de temps plus longues.
Dans une seconde partie, je discute des limites de notre conception actuelle d'une interface de plaque et comment cela limite notre compréhension du comportement à court terme des mega-chevauchements. Je discute tout d'abord du rôle de la migration de l'interface de plaque, lors de processus d'érosion basale ou de sous-plaquage. Je montre que la localisation des ces processus peut être contrainte par une analyse mécanique simple de la topographie. Je montre ensuite que l'extension des grands séismes le long de la subduction chilienne est limitée par ces zones de déformation distribuée. A l'aide de modélisation thermo-mécanique, je discute ensuite du rôle de la transition fragile/ductile sur la morphologie et la déformation des avant-arcs et leur impact potentiel sur le comportement sismogénique des mega-chevauchements. Pour finir, je propose un projet visant à fournir une compréhension physique du comportement des mega-chevauchements.

Je ne présente dans ce manuscrit que les travaux réalisés sur les avant-arcs de subduction. Ces travaux sont le fruit de nombreuses collaborations, je tiens donc à remercier mes collègues et tous les étudiants y ayant participé (par ordre chronologique : Jean-Philippe Avouac, Nadia Lapusta, Yves Leroy, Pauline Souloumiac, Bertrand Maillot, Satish Singh, Baptiste Rousset, Sepideh Pajang, Laëtitia Le Pourhiet, Jean Letouzey, Philippe Agard). Ce travail a également largement bénéficié d'idées et de résultats provenant de travaux réalisés dans d'autres contextes géologiques. Je tiens donc également à remercier Philippe Steer, Harsha Bhat, Yann Klinger, Christian Gorini, Marthe Lefèvre, Louise Jeandet, Juliana Goncalves de Souza et Sarah Visage.

This habilitation to direct research is first of all composed of an extended CV, followed by a short presentation of my teachings and related responsibilities.
The thesis then focuses on the relationships between short- and long-term deformation of subduction forearcs. The thesis begins with a brief introduction on subduction forearcs, their seismogenic behavior, and the potential impact of this behavior on their longer-term construction. The introduction is followed by a synthetic description of all the models that can be used to study the relationships between mechanical behaviour and deformation. I briefly discuss how

each one of them can be used to constrain the properties of the plate interface.
The second part is a summary of the main results of the studies that I have conducted on forearc wedges. First, I present how frictional properties of the megathrust can be constrained from the deformation and the morphology of the forearc. The study of Central Chile allowed me to highlight significant differences in frictional properties between aseismic and seismic zones. These differences are sufficient to induce variations in the morphology and in the distribution of the deformation. They also imply a correlation between the tench-coast distance and the amount of coupling. These differences can also lead to the formation of splay faults, and could be at the origin of the activation of a large normal fault by the Tohoku-Oki earthquake. Once the frictional properties constrained, it is then possible to integrate them into dynamic seismic cycle models to understand the seismogenic behaviour of a subduction zone on longer time scales. Once the short- and long-term relationships established, I then discuss markers of deformation that can help us assess the seismic and/or tsunamigenic hazard, as for instance along Cascadia, or along poorly instrumented subduction zones, like Mentawai or Makran.
In a second part, I discuss the limits of our current conception of a plate interface, and how it limits our understanding of the short-term behaviour of megathrusts. I first discuss the role of plate interface migration, related to either basal erosion or underplating, the location of which can be constrained from a simple mechanical analysis of the topography. In a recently published paper, I show that large earthquakes along the Chilean subduction are bounded by these distributed deformation zones. Then, from thermo-mechanical modeling, I discuss the role of the brittle/ductile transition on the morphology and deformation of forearcs and their potential impact on the megathrust seismogenic behaviour. Finally, I propose a project aimed at providing a true physical understanding of the megathrust behaviour.

I here only present works conducted in forearc settings for sake of conciseness. This work is the result of many collaborations, and I would like to thank my colleagues and all the students who participated (in chronological order : Jean-Philippe Avouac, Nadia Lapusta, Yves Leroy, Pauline Souloumiac, Bertrand Maillot, Satish Singh, Baptiste Rousset, Sepideh Pajang, Laëtitia Le Pourhiet, Jean Letouzey, Philippe Agard). The ideas and results presented here have largely benefited from studies conducted in other geological contexts. I would therefore also like to thank Philippe Steer, Harsha Bhat, Yann Klinger, Christian Gorini, Marthe Lefèvre, Louise Jeandet, Juliana Goncalves de Souza and Sarah Visage.

Table des matières

CV étendu

1.1 Identification

Nadaya Cubas
Née le : 08/04/1978 - 2 enfants (2014 - 2018)
Grade : Maître de conférences, section CNU 36

Adresse : Sorbonne université - ISTeP - UMR 7193 - 4 place Jussieu, 75005 Paris, France
Tel : +33 1 44 27 45 90
Mail : nadaya.cubas@sorbonne-universite.fr
Sites web : http ://istep.upmc.fr/fr/les_equipes/annuaire/cubas_nadaya.htmlz
Research Gate : https ://www.researchgate.net/profile/N_Cubas

1.2 Parcours

Sept 2014-pst	**Maître de Conférences** - **ISTeP**, Sorbonne Université, Paris.
2013-2014	**Post-Doctoral Fellow** - **IPGP**, Paris. Advisors : S. Singh & H. Bhat.
2009–2013	**Post-Doctoral Scholar** - **CalTech**, Pasadena. Advisors : J.-P. Avouac & N. Lapusta.
2008–2009	**ATER** - Préparation à l'Agrégation SVT, Paris Sud Université et ENS Paris.
2005–2009	**PhD Student** - **ENS**, Paris. Advisors : Y. Leroy & B. Maillot. Titre : Séquences de chevauchements, modélisation mécanique, validation analogique et application à l'Agrio Fold-and-thrust belt, Argentine. Soutenue en Février 2009.
2003 – 2005	Licence, Maîtrise, DEA, Magistère Géologie de l'ENS, Paris.
2000 – 2002	DEUG Sciences de la Terre, Université de Cergy.
2000 – 2005	Manipulatrice à temps partiel.
2000	Diplôme de manipulatrice en radiologie médicale.

1.3 Bilan Recherche

Publications Rang A : 22
Publications Rang B : 1
Publications dans Ouvrage : 2
Encadrement de thèse : 6 dont 5 soutenues (encadrement à 2* 20, 1 * 30, 2* 50%)

1.4 Bilan Enseignement

Responsabilités :
2022 - 2023 : UE Mécanique de la lithosphère Master 2 GeoP.
2021 - 2023 : UE Grandes Questions Environnementales Master 1 STEPE.
2020 - 2023 : UE Geosciences 1, partie TP PEIP (Classe préparatoire intégrée à l'Ecole Polytechnique de Sorbonne Université).
2015 - 2018 : Responsable pédagogique de la Licence 3.
2015 - 2018 : UE stage de Terrain L3 3T603.
2015 - 2016 : UE stage de laboratoire L3 3T602.

Temps de service effectué :

2021-2022	2020-2021	2019-2020	2018-2019	2017-2018	2016-2017	2015-2016	2014-2015
233	203.5	192.75	192.2 (CM*)	218.5	231.75	216.5	192 (CM)

*CM = Congé maternité.

1.5 Financements

Financements obtenus en tant que PI :
- **ANR JCJC 2023-2027** : MECHATHRUST, Towards a MECHAnical understanding of megaTHRUST behavior (240 k€).
- **INSU, Tellus, Aleas, AO 2019** : Le soulèvement de la côte Andine, lié au comportement mécanique du mega-chevauchement ? (4 k€).
- **ANR Retour Postdoc 2013-2017** : SEAFRONTERA. SEAmount and FRONTal megathrust Tsunami and Earthquake Risk Assessment of the last seismic gap of Sumatra subduction zone (204 k€).
- **AXA postdoctoral fellowship** : 2 ans de financement, décliné pour l'ANR.

Financements obtenus en tant que partenaire :
- **ANR PRC 2023-2027** : ALBANEO, Active fault systems at an incipient plate boundary in the Alboran sea, PI : Elia d'Acremont (ISTeP). Partenaire WP4 (modélisation analogique, mécanique et numérique), 112 sur 495 k€.
- **ANR PRC 2021-2025** : FLUID2SLIP, Lithospheric Fluid circulation in subduction system : impact on slip mode, PI : Audrey Galve (Nice). Partenaire Task 5 (modélisation mécanique).
- **ANR PRC 2018-2021** : DISRUPT, Deformation and Earthquake Surface Ruptures : from Observation to Processes, PI : Yann Klinger (IPGP). Partenaire WP3 (modélisation analogique), 70.2 sur 470.3 k€.

Projets ANR en phase 2 :
ANR JCJC 2017 - 2018 : CACUQUAKE, Central Andes coastal uplift : earthquake related ?

Projets ANR non retenus :
ANR JCJC 2020 : TOPO2QUAKE, From topography to Physics of Earthquakes.

1.6 Encadrements étudiants

Encadrement de doctorants :

— **Sarah Visage**, Université de Cergy, Oct. 2019- Mars 2023, encadrée à 25%, avec Pauline Souloumiac et B. Maillot (UCP). Modélisation analogique de la déformation off-fault lors de séisme décrochant. 1 article soumis, 1 article en préparation. En post-doc à ISTERRE en avril 2023.
— **Lauriane Baylé**, ISTeP, SU, Oct. 2018-2021, encadrée à 50%, avec Laetitia Le Pourhiet (ISTeP). Le soulèvement de la côte andine, une origine sismique ? Réorientation vers un Diplôme Universitaire.
— **Juliana Goncalves de Souza**, ISTeP, SU, Nov. 2016-Nov 2020, encadrée à 50%, avec Christian Gorini (ISTeP). Fluid overpressure origin and evolution of the Fos d'Amazon bay. 1 article publié à Marine and Petroleum Geology, 1 article en préparation. Suivi d'un postdoc Suisse/ISTeP.
— **Sepideh Pajang**, co-tutelle ISTeP, SU et Zanjang university (Iran) 2018- Juillet 2021, encadrée à 50%, avec Laetitia Le Pourhiet, Short-term deformation of accretionary prism, the role of mechanical and thermal inheritance. Application to Makran. 3 articles publiés (EPSL, Solid Earth, Tectonophysics). Actuellement postdoc à l'université de Pau.
— **Louise Jeandet**, Oct 2015- Déc 2018, Geosciences Rennes, directeurs de thèse Philippe Steer et Dimitri Lague (Geosciences Rennes). Interactions between major seismic events and erosion on the short time scale. 2 articles à GRL, 1 article en co-auteur à Scientific Report. Actuellement postdoc à l'ISTeP.
— **Marthe Lefèvre**, 2014-2018, IPGP, encadrée à 30%, avec Yann Klinger (IPGP). Strike-slip fault segmentation, the Levant fault case. 1 article à Scientific report, 1 article Geology. Suivi d'un post-doc à l'observatoire royal de Belgique.

Encadrement d'étudiants Licence/Master :
— Alvina Kunkoro, M2, 6 mois, co-encadrée avec S. Singh. Risque sismique du dernier gap sismique de Sumatra, 1 article à EPSL.
— Clara Garret, M1, 2 mois, co-encadrée avec L. Le Pourhiet. Influence de la structure de la plaque plongeante sur la déformation du prisme d'accrétion des Manilles.
— Claire Le Dréo, M1, 2 mois, co-encadrée avec O. Lacombe. Kinematical modelling of Sheep Mountain anticline, Wyoming, USA.
— Roxane Tissandier, L3, 6 mois, Erosion basale de l'avant-arc du Chili Nord, 1 article en co-auteur.
— Sofia Harissi, L3, 1 mois, Failles normales de l'avant-arc du Chili Nord.
— Nina Tricot, L1, 1 mois, Métier enseignant-chercheur Géoscience.

1.7 Publications

Supervised students.

24. J. Goncalves de Souza, **N. Cubas**, D. Praeg, C. Gorini, Spatial variations of the deformation of the Amazon deep-sea fan controlled by crustal thermal state, to be submitted.

23. S. Visage, Souloumiac P., **N. Cubas**, Maillot B., Antoine S., Delorme A. and Klinger Y. (2023), Evolution of off-fault deformation of strike-slip fault in a sand-box experiment, **Tectonophysics**, https ://doi.org/10.1016/j.tecto.2023.229704.

22. S. Pajang, M.M. Khatib, M. Heyhat, **N. Cubas**, E. Bessiere, J. Letouzey, M. Mokhtari and L. Le Pourhiet (2022), The distinct morphologic signature of underplating and seamounts in accretionary prisms, insights from thermomechanical modeling applied to Coastal Iranian Makran, **Tectonophysics**, https ://doi.org/10.1016/j.tecto.2022.229617.

21. A. Ahmed et al., (2022), Across and along-strike crustal structure variations of the western Afar margin and adjacent plateau : Insights from receiver functions analysis, **Journal of African Earth Sciences**, doi :10.1016/j.jafrearsci.2022.104570.

20. **N. Cubas**, Agard, P., and Tissandier, R., (2022), Earthquake ruptures and topography of the Chilean margin controlled by plate interface deformation, **Solid Earth**, https ://doi.org/10.5194/se-2021-148.

19. S. Pajang, Le Pourhiet, L., and **N. Cubas** (2022), The topographic signature of temperature-controlled rheological transitions in an accretionary prism, **Solid Earth**, 13, 535–551, doi :10.5194/se-13-535-2022.

18. C. Herviou, P. Agard, A. Plunder, K. Mendes, A. Verlaguet, D. Deldicque, **N. Cubas** (2022), Subducted fragments of the Liguro-Piemont ocean, Western Alps : Spatial correlations and offscraping mechanisms during subduction, **Tectonophysics**, doi.org/10.1016/j.tecto.2022.2

17. S. Pajang, **N. Cubas**, Jean Letouzey, L. Le Pourhiet, S. Seyedali, P. Agard, M. M. Khatib, M. Heyhat, M. Mokhtari (2021), Seismic hazard of the Western Makran subduction zone : insight from mechanical modelling and inferred frictional properties, **Earth and Planetary Science Letters**, doi :10.1016/j.epsl.2021.116789.

16. J. Goncalves de Souza, **N. Cubas**, C. Rabe, J. Letouzey, R. Divies, D. B. Praeg, D. Granjeon, A. Machado Cruz, C. Guizan Silva, A. Tadeu dos Reis, C. Gorini (2020), Controls on overpressure evolution during the gravitational collapse of the Amazon deep-sea fan, **Marine and Petroleum Geology**, doi :10.1016/j.marpetgeo.2020.104576.

15. L. Jeandet, **N. Cubas**, H. Bhat, P. Steer (2020), The Impact of Large Erosional Events and Transient Normal Stress Changes on the Seismicity of Faults, **Geophysical Research Letters**, doi :10.1029/2020GL087631.

14. M. Lefevre, P. Souloumiac, **N. Cubas**, Y. Klinger (2020), Experimental evidence for crustal control over seismic fault segmentation, **Geology**, doi :10.1130/G47115.1.

13. P. Steer, L. Jeandet, **N. Cubas** et al. (2020), Earthquake statistics changed by typhoon-driven erosion, **Scientific Report**, doi :10.1038/s41598-020-67865-y

12. Rolandone et al. (2018), Areas prone to slow slip events impede earthquake rupture propagation and promote afterslip, **Science Advances**, doi :10.1126/sciadv.aao6596.

11. **N. Cubas**, P. Souloumiac, S. Singh (2016), Relationship link between landward vergence in accretionary prisms and tsunami generation, **Geology**, doi :10.1130/G38019.1.

10. A. K. Kuncoro, **N. Cubas**, S. C. Singh, M. Etchebes, P. Tapponnier (2015), Tsunamigenic potential due to frontal rupturing in the Sumatra locked zone, **Earth and Planetary Science Letters**, 432, p.311-322, doi :10.1016/j.epsl.2013.07.037.

9. B. Rousset, C. Lasserre, **N. Cubas**, et al. (2015), Lateral Variations of Interplate Coupling along the Mexican Subduction Interface : Relationships with Long-Term Morphology and Fault Zone Mechanical Properties, **Pure and Applied Geophysics**, doi :10.1007/s00024-015-1215-6.

8. **N. Cubas**, N. Lapusta, J. P. Avouac, H. Perfettini (2015), Numerical modeling of long-term earthquake sequences on the NE Japan megathrust : Comparison with observations and implications for fault friction, **Earth and Planetary Science Letters**, 419, p.187-198, doi :10.1016/j.epsl.2015.03.002.

7. **N. Cubas**, J. P. Avouac, P. Souloumiac, Y. Leroy (2013)c, Megathrust friction determined from mechanical analysis of the forearc in the Maule Earthquake area, **Earth and Planetary Science Letters**, 381,p.92-103, doi :10.1016/j.epsl.2013.07.037.

6. **N. Cubas**, J. P. Avouac, Y. Leroy, A. Pons (2013)b, Low friction along the high slip patch of the 2011 Mw 9.0 Tohoku-Oki earthquake required from the wedge structure and extensional splay faults, **Geophysical Research Letters**, 40, p.4231-4237, doi :10.1002/grl.50682.

5. **N. Cubas**, C. Barnes, B. Maillot (2013)a, Inverse method applied to a sand wedge : estimation of friction parameters and uncertainty analysis, **Journal of Structural Geology**, 55, p.101-113, doi :10.1016/j.jsg.2013.07.003

4. Z. Zhan, D. Helmberger, M. Simons, H. Kanamori, W. Wub, **N. Cubas**, Z. Duputel, R. Chu, V. C. Tsai, J.-P. Avouac, K. W. Hudnut, S. Ni, E. Hetland, F. H Ortega Culaciati (2012), Anomalously steep dips of earthquakes in the 2011 Tohoku-Oki source region and possible explanations, **Earth and Planetary Science Letters**, 353-354, p.121-133, doi :10.1016/j.epsl.2012.07.038.

3. **N. Cubas**, B. Maillot, C. Barnes (2010), Statistics of the experimental growth of a sand wedge, **Journal of Structural Geology**, 32, p.818-831, doi :10.1016/j.jsg.2010.05.010.

2. **N. Cubas**, Y.M. Leroy, B. Maillot, C. Barnes, M. Pubellier (2009), Prediction of thrusting sequence based on maximum rock strength and sandbox validation, **Trabajos de Geología**, 28.

1. **N. Cubas**, Y.M. Leroy, B. Maillot (2008), Prediction of thrusting sequences in accretionary wedges, **Journal of Geophysical Research**, B12412, 21 pages, doi : 10.1029/2008JB005717.

1.8 Ouvrages

N. Cubas (2022), Forearc Topography : Mirror of Megathrust Rupture Properties. In : The Seismic Cycle, p.173-187, John Wiley & Sons, Ltd, doi : 10.1002/9781394173709.ch7.

Rousset, B. et al. (2015), Lateral Variations of Interplate Coupling along the Mexican Subduction Interface : Relationships with Long-Term Morphology and Fault Zone Mechanical Properties. In : Bandy, W.L., Dañobeitia, J., Gutiérrez, C., Taran, Y., Bartolomé, R. (eds) Geodynamics of the Latin American Pacific Margin. Pageoph Topical Volumes. Birkhauser, Cham. doi : 10.1007/978-3-319-51529-8_14

1.9 Conférences

A. Galve et al., Fluids Circulation in Subduction Zones : How Fluids Impact Seismic/Aseismic Slip in Ecuador ? ***oral, AGU**, 2022*.

S. Pajang et al., The brittle-ductile transition signature in accretionary prism, insight from thermomechanical modeling. Application to Makran ***EGU**, 2022*.

S. Visage et al., Experimental strike-slip earthquakes ("ricequakes") ***EGU**, 2022*.

P. Souloumiac, M. Lefèvre, N Cubas, B Maillot, Y Klinger, Control of geometrical and mechanical parameters on strike-slip fault segmentation : insights from sandbox experiments - ***GEOMOD2021, 2021***

N. Cubas, Earthquake ruptures tied to long-lived plate interface deformation, **oral invité, EGU, 2021.**

S. Visage et al., Strike-slip fault in a sandbox : insight of on-and off-fault deformation from analogue modelling ***EGU**, 2021*.

S. Pajang et al., Seismic hazard of the Western Makran subduction zone : Effect of heat flow on frictional properties combining mechanical and thermo-mechanical modelling approaches, ***EGU**, 2021*.

P. Steer et al., Towards a better understanding of the impact of erosion on fault slip and seismicity ***EGU**, 2021*.

L. Baylé et al., Seismic cycle balance in Northen Chile from InSAR, ***EGU**, 2020*.

J. Gonçalves de Souza et al., Geopressure characterization : Preliminary results on 1D/2D modeling associated with gravity tectonics in the Amazon Fan (southeast compartment), Foz do Amazonas Basin, ***EGU**, 2019*.

M. Lefevre, et al., What controls the length of strike-slip fault segments ? Insight from sandbox experiments, ***EGU**, 2018*.

N. Cubas, Impact of great subduction earthquakes on the long-term forearc morphology, insight from mechanical modelling, **oral invité, EGU, 2017.**

N. Cubas, P. Souloumiac, T. Caer, How to predict deformation for geometrically and mechanically non-uniform accretionary wedges, ***EGU**, 2017*.

Leturmy P., P. Souloumiac, **N. Cubas**, Mechanical conditions for the activation of the Main Himalayan Thrust : A view from the limit analysis theory, ***EGU**, 2017*.

Steer et al., Typhoon-driven landsliding induces earthquakes : example of the 2009 Morakot typhoon ***EGU**, 2017*.

Steer et al., Typhoon-driven landsliding induces earthquakes : example of the 2009 Morakot typhoon ***oral invité AGU**, 2016*.

M. Lefèvre, P. Souloumiac, **N. Cubas** and Y. Klinger, Control of geometrical and mechanical parameters on strike-slip fault segmentation : insights from sandbox experiments ***poster, Geomod**, 2016*.

N. Cubas, P. Souloumiac, Landward vergence in accretionary prism, evidence for frontal propagation of earthquakes ? ***poster, EGU**, 2016*.

N. Cubas, P. Souloumiac, S. Singh, Landward thrusting in accretionary wedges : evidence for seafloor rupture ?, ***oral, AGU**, 2015*.

N. Cubas, J.P.Avouac, S. Singh, On the relationship between forearc deformation, frictional properties and megathrust earthquakes, ***oral, EGU**, 2014*.

Y. Klinger, T. K. Rockwell, **N. Cubas**, P. Souloumiac, Along strike-slip faults, do fault segments exist and how long are they ?, ***oral, AGU**, 2013*.

B. Rousset, S. E. Graham, **N. Cubas**, M. Radiguet, C. Lasserre, A. Socquet, M. Campillo, A. Walpersdorf, N. Cotte, C. DeMets, Interseismic deformation along the Mexican Subduction Zone : GPS-constrained coupling, and relationships with seismic and aseismic fault behavior, long term deformation and fault properties, ***poster, AGU, 2013***.

N. Cubas, A. Pons, P. Souloumiac, and Y. M. Leroy Normal faulting during overall compressive events in accretionary wedges, ***oral, EGU**, 2013*.

N. Cubas, J.P. Avouac, N. Lapusta, On the role of thermal pressurization in megathrust rupture : the case study of the 2011 Tohoku-Oki earthquake., **oral invité, EGU, 2013.**

N. Cubas, J.P. Avouac, N. Lapusta, On the relationship between forearc deformation, friction properties, pore pressure, and megathrust ruptures, ***oral, AGU**, 2012*.

N. Cubas, J.P. Avouac, N. Lapusta, Megathrust Friction in the Maule Earthquake Area in Relation to Forearc Morphology and Mechanical Stability, and to Earthquake Rupture Dynamics, ***oral invité, CIG**, 2012*.

N. Cubas, J.P. Avouac, N. Lapusta, Role of Thermal-Pressurization on megathrust ruptures, ***poster, SSA**, 2012*.

N. Cubas, J.P. Avouac, N. Lapusta, Megathrust Friction in the Maule Earthquake Area in Relation to Forearc Morphology and Mechanical Stability, and to Earthquake Rupture Dynamics, ***poster, AGU**, 2011*.

J.P. Avouac, S. Barbot, **N. Cubas**, N. Lapusta, Spatial variations of fault friction : observations and implication for fault dynamics, ***oral, EGU**, 2011*.

N. Cubas, J.P. Avouac, Y.M. Leroy, P. Souloumiac, Evidence for locally lower friction within the high slip area of the 2010 Maule Earthquake : dynamic weakening as an explanation of low apparent friction, ***poster, EGU**, 2011*.

N. Cubas, J.P. Avouac, Y.M. Leroy, P. Souloumiac, A mechanical analysis of the relation between forearc topography and frictional properties, ***poster, AGU**, 2010*.

N. Cubas, J.P. Avouac, Y.M. Leroy, P. Souloumiac, Prediction of forearc deformation based on limit analysis, ***poster, EGU**, 2010*.

B. Maillot, Y. Leroy, P. Souloumiac, **N. Cubas**, K. Krabbenhoft, C. Barnes, Thrust wedge tectonics : analogue, numerical, and analytical approaches, ***oral, Florence, Geomod** 2008.*

N. Cubas, B. Maillot, Y.M. Leroy, C. Barnes, M. Pubellier, Prediction of thrusting sequence based on maximum rock strength and sandbox validation, International meeting of young researchers in structural geology and tectonics,***oral, Oviedo, YORSGET** 2008*.

N. Cubas, B. Maillot, Y. M. Leroy, C. Barnes, Prédiction des séquences de chevauchements des prismes d'accrétion et des chaînes d'avant pays, ***oral, RST** 2008*.

N. Cubas, B. Maillot, C. Barnes, Growth of a sand wedge : experimental uncertainties, and inversion to deduce fault strength, ***poster, EGU** 2008*.

P. Souloumiac, **N. Cubas**, Y.M. Leroy, B. Maillot, Predicting in-situ stress and thrusting sequences in accretionary wedges, ***oral, EGU** 2008*.

N. Cubas, P. Souloumiac, B. Maillot et Y.M. Leroy, Predicting Folding Sequences Based on the Maximum Rock Strength and Mechanical Equilibrium, ***oral, AGU** 2007, Outstanding Student Presentation award*.

N. Cubas, B. Maillot, Y.M. Leroy, Predicting thrusting in normal and out-of sequences in accretionary wedge, ***poster, Montpellier, SUBCO**, 2007*.

N. Cubas, B. Maillot, Y.M. Leroy, Predicting sequences of thrusting in accretionary wedge, ***poster, EGU** 2007*.

1.10 Séminaires

Relations between short- and long-term deformation of subduction zones, Subduction meeting, **ENS, Paris**, 2022.

Assessing seismic and tsunamigenic hazards of Makran from mechanical modelling, **Trigger Conference**, Zajan, Iran.

Relations between forearc deformation, frictional properties and megathrust earthquakes, 2015, invited seminar at **STANFORD**, California, USA.

Relations entre déformation des avant-arcs, propriétés frictionnelles, pressurisation thermique et rupture sismique des megathrusts, 2013-2016 : **ISTERRE Grenoble**, **ISTO Orléans**, **Geoazur Nice**, **IPG Paris**, **ISTEP UPMC, Géosciences Rennes**.

On the relationship between forearc deformation, friction properties, pore pressure, and megathrust ruptures, 05/2013, **UCLA**.

Megathrust Friction in the Maule Earthquake Area in Relation to Forearc Morphology and Mechanical Stability, and to Earthquake Rupture Dynamics, 03/2012, **UCLA**.

Correlation between megathrust frictional properties, seismogenic behavior and forearc morphology, 01/2012 : **Beer Sheva university**, **Weizmann Institute of Science**.

Propriétés frictionelles du megathrust de la région du séisme de Maule Mw 8.8 déduites d'analyses mécaniques et de modélisation dynamique 3D de cycle sismique, 18/01/2012, **ENS, Paris**.

Megathrust Friction in the Maule Earthquake Area in Relation to Forearc Morphology and Mechanical Stability, and to Earthquake Rupture Dynamics, 11/01/2012, **GFZ, Postdam**.

Spatial variations of megathrust frictional properties in the 2010 Maule earthquake area, 05/2011, **GFZ, Postdam**.

Corrélation entre la segmentation morpho-tectonique des avant-arcs et les propriétés frictionnelles des megathrusts, Une analyse mécanique, 04/2011, **GET, Toulouse**.

A mechanical analysis of the relation between forearc topography and frictional properties, 22/02/2011, **Tectonics Observatory, Caltech**.

Relation entre segmentation de l'avant-arc et propriétés frictionnelles des megathrusts, Une analyse mécanique, 01/2011, **Université de Cergy-Pontoise**, **IPGP**.

Mécanique des chaînes plissées : approches de terrain, analogique et numérique, 04/2010, **UPMC**.

Thrusting sequences : mechanical predictions, analogue validation and application to the Pampa Tril Fold (Agrio FTB, Argentina), 10/2009, **Tectonics Observatory, Caltech**.

Séquences de chevauchement, prédictions mécaniques, validation analogique et application à la chaîne de l'Agrio (Argentine), 03/2009, **IFP, France**.

L'Agrio : chaîne thin ou thick-skinned ? Apports de la modélisation mécanique, 10/2008, **Total Pau, France**.

Predicting thrusting sequence by optimization : Application to the Agrio fold-and-thrust belt ?, 11/2007, **Total Austral, Argentina**.

Predicting thrusting sequence by optimization : application to fold-and-thrust belts and accretionary wedges, 12/2007, **Tectonics Observatory, Caltech**.

1.11 Animation recherche

Conférences

— Comité d'organisation du Congrès GEOMOD 2023 (Congrès européen réunissant les différentes communautés de modélisation).

— Comité d'organisation du Workshop FRENSZ juillet 2023.
— Comité d'Organisation des Journées Failles Actives, 13 et 14 Septembre 2022 (colloque scientifique national).
— Convener de la session 'Fold-and-thrust belt session' de l'EGU (2014, 2016, 2017).
— Co-convener de la session 'Mechanical heterogeneity and their transient evolution along fault zones' de l'EGU 2014.

Reviewer

Environ 5 reviews par an (BSGA, EPSL, GJI, Journal of Geodyn., JGR, JSG, Scientific Report, Tectonics, Tectonophysics, ...)

1.12 Responsabilités

Responsabilité au sein du laboratoire

Co-responsable de l'axe Aléa.
Co-responsable des séminaires de l'ISTeP.
Conseil de l'UMR depuis 2019.

Responsabilité au sein de l'UFR

Conseil de la Licence Sciences de la Terre depuis 2023.

Responsabilités nationales :

Jury de thèse

— Gaëlle Bénatre, IPGP, 2022, **examinateur**.
— Pierre Romanet, IPGP, 2017, Fast algorithms to model quasi-dynamic earthquake cycles in complex fault networks, **examinateur**.
— Xiaoping Yuan, ENS, 2016, Extensional collapses in the overpressured frictional upper crust based on Limit Analysis, **rapporteur**.

Comité de recrutement

Comité de selection Maître de conférences : 2019 Université de Nice-Sophia Antipolis, 2018 Université de Cergy.

Commission

Commission d'attribution des primes 2019 ; sélection des ATER 35-36 2018.

Enseignement

2.1 Enseignements

J'interviens essentiellement en :

— Geosciences 1 (L1) : Initiation aux différents domaines des sciences de la Terre externe (circulation atmosphérique et océanique, hydrologie, paléoclimatologie) et interne (minéraux et roches, tectonique, sismicité, géodynamique, géomorphologie, ressources,..)
— Geodynamique (L3) : Etude des grands contextes géodynamiques (méthodologie : cinématique, mécanismes aux foyers, géodésie, sismique réfraction et refléxion, gravimétrie).
— Stage de Cartographie de Barles (L2 - L3)
— Géomorphologie (M1) : Introduction - origine de la topographie, Interactions court-terme tectonique/érosion, projet de modélisation et bibliographique.
— Grandes Questions Environnementales (M1) : Synthèse écrite et orale d'articles autour d'une grande question environnementale.
— Leçon à l'Agrégation.
— Mécanique de la lithosphère (M2, sous différentes versions).
— Géorisques (M2) : le risque sismique.
— Intéractions fluides-roches (M2) : Fluides et sismicité
— je suis également intervenue en Geophysique (L3) Théorie du prisme critique, Problème inverse, Modélisation analogique, Informatique (L1), ...

2.2 Responsabilités enseignements

Je suis responsable TP de l'UE Geosciences 1 pour les PEIP (préparation intégrée pour Polytech), ce qui implique la gestion de l'organisation des TP, des examens, des jurys. Je suis également responsable des UE Grandes Questions Environnementales en M1 et Mécanique de la lithosphère en M2. J'ai été responsable de l'UE Stage en laboratoire, ce qui implique la mise en place d'une banque de propositions de stage, l'orientation des étudiants, la mise en place de stage pour les étudiants ne trouvant pas de stage, et l'évaluation de l'UE durant 2,5 jours par présentation de poster. De 2015 à 2018, j'ai été responsable de l'UE Stage de terrain, ce qui implique l'organisation de la réunion de présentation des stages, l'orientation des étudiants, de repartir les étudiants pour optimiser le nombre de stage, de s'assurer de la bonne organisation des ces stages.

2.3 Responsabilités pédagogiques

Afin de mieux connaitre la formation dispensée à SU, j'ai pris à mon arrivée la responsabilité pédagogique de la Licence 3. Cela m'a permis de découvrir le système universitaire, les

différents parcours dispensés, et d'aquérir un regard critique sur les méthodes d'enseignement. J'ai quitté cette responsabilité en 2018, pour me réinvestir dans la recherche et préparer HDR et projets. Avec environ 150 étudiants par an, cette responsabilité implique de prendre en charge :

- l'accompagnement et l'orientation des étudiants :
  - accueil/discussion avec étudiants pour choix d'options, de stage (en labo, de terrain, mais aussi stage sur plusieurs mois), choix de master
  - l'organisation de présentations d'UE et présentation de master.
  - l'accompagnement d'étudiants en difficulté (santé, personnelle, en échec scolaire)
  - la participation aux JOR (journées d'orientation réfléchies), JPO (journées portes ouvertes).
- l'organisation de l'emploi du temps (vérification de l'emploi du temps, réunions, stages de terrain, jury)
- la Préparation des jurys (voire préparation des PV) de Licence et Bi-disciplinaire
- la mise en place et traitement des sondages d'évaluation des UE
- la discussion avec les équipes enseignantes des méthodes d'évaluation
- la synthèse des UE de la licence avec descriptif, mode d'évaluation, compétences requises et compétences finales.
- l'évaluation des dossiers campus France, commission pour étudiants souhaitant intégrer notre formation après prépa et une année passes
- la participation et l'organisation de réunions pédagogiques : entre équipes pédagogiques de toutes les formations avec la direction, pour la préparation hceres, commissions pédagogiques de l'UFR, cafés pédagogiques de notre formation.
- la participation à divers commissions pédagogiques

Recherche :
From long- to short-term deformation of forearc wedges

3.1 Introduction

What controls the location and extent of mega-earthquakes in subduction zones is a long-standing problem in earth sciences. Many authors have searched for correlations, such as with convergence rate, slab age, sediment thickness, upper plate absolute motion or strain, without obtaining clear convincing trend [e.g., Heuret et al., 2011, 2012, Bletery et al., 2016]. Nowadays, the prevalent explanation relies on the megathrust frictional properties, described within the framework of rate-and-state friction laws, 2D empirical laws established to fit lab experiments [Dieterich, 1979, Rice and Ruina, 1983, Ruina, 1983, Scholz, 1998, Perfettini et al., 2010]. Along with these properties, pore fluid pressure [Saffer and Tobin, 2011], inherited stress states [Konca et al., 2008, Kaneko et al., 2010] or seafloor roughness and geometry [Kodaira et al., 2000, Wang and Bilek, 2014, Bletery et al., 2016, Lallemand et al., 2018, van Rijsingen et al., 2018] are also commonly incriminated.

The prediction of the location and spatial extent of mega-earthquakes mostly relies on Global Navigation Satellite Systems providing patterns of slip deficit between tectonic plates [e.g., Moreno et al., 2010]. The inferred coupling models are interpreted withing the elasto-dynamics and rate-and-state friction laws framework. However, most geodetic observations are made onshore, often at large distances from the locked portion of the megathrust, with poor resolution near the trench [e.g., Loveless and Meade, 2011]. Moreover, geodetic observations represent only a small fraction (tens of years) of an interseismic earthquake cycle (hundreds of years), which might vary with time [e.g., Marill et al., 2021], and needs to be corrected from potential short (days-) to extremely long (decadal-scale) transient events [e.g., Radiguet et al., 2012, Mavrommatis et al., 2014]. The viscoelastic relaxation can also cause evolution of the observed deformation during the interseismic period [Wang et al., 2003, 2012].

Furthermore, the more we monitor subduction zones, the more we detect temporal changes in behaviors that are incompatible with the sole application of the rate-and-state friction laws. For instance, along the Ecuadorian and Chilean subduction zones, different slip behaviors, of supposed opposite frictional properties (rate-strengthening vs rate-weakening) have been recorded along the same megathrust portion [Rolandone et al., 2018, Tissandier et al., 2023]. Along the Chilean and Japan subduction zones, large earthquakes or large slip areas unexpectedly occurred along weakly coupled patches [Perfettini and Avouac, 2014, Béjar-Pizarro et al., 2013]. Studies of exhumed fault zones show that faults are not discrete planes but rather complex zones, composed of linked segments embedded in a damage zone [e.g., Faulkner et al., 2010, Vannucchi et al., 2012]. Moreover, as shown by core sampling, faults resemble more to melange shear zones, that can experience both ductile and brittle deformation controlled by temporal changes

in strain rate or effective stress [Fagereng and Sibson, 2010, Fagereng and Beall, 2021]. Consequently, megathrust cannot be considered as formed of a unique plane, with a single composition and a single depth-dependent rheology.
Seafloor roughness, inducing upper plate damage, has been repeatedly invoked as acting as barriers to earthquake propagation [Kodaira et al., 2000, Wang and Bilek, 2014, Geersen et al., 2015]. As a consequence, megathrust can neither be considered as a unique fault plane embedded in an homogeneous nor purely elastic medium.
Although models based on rate-and-state friction laws are a powerful tool to mimic earthquake cycles [e.g., Barbot et al., 2012, Cubas et al., 2015, Thomas et al., 2017], they are far too idealized to account for the rheological and geometrical complexity of plate interfaces. Hence, they heavily rely on frictional complexity along a simplified interface to explain a posteriori complex observations making their utility for prediction minimal and their cross-validation with observation impossible. To improve our capacity to assess seismic hazard, it is crucial to develop a true physical understanding of the megathrust behavior and of the slip deficit patterns.

In 1983, Savage proposed that the upper plate deformation acquired during a seismic cycle was purely elastic and thus non-permanent. The co- and post-seismic subsidence was thought to entirely counterbalance the coastal interseismic uplift [Plafker and Savage, 1970], leaving in the dark the question of the construction of the upper-plate relief. In 1996, Ruff and Tichelaar [1996] showed a correlation between the location of the downdip edge of the seismogenic zone with the coastline, suggesting a link between the seismogenic behavior of the megathrust and the upper plate morphology. In 2003, Song and Simons published an impacting study showing a correlation between negative anomalies of gravity (mostly related to forearc basins) and large seismic asperities for a certain number of subduction zones. Positive anomalies appeared correlated to aseismic zones. These anomalies were interpreted as reflecting spatial variations of the frictional and rupture properties of the megathrust. **These correlations imply an along-dip and along-strike persistence of the megathrust properties over several hundred thousand years. This persistence assumed, the topography and upper plate deformation could then directly mirror the mechanical properties of the megathrust.**

During the past decade, my research focused on the relationships between the short- and long-term deformation of forearcs. From mechanical analysis of the topography and of the deformation, I have searched to constrain the mechanical properties and the rheological and geometrical complexities of the plate interface. By comparing these properties and complexities with the megathrust seismogenic behavior, I have searched to decipher the fundamental parameters controlling the extent of mega-earthquakes.

In this HDR, I first start with a brief description of the structure and seismogenic behavior of forearcs. I present the main parameters invoked to explain the along-dip and along-strike variation of the slip behavior of megathrusts. I then present the different mechanical methods used to study forearcs, and briefly discuss how each one of them can be used to constrain the properties of the plate interface. The second part is dedicated to the main results of the studies that I have conducted on forearc wedges. I show how the deformation and the morphology of the forearc provide an access to the properties of the megathrust. Once the short- and long-term relationships established, I discuss how the deformation and the morphology can help us to improve the assessment of seismic and/or tsunamigenic hazard of a subduction zone, in particular in weakly constrained regions. I then discuss the limits of our actual conception of a plate interface, and how it limits our understanding of megathrust short-term behaviour. In recently published papers, I show how structural and rheological complexities along the plate interface can affect earthquakes propagation and the overall seismic cycle. Finally, I propose a project aiming at providing a true physical understanding of the megathrust behaviour.

Although not presented here for sake of conciseness, the work presented here has largely benefited from studies conducted in parallel with other PhD students in different contexts. For

example, the work of Marthe Lefèvre (Segmentation of strike-slip faults, the case of the Levant fault) and Sarah Visage (Evolution of aseismic and seismic off-fault deformation of strike-slip faults, insight from analogue modelling) have helped me to understand the fundamental role of the segmentation of faults and of the off-fault deformation on the initiation, propagation and arrest of earthquakes. The work of Juliana Goncalves de Souza, on the origin and evolution of fluid overpressures in the Amazon gravitational prism, allowed me to understand the different processes generating overpressures, their different impacts on deformation, and their dependence on the thermal state of the crust. Finally, the work of Louise Jeandet allowed me to understand the role of a small variation in the topographic load on a fault seismic cycle and on the regional seismicity.

3.2 Forearc wegdes

3.2.1 Forearc structure

Forearc wedges constitute the frontal part of subduction zones. They are often described as composed of an outer wedge at the front separated from an inner wedge by an outer-arc-high (Figure 3.1). The outer wedge is formed by imbricated slices generating a topographic slope. The thrusts are generally of seaward vergence. The inner wedge is formed by older, more consolidated and possibly metamorphized accretionary and continental crust material. The inner wedge is usually covered by a basin, reducing the local topographic slope [e.g., Noda, 2016a]. In general, the forearc basin shows neither compressional nor extensional deformation [Byrne et al., 1988, Noda, 2016a]. The outer-arc-high is often associated to fore- or back-thrust splay faults.

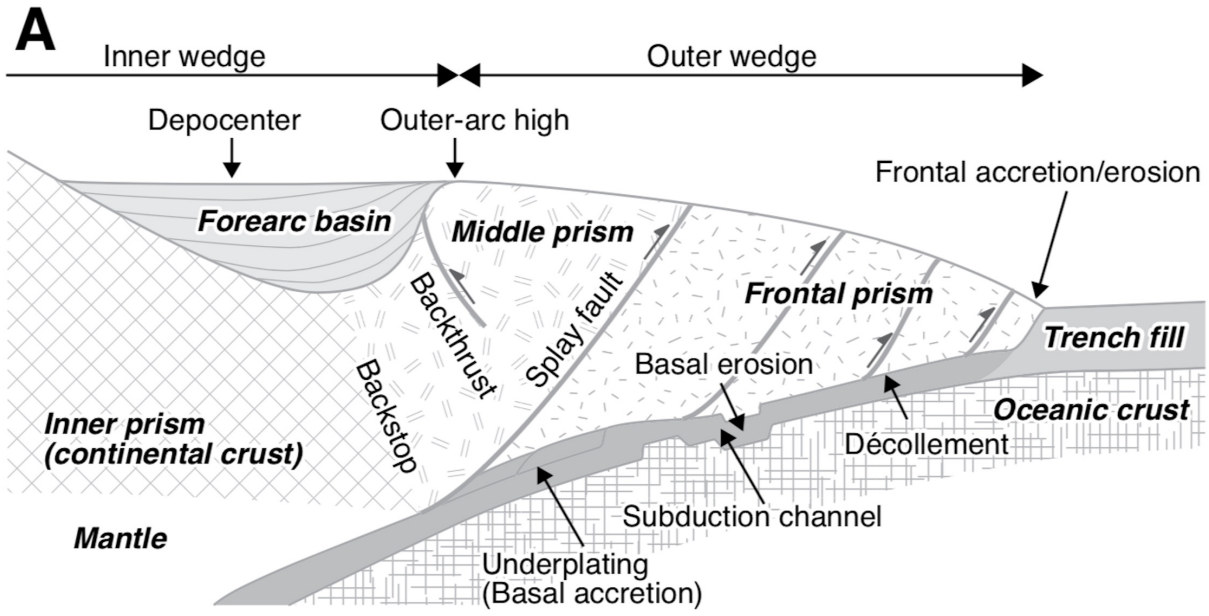

FIGURE 3.1 – Forearc wedges structure, extracted from Noda [2016a].

Forearcs are classified according to the thickness of their sediment income as either accretionary or erosional [Von Huene and Scholl, 1991, Clift and Vannucchi, 2004, Noda, 2016a] (Figure 3.2a-c). Along accretionary prisms, the fluid-rich sediments of the subducting plate are accreted by thrusting to the overriding plate, forming a long imbricated thrust zone, and can also be partly subducted beneath the wedge (Figure 3.2a). These sediments may return deeper to the overriding plate through underplating (Figure 3.1). Some margins characterized by very

thin to no sediment income, have only very narrow and steep frontal prisms composed of very few slices originating from the thin sedimentary layer or material from the upper plate (Figure 3.2d-e). These margins are described as erosional : the upper plate is eroded by abrasion due to the roughness of the subduction plate, related to old horst and grabben structure or seafloor features such as ridges or seamounts [Hilde, 1983, Von Huene and Scholl, 1991, Clift and Vannucchi, 2004] (Figure 3.2d-e). Along northern Chile, the long-term erosional state of the margin was deduced from the presence of outcrops of Mesozoic volcanic arcs in coastal cliffs and from the landward migration of volcanic arcs during the past 100 Myr [Rutland, 1971, Hartley et al., 2000, Scholl and von Huene, 2007]. Along the Peru and Japan (Honshu) margins, basal erosion was deduced from the forearc subsidence [von Huene and Lallemand, 1990]. Accretionary or erosional forearc wedges can both be associated with either compressional or extensional deformation, although normal faulting, that may result from the removal of the forearc material [von Huene and Ranero, 2003, Dominguez et al., 1998] is more commonly observed along erosional margins.

The origin of some prism features remain unexplained. For instance, along some sections of the Cascadia and Sumatra acrretionary prisms, the thrust sequence is of landward vergence instead of the classical seaward one (Figure 3.3). Along a décollement, the maximum compressional principal stress plunges seaward [Hafner, 1951]. Hence, landward-vergent thrusts have larger dips than seaward-vergent thrusts. Uplifting material above a seaward-vergent thrust requires less gravitational energy than along a landward-vergent thrust, which explains the predominance of seaward vergence. For negligible basal shear stress and a strong wedge, conjugate faults tend to have the same dip. In that case, both faults can be active and form a pop-up [Hafner, 1951]. Based on this argument, and the low tapers measured along these landward prisms, the landward vergence has repeatedly been attributed to a low basal friction [MacKay, 1995, Adam et al., 2004, Gulick et al., 1998]. This low basal friction has been suggested to result from a high pore pressure, built from the compaction of a large amount of sediments [Adam et al., 2004]. However, some accretionary prisms displaying both very large sediment thickness (>4 km) and high pore pressure, such as Barbados [Bangs et al., 1990] or Makran (Pakistan) [Kukowski et al., 2001], did not develop landward-vergent thrusts. Moreover, no over-pressure as been inferred from drilling and Vp measurements along the landward accretionary prism of Cascadia [Han et al., 2017]. Clear landward vergence in analogue models has only been obtained with a viscous basal layer submitted to strong lateral wall effects [Gutscher et al., 2001, Zhou et al., 2016]. Moreover, the deformation style of the Cascadia wedge is not in good accordance with a viscous behaviour [Adam et al., 2004] and strike-slip faults are not systematically observed to justify strong lateral effects. The Cascadia wedge though shows one specificity compared to common prisms : according to coupling models, the wedge is locked up to the trench [Michel et al., 2019, Small and Melgar, 2021] and the location of this landward vergence matches with high slip patches of the 1700 Mw 9 earthquake [Wang et al., 2013] (Figure 3.4b). The landward profiles along the Sumatra subduction zone also correlate with co-seismic ruptures up to the front (Figure 3.4a).

The geological and mechanical conditions leading to the forearc segmentation (accretionary prism, outer-arc-high and forearc basin) are not clearly resolved yet. Mutliple explanations have been advanced to explain forearc basins. These basins were first thought to result from the seaward widening by accretion at the trench and from the tilting by uplift of the outer-arc high [Seely, 1979, Noda, 2016a]. Some authors have linked the basins to temperature and strength-controlled changes [Byrne et al., 1988, Saffer and Bekins, 2002], to subduction erosion [Vannucchi et al., 2001, von Huene et al., 2004], or to the simple accommodation space created by the landward deepening of the slab [von Huene et al., 2004, Fuller et al., 2006]. A correlation between negative anomalies of gravity, forearc basins and large seismic asperities for about 70% subduction zones led other authors to relate these basins to the seismogenic behaviour of

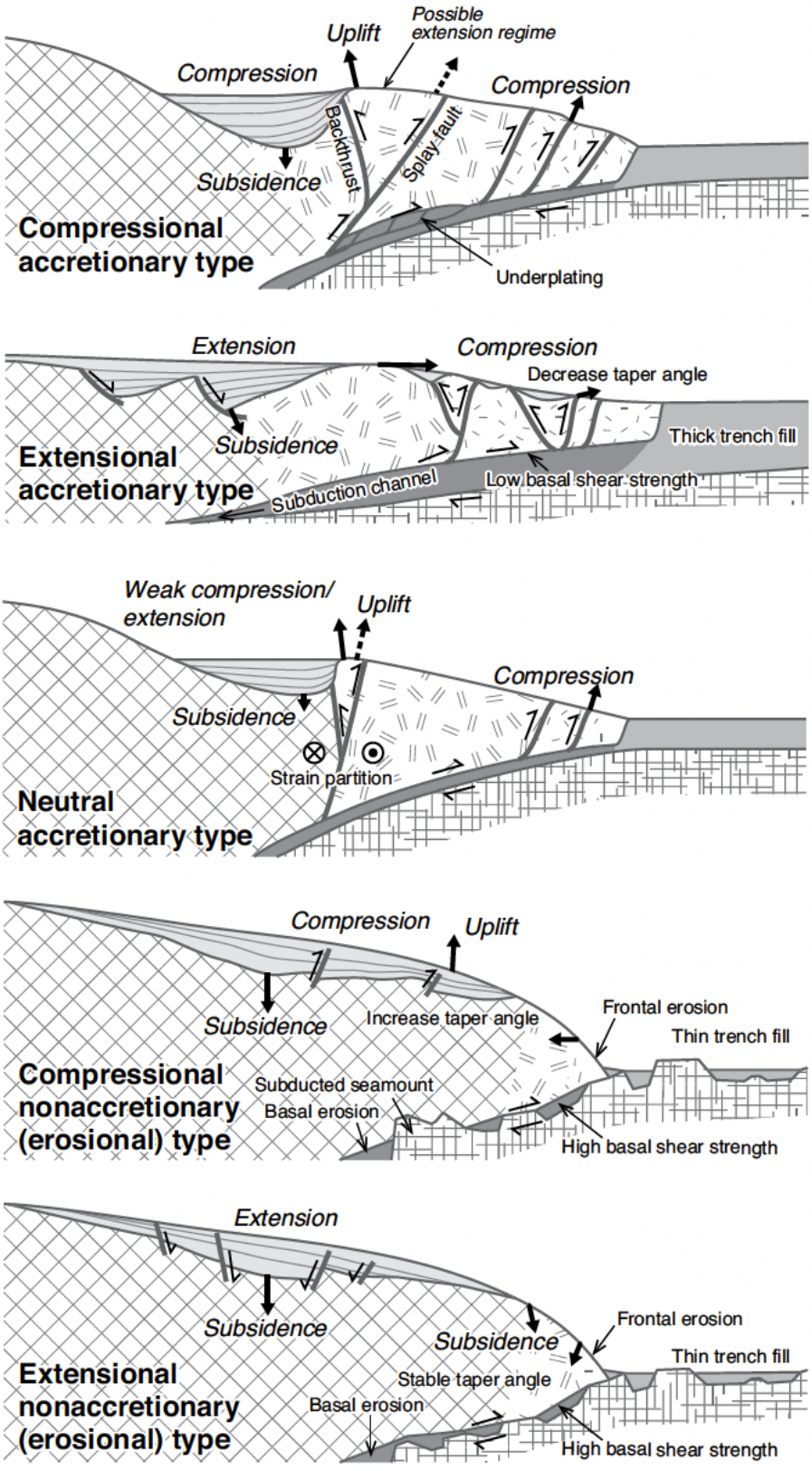

FIGURE 3.2 – Classification of forearc wedges, extracted from [Noda, 2016a].

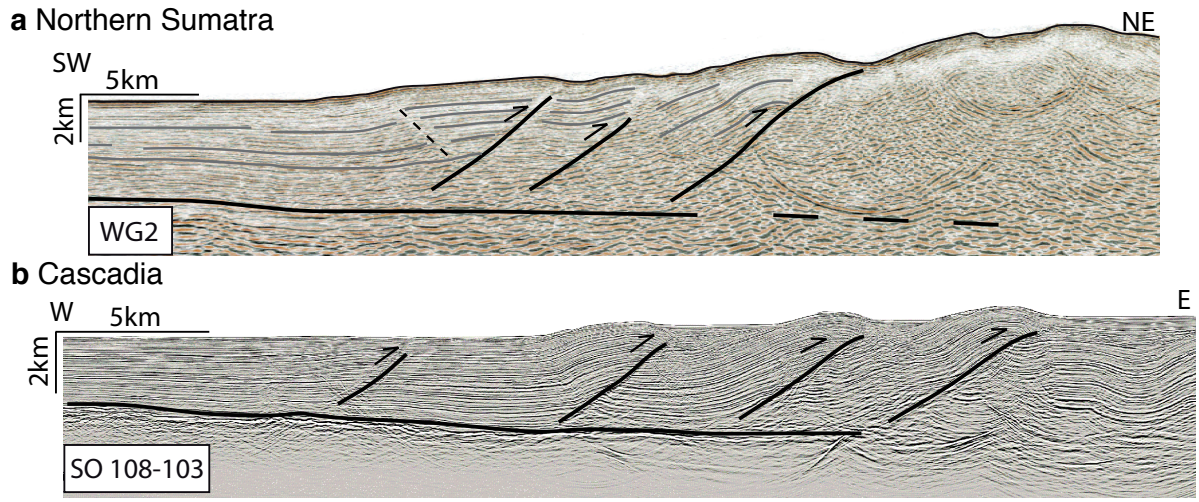

FIGURE 3.3 – Landward-vergent accretionary prisms. a. Seismic profile WG2 in northern Sumatra [Moeremans et al., 2014], location on Figure 3.4. b. Seismic profile SO 108–03 in Cascadia [Adam et al., 2004], location on Figure 3.4.

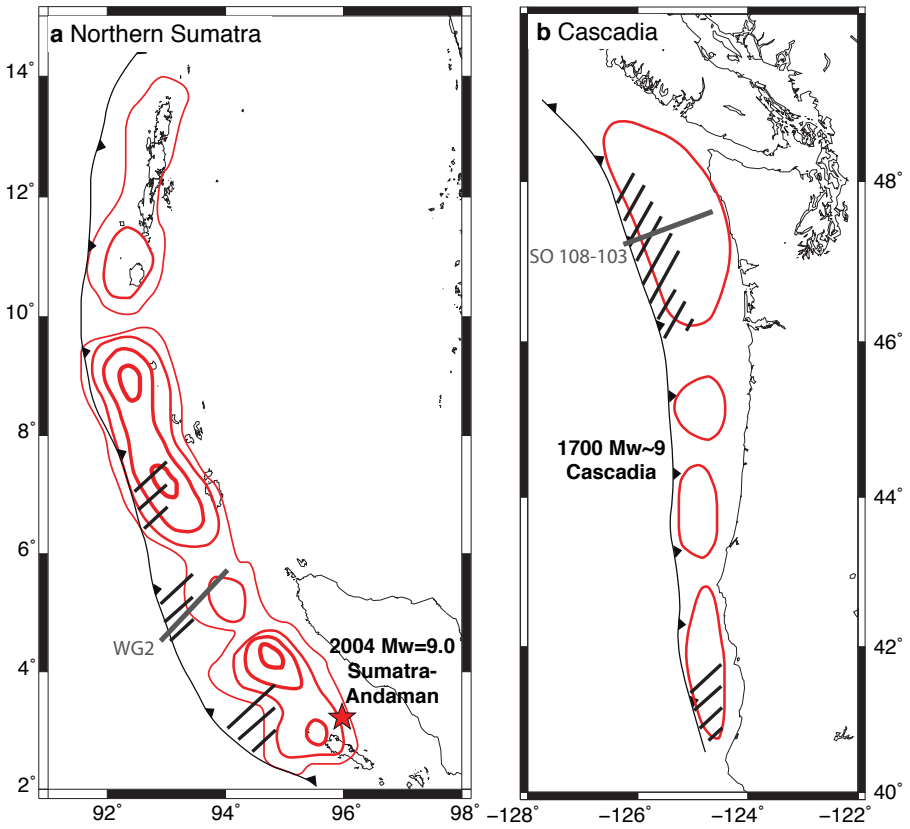

FIGURE 3.4 – a. Comparison of the observed landward-vergent thrusts in northern Sumatra (black lines ; compilation from [Dean et al., 2010, Gulick et al., 1998, Moeremans et al., 2014] with coseismic slip of the 2004 Mw 9.1 Sumatra-Andaman earthquake (slip contours in red every 5 m increment ; [Chlieh et al., 2007]. b. Comparison of the observed landward-vergent thrusts in Cascadia (black lines ; compilation from MacKay [1995], Adam et al. [2004], Gulick et al. [1998] with the estimated slip contours of the 1700 Cascadia earthquake considering a trench-breaking rupture scenario with a Mw 8.9 [Wang et al., 2013].

the megathrust [Song and Simons, 2003, Wells et al., 2003] (Figure 3.5).

Splay faults are another intriguing feature. As the Nankai splay fault, they usually mark the limit between this forearc basin and the accretionary prism (Figure 3.7), and are assimilated to out-of-sequence thrusts whose reactivation relates to the conservation of the critical taper, changes in pore pressure, to the incoming plate roughness or underplating [Strasser et al., 2009]. In addition, the Nankai fault seems to mark the up-dip limit of the seismogenic zone, and as such, is associated to a high tsunamigenic risk [Park et al., 2002, Strasser et al., 2009]. The correlation between its location and the up-dip limit of the locked zone suggests a possible link between these features and the seismogenic behaviour of the megathrust [Park et al., 2000, 2002, Cummins and Kaneda, 2000].

From these observations, it clearly appears that the understanding of the forearc structure can not be fully captured without considering its mechanics at the seismic cycle scale.

3.2.2 Seismogenic behaviour of forearc wedges

Contrasting modes of slip

The surge of great subduction earthquakes during the 2004-2014 decade and the development of geodetic studies have led to a refined image of the megathrust behaviour. Megathrust are now described as paved of interfingered seismic and aseismic patches [Chlieh et al., 2008, Perfettini et al., 2010, Lay et al., 2012]. In a simplified view, megathrust are segmented in four major domains [Lay et al., 2012] (figure 3.7) :

— a shallow aseismic segment, from the trench to 10-15 km depth, where tsunami earthquake can occur (Domain A) ;
— a seismogenic zone usually located between 15 to 35 km depth, composed of seismic patches where large earthquakes nucleate (Domain B, figure 3.7) ;
— a transitional zone, partly creeping and where intermediate earthquakes can also nucleate, located from the down-dip limit of the fully locked zone to the deep creeping zone (Domain C, figure 3.7) ;
— a deep creeping zone or a deep segment characterized by slow slip events and seismic tremors (ETS) before reaching the brittle/ductile transition (Domain D, figure 3.7).

This description though does not account for the significant variations of slip modes along strike [e.g., Nocquet et al., 2014, 2017] (Figure 3.8).

The along-dip and along-strike segmentation is interpreted as resulting from depth-varying megathrust frictional properties and pore fluid pressure [Perfettini et al., 2010, Kaneko et al., 2010, Saffer and Tobin, 2011] as well as inherited stress states [Konca et al., 2008, Kaneko et al., 2010] seafloor roughness and geometry [Kodaira et al., 2000, Wang and Bilek, 2014, Bletery et al., 2016]. I now describe in more details how these properties control the mechanical behaviour of the megathrust.

Depth-dependent megathrust frictional properties

Fault zones are described as composed of an upper brittle part, governed by pressure dependent frictional sliding, that progressively transitions to a deeper ductile behaviour with a grain, temperature and rate-dependent viscous rheology. In the brittle domain, fault gouges are composed of cataclasites, with one or more discrete fault cores embedded in a fractured damage zone [Faulkner et al., 2010]. The deeper viscous part is characterized by mylonites within broad (>km) foliated shear zones [Carreras, 2001, Rennie et al., 2013]. Classical strength profiles usually describe abrupt frictional-viscous transition. However exhumed rocks rather show a more gradual transition, depending on not only pressure, temperature and grain size but also strain rate, fluids, and microstructure [e.g., Sibson, 1980, 1982, Hobbs et al., 1986, Shimamoto,

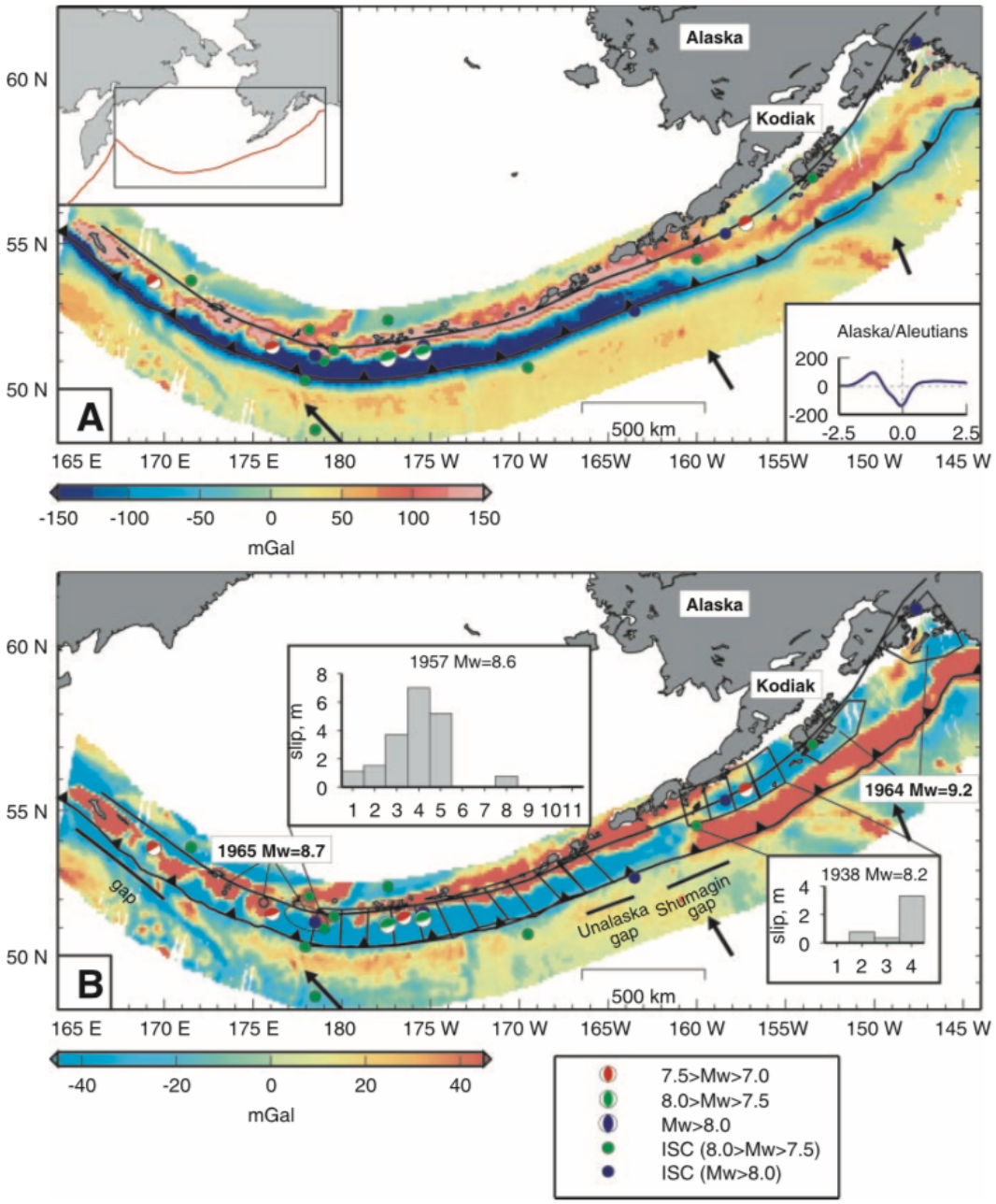

FIGURE 3.5 – a. Observed free-air gravity anomaly for the Alaska/Aleutian subduction zone. b. Estimated Trench Parallel Gravity Anomaly (TPGA) for the Alaska/Aleutian subduction zone. The color bar shows the amplitude of TPGA. Areas with large coseismic slip during the 1964 Alaska and 1965 Aleutian earthquakes are outlined in black lines. Trench location and 50-km slab isodepth contour are indicated by the barbed and thick black lines, respectively. Directions of relative plate convergence are shown as arrows. Extracted from [Song and Simons, 2003] .

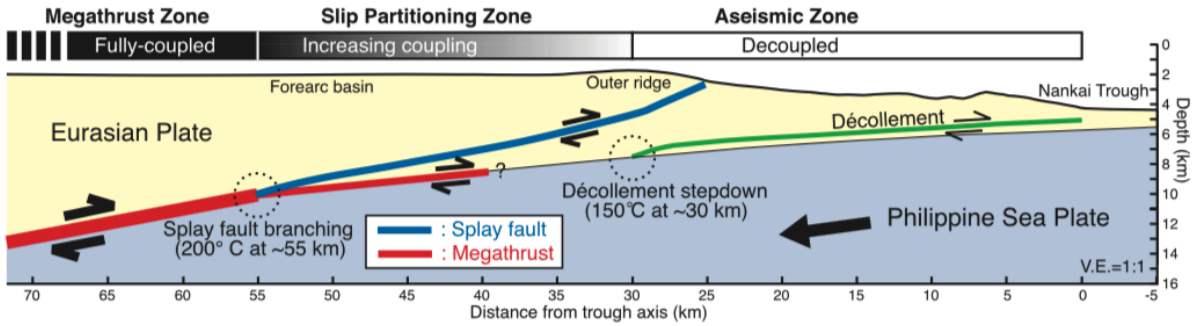

FIGURE 3.6 – Nankai splay fault : updip limit of the seismogenic zone. Gray scale shows degree of interplate coupling. Extracted from [Park et al., 2002].

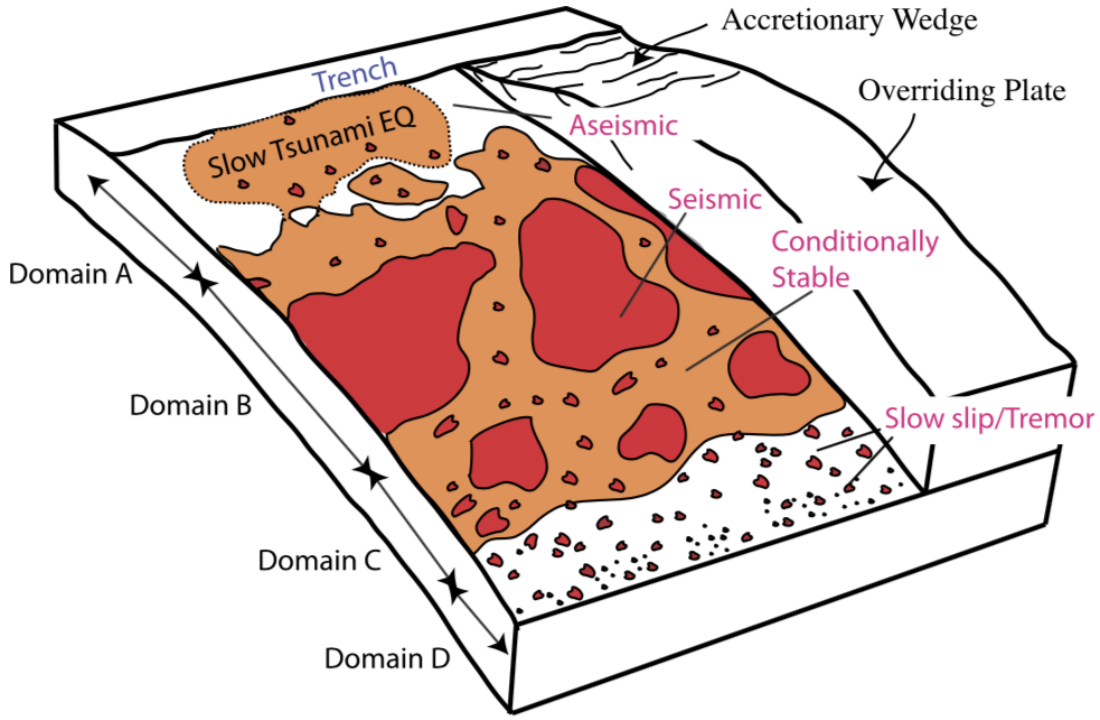

FIGURE 3.7 – Spatial variation of megathrust rupture characteristics from Lay [2015]. Red : Seismic asperities, where earthquakes can nucleate ; orange and white : aseismic stable or episodic sliding. Domain A : can generate tsunami earthquakes related to high pore fluid pressure. Domain B : generate large megathrust earthquakes with modest amount of short-period radiation. Domain C : patchy, can generate intermediate slip earthquakes with coherent short-period radiation. Domain D : dominated by aseismic sliding, with small unstable patches triggering tremors when slow slip events occur.

1989, White, 1996, Lin et al., 2005, Kirkpatrick and Rowe, 2013].

Along the brittle/frictional part of the fault, the depth-dependence of the seismogenic behaviour is described using the phenomenological rate-and-state friction laws, formulated to fit lab experiments [Dieterich, 1979, Rice and Ruina, 1983, Ruina, 1983]. The ageing formulation writes :

$$\tau = (\sigma - p)\left(\mu_o + a \ln \frac{V}{V_o} + b \ln \frac{V_o \theta}{L}\right) , \tag{3.1}$$

$$\dot{\theta} = 1 - \frac{V\theta}{L} , \tag{3.2}$$

where σ is the normal stress, p is the pore pressure, $\sigma - p = \sigma^{eff}$ is the effective normal stress,

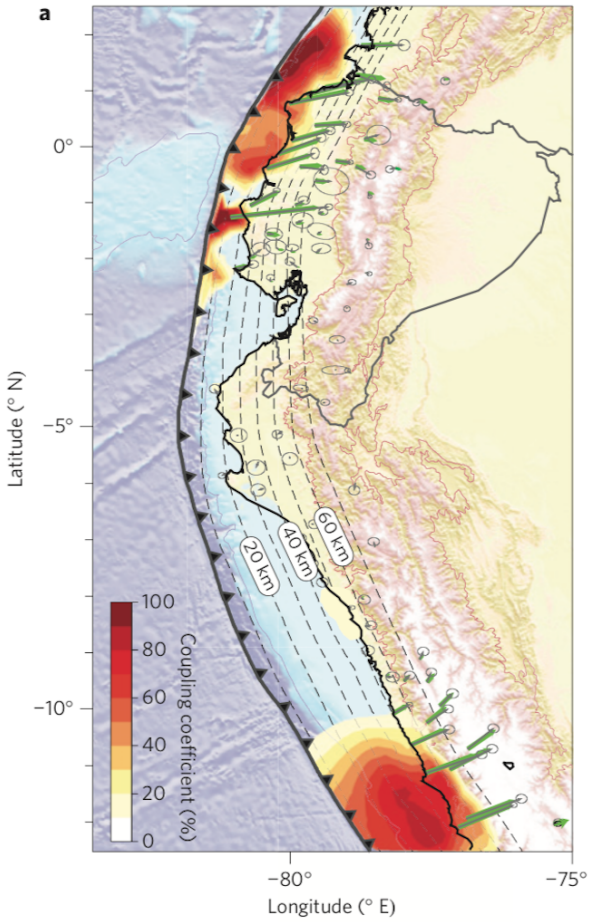

FIGURE 3.8 – Spatial distribution of interseismic coupling along Ecuador and Peru subduction zone. From 3 to 10^oS, the megathrust is uncoupled. Dashed lines are depth contours of the subduction interface every 10 km. From Nocquet et al. [2014].

μ_o and V_o are the reference friction coefficient and slip rate, V the slip rate, $a > 0$ and $b > 0$ are rate and state parameters, θ is a state variable which can be interpreted as the average age of the population of contacts between two surfaces, and L is the characteristic slip for state evolution [Dieterich, 1979, Rice and Ruina, 1983, Ruina, 1983].

At constant slip rate, the shear stress τ evolves towards steady state :

$$\tau_{ss} = (\sigma - p)\left(\mu_o + (a-b)\ln\frac{V}{V_o}\right) . \tag{3.3}$$

With a $a - b < 0$, the friction is rate-weakening and leads to a stick-slip behaviour on large enough fault patches (larger than the nucleation size). For $a - b > 0$, the friction is rate-strengthening and, since no acceleration is possible, leads to stable sliding. Note, that rate-strengthening areas can also be locked, for example, after they experience seismic slip that drops their shear stress levels [Noda and Lapusta, 2013] ; and although rate-strengthening areas can not nucleate earthquakes, seismic slip can however propagate along these patches for high enough stresses. The primary parameter that determines stability, $a - b$, is a material property. This framework considers that rate-strengthening prevails at shallow depths where poorly lithified rocks accommodate displacement by granular flow and below the seismogenic zone, at the onset of quartz crystal plasticity [Blanpied et al., 1991, 1995]. In a simplistic view, low coupled patches inferred from geodesy are usually associated to a rate-strengthening behaviour of the megathrust, and highly coupled patches to rate-weakening.

Mineralogy transition

To the very first order, up- and down-dip limits of the seismogenic zone appear thermally controlled [Hyndman et al., 1997, Oleskevich et al., 1999]. Consequently, this depth-dependence transition of behaviour has been interpreted as resulting from the progressive diagenesis and mineralogical transformation of the subducting clay rich sediments. The up-dip limit of the seismogenic zone, ranging between 100-150^o is attributed to the smectite/illite transition [Hower et al., 1976, Hyndman et al., 1997, Oleskevich et al., 1999], and supported by experimental studies [Den Hartog et al., 2012], although other mineralogy transformations (as illite to muscovite) might also enter into play [Den Hartog et al., 2013]. The down dip 350^o limit corresponds to the onset of crystal plasticity of quartz, the most ductile of the major minerals of crustal rocks [Blanpied et al., 1991, 1995], and would thus correspond to the brittle/ductile transition [Hyndman et al., 1997, Oleskevich et al., 1999]. For cold subduction zone, this isotherm might be crossed below the upper plate Moho, and brittle-ductile transition related to serpentinite [Hyndman and Peacock, 2003].

Fluid pressure

Fluids are trapped in inter-granular and fracture porosity of the subducting sediments and igneous crust and present within hydrous minerals. These fluids are progressively released during the subduction process. The first release mechanism is related to compaction, rapid burial generating disequilibrium compaction between 3-7km depth [Bekins and Dreiss, 1992, Bray and Karig, 1985]. As depth and temperature increase, fluids are then released by dehydration reactions, the largest dehydration fluid source being the smectite-illite transition [Bethke and Altaner, 1986]. Other reactions take place between 150-300^o, however, their depth range and importance are less constrained [Saffer and Tobin, 2011]. The depth distribution of these processes obviously depends on the thermal state and composition of incoming sediments and oceanic plate. From the compilation of borehole, seismic reflexion, vp/vs ratio, critical taper theory and stress drops results, Saffer and Tobin [2011] have proposed the following general picture for the pore fluid evolution with depth :

— At the up-dip limit of the seismogenic zone, near-lithostatic pore pressure might prevail if coincident with the smectite-illite window, as observed in Costa Rica and Nankai [Calahorrano et al., 2008, Ranero et al., 2008, Tobin and Saffer, 2009]. Near lithostatic pore pressure is also suspected where shallow SSE, VLFE and tremors have been recorded as in Nankai and Hikurangi [Bell et al., 2010, Ito and Obara, 2006, Obana and Kodaira, 2009].

— Along the seismogenic zone, moderate overpressure along the seismogenic zone has been infer from VP/VS ratio along Southern Chile [Moreno et al., 2018]. However, this moderate pore pressure is inconsistent with effective friction estimates from mechanical analysis [Cubas et al., 2013b], heat flow measurements [Gao and Wang, 2014] and stress drops [Magee and Zoback, 1993]. Additional weakening mechanisms related to thermal pressurisation and/or dehydration reaction might occur during earthquake propagation [e.g., Faulkner et al., 2011, Cubas et al., 2015], reconciling interseismic moderate pore pressure and extremely low dynamic effective friction impacting the heat flow and topography.

— Down-dip, pore pressure might increase again, in particular where SSE and tremors are recorded [e.g., Audet et al., 2009]. High pore pressure in SSE and tremors regions are also supported by mechanical analysis [Liu and Rice, 2007].

Seafloor roughness

Oceanic seafloor, in particular those with a poor sedimentary cover, are marked by seamounts, aseismic ridges and fracture zones. Seamounts were first thought to increase the resistance along the megathrust and hence the coupling [Scholz and Small, 1997, Cloos, 1992]. However, from the comparison of geodetic data with the distribution of incoming plate roughness [Wang and Bilek, 2014, Lallemand et al., 2018] or gravimetric anomalies [Bassett and Watts, 2015], aseismic creep appears as the predominant mode of slip of rugged megathrust. Indeed, the subduction of bathymetric features induces a strong upper plate damage revealed by seismic reflection [Kodaira et al., 2000, Ranero and von Huene, 2000, Bangs et al., 2006, Collot et al., 2008, Bell et al., 2010, Geersen et al., 2015] ; observed along exhumed subduction zones [Vannucchi et al., 2006] ; and predicted by sandbox or numerical models [Dominguez et al., 1998, Ruh et al., 2016]. This dense fracture network increases the number of potential faults but decreases their size and hence earthquakes magnitude, favors aseismic slip and impedes the propagation of large ruptures [Wang and Bilek, 2014]. Only few seismic surveys have however imaged seamounts surrounding a large rupture [Kodaira et al., 2000, Geersen et al., 2015].

According to Gao and Wang [2014], smooth megathrusts producing great earthquakes tend to be weaker and therefore dissipate less heat than geometrically rough megathrusts that slip mainly by creep.

3.3 Forearc Modelling

3.3.1 Modelling of the long-term deformation

The CTT

The critical taper theory (CTT, Davis et al. [1983]) describes the mechanics of forearc wedges, analogous to fold-and-thrust belts in continental settings. This theory was established in the early 1980s, from the analogy between accretionary prisms and sand pushed by a moving bulldozer [Davis et al., 1983]. In a compressive setting, sand, sediments, or rocks are deformed by a sequence of thrusts, above a basal décollement to form a prism, also called a wedge (Figure 3.9a). Once the wedge reaches a certain critical taper, formed by the topographic slope α and the décollement dip β, it slides along its décollement. If no material is encountered at the toe, the wedge slides without inducing internal deformation. In the contrary case, the wedge grows self-similarly to maintain the critical taper. For a non-cohesive prism, the critical taper relates to the angle formed by the maximum principal stress σ_1 and the topography ψ_0, and the angle formed by σ_1 and the décollement ψ_b (Figure 3.9a) [Dahlen et al., 1984] :

$$(\alpha + \beta)_c = \Psi_B - \Psi_0 \tag{3.4}$$

with

$$\Psi_B = \frac{1}{2} arcsin\left(\frac{sin\phi'_b}{sin\phi_b}\right) - \frac{1}{2}\phi'_b \,, \tag{3.5}$$

$$\Psi_0 = \frac{1}{2} arcsin\left(\frac{sin\alpha'}{sin\phi_{int}}\right) - \frac{1}{2}\alpha', \tag{3.6}$$

with ϕ_{int} the internal friction of the prism and ϕ_b the friction of the décollement, such that $\mu_{int} = tan\phi_{int}$ and $\mu_b = tan\phi_b$, and :

$$\phi'_b = arctan\left[\left(\frac{1-\lambda_b}{1-\lambda}\right) tan\phi_b\right] , \tag{3.7}$$

$$\alpha' = arctan\left[\left(\frac{1-\rho_w/\rho}{1-\lambda}\right) tan\alpha\right] . \tag{3.8}$$

The ratio between the Hubbert-Rubbey fluid pressures λ and λ_b [Rubey and King Hubbert, 1959] are defined as in Davis et al. [1983]

$$\lambda = \frac{P - \rho_w g D}{|\sigma_z| - \rho_w g D}, \tag{3.9}$$

$$\lambda_b = \frac{P_b - \rho_w g D}{|\sigma_z| - \rho_w g D}, \tag{3.10}$$

with ρ and ρ_w the density of the prism and of water respectively, and D the water depth. The solution is exact if $\lambda = \lambda_b$ [Wang et al., 2006], but the approximation is valid for small angles $\alpha + \beta$, as in our case study.
In a topographic slope α vs slab dip β graph, this relation corresponds to the lower branch of the envelope (Figure 3.9b). For other branches, the solution differs based on the system of active or passive stresses [Lehner, 1986].

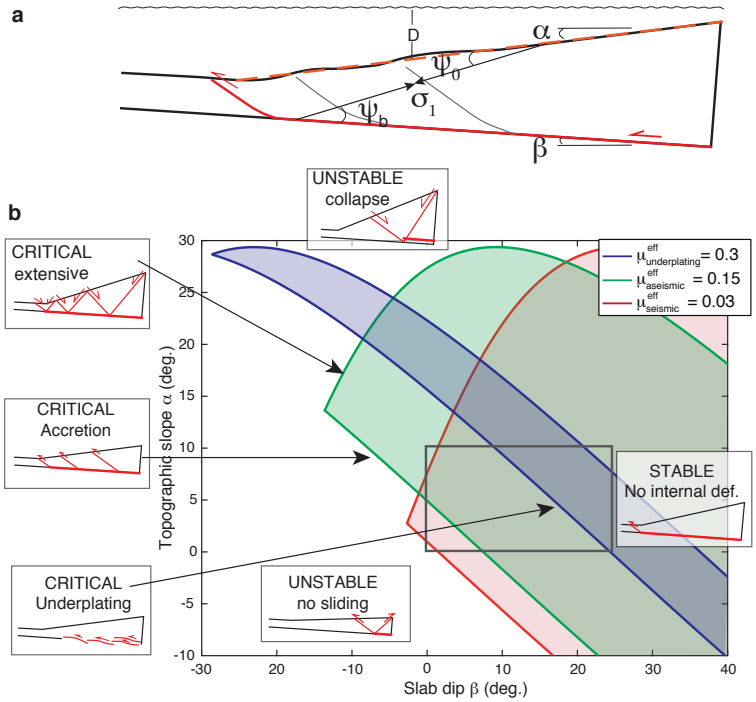

FIGURE 3.9 – Critical taper theory, a. The critical taper is formed by the topographic slope α and the décollement dip β, and depends on the angles Ψ_0 and Ψ_b. b. Critical envelopes, mechanical states and associated deformation for different décollement frictions and for $\lambda = 0.4$. (Blue curve : $\phi_{int}^{eff} - \phi_b^{eff} = 1^o$). The subduction zones are generally located in the gray rectangle.

If the angle formed by $\alpha+\beta$ is smaller than the critical taper represented by the envelope, the décollement cannot be activated. A thrust fault forms at the back of the wedge to increase the topographic slope and reach the critical envelope. If the critical taper is reached, the wedge is on the verge of Coulomb failure in its whole volume. However, since no geological structure is ever perfectly homogeneous, the critical state involves the activation of the décollement and of internal thrust faults which generally correspond to pre-existing structures. If the topographic slope is larger than the critical taper, the wedge enters a stability domain. The wedge slides along its décollement without inducing any internal deformation, and with a single active thrust fault at the front. With steeper slopes, the wedge can reach the upper branch of the critical envelop, and be on the verge of extensional Coulomb failure. In the conditions given in figure 3.9b, while sliding along its décollement, the wedge collapses through a series of normal faults that bring the prism back into the stable domain. If the topographic slope exceeds the envelope,

the prism collapses under its own weight. The lower branch of the critical envelope corresponds to the least-effort mechanical state. Consequently, this branch is the preferred mechanical state.

As shown by equations 3.4 and 3.5, the critical taper depends on the décollement friction. The smaller the basal friction, the larger the envelope. Consequently, the smaller the basal friction, the smaller the compressional critical taper (figure 3.9b). It also depends on the fluid pressure : as the fluid pressure increases, the slope of the envelope decreases. Consequently, the higher the fluid pore pressure, the smaller the extensional critical taper. Moreover, the difference between the internal and basal effective friction controls the dip of internal thrusts : the larger the difference, the larger the angle between internal thrusts and décollement. For very small differences, as the blue curve on figure 3.9b, internal thrust faults parallel the décollement allowing for underplating. Along subduction zones, the décollement is termed megathrust, and the décollement dip corresponds to the slab dip.

This simple theory, with its 4 analytical solutions, is particularly suited for inversion. Averaged frictional properties of the décollement can be retrieved from the co-variation of the topographic slope and slab dip, if the wedge is at critical state. However, the CTT is a purely brittle and static analysis that considers a uniform wedge, and can only predict the topographic slope for critical wedges but neither the location nor the evolution of its internal faults. To go beyond this static approach, analogue and numerical models have been developed.

Analogue modelling

Analogue models present the advantage to be intrinsically 3D and surface deformation can be quantified thanks to imagery analysis. However, internal structures are only accessible through tomographic techniques or cake cuts. These models have been widely used by the community to either validate theoretical developments such as the CTT [Davis et al., 1983, Malavieille, 1984] or the limit analysis that we will discuss later [Cubas et al., 2013c] or to test the influence of one or a set of parameters on the structure and dynamics of the wedge. As presented in the review of Graveleau et al. [2012], analogue models have investigated, among many other parameters, the influence of the geometry [Dahlen et al., 1984, Davis et al., 1983, Koyi and Vendeville, 2003, Smit et al., 2003], of the basal friction [Colletta et al., 1991, Lallemand et al., 1994, Mulugeta, 1988, Nieuwland et al., 2000], of multiple décollements [Konstantinovskaya and Malavieille, 2005, Bonnet et al., 2007, Konstantinovskaya and Malavieille, 2011], surface processes [Bonnet et al., 2007, Konstantinovskaya and Malavieille, 2005, Leturmy et al., 2000, Storti and McClay, 1995], of a viscous décollement [Bonini, 2007, Borderie et al., 2018, Costa and Vendeville, 2002, Couzens-Schultz et al., 2003, Gutscher et al., 2001, Pichot and Nalpas, 2009, Smit et al., 2003], or the effect of seamount subduction [Dominguez et al., 1998]. These models are now often faced to scaling issues to achieve a higher degree of complexity [e.g., Graveleau et al., 2012].

Numerical modelling

Foreac wedges have also been intensively studied by numerical models. Based on either finite element or finite difference methods, they consider visco-plastic rheologies and solve for conservation of mass and momentum, assuming an incompressible fluid. Numerical models present the advantage of investigating a large range of parameters and of providing a complete set of results (finite or total strain, strain rate, stress and energy dissipation, ...) Beyond the validation of the CTT [Buiter, 2012, Buiter et al., 2016], these models have studied the effect of complexities in wedges, such as various décollements, viscous behaviour [Ruh et al., 2012], underplating [Ruh, 2020], seamount subduction [Ruh et al., 2016], or surface processes [Buiter, 2012, Willett, 1999, Simpson, 2006, Stockmal et al., 2007]. Up to S. Pajang thesis work that will be presented later on, none of these numerical models had accounted for heat conservation

nor temperature dependant rheological transitions. Beyond the fact that these models do not easily incorporate real velocity discontinuities in the brittle domain, their major limitation lies in their high time/cpu consumption, which prevents conducting inversion studies.

Limit analysis

The limit analysis method [Chandrasekharaiah and Debnath, 1994, Salençon, 2002] is based on the principle of virtual powers and the theorem of maximum rock strength [Maillot and Leroy, 2006]. For accretionary wedge case studies, the Coulomb criterion is used for maximum rock strength. The principle of virtual power consists in applying a virtual displacement over the structure. The kinematic approach of limit analysis then provides the optimum collapse mechanism (set of faults) leading to the least upper bound of the tectonic pushing force. This static approach can be applied to evolving accretionary prisms : we first search for the set of faults minimizing the tectonic force, the structure then evolves by translation of rigid blocks along the predicted faults, following a predefined kinematics [Suppe, 1983]. To do so, the virtual velocity field is transformed into an incremental displacement field, by suppressing the dilatant part of every virtual velocity jump across the discontinuities. At the following shortening step, the system compares the force required to slide along the pre-existent structures with the force required to form a new set, and selects the optimal one. The repetition of the optimization and of the geometrical evolution for each increment leads to an approximate solution for the wedge growth upon shortening [Cubas et al., 2008, Mary et al., 2013]. The limit analysis method allows to predict position, dips, and lifetime of internal faults (real velocity discontinuities) of forearc wedges, based on their frictional properties [Cubas et al., 2008] and has been validated by comparison with experiments of sand wedges [Cubas et al., 2013c].

Compared to the CTT, there is no need to assume homogeneous mechanical properties nor to be at critical state. The limit analysis also allows for fast computing and hence inversion, as done in the studies that will be later presented. However, the method is again purely brittle and does not incorporate temperature-dependent transitions of rheology.

3.3.2 Short-term modelling of megathrust mechanics

To fully capture the megathrust and forearc mechanics, the dynamics of earthquakes needs to be taken into account. We here recall the different methods developed and their main results.

The dynamic CTT

This theory, developed by Wang and Hu [2006], is based on static stress equilibrium and ignores inertial forces and seismic wave propagation. The word 'dynamic' is used to emphasize temporal variations of stresses and deformation mechanisms from elastic to plastic. In this work, the authors assumed that the outer and inner wedges respectively correspond to the rate-strengthening and rate-weakening segments of the megathrust. According to the authors, due to the strengthening nature of the megathrust, the outer wedge switches from stable to critical state from the interseismic to the coseismic period. The outer wedge topography should thus be controlled by its peak strength acquired after earthquakes. The inner wedge, with its rate-weakening friction, may switch from critical to stable state from the interseismic to the coseismic period. This concept provides an explanation to the slope break between the outer and inner wedge.

Dynamic seismic cycle

Understanding earthquake dynamics requires to consider multiple seismic periods, and the full range of fault slip behaviours. Numerical models simulating seismic cycle sequences, have arisen during the last 2 decades [Erickson et al., 2020, Jiang et al., 2022, and references therein]. These models reproduce both earthquakes and aseismic slip, some taking into account the radiation of seismic waves, for a planar fault governed by rate-and-state friction embedded in a homogeneous elastic medium. This community has investigated the effects of additional physical factors, such as shear heating [Noda and Lapusta, 2010], pore fluid pressure [Madden et al., 2022, Zhu et al., 2020b], thermal pressurization [Noda and Lapusta, 2013, Cubas et al., 2015, Jiang and Lapusta, 2016], wave-mediated inertial effects during dynamic rupture [Thomas et al., 2014], pressure solution creep [Noda, 2016b], semi-brittle rheologies[Goswami and Barbot, 2018, Lavier et al., 2021] ; a viscoelastic medium [Miyake and Noda, 2019, Allison and Dunham, 2018] ; or asthenospheric flow [Barbot, 2018].

These models have allowed to identify the role of these different physical factors on the seismic cycle and earthquake dynamics, and can provide statistics of behaviours. They have for instance demonstrated that the variability observed in a segment from a large rupture to several small ruptures could arise from the influence of non-permanent barriers, zones with locally lower pre-stress due to past earthquakes [Kaneko et al., 2010]. They have also demonstrated that pore pressure and hydrothermal effects can significantly enhance seismic slip [Noda and Lapusta, 2010, 2013, Madden et al., 2022]. Although some models now incorporate off-fault plasticity [Thomas and Bhat, 2018], fault complexity and fault networks [Romanet et al., 2018], the homogeneous medium and simplified fault plane of most of these models do not permit to study in a systematic manner the relationships between earthquakes and the long-term deformation.

Seismic thermo-mechanical models

More recently, the thermo-mechanical modelling community has started to incorporate rate-and-state like behaviour to combine long-term geodynamical subduction models and earthquake sequences simulations [Van Dinther et al., 2013, Sobolev and Muldashev, 2017, Dal Zilio et al., 2022]. In the first model attempts, due to time resolution issue, the slip transients had to last decades [Van Dinther et al., 2013]. Sobolev and Muldashev [2017] succeeded to develop a cross-scale model of subduction with earthquake cycles using an adaptive time stepping algorithm, without considering rupture propagation process and seismic waves generation. They found that low-angle subduction and low friction favor the generation of giant earthquakes by increasing the seismogenic zone width [Muldashev and Sobolev, 2020]. To overcome the time-stepping limitation, the geodynamical subduction models have been coupled to dynamic rupture model [Van Zelst et al., 2019]. At a seismic cycle initiation, the self-consistent fault and surface geometry, fault stress and strength, and heterogeneous material properties are exported to a dynamic model to capture the nucleation, propagation and arrest of the earthquake. This model has allowed to investigate the effect of a pre-existent splay fault on the rupture, and have shown the effect of seismic wave reflections from the free surface on shallow slip accumulation. However, both models are run at subduction scale, impeding a fine study of the forearc deformation and its interactions with earthquake sequences. More recently, Dal Zilio et al. [2022] have developed a computational method to simulate earthquake sequences, with a time-stepping approach equivalent to the dynamic seismic cycle codes [Lapusta et al., 2000]. They modelled a megathrust governed by rate-and-state friction embedded in a visco-elasto-plastic medium, at forearc scale, investigating how inertia, radiation damping, thermally activated non-linear rheology and off-megathrust splay-fault events can affect sequences of seismic and aseismic slip. Although still simplistic in terms of upper plate structure, this work is particularly promising.

Seismo-tectonic analogue models

Thanks to advances in monitoring techniques such as digital correlation, and the use of new materials with elastic and stick-slip properties, analogue models are now also used to study earthquakes and seismic cycles [Rosenau and Oncken, 2009, Rosenau et al., 2009, Corbi et al., 2013, 2017, Rosenau et al., 2019, Caniven and Dominguez, 2021, Mastella et al., 2022]. These models can simulate hundreds of seismic cycle overcoming the short observational time faced by geodetic methods, and enabling robust statistical analysis. Some of them incorporate a elasto-plastic forearc wedge, allowing to investigate the relationships between short-term earthquakes and long-term tectonic deformation. These models have shown that a few percent of the plate convergence is converted in permanent deformation through splay faulting taking place up- and down-dip of the seismogenic zone [Rosenau and Oncken, 2009, Rosenau et al., 2009, Kosari et al., 2022]. If these models can fill the gap between short- and long-term deformation, their properties are predefined and not the result of the evolution of tectonic stresses, temperature and pressure.

3.4 Morphology and deformation of the forearc : mirror of the plate interface properties

3.4.1 Morphology of the wedge reveals spatial variations of megathrust frictional properties [Cubas et al., 2013b]

Determining the frictional properties of a megathrust is of primary importance for the understanding of earthquake mechanics as well as for the understanding of the construction of continental margins [Lamb and Davis, 2003, Lamb, 2006]. We have seen that the shallower, presumably rate-strengthening, portion of the megathrust is thought to coincide with the extent of the outer accretionary prism, the most frontal part of the forearc formed of imbricated thrust sheets of accreted sediments, which is considered to deform internally [Byrne et al., 1988, Ruff and Tichelaar, 1996, Fuller et al., 2006, Wang and Hu, 2006]. The limit between the deforming wedge and the more internal stable part of the wedge would then mark the up-dip portion of the seismogenic zone as suggested from the correlation between the rupture extent of large megathrust earthquakes with shelf-terraces or forearc basins marked by local gravity lows [Song and Simons, 2003, Wells et al., 2003]. Splay faults are commonly observed at the backstop of the deforming wedge and their location seem to mark the updip limit of megathrust ruptures [Collot et al., 2008]. The fact that splay faults form at the transition between aseismic and seismic patches has also been observed in analog experiments [Rosenau and Oncken, 2009]. As the morphology of the deforming accretionary prism naturally evolves toward a critical geometry determined by the friction along the megathrust and the wedge strength [Davis et al., 1983], the frictional properties could then control both the seismogenic behaviour and the forearc morphology.

The Mw 8.8 Maule earthquake occurred in 2010 along the Central Chilean forearc, north of the 1960 Mw 9.5 Valdivia rupture (figure 3.10a). Following this earthquake, two major normal fault aftershocks (Mw = 6.9 and 7.0) occurred near the town of Pichilemu [Farías et al., 2011] (figure 3.10a,b). These aftershocks ruptured a crustal normal fault rooting down to the interplate, as illuminated by the seismicity [Farías et al., 2011]. Evidence of activation of a thrust fault within the forearc was also found on the Santa Maria island (figure 3.10a,b). The elevated topography of the island results from a backthrust fault which most probably roots at depth into the megathrust [Melnick et al., 2006]. The island is located close to the updip limit of the coseismic rupture (figure 3.10b). The splay fault, activated during or shortly after the mainshock,

uplifted the island by 1.6 m during the 2010 earthquake [Melnick et al., 2012]. Darwin [1851] reported a 2.4 m to 3 m uplift two and six weeks after the 1835 M > 8 earthquake [Lomnitz, 1970] ; Melnick et al. [2006] inferred a 6 m of uplift related to the 1751 M > 8 event.

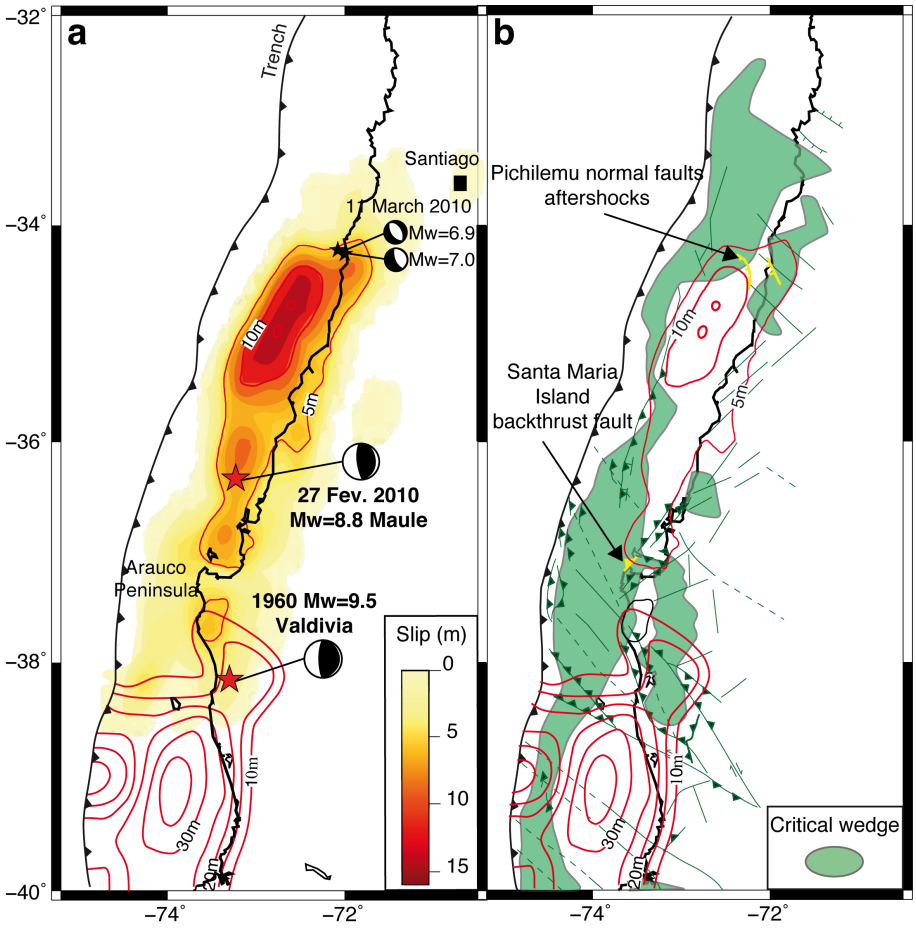

FIGURE 3.10 – a. Co-seismic slip models of the 2010 Mw 8.8 Maule [Lin et al., 2013], and 1960 Mw 9.5 Valdivia earthquakes (slip contours in red) [Moreno et al., 2009]. Large red stars : locations of hypocenters, small black stars : Pichilemu normal aftershocks. b. Segments at accretionary critical state (in green). Known (plain) and suspected (dashed) active faults are shown in dark green. The crustal faults activated right after the Maule earthquake are represented in yellow. Modified from Cubas et al. [2013b].

In Cubas et al. [2013b], I used both the CTT and Limit Analysis to constrain the spatial variation of the megathrust effective friction along the Central Chilean subduction zone from the wedge morphology and the modelling of the splay faults activated by the earthquake. We showed that the outer wegde as well as the Arauco peninsula and portions of the Coastal Cordillera, are at critical state, consistent with the distribution of known active faults (figure 3.10b). All other areas are mechanically stable. We also showed that the ruptures coincide with stable areas of the forearc and are surrounded with critical areas. The updip limit of the 2010 rupture coincide well with the maximal extent of the critical outer wedge. The coseismic slip of the 1960 rupture seems to taper down quite abruptly beneath the critical outer wedge. We also observe that most of the wedge forearc seems critical in the Arauco Peninsula which separates the 1960 and 2010 ruptures, and in the area just North of the 2010 rupture. The critical patches along the coastal cordillera also delimit the down-dip extent of the coseismic slip. Similarly, we observe that postseismic deformation partly coincide with areas at critical states and that the megathrust beneath the stable areas of the forearc wedge was mostly locked in the interseismic period (figure 3.11a,b). These observations support the claim that the propagation of a megathrust seismic rupture is probably inhibited by critical outer wedge and coastal areas.

Furthermore, the observed correlations are consistent with the notion that the forearc is stable above the seismogenic portions of the megathrust, while the updip rate-strengthening portion of the megathrust is maintained in critical state as a result of the stress transfer operated by coseismic and postseismic deformation [Wang and Hu, 2006, Hu and Wang, 2008]. The critical state of stress in the coastal area would rather be maintained by interseismic stress build up as aseismic creep proceeds downdip of the coseismic rupture. According to this model, all the deformation is accommodated along the megathrust in the seismogenic zone, no deformation being transferred to the upper plate. This model explains the correlation between forearc basins or regions with negative gravity anomalies [Wells et al., 2003, Song and Simons, 2003] and seismic asperities. On the other hand, in the creeping areas, the forearc is at or close to critical state, and as a consequence, a small fraction of the convergence has to be accommodated by the upper plate leading to coastal uplift, active faulting in the accretionary prism and thrusting at the transition from the inner to the outer wedge.

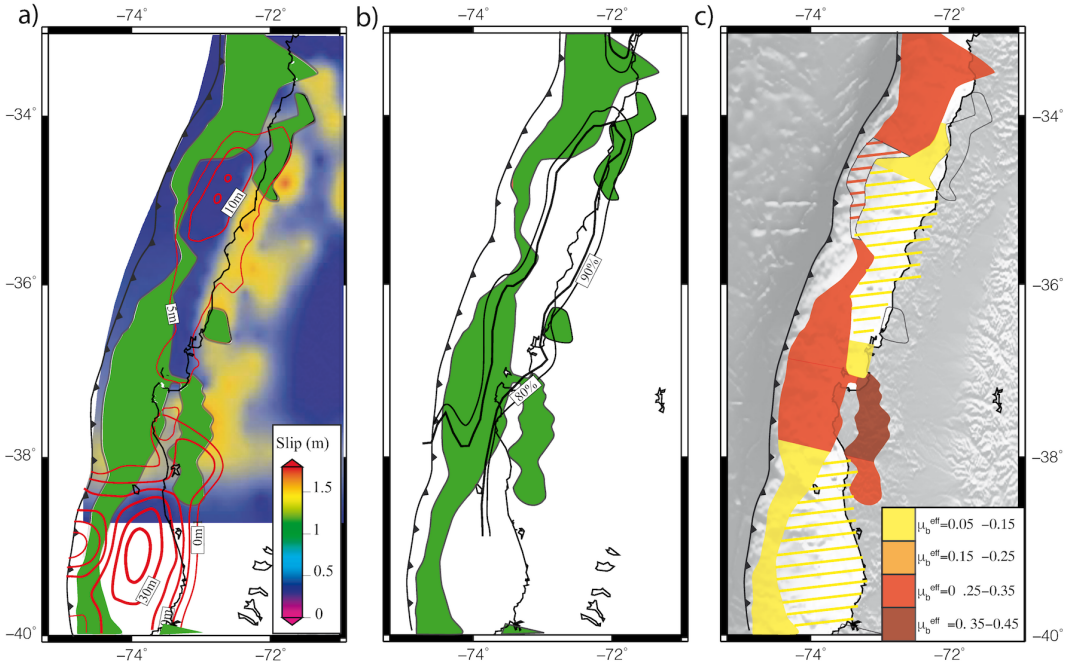

FIGURE 3.11 – Comparison of critical areas in green with a. Maule and Valdivia earthquake coseismic slip models (in red, Lin et al. [2013], Moreno et al. [2010]) and Maule postseismic slip model [Lin et al., 2013] with b. interseismic strain accumulation model (in black) from Métois et al. [2012]. c. Effective basal friction map based on critical taper and limit analysis results, hatching : extrapolation of results. Modified from Cubas et al. [2013b].

From inversions of critical envelops, we found a low effective friction along the outer wedge of the Valdivia segment (0.1) and a higher effective friction along the outer wedge of the Maule segment (between 0.1 to 0.3). The effective friction along the coastal cordillera is relatively high (~0.4). We also found a hydrostatic upper plate, and a slight overpressure in the outer wedge of the Valdivia segment. If the frontal aseismic outer wedge is rate-strengthening, then the effective basal friction found in this study should be an average value of the higher friction most probably attained after megathrust rupture as the outer wedge is then brought closer to failure [Wang and Hu, 2006]. The seismogenic zone is characterized by a lower effective basal friction. With the limit analysis, we found that to reproduce the Santa Maria backthrust splay fault, the effective friction of the seismogenic zone has to be lower than 0.07. To activate the Pichilemu normal fault, the effective friction along the seismogenic zone has to be lower than 0.14. Since the Santa Maria backthrust has been activated during the main event, and if we consider the normal sequence of Pichilemu a consequence of the main shock, the deduced friction is most probably

representative of the effective dynamic friction. An intrinsically low friction is a possibility in principle. This explanation seems improbable as the static friction retrieved for the surrounding aseismic zones is generally larger, and already at the lower end of the range that can be explained with low friction minerals, i.e. clays of the accretionary prism. The low effective basal friction in the seismogenic zone could alternatively reflect a high basal pore pressure, either permanent or due to a dynamic increase by thermal-pressurization.

These local results are consistent and supported by larger scale results obtained from the modelling of heat-flow data for a large number of subduction zones [Gao and Wang, 2014]. They found that megathrusts producing large magnitude events with apparent frictions lower than 0.05 are weaker than creeping segments, with apparent frictions larger than 0.1.

3.4.2 Trench-coast distance controlled by the megathrust frictional and rupture properties [Rousset et al., 2016]

Since the seismogenic part of the megathrust only slides during earthquakes, the resulting deformation should thus be controlled by the dynamic friction of the megathrust. If the effective friction of aseismic megathrust is larger than the dynamic effective friction, then according to the CTT, we should expect large tapers above aseismic segments, and lower tapers above highly coupled segments (figure 3.12a). For equivalent trench depth, we should then expect short trench coast-distance above aseismic segments, and larger trench-coast distance above highly coupled segments.

In Rousset et al. [2016], we indeed observed a strong correlation between along-strike variations of coast-to-trench distances and variations of GPS-derived forearc coupling along the Mexican subduction zone, from Guerrero to Oaxaca (figure 3.12b).

The same correlation has been obtained along the central and northern Chilean subduction zone [Saillard et al., 2017].

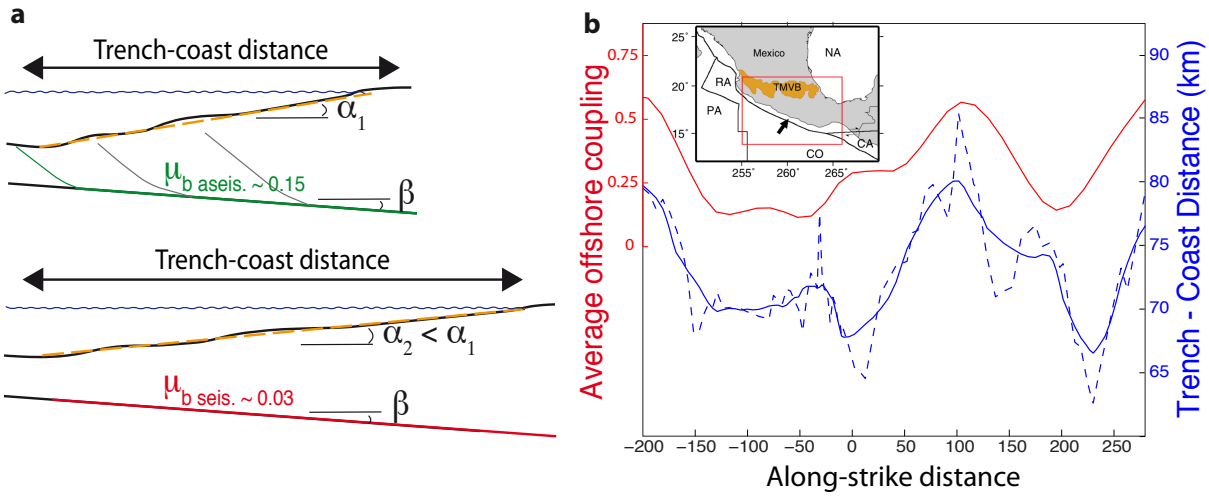

FIGURE 3.12 – a. Scheme representing the trench-coast distance for segments with aseismic or seismic effective basal friction. b. Example of the Guerrero subduction in Mexico. The trench-coast distance (in blue) correlates with the average coupling (in red). Modified from Rousset et al. [2016].

3.4.3 Splay faulting induced by transition of frictional properties [Cubas et al., 2013a,b]

The 2011 Mw 9.0 Tohoku-Oki earthquake ruptured the plate interface between the Pacific Plate and NE Japan generating a very large slip, probably exceeding 50 m at depth between 10

and 15 km, and a major tsunami [Ozawa et al., 2011, Wei et al., 2012, Ide et al., 2011] (figure 3.13a). Large shallow slip is attested from the displacement of ocean bottom gauges [Ito et al., 2011] and comparison of bathymetric profiles measured in 1999 and late March 2011 [Fujiwara et al., 2011]. While many magnitude 7.5 earthquakes had occurred along this margin, the large shallow slip came as a surprise since (1) the upper portion of the megathrust is commonly thought to slip aseismically [e.g., Oleskevich et al., 1999], (2) previous magnitude 7.5 earthquakes had only been instrumentally recorded along the deeper portion of the megathrust and (3) interseismic strain accumulation models were not showing a locked patch near the trench [Hashimoto et al., 2009, Loveless and Meade, 2011]. It should be noted, however, that the creep at shallow depth inferred from the interseismic models [Hashimoto et al., 2009, Loveless and Meade, 2011] was essentially due to the assumed initial condition and lack of resolution near the trench of the onshore geodetic data used in these inversions [Loveless and Meade, 2011]. Another intriguing observation is that the earthquake activated a landward dipping normal fault [Ito and Obara, 2006, Tsuji et al., 2011], located slightly updip of the maximum slip area (figure 3.13a,d). The landward normal fault marks the lower limit of an outer wedge formed by a stack of thrust sheets. The fault, which extends parallel to the trench for several tens of kilometers, could have contributed to the tsunami [Tsuji et al., 2011, McKenzie and Jackson, 2012], and its activation is consistent with the trench-perpendicular horizontal extension of the hanging wall revealed by aftershocks [Ide et al., 2011, Asano et al., 2011] (figure 3.13c). In this study, we again used the CTT and Limit Analysis to constrain spatial and temporal variations of the megathrust effective friction, and study how it could relate to the unexpected large shallow slip (figure 3.14).

We first found that the outer wedge closely follows the prediction of the CTT in horizontal compression (figure 3.14a). The best fitting model corresponds to a high pore pressure ratio in the wedge ($\lambda = 0.8$), and a low effective basal friction ($\phi_{eff} = 7.5^o$, $\mu_{eff} = 0.13$) (figure 3.14a,c). To reach the extensional critical state at the landward normal fault location, a decrease of the effective friction down to $\mu_{eff} = 0.003$ is required (figure 3.14b). If the intrinsic friction is maintained, then the pore pressure would need to have increased from $\lambda = 0.8$ to 0.995. Such a low friction could have resulted from very efficient dynamic weakening, as suggested by some aspects of the rupture [Ide et al., 2011], possibly resulting from thermal pressurization [Noda and Lapusta, 2013]. However, since the taper trajectory is not parallel to the extensional branch of the envelope, it is not clear that the CTT is applicable in this way. Also, if the same properties apply to the whole outer wedge, the frontal part of the wedge should then collapse due to internal normal faulting, and slip should gradually increase toward the trench which was not observed. Actually, it is probably incorrect to assume that the whole wedge has been brought to the verge of failure in extension. We therefore explored an alternative explanation : the normal fault could rather be interpreted as a splay fault resulting from changes in frictional properties along the megathrust.

We used the properties found based on the CTT for the bulk and the inner wedge megathrust ($\mu = 0.8$, $\mu_{\mathrm{BI}}^{eff} = 0.13$). The inner megathrust pressure ratio is set equal to the internal pressure ratio ($\lambda_{\mathrm{BI}} = \lambda_{int} = 0.8$). To account for dynamic weakening during seismic sliding, we decrease μ_{BI}^{eff} from 0.13 to 0.1. The down-dip part of the wedge is thus in a stable state. Two possibilities are studied with Limit Analysis : in the first case, the basal friction coefficient angle decreases toward the trench $\phi_{\mathrm{BI}} > \phi_{\mathrm{BF}}$ (figure 3.15b), in the second case, it increases $\phi_{\mathrm{BI}} > \phi_{\mathrm{BF}}$ (figure 3.15c). We also vary the pore pressure along the frontal part of the megathrust, hence, the effective basal frontal friction μ_{BF}^{eff}.

If the effective frontal basal friction is too large ($\mu_{\mathrm{BF}}^{eff} > 0.13$), the taper is then in the unstable field (figure 3.15a), no sliding is allowed along the updip part of the wedge and conjugate thrust faults are formed at the transition in order to increase the taper (figure 3.15b,c). If the effective frontal basal friction decreases and the wedge reaches the compressional limit

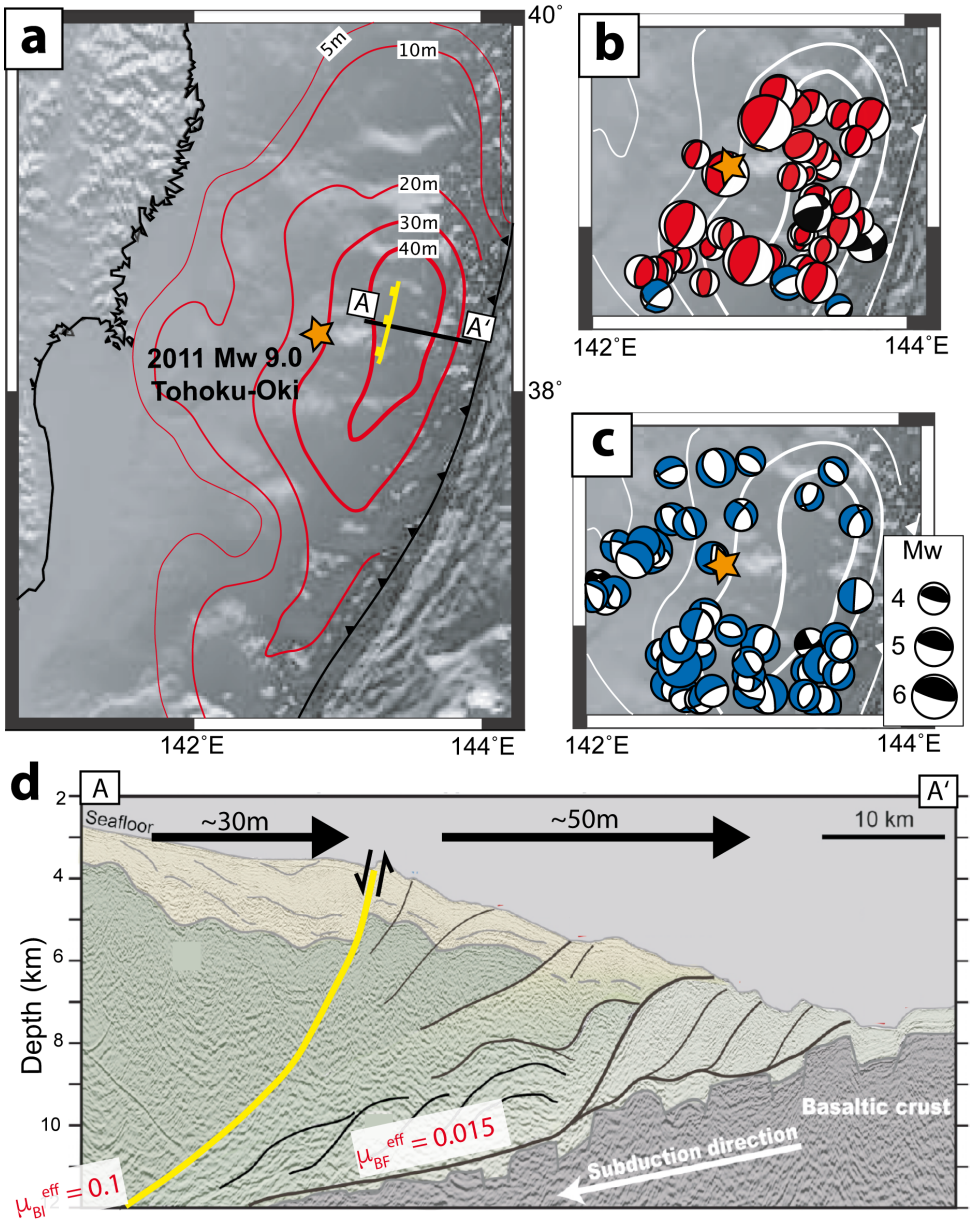

FIGURE 3.13 – a. Slip contours of the 2011 Tohoku-Oki earthquake, Mw 9.0 (Japan) and location of the normal splay fault that was activated during the earthquake. The mainshock epicenter is indicated by the star. b. Spatial distribution of CMTs of earthquakes before the mainshock (from January 2003 to March 11 2011), and c. non-interplate aftershocks in the hanging-wall (from March 11 to March 24 2011) in the studied area from Asano et al. [2011]. In red : compression, blue : extension, black : strike-slip. d. Seismic profile recorded before the earthquake Tsuji et al. [2011] ; 30 m and 50 m : displacements measured by gauges placed on the seafloor on either side of the normal fault Ito et al. [2011]. μ_{BI}^{eff} , μ_{BF}^{eff} : effective basal frictions estimated from the observed displacements Cubas et al. [2013a]. Modified from Cubas et al. [2013a].

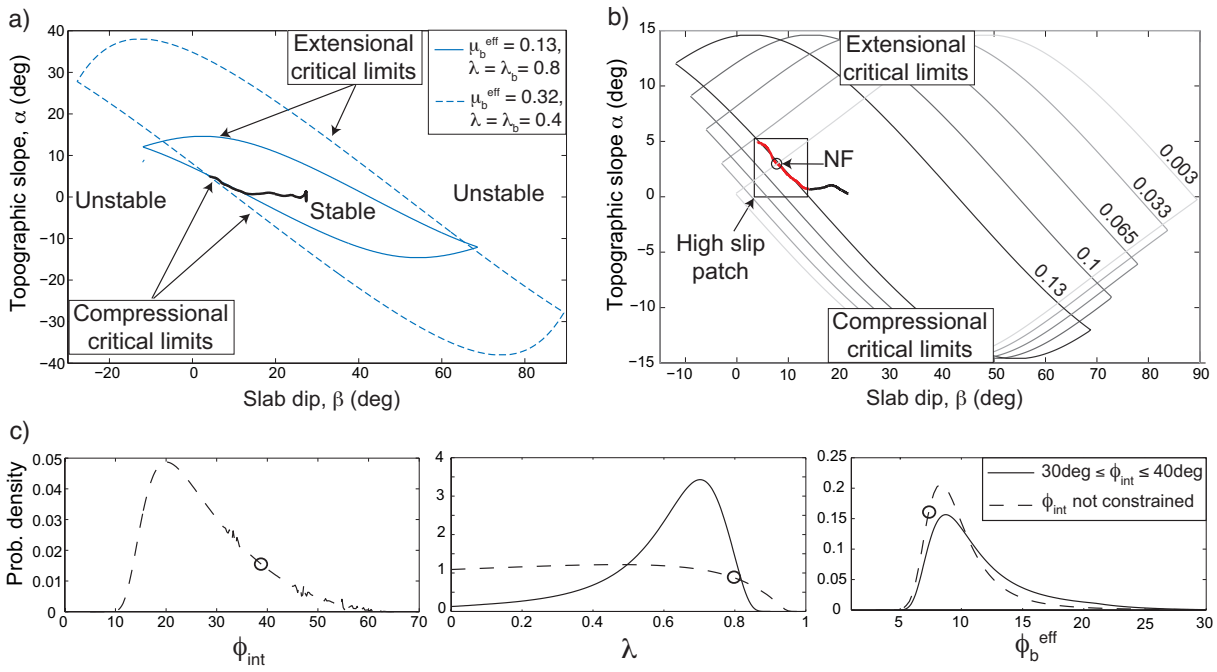

FIGURE 3.14 – a. Theoretical critical envelopes for two different sets of frictional properties compared to the taper of the swath profile of the studied area (ϕ_{int}=38.75°). b. The portion of the taper considered at critical state is overlined in red and corresponds to the high slip patch of the Tohoku-Oki earthquake. The effective basal friction is decreased in order to reach the extensional limit for the taper measured at the location of the landward normal fault marked by a black circle (ϕ_{int}=38.75°, λ=0.8). c. Probability densities for the three independent parameters ϕ_{int}, ϕ_b^{eff} and λ_{int} without constraints on ϕ_{int} (dashed line), for ϕ_{int} in the 30-40 degree range (plain line). The densities are determined from fitting the portion of the wedge presumed to be at critical state with the theoretical envelope. Best fit values of the three parameters inversion are marked by a black circle. Extracted from Cubas et al. [2013a].

($\mu_{BF}^{eff} = 0.13$), the décollement is then fully activated, and a thrust fault appears at the transition to accommodate the difference of slip along the upper and lower part of the megathrust generated by the difference in basal friction. For $\phi_{BI} > \phi_{BF}$, a shallow dipping forethrust is formed, while $\phi_{BI} < \phi_{BF}$ leads to a backthrust. If the effective frontal basal friction is decreased, the frontal wedge enters the stable domain, and fore- and back-thrust get steeper. If the effective friction decreases again, the extensional critical limit is reached ($\mu_{BF}^{eff} = 0.003$) and dips increase again resulting in a seaward normal fault for $\phi_{BI} > \phi_{BF}$, and a quasi-vertical normal fault for $\phi_{BI} < \phi_{BF}$. This exercise demonstrates that a transition in frictional properties (friction and/or pore pressure ratios) implies the development of a splay fault. The vergence of the splay is controlled by the friction, while the slip mode (thrust or normal faulting) depends on the effective friction change. To reproduce the amount of slip inferred along the megathrust and on the normal fault, the limit analysis requires an effective basal friction below the frontal wedge ranging between $0.002 < \mu_{BF}^{eff} < 0.015$.

The low effective basal friction inferred in this study is consistent with the dynamic overshoot proposed by Ide et al. [2011] and could have resulted from thermal pressurization of the updip part of the megathrust as suggested by Noda and Lapusta [2013]. By contrast, the long term high pore pressure along the megathrust could be a permanent feature maintained by continuous dehydration of siliceous sediments and clays dragged along the megathrust [Kimura et al., 2012] and by a low permeability. The different effective friction coefficient beneath the inner and outer wedge could reveal a different mineralogy resulting in a more efficient up-dip dynamic thermal pressurization and thus a dynamic increase of the pore pressure beneath the outer wedge.

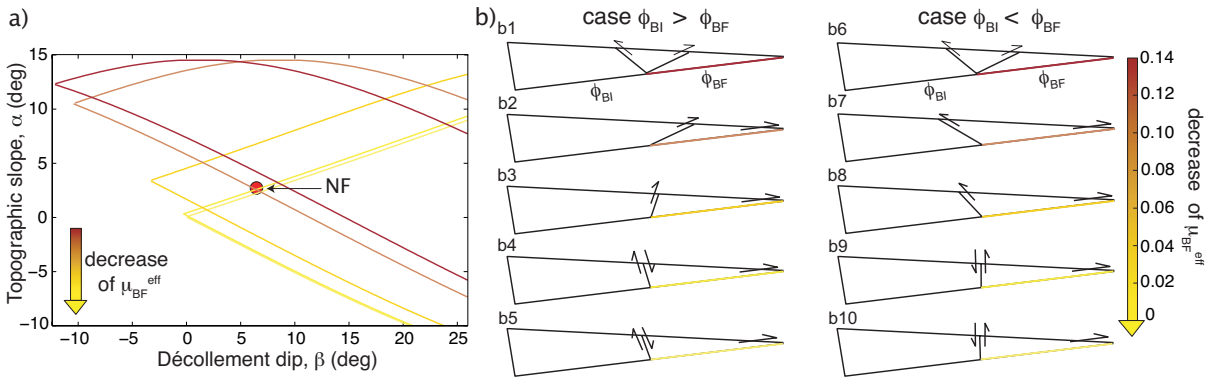

FIGURE 3.15 – a. Critical envelopes representative of the frontal part of the wedge of figure b and c (for ϕ_{int}=38.75°, λ_{int}=0.8, and decreasing μ_{BF}^{eff} from 0.135, to 0.13, 0.037 and 0.003). Expected associated splay faults in the case of b. a decrease or c. an increase of the basal friction, for the different effective frontal basal frictions μ_{BF}^{eff} of figure a. Extracted from Cubas et al. [2013a].

After activation of slip along the megathrust, the compressional stress must build up again to bring the outer wedge back to a critical state. The stress build up can result from interseismic strain or, more probably, from the stress transfer due to ruptures along the deeper portion of the megathrust, similar to the numerous Mw < 7.5 earthquakes reported historically [Hashimoto et al., 2009], and afterslip [Hu and Wang, 2008]. On the long-term, the outer wedge would thus maintain a compressional critical taper.

Normal faults in forearcs have often been interpreted as a consequence of basal erosion [e.g., von Huene et al., 2004]. Our interpretation might provide an alternative explanation for these faults and normal faulting aftershocks sometimes recorded after such earthquakes (as the Maule event). Forearc normal faults could be evidence for very efficient dynamic weakening along the megathrust. When located at the transition between outer and inner wedges [McKenzie and Jackson, 2012, e.g.,], these faults could indicate up-dip propagation of earthquakes and typify megathrust with high tsunamigenic potential. After the Tohoku-Oki earthquake, a similar large active landward crustal-scale normal fault was identified along the Shumagin Gap in Alaska [Bécel et al., 2017], rising large concern.

3.4.4 Thermal pressurization [Cubas et al., 2015]

As stated above, the large shallow slip of the Tohoku earthquake (figure 3.16a) took the community by surprise, in particular because interseismic strain accumulation models were not showing a locked patch near the trench [Hashimoto et al., 2009, Loveless and Meade, 2011]. Although it was suggested to result from a lack of resolution near the trench [Loveless and Meade, 2011], the seafloor measurements (as reported in Sato et al. [2013]) do require some amount of interseismic creep near the trench. Moreover, all the historical Mw 7.5 earthquakes were located in the highly coupled area, with the exception of the 1896 Sanriku tsunami earthquake (figure 3.16b). It thus seems that the shallow portion of the Japan megathrust could creep aseismically, e.g. as afterslip and interseismically, as well as accumulate substantial slip during large tsunamigenic earthquakes. The Tohoku-Oki earthquake was remarkable in two other ways. The large shallow slip area did not radiate much seismic energy at high frequencies compared to the deeper portion of the megathrust which experienced less slip [Ide et al., 2011, Simons et al., 2011, Meng et al., 2011, Wei et al., 2012]. A complex propagation was also observed, with a small initial phase of deep rupture up to 40 s, followed by extensive shallow rupture at 60-70 s, and a continuing deep rupture lasting over 100 s [Ide et al., 2011]. Finally, from tsunami records [Sawai et al., 2012], the last earthquake in the area with comparable tsunami deposits occurred in AD 869 and hence the recurrence time of the Tohoku-Oki-like events, unless irregular, was

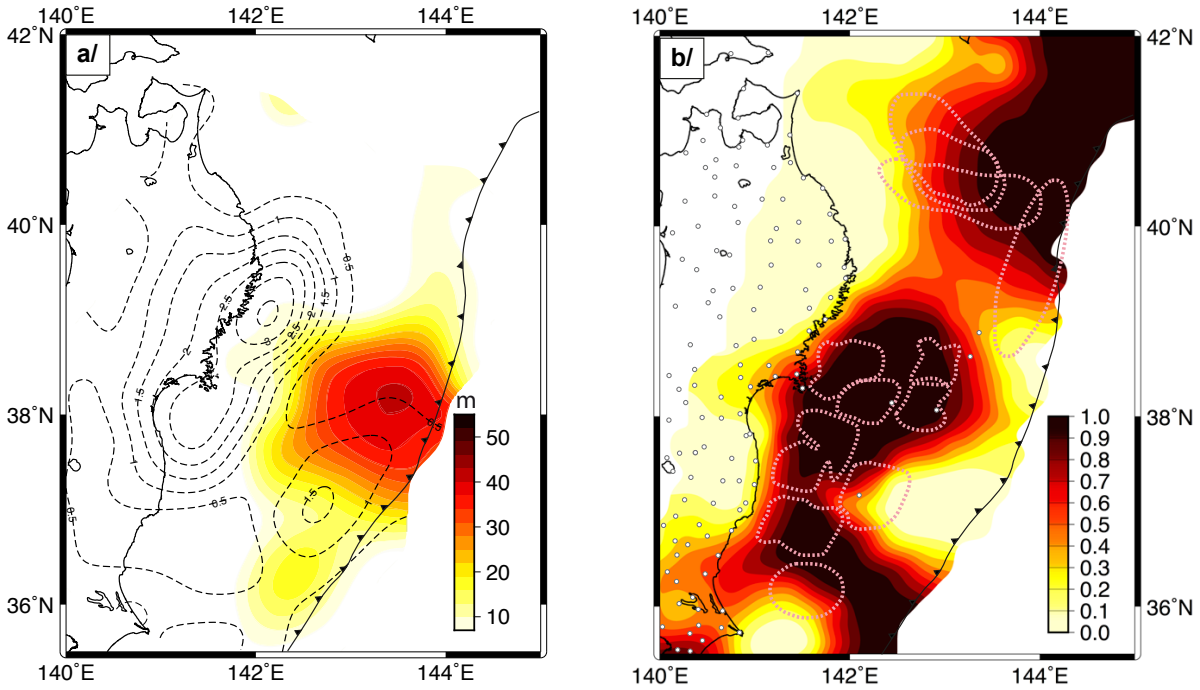

FIGURE 3.16 – a. Coseismic (colors) and postseismic (black dashed lines) slip from Yamagiwa et al. [2015] derived from the modeling of on-shore and seafloor displacements. b. Interseismic coupling ratio (colors) from an updated inversion of onshore and offshore geodetic measurements based on Perfettini and Avouac [2014] but including the interseismic seafloor displacements of Sato et al. [2013]. The dotted pink contour lines show the estimated location of rupture areas of smaller (~ M7.5) historical earthquakes [Yamanaka and Kikuchi, 2004, Shibazaki et al., 2011]. Extracted from Cubas et al. [2015].

estimated of 1000 years.

To reconcile these observations, Noda and Lapusta [2013] have suggested that the shallow megathrust could undergo aseismic slip at low slip rates, due to its rate-strengthening properties, as well as substantial coseismic slip due to efficient weakening by thermal pressurization of pore fluids [Sibson, 1973, Lachenbruch and Sass, 1980, Mase and Smith, 1984, 1987, Rice, 2006]. This dual behaviour, rate-strengthening at low slip rates and strong weakening at seismic slip rates, was also observed for lab experiments on wet clays characteristic of shallow megathrusts, and attributed to thermal pressurization at high slip rates [Faulkner et al., 2011].

However, thermal pressurization can explain the large coseismic slip regardless of the rate-strengthening or rate-weakening behaviour of the shallow zone. Since it is uncertain that the megathrust was fully locked up to the trench before the Tohoku-Oki event, the properties of the interface could be rate-weakening at low slip rates. Determining if the observed behaviour of the megathrust that hosted the 2011 Tohoku-Oki event is due to an unusual rate-weakening shallow patch or to co-seismic weakening of an otherwise rate-strengthening shallow portion of the fault is of fundamental importance for future seismic and tsunamigenic risk assessment.

In this paper, we followed up on the study of Noda and Lapusta [2013]. We used 2D dynamic model of seismic cycles developed by Noda and Lapusta [2010] to investigate several possible scenarios of the megathrust properties, incorporating the frictional parameters deduced from the morphological analysis [Cubas et al., 2013a]. The approach allows to simulate slow fault slip as well as self-driven rupture propagation with all inertial effects under slow tectonic-type loading in a mode II configuration while accounting for shear heating and pore pressure changes. A planar fault is embedded in a homogeneous elastic medium and governed by the ageing form of the rate-and-state friction law [Dieterich, 1979, Rice and Ruina, 1983, Ruina, 1983]. For the set-up, we considered 4 segments (figure 3.17) : (1) a deep rate-strengthening zone below

the seismogenic zone, (2) a seismogenic zone corresponding to the extent of the historical Mw 7.5 earthquakes, (3) a shallow patch prone to thermal pressurization along which we explored the dependency on the rate and state parameter ($a - b$), and (4) an updip rate-strengthening patch where coseismic slip tapers off and postseismic slip was observed. We attributed to these segments the frictional values deduced from the previous mechanical analysis [Cubas et al., 2013a]. To get efficient thermal-pressurization in patch 3, we used relatively small hydraulic diffusivity there and larger values elsewhere, with all values within laboratory measurements of Tanikawa and Shimamoto [2009]. In the shallowest patch 4, we chose a larger hydraulic diffusivity to simulate unconsolidated clays close to the trench. In patch 3, we chose parameters enabling only relatively large slips of the order of 10 m to activate efficient weakening.

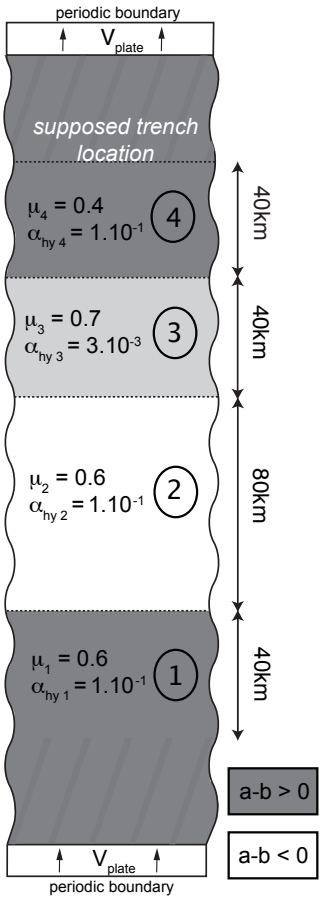

FIGURE 3.17 – Model set-up. Patch 3 has a higher reference friction coefficient consistent with the study of Cubas et al. (2013) and lower hydraulic diffusivity to get efficient thermal pressurization and enhanced slip. Different values of parameter ($a - b$) are explored along this patch. Extracted from Cubas et al. [2015].

We found that regardless of the rate properties at low slip rates of the shallow portion of the fault (between 40 and 80 km in our models), an efficient thermal pressurization along this portion allows reproducing the alternation between several deeper moderate (M 7.5) events and much larger (M 9) events accumulating significant slip close to the trench (figure 3.18). Both behaviours also reproduced dominant high-frequency radiation from the deeper portions of the fault as well as the complex up- and down-dip rupture propagation. There are however, important differences. Since no interseismic slip takes place along patch 3 within the rate-weakening patch 3 model, the recurrence time of large events is short (200-250 years). On the contrary, the recurrence time increases, up to several thousand years, with larger rate-strengthening ($a - b$) parameter. Neither changes of the hydraulic diffusivity, nucleation size, nor the addition of

a rate-strengthening barrier allowed to significantly increase the recurrence time. The rate-strengthening properties result in interseismic creep in addition to occasional significant co-seismic slip, allowing the model to reproduce the inferred recurrence times of the order of 1000 years. These properties near the trench can also explain the lack of smaller seismicity near the trench in the last 300 years (except for the rare large events), as observed along the Japan megathrust as well as along most subduction megathrusts worldwide [Byrne et al., 1992]. The local variation in permeability allowing for efficient thermal pressurization could be related to the low incoming sediment thickness or the disrupted oceanic crust by horst and grabben.

This paper demonstrates how combining long- and short-term modelling can bring important insights on earthquake mechanics.

3.4.5 Seismic and tsunamigenic risk assessment

Today, the prediction of earthquake extent mostly relies on geodetic observations of interseismic coupling [e.g., Moreno et al., 2009]. However, the majority of these observations are made onshore, often at large distances from the locked portion of the fault, and as discussed above, with poor resolution near the trench [e.g., Loveless and Meade, 2011]. Moreover, geodetic observations usually represent a small fraction (tens of years) of an interseismic earthquake cycle (hundreds of years) with patterns of deformation inferred from surface motions evolving with the viscoelastic relaxation [Wang et al., 2012]. A larger time span can be obtained from records of the relative sea level change extracted from corals, that can help to constrain sequences of large events [e.g., Sieh et al., 2008, Philibosian et al., 2017]. However, this method can not be applied worldwide, and the number of recorded events is limited to provide statistically robust predictions.

In the Cubas et al. [2013b,a] studies, through the search of critical segments and the study of splay faults, we have demonstrated a relationship between the long- and short-term deformation of the forearc. If seismic asperities are persistent through time and space, then morphology and deformation should act as a mirror of the plate interface properties and could help improving seismic and tsunamigenic hazard assessment. This is of particular importance in very poorly instrumented regions where topography and deformation are the only easily accessible information.

In the following papers, I show how the study of the criticality, vergence, and type of faults of the outer wedge can bring information about potential shallow ruptures. I also discuss how the search of patches of low friction could be used to delineate seismic asperities.

Outer wedge deformation reflects the slip behaviour of the shallow megathrust [Cubas et al., 2016]

The two last giant earthquakes of magnitude >9 of the 21st century (2004 Sumatra and 2011 Japan) took both scientists and government agencies by surprise, with frontal ruptures that led to devastating tsunamis with enormous loss of lives, properties and a near-nuclear disaster.

During the 2000-2010 decade, Sumatra experienced the most intense sequence of earthquakes ever recorded on Earth, starting with the Mw 9.1 December 26 2004 Sumatra-Andaman earthquake, that ruptured 1300 km from the Simeulue Island to the northern Andaman Islands [Ammon et al., 2005, Lay et al., 2005] (figure 3.20c). This earthquake was followed three months later by the Mw 8.7 2005 Nias earthquake located just south that did not generate a significant tsunami [Hsu et al., 2006] (figure 3.19). The sequence resumed in 2007, with two relatively deep events along the Mentawai segment [Konca et al., 2008]. The frontal part of the 2007 Mentawai earthquake ruptured in 2010 with a Mw 7.8 [Lay et al., 2011] (figure 3.19). This event, qualified as a tsunami earthquake, generated waves of 3 up to 9 m [Lay et al., 2011]. A 500 km long northern Mentawai segment is now the only major gap left in the Sumatra region (figure 3.19).

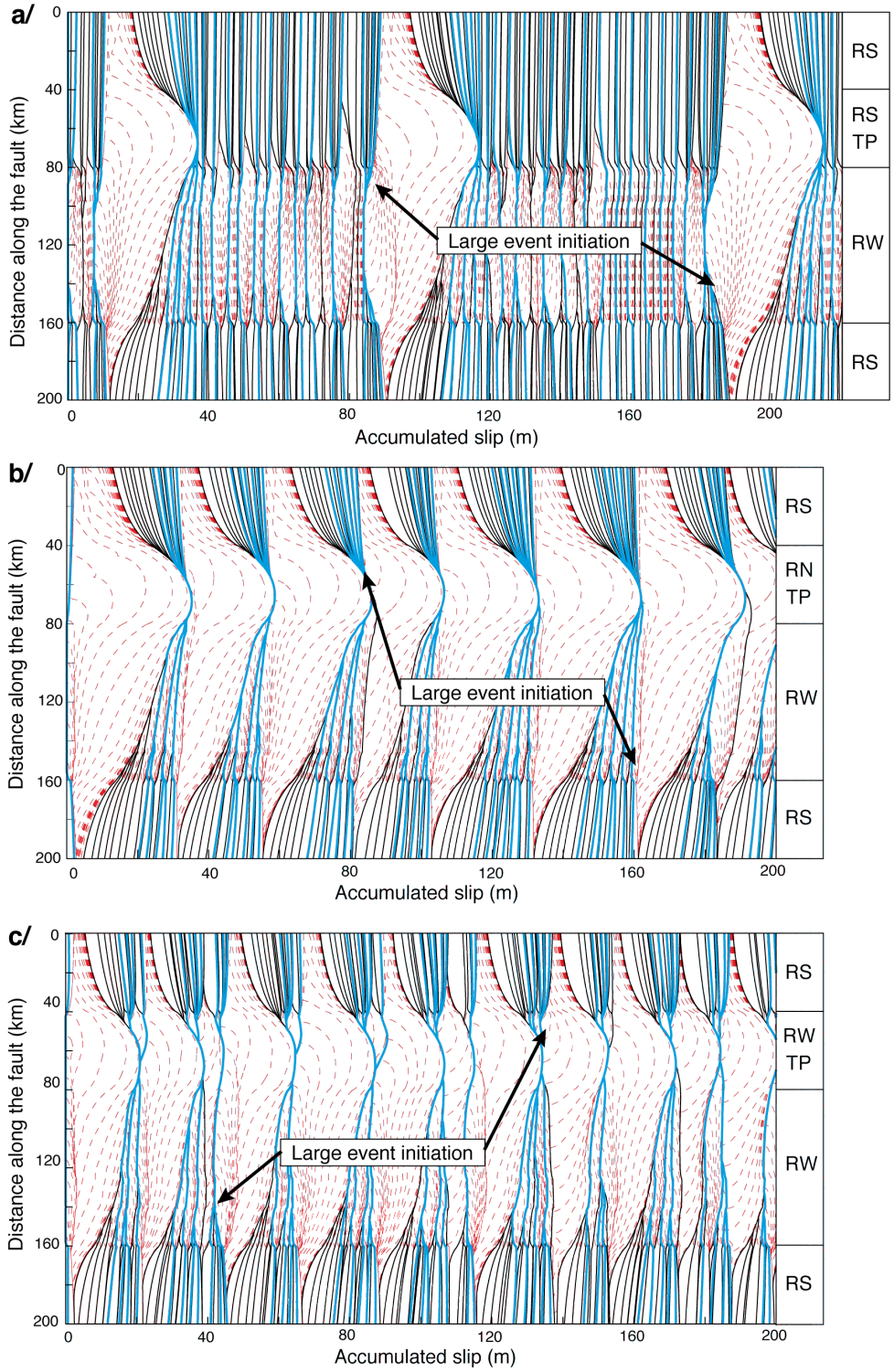

FIGURE 3.18 – Accumulated slip as a function of the distance along the fault, for a. Model A1, rate-strengthening patch 3 ($a - b = 0.009$) ; b. Model B, rate-neutral patch 3 ($a - b = 0.0$) ; c. Model C1, rate-weakening patch 3 ($a - b = -0.004$). Dashed red lines show coseismic slip every 4 seconds, thick blue lines indicate interseismic slip every 50 years, thin black lines signify the end of each earthquake. Zero slip corresponds to fault slip after several tens of simulated earthquakes, to focus on the long-term response of the model. Extracted from Cubas et al. [2015].

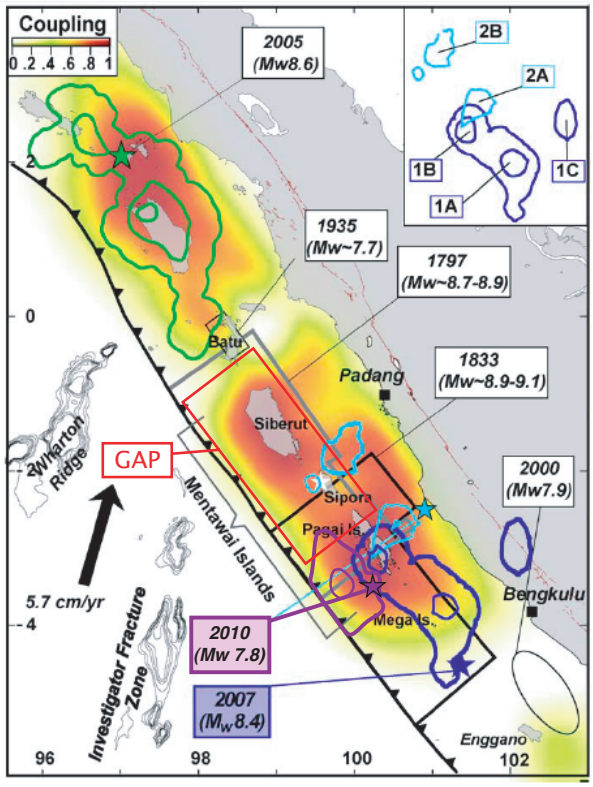

FIGURE 3.19 – Coupling pattern derived from the modeling of geodetic and paleo-geodetic data, compared to major historical and recent earthquakes. Modified from Konca et al. [2008].

Following the 2004 Sumatra Andaman earthquake, a correlation between landward vergent thrusts and shallow propagation of earthquakes was suggested by some authors [Gulick et al., 2011, Moeremans et al., 2014]. Several landward vergent thrusts have been observed at the front of the accretionary wedge where the 2004 earthquake seems to have reached the seafloor [Chlieh et al., 2007, Gulick et al., 2011] (figure 3.20a,c). The 2010 Mentawai earthquake occurred along a prism showing landward vergent thrusts [Moeremans et al., 2014, Cubas et al., 2016]. The seismic gap along the Sumatra subduction zone also shows frontal landward vergent structures [Kuncoro et al., 2015]. Along this portion, the 1797 Mw~8.7 event generated a very large tsunami with run-up heights of ~10 m in Padang [Newcomb and McCann, 1987]. On the contrary, no landward-vergent thrusts have been reported along the Nias segment where the 2005 earthquake was limited to the 'standard' seismogenic zone [Cook et al., 2014, Konca et al., 2008].

Normal sequences of landward-vergent thrusts have also been reported along the Cascadia subduction zone offshore the Oregon-Washington (USA) margin (figure 3.20b,d) [MacKay, 1995, Adam et al., 2004] and north of the Mendocino triple junction [Gulick et al., 1998]. This subduction zone is known to generate Mw~9 earthquakes every 300-500 yr with tsunamis crossing the whole Pacific ocean [Satake et al., 1996, Atwater and Griggs, 2012]. In this region, the extent of the landward vergence in accretionary prism matches well with the location of high slip patches of the 1700 earthquake [Wang et al., 2013] (figure 3.20).

Hence, understanding the mechanical requirements for landward vergence and its possible link with frontal propagation of earthquakes is fundamental for seismic and tsunamigenic risk assessment, for the last Sumatra gap as for Cascadia.

In this 2016 paper, we used the Limit Analysis method to explore the mechanical conditions necessary for this type of vergence. In addition to an extremely low megathrust effective friction, we found that landward vergence is favored by a low strength ratio between the megathrust and the wedge. For Cascadia and northern Sumatra, only a narrow range of properties

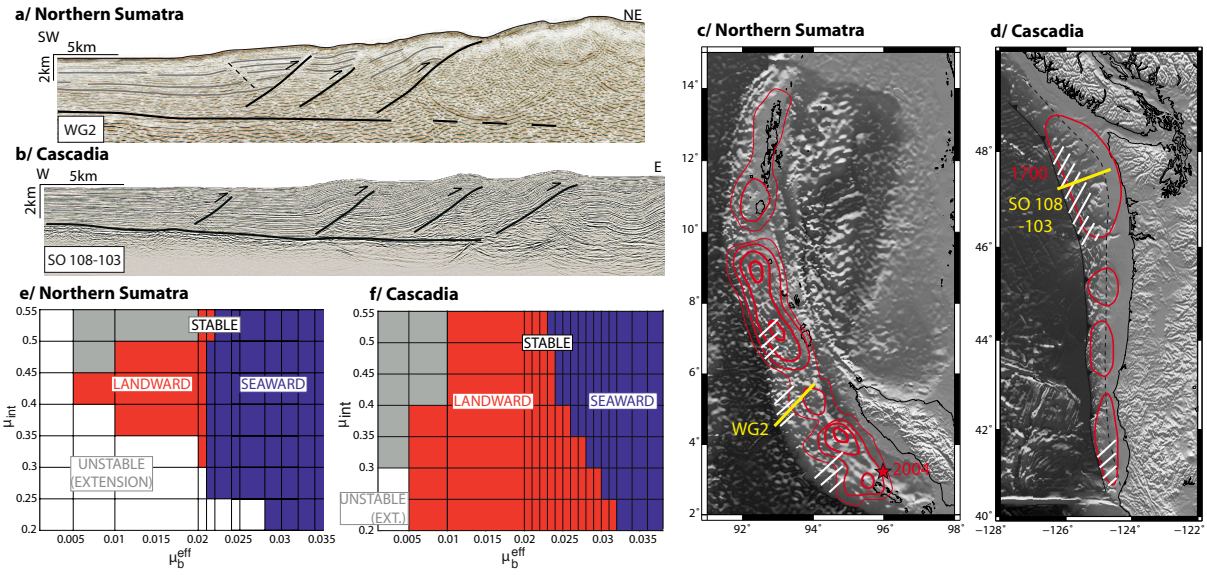

FIGURE 3.20 – Landward-vergent accretionary prisms and frictional properties. a. Seismic profile WG2 in northern Sumatra [Moeremans et al., 2014]. b. Seismic profile SO 108–03 in Cascadia [Adam et al., 2004]. c. Comparison of the observed landward-vergent thrusts in northern Sumatra (hachured white lines ; compilation from Dean et al. [2010], Gulick et al. [2011], Moeremans et al. [2014] with coseismic slip of the 2004 Mw 9.1 Sumatra-Andaman earthquake (slip contours in red every 5 m increment ; Chlieh et al. [2007]). d. Comparison of the observed landward-vergent thrusts in Cascadia (hachured white lines ; compilation from MacKay, 1995, Gulick et al. [1998], Adam et al. [2004]) with the estimated slip contours of the 1700 Cascadia earthquake considering a trench-breaking rupture scenario with a Mw 8.9 [Wang et al., 2013] ; the downdip end of the highly locked zone is shown by the black dotted line [Wang et al., 2013]. e, f. Vergence is shown as a function of the internal friction (μ_{int}) and the megathrust effective friction (μ_b^{eff}) for northern Sumatra and Cascadia. In the studied frictional range, the prism can either be at stable state (the full megathrust is activated as well as a frontal thrust) or at extensional unstable state (white domain, corresponding to a gravitational collapse). At stable state, the frontal thrust can either be landward (red domain) or seaward (blue domain) vergent. The gray domain stands for the propagation of the deformation toward the tip of the wedge. Extracted from [Cubas et al., 2016]

could reproduce this vergence, with extremely low effective megathrust friction ($\leq$ 0.02 and $\leq$ 0.032 respectively, figure 3.20). We obtained a larger range for southern Sumatra, with still low effective megathrust friction ($\mu_{eff} \leq 0.13$).

The very low effective friction could either be due to long-term pore pressure or dynamic weakening mechanisms such as thermal pressurization. However, we have also shown that landward vergence only develops if a wedge lies in the upper and left part of the stable domain established by the critical taper theory, close to the extensional critical limit (figure 3.21a). Yet, a wedge usually tends to stay close to its compressional critical state, which is the less expensive state. Only two conditions can lead a wedge to diverge from this limit : (1) a very high sedimentation rate impeding the wedge to recover the compressional critical state, or (2) sudden and successive decreases of the effective megathrust friction (figure 3.21b). No high sedimentation rate has been reported for either southern Cascadia [MacKay, 1995] or the Sumatra margin. We therefore favored hypothesis 2.

This hypothesis was further supported from VP and VP/Vs ratios attesting of a high pore fluid pressure where the accretionary prism is seaward and a moderate one where the wedge has a landward vergence [Han et al., 2017, Zhu et al., 2020a].

The deformation of accretionary prisms can thus provide strong insights on past seafloor ruptures and tsunamigenic potential (figure 3.21c). Accretionary prisms with seaward-vergent

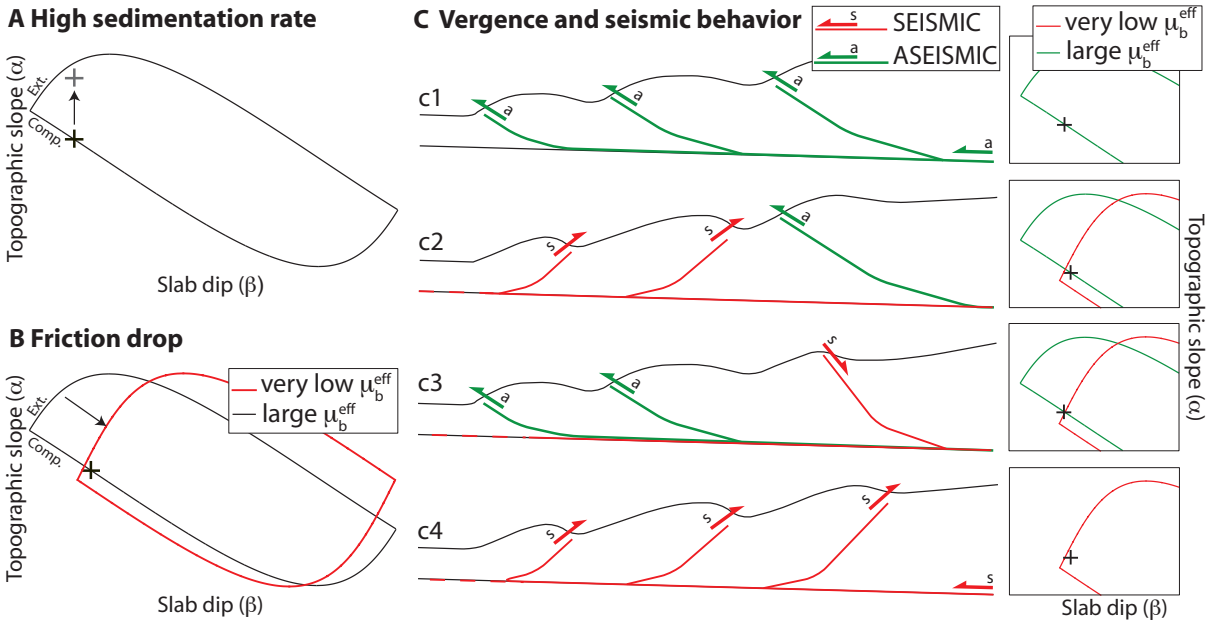

FIGURE 3.21 – Mechanical explanations for landward vergence in accretionary prisms. A : A strong sedimentation rate can increase the topographic slope, transferring the prism from the compressional (comp) critical state (black cross) to the landward domain (gray cross). ext.— extension. B : A sudden decrease of the effective megathrust friction can bring the prism (black cross) from the compressional critical state associated with a relatively high megathrust effective friction to the stable landward domain of a low effective megathrust friction envelope (μ_b^{eff}, effective basal friction). C : Relations between thrusting, normal faulting, and vergence with the seismic behaviour. Seaward-vergent thrust faults of a prism at compressional critical state are expected to be aseismic. Landward-vergent thrust faults and normal faults can be related to a dynamic decrease of the effective megathrust friction. Extracted from [Cubas et al., 2016]

faults (c1 in figure 3.21c), close to their critical state and characterized by megathrust frictions > 0.1, such as Central Chile, are probably only deformed aseismically [Gao and Wang, 2014, Cubas et al., 2013b]. No clear conclusion can be drawn for seaward-vergent prisms at stable state with very low effective friction. Accretionary prisms showing two styles of deformation, seaward- and landward-vergent thrusts (c2) such as southern Sumatra or thrust and normal faults (c3) as the Tohoku-Oki prism, could undergo both aseismic and seismic slip. At a slow slip rate, the wedge is most probably at compressional critical state, characterized by friction ~ 0.1, but during frontal propagation of an earthquake, the dynamic decrease of the effective friction would displace the wedge either in the landward domain or at the extensional critical limit. Accretionary prisms with only landward-vergent thrusts such as Cascadia and some portions of Sumatra (c4) are probably mainly deformed during or shortly after the frontal propagation of earthquakes. Hence, appropriate measures should be taken to mitigate tsunamigenic risks along the Mentawai and Cascadia gaps.

Looking for spatial variations of frictional properties to identify seismic asperities [Pajang et al., 2021]

The 1000 km long Makran is one of the few subduction zones left with a largely unconstrained seismogenic potential. The region indeed lacks historical records due to the sparsity of past settled population and is still very poorly instrumented. Along the Pakistani side, only three significant events in 1756, 1851 and 1945 have been reported [Byrne et al., 1992]. The last one, with an estimated magnitude of 8.1, is the only major event instrumentally recorded so far (figure 3.22a). Along the Iranian side, one major event dated back to 1483 could be linked to

the subduction [Ambraseys and Melville, 1982], but its location and date are strongly debated [Musson, 2009]. Recent geodetic and InSAR studies have shown that some accumulation of elastic strain along the plate interface is required to explain the velocity profiles on both the Pakistani and Iranian sides [Lin et al., 2015, Frohling and Szeliga, 2016, Penney et al., 2017] (figure 3.22b). All studies proposed a relatively strong coupling along eastern Makran (where the 1945 earthquake occurred), a decrease along the central part, and a possible increase westward. However, due to the sparsity of stations (figure 3.22b), large trench-coast distance, and limited constraints on slab dip, these studies were unable to constrain neither the along- dip nor the along-strike extent of possible coupled zones [e.g., Penney et al., 2017].

The Makran subduction zone is famous for its impressive ~7.5 km thick and 400 km wide accretionary prism, half of it subaerial [Kopp et al., 2000]. Large accretionary prisms have often been considered of limited seismic and tsunamigenic risk because of the rate-strengthening nature of their unconsolidated sediments [Oleskevich et al., 1999, Scholz, 1998]. This classical view, the particular dimension of the Makran prism, and the lack of historical earthquake led many authors to disregard the seismogenic potential of the area. However, the idea of limited extent of earthquakes to accretionary prisms was strongly challenged by the 2011 Mw 9.0 Tohoku-Oki and the 2004 Mw 9.1 Sumatra Andaman events.

As we have seen before, megathrust effective friction appears to differ significantly between aseismic or seismic areas. Megathrusts undergoing mostly aseismic deformation are characterized by intermediate values of effective friction ($\mu_b^{eff} > 0.1$), whereas lower effective (or apparent) friction is found where major earthquakes occur ($\mu_b^{eff} < 0.01$-0.03) [Gao and Wang, 2014, Cubas et al., 2013b]. Such differences in effective friction are significant enough to produce wedge segments with varying morphologies and deformation patterns. For instance, a wedge characterized by aseismic slip and thus intermediate friction along the megathrust will reach more easily its critical state generating internal deformation. On the contrary, seismic asperities characterized by very low effective friction coefficients are expected to construct a stable wedge, impeding any internal deformation. Moreover, the transition of effective friction coefficients from aseismic to seismic asperities can also induce activation of splay faults. As a consequence, the accretionary wedge deformation can bring significant information on the slip behaviour of the megathrust.

The Western Makran accretionary prism appears as an ideal candidate to study and link the finite deformation with spatial variations of megathrust frictional properties and seismic behaviour. In this study, we took advantage of seismic profiles released by NIOC along the whole Iranian side to improve the assessment of seismic and tsunamigenic hazards of the region. A structural map along the Iranian part of the Oman Sea was first built and three N-S seismic profiles were then investigated (orange lines figure 3.22). The profiles are characterized by a long imbricated thrust zone that takes place at the front of the wedge. A diapiric zone of shallow origin lies in between the imbricated zone and the shore. Along the eastern and western shores, active listric normal faults seem to root down to the megathrust. Eastern and western domains have developed similar deformation, with three zones of active faulting : the normal faults on shore, thrusts ahead of the mud diapirs, and the frontal thrusts. On the contrary, no normal faults are identified along the central domain, where a seamount is entering into subduction. Two mechanical analyses were performed to retrieve the frictional properties of the megathrust. We first applied the critical taper theory to constrain the pore fluid pressure of the wedge. We then applied the limit analysis on two selected profiles. Along the eastern profile, a transition from very low to extremely low friction is required to activate the large coastal normal fault (from μ_b^{eff} = 0.01-0.06, to μ_b^{eff} = 0.003-0.012, figure 3.23). To propagate the deformation to the front, an increase of friction along the imbricated zone is necessary (μ_b^{eff} = 0.017-0.031, figure 3.23). The method could not be applied on the incomplete western profile. However, since the deformation is similar to the eastern profile, the same transitions of friction are expected.

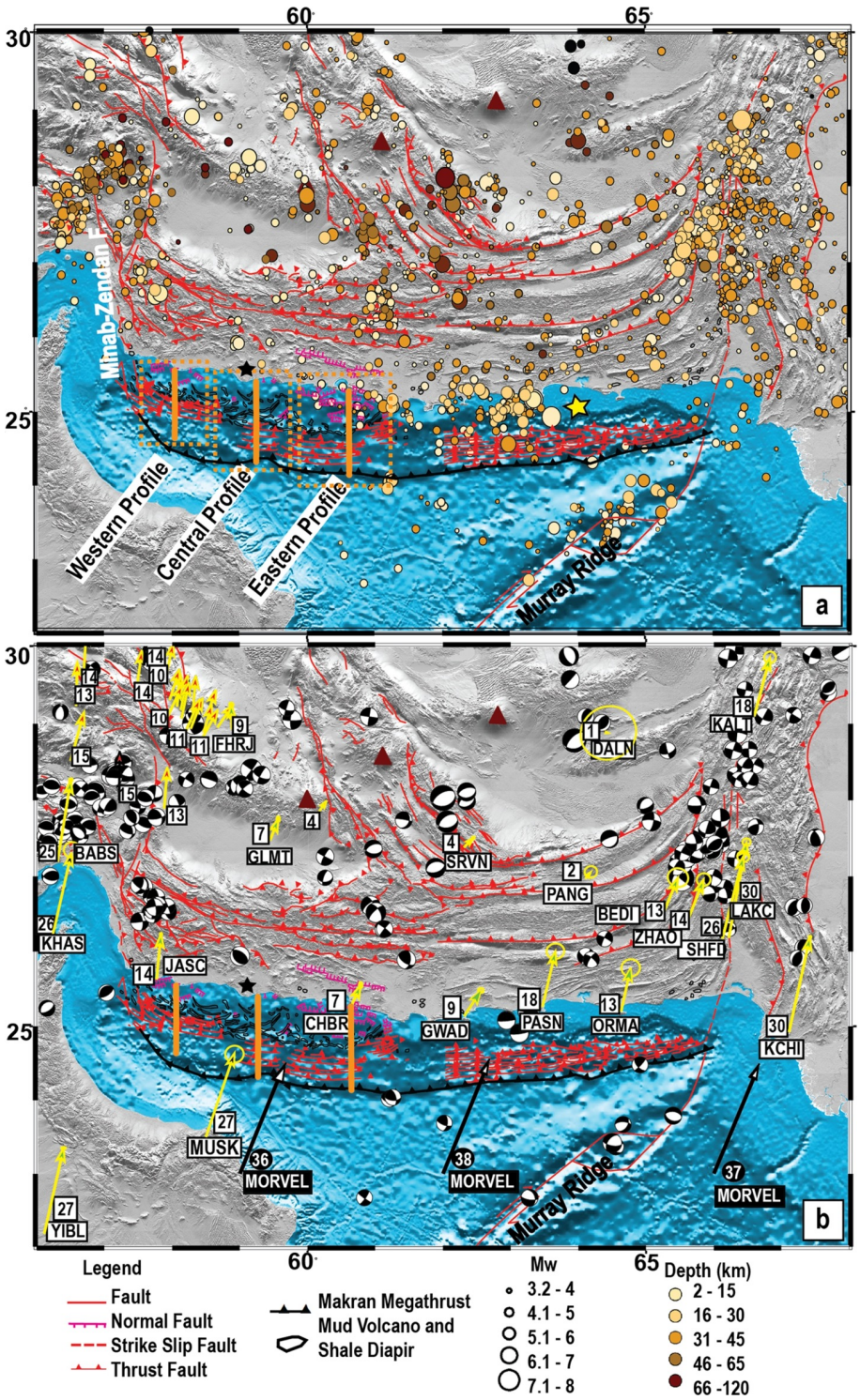

FIGURE 3.22 – Seismo-tectonic map of Makran a. Seismicity, with earthquakes of magnitude≥3.5 from 1945 to 2013 shown as coloured circles. Red lines indicate known faults, mud volcanoes are shown by black contours. Positions of active mud volcanoes within Pakistani side from Kassi et al. [2013]. Imbricate thrust faults in the Pakistani side from Smith et al. [2012] picked from MCS data (multichannel seismic reflection) and correlated with bathymetric data. On the Iranian side, mud volcanoes, imbricate thrust faults, and normal faults are picked from PC2000 data released by NIOC. The onshore well in Iran is indicated by black star and the 1945 Mw 8.1 earthquake by yellow star. Thick orange lines indicate the 2D seismic lines used in this study. Based on the structural analysis western Makran can be separated in three different structural domains (Western, Central and Eastern) which are identified by dashed-orange boxes. b. Relative motions with respect to stable Eurasia. Yellow arrows are GPS velocity vectors with 95 per cent confidence ellipses [Masson et al., 2007, Frohling and Szeliga, 2016] ; MORVEL velocities from DeMets et al. [2010]. Focal mechanisms reported by gCMT. Extracted from Pajang et al. [2021]

The Central domain is also characterized by very low effective friction ; but, the absence of normal fault does not allow to evidence any frictional transition.

Since dynamic effective friction coefficients are significantly lower than frictions at slow slip rate, the region of extremely low friction between the normal fault and the imbricated zone might reveal the location of a seismic asperity (figure 3.24). The along-dip extent of these potential asperities would be very similar to the 1851 and 1945 events, which supports our hypothesis. The difference in deformation along strike would thus reveal the existence of two different asperities, one along the eastern domain and a second along the western domain. Since no earthquake have occurred in the region for, at least, the last 1000 years, an event of large magnitude may strike the Iranian Makran, in particular its Eastern domain.

3.4.6 Accounting for structural and rheological complexities of the megathrust

The more we monitor subduction zones, the more we detect temporal changes in behaviours that are incompatible with the sole application of the rate-and-state friction laws. For instance, around the 2016 Mw 7.8 Perdenales rupture zone large and rapid afterslip, governed by rate-strengthening properties, developed at discrete areas of the Ecuadorian megathrust that had previously hosted slow slip events, of rate-weakening behaviour [Rolandone et al., 2018]. Afterslip occurred within the coseismic area of the 2015 Mw 8.3 Illapel earthquake [Tissandier et al., 2023]. The same type of contradictory observations has been recorded along continental faults [e.g., Thomas et al., 2017]. A tsunami earthquake and SSEs occurred along the same portion of the Hikurangi margin megathrust [Wallace et al., 2016]. Along the Chilean and Japan subduction zones, large earthquakes or large slip areas unexpectedly occurred along weakly coupled patches, of supposed rate-strengthening behaviour [Perfettini and Avouac, 2014, Béjar-Pizarro et al., 2013].

From seismic imaging and exhumed fault zone studies, we know that plate boundaries are not discrete planes but rather complex zones, with a finite width, composed of linked segments embedded in a damage zone, of typically a few tens to hundreds of meters [Vannucchi et al., 2012, and references herein]. Moreover, the plate boundary undergoes regular vertical migration : downward migration during underplating and underthrusting events [Gutscher et al., 1998, Park et al., 2002, Collot et al., 2008, 2011] ; upward migration during basal erosion events, related to seafloor reliefs such as seamounts, ridges or horts and grabbens [e.g., von Huene and Lallemand, 1990, McIntosh et al., 1993, Ranero and von Huene, 2000, Clift et al., 2003, Vannucchi et al., 2003, von Huene and Ranero, 2003] . This seafloor roughness and its subsequent upper plate damage, has repeatedly been invoked as acting as barriers to earthquake propagation [e.g., Kodaira et al., 2000, Wang and Bilek, 2014, Geersen et al., 2015]. In addition, as shown by core sampling and exhumed fault zone, faults resemble more to melange shear zones, that can experience both ductile and brittle deformation controlled by temporal changes in strain rate or effective stress, and brittle-ductile transition are not as sharp as proposed in the rate-and-state paradigm [e.g., Fagereng and Sibson, 2010, Fagereng and Beall, 2021]. Hence, megathrust cannot be considered as formed of a unique plane, with a single composition and a single depth-dependent rheology. Inconsistent observations might be related to the over-simplification imposed by the rate-and-state paradigm.

In the following study [Cubas et al., 2022], from a CTT analysis applied along the Chilean forearc, we explored the role of plate boundary migration and its resulting distributed deformation, on mega-earthquake extent and slip behaviours. This work led us to propose that slip deficit patterns and earthquake segmentation could actually reflect the along-dip and along-strike distribution of the plate interface deformation.

In the framework of Sepideh Pajang's thesis, we used thermo-mechanical models accounting

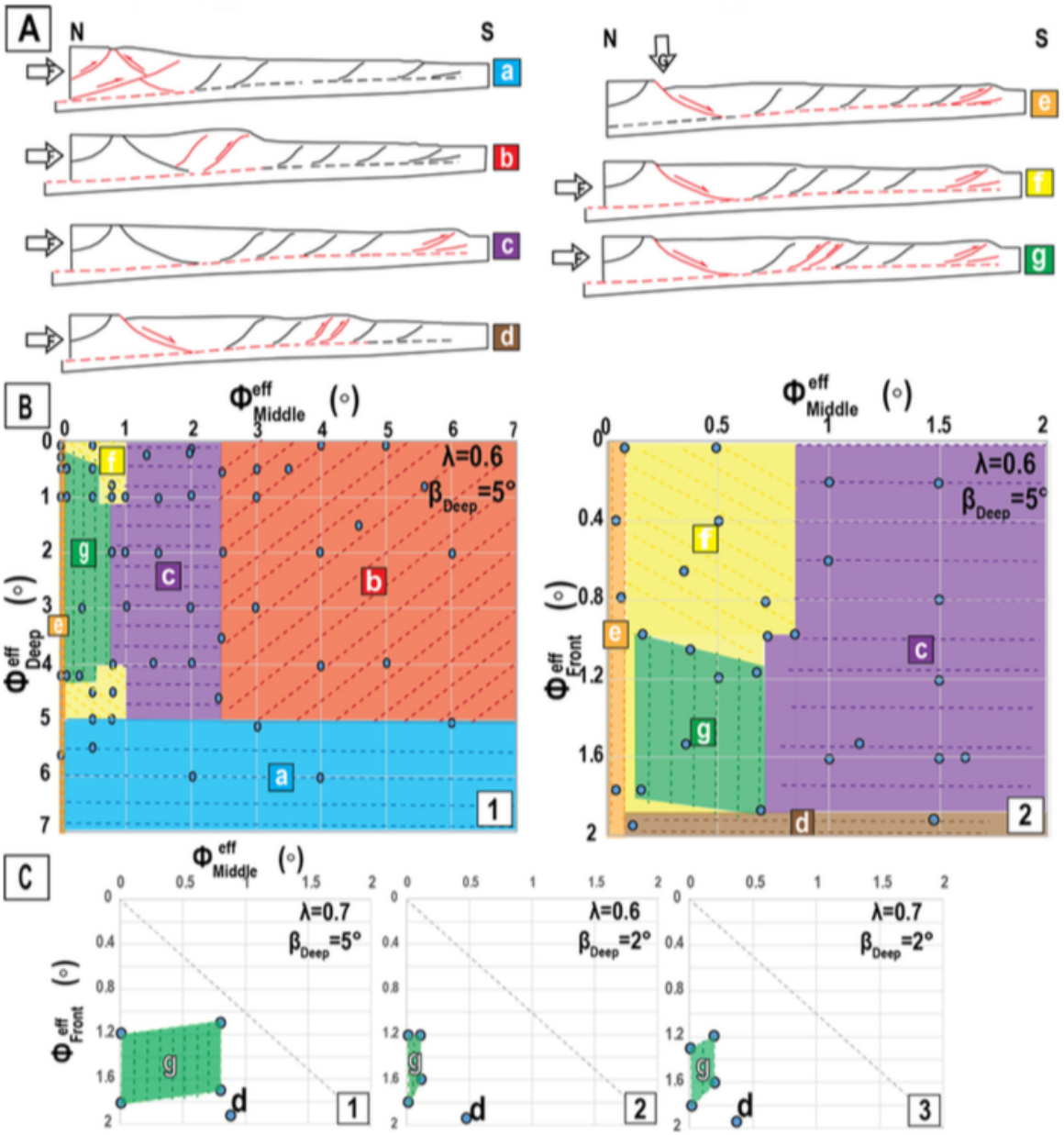

FIGURE 3.23 – A. Kinematics obtained for the range of effective frictions along the décollement provided in figure B and C. a-f are failure models, g is the kinematics we seek to reproduce (a : Normal fault acts as reverse and décollement not active, b : Normal fault and décollement non-active, c : Normal fault and out-of-sequence thrust faults non-active, d : Décollement partially active, e : Gravitational normal fault, f : Normal faulting but non-active out-of-sequence thrust faults, g : Normal faulting, out-of-sequence thrust faults and full décollement active). B.1 Exploration of kinematics for varying effective friction coefficients along the middle and deep décollement. Circles correspond to simulations, coloured areas to kinematical domains, with kinematics g in green. B.2 Exploration of kinematics for varying effective friction coefficients along the frontal and middle décollement. C. 1-3. Frictions along the frontal and middle décollement reproducing kinematics g. Two different pore pressure ratios (λ= 0.6 and 0.7) and two different décollement dips (β = 2^o and 5^o) are investigated. Extracted from Pajang et al. [2021]

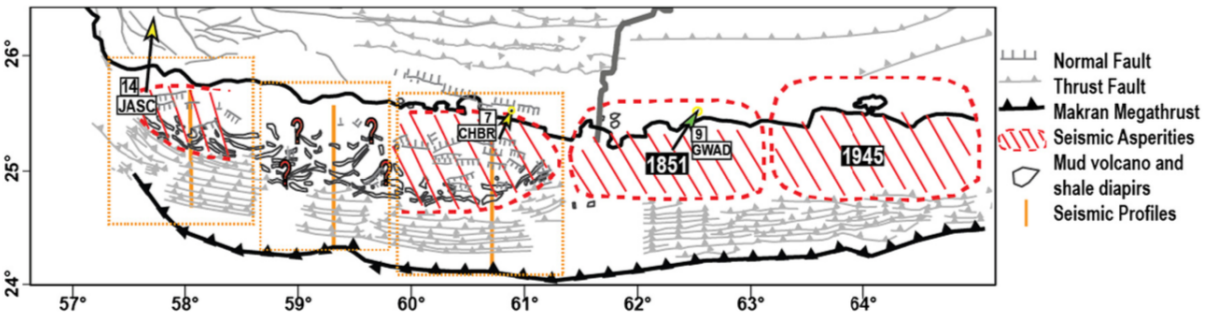

FIGURE 3.24 – Areas of high seismogenic potential along the Makran subduction zone, according to our structural and mechanical analysis and past seismic ruptures from Lin et al. [2015]. Extracted from Pajang et al. [2021]

for temperature evolution to capture how thermally controlled rheological transitions can affect the deformation and topography of accretionary prisms. The model has then been applied to Makran, to locate the brittle/viscous transition and to propose a possible origin for the large coastal normal faults.

Earthquake ruptures and topography of the Chilean margin controlled by plate interface deformation [Cubas et al., 2022]

Solid Earth, 13, 779–792, 2022
https://doi.org/10.5194/se-13-779-2022

Solid Earth Open Access EGU

Earthquake ruptures and topography of the Chilean margin controlled by plate interface deformation

Nadaya Cubas[1], **Philippe Agard**[1], **and Roxane Tissandier**[2]

[1]CNRS-INSU, Institut des Sciences de la Terre Paris, Sorbonne Université, ISTeP UMR 7193, 75005 Paris, France
[2]Institut de Physique du Globe de Paris, Université de Paris, CNRS, 75238 Paris, France

Correspondence: Nadaya Cubas (nadaya.cubas@sorbonne-universite.fr)

Received: 13 December 2021 – Discussion started: 20 December 2021
Revised: 15 February 2022 – Accepted: 22 February 2022 – Published: 1 April 2022

Abstract. What controls the location and segmentation of mega-earthquakes in subduction zones is a long-standing problem in Earth sciences. Prediction of earthquake rupture extent mostly relies on interplate coupling models based on Global Navigation Satellite Systems providing patterns of slip deficit between tectonic plates. We here investigate if and how the strongly and weakly coupled patches revealed by these models relate to the distribution of deformation along the plate interface, i.e., basal erosion and/or underplating. From a mechanical analysis of the topography applied along the Chilean subduction zone, we show that extensive plate interface deformation takes place along most of the margin. We show that basal erosion occurs preferentially at 15 km depth while underplating does at 35 ± 10 and 60 ± 5 km depth, in agreement with P-T conditions of recovered underplated material, expected pore pressures and the spatial distribution of marine terraces and uplift rates. South of the Juan Fernández Ridge, large sediment input favors shallow accretion and underplating of subducted sediments, while along northern Chile, extensive basal erosion provides material for the underplating. We then show that, along the accretionary margin, the two last major earthquakes were limited along their down-dip end by underplating while, along the erosive margin, they were surrounded by both basal erosion and underplating. Segments with heterogeneously distributed deformation largely coincide with lateral earthquake terminations. We therefore propose that long-lived plate interface deformation promotes stress build-up and leads to earthquake nucleation. Earthquakes then propagate along fault planes shielded from this long-lived permanent deformation, and are finally stopped by segments of heterogeneously distributed deformation. Slip deficit patterns and earthquake segmentation therefore reflect the along-dip and along-strike distribution of the plate interface deformation. Topography acts as a mirror of distributed plate interface deformation and should be more systematically studied to improve the prediction of earthquake ruptures.

1 Introduction

Predicting the extent of subduction zone seismic ruptures mostly relies on geodetic observations of interseismic coupling (e.g., Moreno et al., 2010), notwithstanding spatial resolution issues (Loveless and Meade, 2011). Some earthquakes have however ruptured low coupled zones (Noda and Lapusta, 2013) or ruptured only parts of the highly locked patches (e.g., Konca et al., 2008). This was the case for the 2014 M_w 8.4 Iquique earthquake, which only ruptured the northern end of the north Chile gap (last broken in 1877; Ruiz et al., 2014a), or the Tocopilla M_w 7.8 earthquake, which struck the down-dip and less coupled part of the same gap 7 years before (Delouis et al., 1998; Metois et al., 2016; Fig. 1). Predicting the location and extent of earthquakes clearly requires a better understanding of earthquake mechanics.

Subduction earthquake propagation has so far been either related to megathrust frictional and pore fluid pressure properties (Perfettini et al., 2010; Kaneko et al., 2010; Moreno et al., 2014), inherited stress states (Konca et al., 2008; Kaneko et al., 2010) or seafloor roughness (Kodaira et al., 2000; Wang and Bilek, 2014; Bletery et al., 2016). Megathrusts, commonly regarded as interfingered seismic and aseismic patches with contrasting frictional properties, are con-

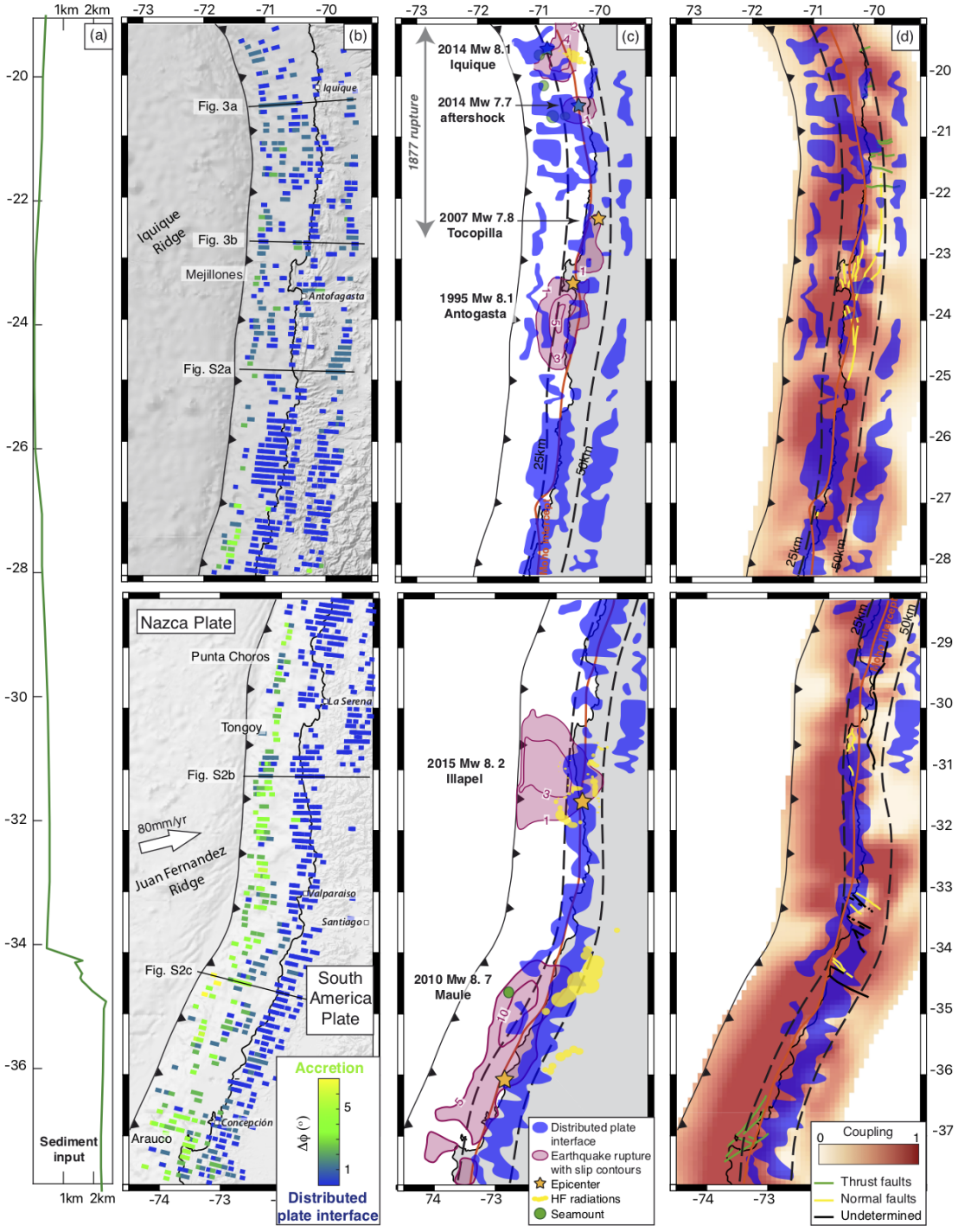

Figure 1. **(a)** Sediment thickness at the trench (Santibáñez et al., 2018; Tréhu et al., 2019). **(b)** Difference between internal and basal effective friction of identified critical segments. Large differences lead to standard accretion with thrust faults reaching the surface, while small differences lead to the development of faults parallel to the plate interface, allowing for either basal erosion or underplating. **(c)** Interpreted patches with distributed deformation along the plate interface related to either basal erosion or underplating compared to last major events: Antofagasta 1995 (Chlieh et al., 2004), Tocopilla 2007 (Béjar-Pizarro et al., 2013), Maule 2010 (Lin et al., 2013), Iquique 2014 and its aftershock (Ruiz et al., 2014b) and Illapel 2015 (Tilmann et al., 2016). Orange stars: Global Centroid Moment Tensor (GCMT) solutions, blue stars: Community Seismic Network (CSN) catalog. High-frequency radiation (yellow; Wang and Mori, 2011; Meng et al., 2015, 2018), identified seamounts (green; Geersen et al., 2015; Maksymowicz et al., 2015), slab depths (dashed black; Hayes et al., 2018) and slab-Moho intercept (orange; Tassara and Echaurren, 2012). **(d)** Interpreted patches with a distributed plate interface compared to coupling model (Metois et al., 2016) with known active faults (Santibáñez et al., 2018).

ventionally sub-divided into four domains with depth (A–D; Lay et al., 2012). The highly coupled domain-B hosts mega-earthquakes, while the partly coupled domain-C is characterized by moderate slip earthquakes generating significant high-frequency seismic radiation (Lay et al., 2012).

The distribution of these patches might persist over timescales of up to millions of years and control forearc morphology (Song and Simons, 2003). A spatial correlation between the coastline and the down-dip limit of the strongly locked zone has indeed been evidenced along the northern Chilean margin (Béjar-Pizarro et al., 2013; Metois et al., 2016). Coastal uplift rates inferred from marine terraces, between 0.1 and 0.3 mm a^{-1} over the last 400 kyr (Saillard et al., 2017), have been linked to the change of mechanical coupling between domain-B and domain-C (Saillard et al., 2017) and to underplating (Delouis et al., 1998; Adam and Reuther, 2000; Clift and Hartley, 2007). Numerical investigations recently suggested that underplating, through transient stripping of the slab-top near the base of the forearc crust, may generate periodic multi-million-year-long uplift sequences and a trackable 100 m high topographic signal (Menant et al., 2020).

Bathymetric features are considered as potential seismic barriers, based on the distribution of incoming plate roughness (Wang and Bilek, 2014; Lallemand et al., 2018) or gravimetric anomalies (Bassett and Watts, 2015). Subduction of bathymetric features induces large fracture networks, promoting removal of material from the bottom of the overriding plate (basal erosion, Ranero and von Huene, 2000) and potentially characteristic topographic features (Dominguez et al., 1998; Collot et al., 2008; Ruh et al., 2016). Heterogeneities in the structure of the damaged plate interface and stress field, as a result, would favor aseismic slip and impede the propagation of large ruptures (Wang and Bilek, 2014). Very few seismic surveys, however, have imaged seamounts surrounding a large rupture (Kodaira et al., 2000; Geersen et al., 2015).

We herein explore an alternative explanation: rather than variations of frictional properties or of seafloor roughness, earthquake segmentation might relate to the distribution of deformation along the plate interface (Wang and Bilek, 2014), as observed along strike-slip faults (Wesnousky, 2006). Both underplating and basal erosion require the redistribution of deformation, ultimately leading to the migration of the plate boundary (Vannucchi et al., 2012; Agard et al., 2018). We here show that the location of such distributed deformation along the plate interface can be captured from a simple mechanical analysis of the topography, since underplating and basal erosion both impact forearc morphology. This method is applied over a 2000 km long stretch along the Chilean margin, known to transition from erosive to accretionary from north to south, as incoming sediment thickness increases (von Huene and Ranero, 2003; Clift and Vannucchi, 2004; Clift and Hartley, 2007; Fig. 1a). This margin is one of the best instrumentally documented subduction zones, along which five mega-earthquakes, including a domain-C event, have occurred during the last 25 years (Fig. 1c). We first map out the location of the distributed deformation zones associated with basal erosion and underplating and compare them with the megathrust segmentation proposed so far. We then discuss how distributed deformation along the plate interface impacts and therefore can be used to constrain earthquake extent and mechanics.

2 Methodology

We applied the critical taper theory (CTT; Davis et al., 1983, Fig. 2). The theory predicts the topographic slope of a wedge on the verge of failure as well as dips of its internal faults, from the frictional and pore fluid pressure properties of the wedge and megathrust (Dahlen, 1984). We used the solution of Dahlen (1984) for a non cohesive wedge, describing the critical taper, formed by the topographic slope α and the slab dip β, as a function of the angle Ψ_B, formed by the maximum principal stress σ_1 and the base of the wedge and the angle Ψ_0, formed by σ_1 and the top of the wedge. The solution for the lower compressional branch is

$$(\alpha + \beta) = \Psi_B - \Psi_0 \ , \tag{1}$$

with

$$\Psi_B = \frac{1}{2}\arcsin\left(\frac{\sin\phi'_{\mathrm{b}}}{\sin\phi_{\mathrm{b}}}\right) - \frac{1}{2}\phi'_{\mathrm{b}} \ , \tag{2}$$

$$\Psi_0 = \frac{1}{2}\arcsin\left(\frac{\sin\alpha'}{\sin\phi_{\mathrm{int}}}\right) - \frac{1}{2}\alpha'. \tag{3}$$

The angles ϕ_{int} and ϕ_{b} are the internal and basal coefficients of friction defined as $\mu_{\mathrm{int}} = \tan\phi_{\mathrm{int}}$ and $\mu_{\mathrm{b}} = \tan\phi_{\mathrm{b}}$, and

$$\phi'_{\mathrm{b}} = \arctan\left[\left(\frac{1-\lambda_{\mathrm{b}}}{1-\lambda}\right)\tan\phi_{\mathrm{b}}\right] , \tag{4}$$

$$\alpha' = \arctan\left[\left(\frac{1-\rho_{\mathrm{w}}/\rho}{1-\lambda}\right)\tan\alpha\right] . \tag{5}$$

The internal and basal Hubbert–Rubbey fluid pressure ratios λ and λ_{b} are defined in Davis et al. (1983) as

$$\lambda = \frac{P - \rho_{\mathrm{w}} g D}{|\sigma_z| - \rho_{\mathrm{w}} g D} \ , \tag{6}$$

$$\lambda_{\mathrm{b}} = \frac{P_{\mathrm{b}} - \rho_{\mathrm{w}} g D}{|\sigma_z| - \rho_{\mathrm{w}} g D} \ , \tag{7}$$

where ρ and ρ_{w} are the wedge material and water densities and D is the water depth. The solution is exact if $\lambda = \lambda_{\mathrm{b}}$ and the approximation is valid for small tapers as used in this

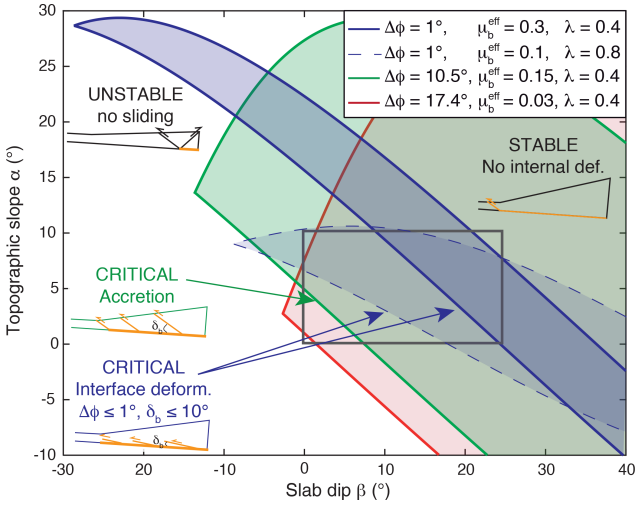

Figure 2. Critical taper theory with different mechanical states. The gray rectangle represents the standard range of topographic slope α and slab dip β of subduction zones. With extremely low effective friction along the megathrust (red curve), the wedge systematically falls in the stable domain. With larger effective friction, and large difference of effective friction between the megathrust and the wedge (green curve), the wedge can reach the accretionary critical state characterized by internal faulting. With a reduced difference (blue curves), a wedge can still reach the critical state but the dip of internal faults within the wedge will decrease and become parallel to the plate interface. High pore fluid pressure facilitates interface deformation for low slab dips (dashed blue curve), whereas lower pore fluid pressure induces interface deformation at larger slab dip (plain blue curve).

study (Wang et al., 2006).

The relationship between the topographic slope α and the slab dip β forms an envelope separating different mechanical states (Fig. 2). The wedge is at critical state if the taper formed by α and β follows a critical envelope. In that case, activation of the megathrust requires internal faulting. In contrast, if the taper exceeds this critical limit, the wedge enters in a stable domain (in the sense of the CTT), where the only possible active fault is the megathrust.

Dynamic effective friction of seismogenic zones has been shown to reach extremely low values ($\mu \sim 0.01$–0.03; Fulton et al., 2013; Gao and Wang, 2014). As a consequence, a forearc above a seismogenic megathrust, with standard α and β, will systematically fall in the CTT stable domain (Fig. 2). In contrast, aseismic megathrusts are characterized by larger effective friction ($\mu \sim 0.1$–0.15; Cubas et al., 2013; Gao and Wang, 2014), allowing the wedge to reach critical conditions (Cubas et al., 2013) (Fig. 2). Furthermore, at critical state, if the basal effective friction of the wedge approaches the internal effective friction, the dip of internal faults within the wedge will decrease and become parallel to the plate interface. A small difference of friction will thus lead to deformation either by basal accretion (in the lower plate) or by basal erosion (in the upper plate), instead of standard accretion characterized by thrust faults reaching the surface (Dahlen, 1984; Fig. 2). If the basal effective friction reaches the internal one, a highly fractured forearc is even expected.

We here used inversion to retrieve the effective basal friction, the internal friction and the internal pore pressure ratio from the $\alpha - \beta$ co-variation. To do so, we followed the procedure developed by Cubas et al. (2013) and detailed in the Supplement. We used the ETOPO 1 model (Amante and Eakins, 2009) to derive the bathymetric and topographic slope, and slab 2.0 (Hayes et al., 2018) for the slab dip. We built swath profiles perpendicular to the trench every 0.1° along trench to get average topographic slopes and slab dips with their standard deviations necessary to the inversion procedure (Fig. S1 in the Supplement). We explored from 10 to 45° for ϕ_{int}, from 1 to 44.9° for $\phi_{\text{b}}^{\text{eff}}$ and from 0.35 to 0.975 for λ. Along the $\alpha - \beta$ profiles, we selected segments with a slope comprised between the two extreme theoretical envelops of the parameter set (Figs. 3 and S2 in the Supplement). For each of these segments, we retrieved probability density functions for the friction of the wedge, the pore pressure ratio of the wedge and the effective friction of the megathrust (Fig. S3 in the Supplement) and best misfit sets (Fig. S4 in the Supplement). We only kept segments with misfits lower than 0.1, and with values consistent with standard friction: from 25 to 43° for ϕ_{int} (consistent with lab experiment values (Byerlee, 1978)), from 1 to 42.9° for $\phi_{\text{b}}^{\text{eff}}$ (same range as the internal friction but considering additional pore fluid pressure effect) and from 0.35 to 0.975 for λ. Figure 3a–c shows the fit between the $\alpha - \beta$ profiles and the envelops corresponding to the best misfit of the identified critical segments. These segments (Fig. 3b–d) have then been reported on Fig. 1b.

The CTT inversion only provides internal pore pressure, which can be considered as a lower bound for the megathrust pore pressure. Moreover, close effective internal and basal friction implies close internal and megathrust pore pressure.

3 Results

3.1 Locating plate interface deformation

Since we seek to capture distribution of deformation along the plate interface, we compared the internal and megathrust effective friction and mapped the difference (Fig. 1b). A 1° difference implies a dip difference $< 10°$ between the megathrust and the forward-verging thrusts. This representation allows inferring areas prone to either standard accretion, or to basal erosion/accretion, the latter being herein defined as distributed deformation along the plate interface.

The transition from erosion to accretion is particularly well captured by the method despite its relative simplicity (Fig. 1a–b). North of 26° S (i.e., at the transition between erosive and accretionary subduction), the difference in effec-

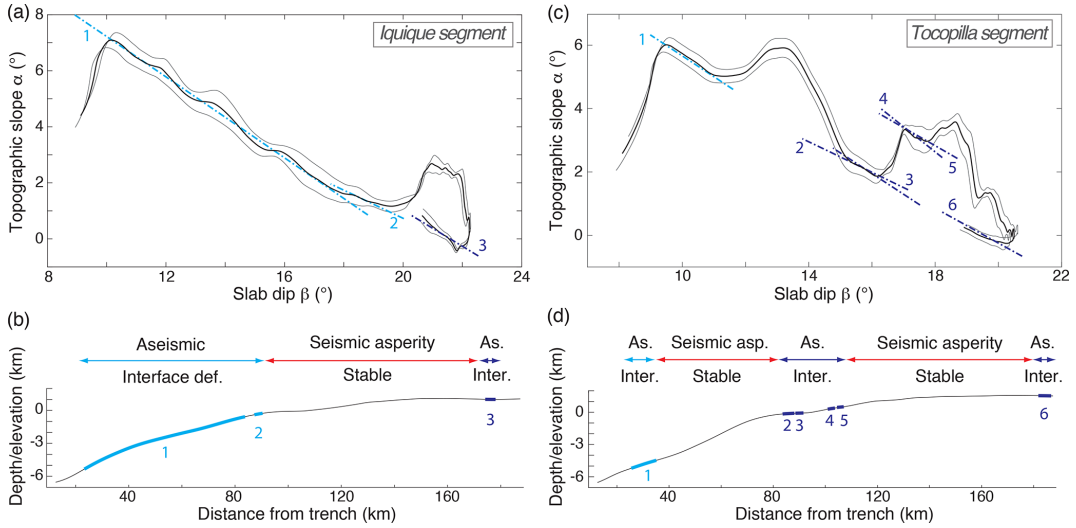

Figure 3. (a) Topographic slope (α) versus slab dip (β) for a swath profile along the Iquique segment (locations on Fig. 1b). Gray: swath plus or minus standard deviation. Segments at critical state, according to inversion, are shown in blue. For every segment, the difference between the effective internal and basal friction is lower than 1 (properties of each segment are provided in Table 1 in the Supplement). They are thus interpreted as regions of favorable plate interface deformation, shown in light blue when probably erosive and dark blue for probable underplating. Depth and distance to the trench can be viewed in Fig. S5 in the Supplement. **(b)** Relocation of the critical segments on the swath profile. **(c)** Topographic slope (α) versus slab dip (β) and **(d)** relocation of the critical segments for a swath profile along the Tocopilla segment.

tive friction is systematically lower than 2°, and mostly lower than 1°, which means that deformation is essentially located along the plate interface. The difference increases notably south of the Juan Fernández Ridge, and progresses inland towards the south, consistent with active faults mapped near the Arauco Peninsula (Fig. 1d). The method also captures basal erosion linked to the few subducted seamounts imaged around the Iquique rupture (Geersen et al., 2015; Fig. 1c).

To interpret the origin of plate interface deformation, we set the limit between accretion and interface deformation for a difference of friction angle of 1° and then searched for the depth distribution of each process (Fig. 4a–b). Results for different thresholds are also presented.

Accretion mostly occurs at depths shallower than 20 km, whereas distributed deformation along the plate interface is found at every depth with three favorable peaks: a first one at 15 km depth, a second at 35 ± 10 km depth and a third at 60 ± 5 km depth. Basal erosion due to bathymetric features is known to be efficient at shallow depth (von Huene et al., 2004), but might also occur slightly deeper as testified by subsidence of forearc basins (Clift and Hartley, 2007). Underplating has been observed at shallow depth (Kimura et al., 2010; Tréhu et al., 2019; Bangs et al., 2020), even for seamount moats (Clarke et al., 2018), but mostly occurs below 30–40 km, i.e., the long-term coupling–decoupling transition (Agard et al., 2018). The compilation of P-T conditions for recovered underplated material shows a similar distribution as CTT, with peaks at depths of 30 ± 5 km and 50 ± 5 km and a gap in between (Fig. 4b). Numerical modeling also suggests that erosion predominates over underplating at depths shallower than 20 km (Menant et al., 2020). As a consequence, we assume that the interface deformation documented here mostly relates to basal erosion for depths < 20 km, whereas underplating dominates at greater depths, in particular below the coast.

This depth divide between basal erosion and underplating is strengthened by estimates of the pore fluid pressure ratio (Fig. 4d–f). If low pore fluid pressure is mainly found in accretion conditions, higher fluid pressure dominates where basal erosion occurs (von Huene and Ranero, 2003; Vannucchi et al., 2012). Conversely, recovered underplated material from greater depth present very consistent P-T conditions of lithostatic pressure, which rules out any significant fluid overpressure (Agard et al., 2018). The first peak for basal erosion at low pore fluid pressures in Fig. 4e could be related to the 20 km depth assumption and reveal the minor occurrence of underplating at shallower depth. The trimodal distribution deduced from CTT (one peak for basal erosion and two peaks for underplating) and differences in pore pressure remains for a 0.5° or a 2° difference of friction.

Most of the critical segments attesting to distributed interface deformation have lengths smaller than 7 km, and do not exceed 20 km (Fig. 4c). This is in good agreement with the length of graben and horst and seamounts observed on the subducting plate (von Huene and Ranero, 2003; Geersen et al., 2015). This is also consistent with seismic observations (Kimura et al., 2010; Tréhu et al., 2019; Bangs et al., 2020) and the long-term rock record showing gen-

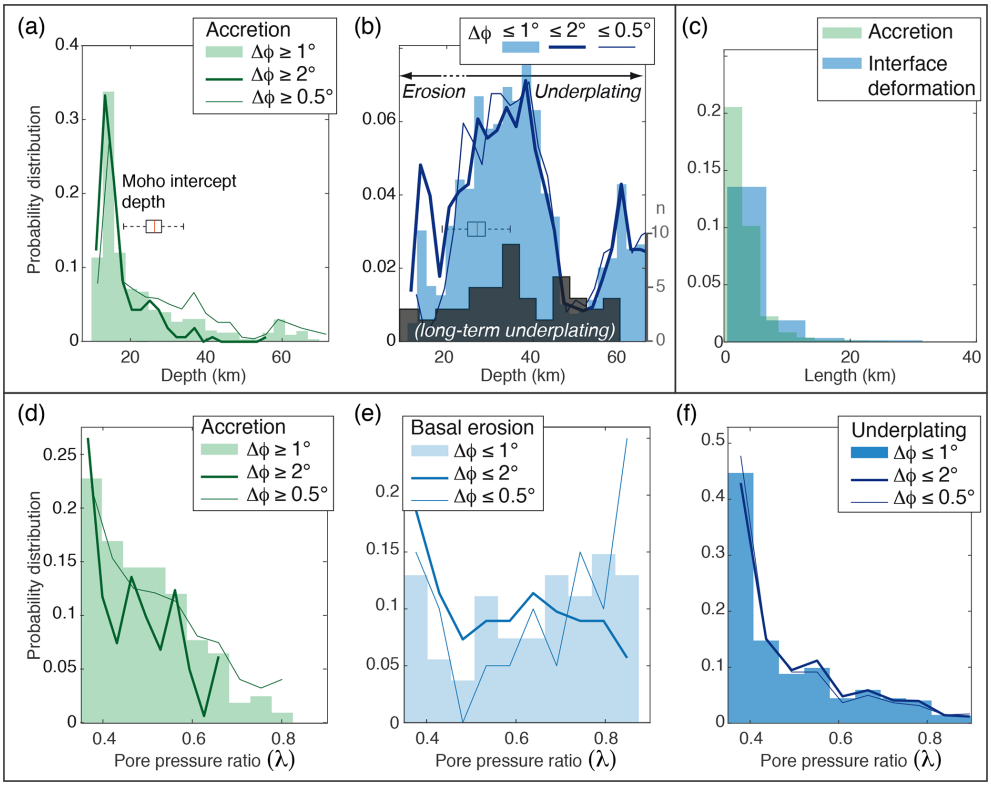

Figure 4. **(a)** Mean depth of segments at accretionary critical state and **(b)** distributed plate interface deformation critical state, compared to a compilation of the maximum burial depth reached by exhumed tectonic slicing (grey; Agard et al., 2018), and to the box plot of the Moho intercept depth (Tassara and Echaurren, 2012). **(c)** Length of segments at accretionary and distributed plate interface deformation critical state. **(d)–(f)** Pore fluid ratio λ of segments at accretionary, basal erosion and underplating critical state, assuming that basal erosion prevails above 20 km depth, and underplating below. Histogram curves are shown for a 1° difference of internal and basal effective friction, thin line for a 0.5° difference and bold line for 2° (curves were chosen for sake of clarity).

erally ≤ 300–500 m thick exhumed slices from the top of the slab (Agard et al., 2018) extending 5–10 km downdip at most (Plunder et al., 2012, 2013). Such tabular shape ratios, with seamounts probably near the higher bound (Bonnet et al., 2019), further support interface deformation parallel to the megathrust (Fagereng and Sibson, 2010; Rowe et al., 2013).

3.2 Relating plate interface deformation with long-term coastal uplift

In order to approach internal effective friction, the basal friction of the wedge needs to be relatively high (Fig. 2a). Deformation captured at depth by CTT therefore corresponds to underplating in the making, when deformation is still distributed: once tectonic slicing is achieved, basal friction will reach low values characteristic of mature faults, bringing the taper in the stable domain and impeding detection by CTT.

We here show that active, incipient underplating takes place along most of the Chilean margin (Figs. 1, 5a), whether or not strain accumulation ultimately turns these critical zones into tectonic slices (Agard et al., 2018; Bonnet et al., 2019; Kimura et al., 2007). Along the Tocopilla and Maule segments, incipient underplating takes place below the slab – continental Moho intercept (orange curve on Fig. 1c), whereas it is located above and near the intercept between 25 and 33° S. Along the northern erosive margin (Fig. 5a–b), the thin oceanic sediment is covered together with eroded material, and pieces stripped from the subducting plate are being possibly underplated. Southward, larger sediment input favors shallow accretion and underplating of subducted sediments (Fig. 5a–b), as locally observed by seismic surveys (Tréhu et al., 2019).

To evaluate the possible link between coastal uplift and regions of distributed deformation along the plate interface, we compare our spatial distribution of underplating with documented marine terraces and uplift rates (Saillard et al., 2017; Fig. 5a–c). While the irregular distribution of marine terraces may relate to fragmentary preservation rather than discontinuous underplating, most of them coincide with segments of underplating (or with standard accretion near the Arauco peninsula). The typical length of the segments showing distributed deformation along the interface is modest (∼ 10–20 km). This advocates for propagation of deformation only

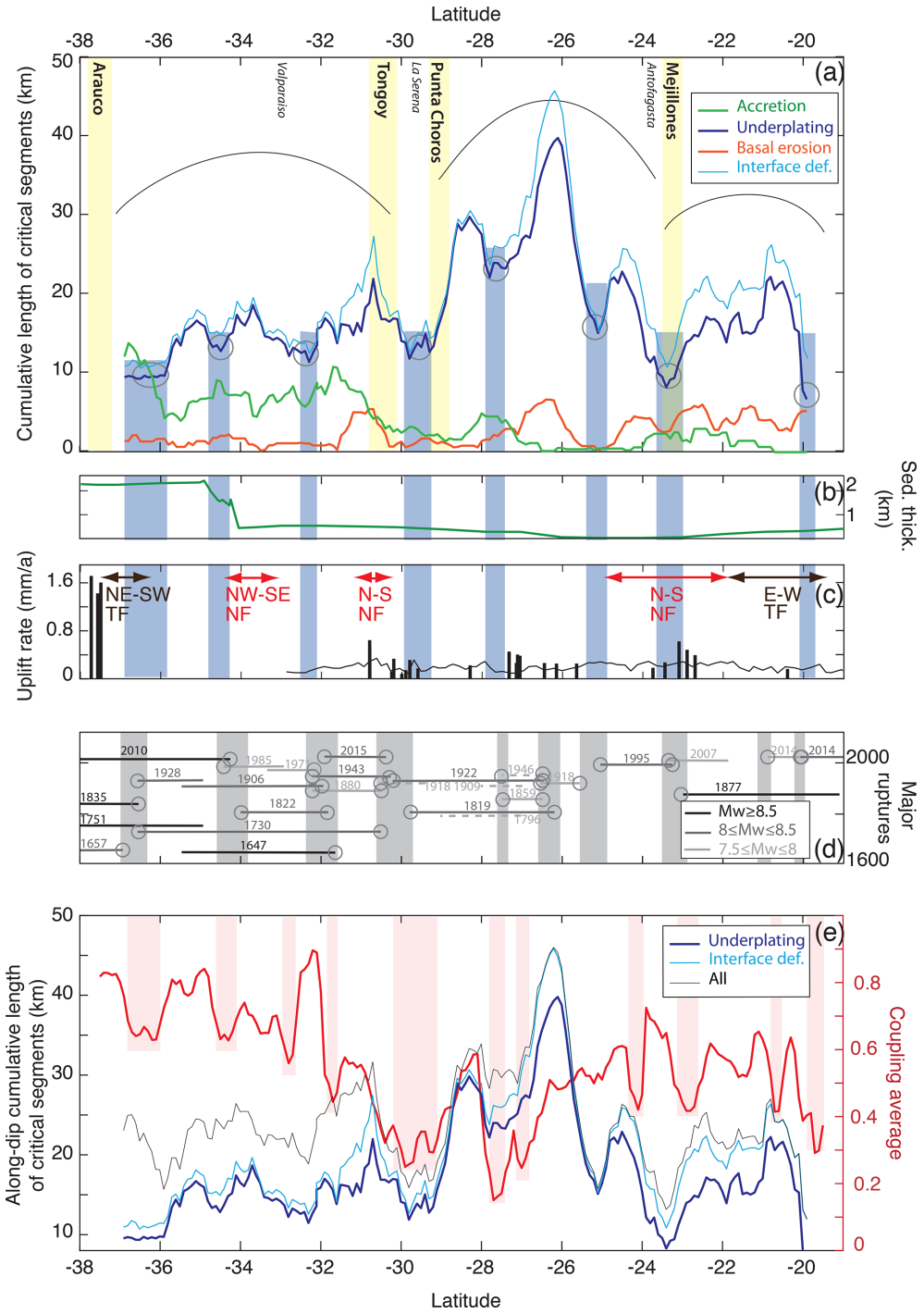

Figure 5. **(a)** Along-dip cumulative length of segments at accretionary (green), underplating (dark blue) or basal erosion (orange) critical state (length smoothed by a rectangular window over eight profiles). The light blue curve shows the cumulative length of segments with interface deformation (basal erosion + underplating). Regions with limited underplating (and interface deformation) length are represented by blue bands. **(b)** Thickness of sediment income (green; Santibáñez et al., 2018; Tréhu et al., 2019). **(c)** Quaternary uplift rates of marine terraces (black bars, largest average rate since terrace abandonment; Saillard et al., 2017), coastal uplift rate obtained from a landscape evolution model (black curve; Melnick, 2016) and extent of known active faults (NF: normal fault, TF: thrust fault; Santibáñez et al., 2018). **(d)** Along-strike extent of historical megathrust ruptures (Saillard et al., 2017). **(e)** Comparison between the cumulative length of segments at critical state (thin black), with underplating (thick blue), with both underplating and basal erosion (light blue) and the average coupling value along profiles from Metois et al. (2016) corrected by Klein et al. (2018) between 24.5 and 28° S (plain red curve). Red bands show segments of decreasing coupling. Correlation factor between coupling and underplating: $r = -0.36$, between coupling and underplating + basal erosion: $r = -0.39$.

into the topmost part of the subducting plate, e.g., into the stack of oceanic/eroded material or along a hydrated basalt layer within the crust. Although the comparison with uplift rates inferred from morphometric analysis and modeling of landscape evolution (Melnick, 2016) shows no particular pattern, underplating of relatively thin slices would be consistent with both the low uplift rates and the rock record (Agard et al., 2018).

Shallow normal faults identified along northern Chile have been related to potential underplating (Adam and Reuther, 2000; Clift and Hartley, 2007). We here show that they are located above underplating areas, and that normal faults transition southward to thrusts where accretion prevails (Fig. 5a–c).

3.3 Large megathrust earthquakes surrounded by plate interface deformation

We now compare zones of distributed deformation with areas struck by recent large earthquakes (Fig. 1c). The M_w 8.1 2014 Iquique earthquake is surrounded by patches of distributed deformation associated with basal erosion according to their depth and to seamounts detected in the area (Geersen et al., 2015). The aftershock, located 50 km south of the main event, also falls in between patches of distributed deformation. The M_w 7.8 2007 Tocopilla earthquake is limited up-dip as well as to the south by interface deformation attributed to underplating. The M_w 8.1 1995 Antofagasta earthquake seems limited up- and down-dip by distributed deformation along the plate interface. The high slip areas of the M_w 8.2 2015 Illapel and the M_w 8.7 2010 Maule earthquakes are both limited down-dip by plate interface deformation. Their frontal extent partially propagates in areas at critical state but corresponding to standard accretion. A small portion of the earthquake ruptures do overlap with the plate interface deformation, but high slip areas are always clearly limited by plate interface deformation. Moreover, Fig. 6 shows the diversity of published co-seismic models, emphasizing the uncertainties related to the proposed slip areas, that need to be taken into account for the comparison.

To summarize, along the accretionary part of the margin, mega-earthquakes are delimited down-dip by underplating whereas along the erosive domain, the extent is controlled by both basal erosion and underplating.

We now investigate the relationships between the critical segments characterized by relatively high effective basal friction, hence expected to behave aseismically, both with the along-strike segmentation inferred for large historical earthquakes ($M_w \geq 7.5$; Saillard et al., 2017, Fig. 5a–d) and with the estimates of coupling (Metois et al., 2016; Klein et al., 2018, Fig. 5a–e). Segments with limited plate interface deformation (< 15 km) coincide with a significant number of rupture terminations (blue and gray overlays, respectively: Fig. 5a–d), particularly in the southern region. Between 29 and 24° S, rupture terminations coincide with segments where plate interface deformation is reduced. The underplating segments also show a long wavelength distribution (4 to 8° latitude) corresponding to the three main seismic regions visible on Fig. 5a, d (respectively, located north of Mejillones, between Mejillones and Punta Choros, and to the south of Punta Choros). No correlation exists with sediment input (Fig. 5b). The proportion of a swath profile at critical state is then compared to the average estimate of coupling along this profile (Fig. 5e). A positive correlation is evidenced at small scale (1.5 and 2° latitude, Fig. S7 in the Supplement) between the segments with minimal underplating (blue overlays; Fig. 5a) and the regions of minimal coupling (red overlays; Fig. 5e). On a larger scale (4 and 8° latitude, Fig. S7), an anti-correlation is observed with coupling: zones of high coupling correspond to domains where underplating is somewhat more limited (e.g., between 31 and 38° S). As shown by Fig. 1d, areas marked by intense plate deformation are mostly located down-dip of the highly locked patches, in particular in the south. Continuous and voluminous sediment influx provides spatially and temporally stable mechanical conditions (Olsen et al., 2020). This leads to stationary seismic asperities followed, once the Moho is crossed, by the regular underplating of very thin and relatively short slices (typically 300–500 m thick, 5–10 km long). This spatial and temporal stability promotes topographic build-up, explaining the spatial coincidence between strongly coupled patches and efficient underplating. In contrast, segments with limited underplating might reveal spatially and temporally heterogeneous conditions along the megathrust (Olsen et al., 2020), i.e., heterogeneous deformation impeding earthquake propagation and significant topographic build-up.

Noteworthily, the hypocenters of the last major events lie at the boundary with a patch of distributed deformation. Finally, we show that the high-frequency radiation generated by the Maule and Illapel earthquakes (Wang and Mori, 2011; Meng et al., 2015, 2018) coincide with areas of extensive interplate deformation (Fig. 1c), along which spatially restricted fault planes might have been dynamically triggered.

4 Discussion

4.1 Link between earthquake ruptures and plate interface deformation

We herein show two major results: (1) recent earthquakes are bounded by extensive plate interface deformation characterized, along the southern accretionary part of the margin by underplating at their down-dip edge and, along the northern erosive part of the margin by both basal erosion and underplating (Fig. 1); (2) along strike, segments characterized by minimal interplate deformation largely coincide with lateral earthquake terminations (circles; Fig. 5d). These observations demonstrate a close link between distributed interplate deformation and earthquake segmentation.

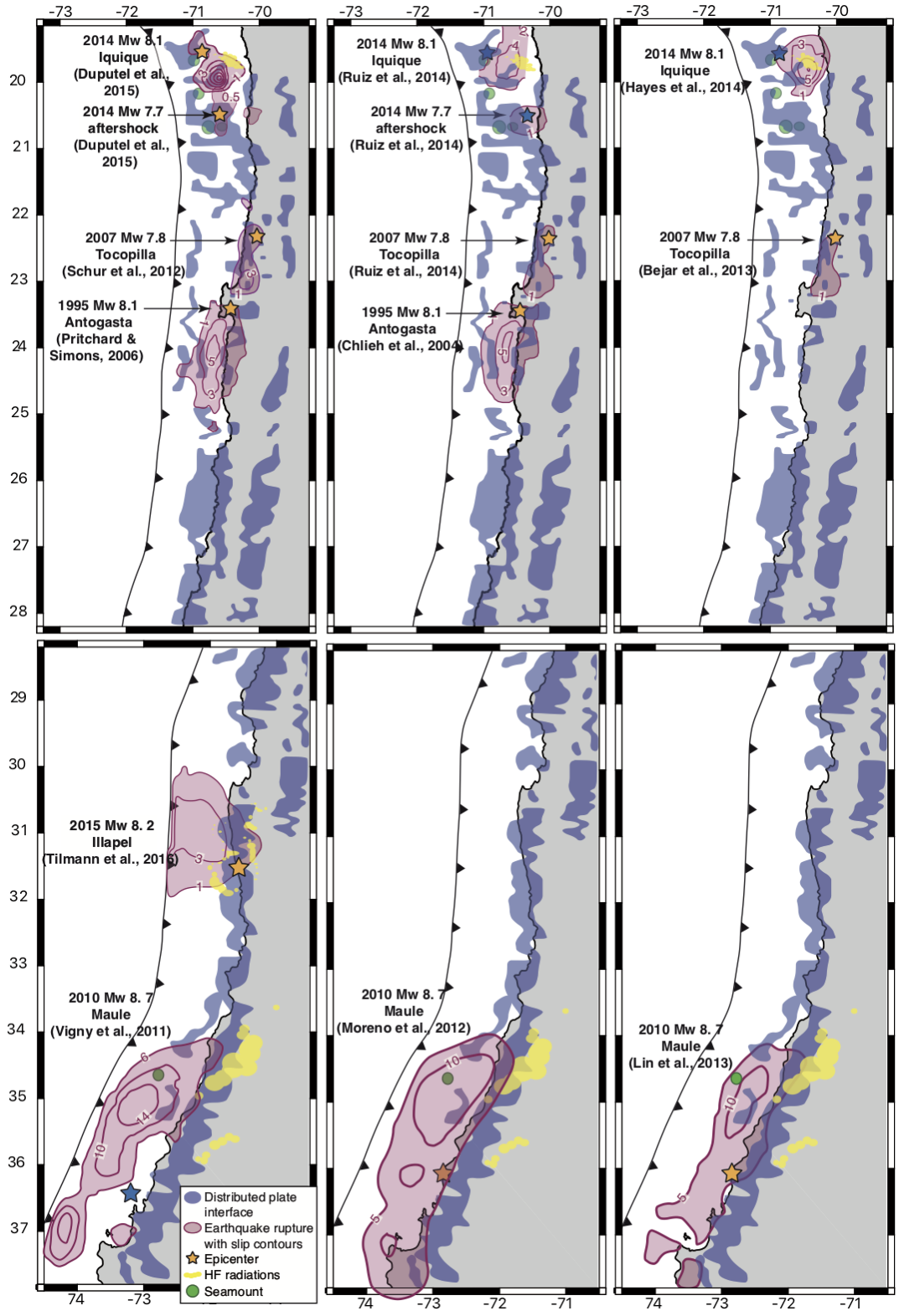

Figure 6. Areas prone to distributed deformation along the plate interface compared to various published co-seismic slip models (Duputel et al., 2015; Schurr et al., 2012; Pritchard and Simons, 2006; Tilmann et al., 2016; Vigny et al., 2011; Ruiz et al., 2014b; Chlieh et al., 2004; Moreno et al., 2010; Hayes et al., 2014; Béjar-Pizarro et al., 2013; Lin et al., 2013). Orange stars: GCMT solutions, blue stars: CSN solution.

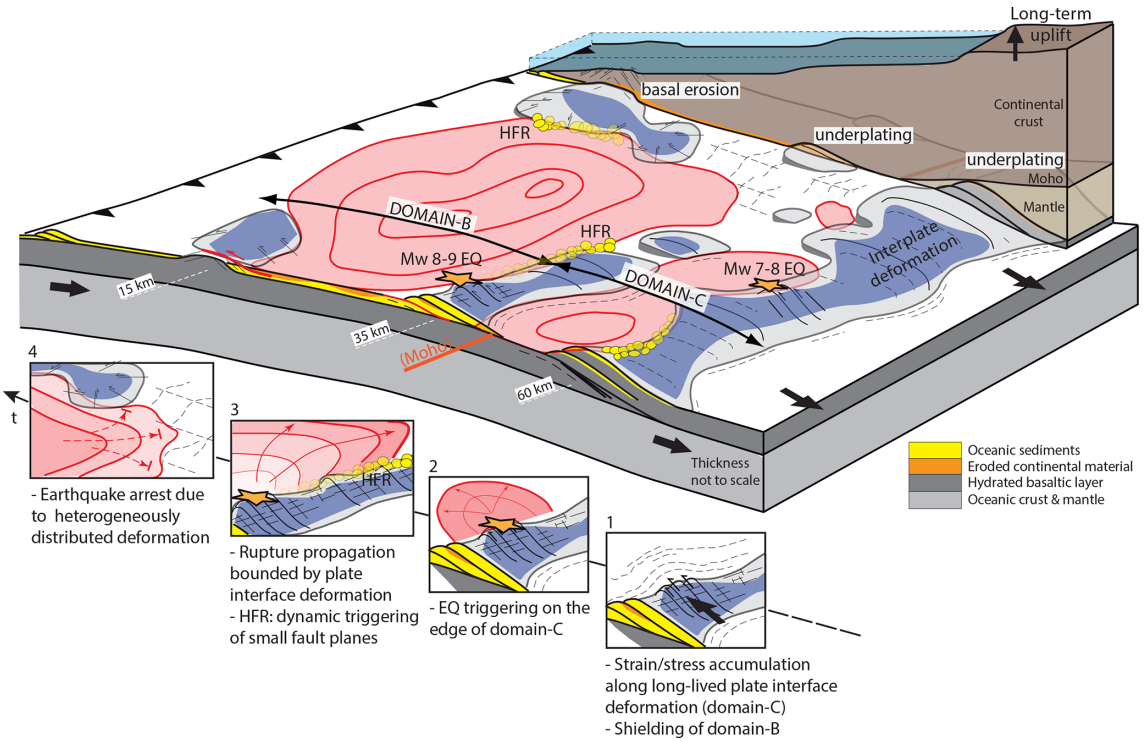

Figure 7. 3D view of the subduction plate interface depicting the mutual spatial relationships between earthquake ruptures (in red) and longer-lived deformation determined from the CTT analysis (blue patches). Stages 1–4 illustrate how this deformation controls the triggering and limits seismic ruptures. HFR: high-frequency radiation. See text for further discussion.

We therefore propose that plastic deformation and stress build-up associated with interplate deformation along distributed fault planes of limited extent (Fig. 7 – step 1) eventually lead to mega-earthquake nucleation (Fig. 7 – step 2). This is suggested by the location of hypocenters at boundaries with distributed deformation (Fig. 1). This interseismic deformation might be accompanied by some microseismicity, as observed prior to the Iquique rupture (Schurr et al., 2020) and in the upper plate in northern Chile (Sippl et al., 2018). If high pore fluid pressure prevails, this deformation could also be accompanied by transient seismic/slip events (Liu and Rice, 2007; Kimura et al., 2010; Collot et al., 2017), which agrees with observations for the Iquique earthquake (Ruiz et al., 2014a; Meng et al., 2015; Socquet et al., 2017) and others elsewhere (Tohoku, Kato et al., 2012; Guerrero, Radiguet et al., 2016).

Once nucleated, large earthquakes propagate along well-localized and smoothed rate-weakening fault planes (Bletery et al., 2016) limited by elongate zones of underplating which, in addition, inhibit further rupture propagation and slip (Figs. 1, 7 – step 3).

These earthquakes abut regions of heterogeneously distributed deformation and stress concentrations (Fig. 7 – step 4), impeding the development of well-localized slip zones (Wang and Bilek, 2014), and again significant slip (Wesnousky, 2006). Some of these fractures might however slip seismically during large events and produce the observed high-frequency radiation (Meng et al., 2018, 2015).

4.2 Down-dip segmentation and plate interface deformation

Within this framework, domain-C (Lay et al., 2012) would correspond to the region of incipient underplating, and domain-B to the smoothed rate-weakening fault zone. This is consistent with partial coupling of domain-C, where deformation is dominated by creep mechanisms, and elastic strain is accumulated along undeformed segments of the megathrust, producing moderate slip earthquakes with a higher recurrence time and significant coherent short-period seismic radiation. Domain-C might more specifically be delimited by the two underplating peaks (Fig. 4), the upper one corresponding to the slicing of oceanic sediments and/or eroded continental material, the second to the propagation of deformation into the hydrated basalt layer once the continental Moho is crossed (Agard et al., 2018), a process ultimately leading to the underplating of very thin and relatively short slices (typically 300–500 m thick, 5–10 km long; Agard et al., 2018).

Data suggest that domain-C, by locally concentrating interplate permanent deformation due to specific geometry (i.e., morphological asperities) and/or mechanical behavior

(i.e., frictional properties, fluid content, porosity), shields the rate-weakening domain-B from long-lived deformation (Fig. 7). Contrary to the prevalent paradigm, domain-B should not be regarded as an "asperity", i.e., a strongly coupled yet mechanically weak zone with high recurrence time earthquakes, but instead as a relatively weak zone devoid of permanent deformation which only stores elastic energy. In this new paradigm, loading along domain-C tightly controls slip deficit as well as rupture nucleation and extent along domain-B (Fig. 7), explaining the correlation observed between historical earthquakes, earthquake terminations and distributed plate interface deformation (Fig. 5a, d). In the short term, elastic deformation generates subsidence at the coast during domain-B earthquakes and uplift for domain-C events (Melnick, 2016). In the long term, the thin underplated slices ultimately build a topographic signal over millions of years of slow uplift, particularly difficult to capture with geodetic measurements due to the interplay of elastic and plastic deformation (Menant et al., 2020). The Coastal Cordillera present along much of the Chilean margin could result from this long-term underplating process. The absence of upper plate deformation above the seismogenic zone in conjunction with topographic build-up above underplating areas account for the correlation between seismic behavior and gravity anomalies (Song and Simons, 2003).

5 Conclusions

We herein show, through a simple CTT analysis of topography, that, along the Chilean subduction zone, earthquakes are bounded by long-lived, extensive plate interface deformation occurring preferentially at 35 ± 10 and 60 ± 5 km depth. Along the central Chilean margin, earthquakes are limited along their down-dip edge by underplating while, along northern Chile, they are surrounded by distributed deformation related to both basal erosion and underplating. Plate interface deformation might control earthquake nucleation, extent and arrest, and its distribution provides a relatively reliable image of the seismic potential at depth. This topography analysis may also remedy the lack of preserved marine terraces or weakly constrained coupling models. This method could therefore be used more systematically to identify regions with precursory transient signals and to enhance predictions of future earthquakes' extent.

Code and data availability. Data are provided in the Supplement. The code is available on demand.

Supplement. See the Supplement for details on the method, supporting figures, and data. The supplement related to this article is available online at: https://doi.org/10.5194/se-13-779-2022-supplement.

Author contributions. NC designed the study; NC and RT ran the simulations; NC, RT, PA analyzed the results; NC and PA wrote the paper.

Competing interests. The contact author has declared that neither they nor their co-authors have any competing interests.

Disclaimer. Publisher's note: Copernicus Publications remains neutral with regard to jurisdictional claims in published maps and institutional affiliations.

Acknowledgements. We thank the two anonymous reviewers for their helpful comments.

Financial support. This research has been supported by the Agence Nationale de la Recherche (grant no. ANR-13-PDOC-0013–01).

Review statement. This paper was edited by Stefano Tavani and reviewed by two anonymous referees.

References

Adam, J. and Reuther, C.-D.: Crustal dynamics and active fault mechanics during subduction erosion. Application of frictional wedge analysis on to the North Chilean Forearc, Tectonophysics, 321, 297–325, 2000.

Agard, P., Plunder, A., Angiboust, S., Bonnet, G., and Ruh, J.: The subduction plate interface: rock record and mechanical coupling (from long to short timescales), Lithos, 320, 537–566, 2018.

Amante, C. and Eakins, B. W.: ETOPO1 1 arc-minute global relief model: procedures, data sources and analysis, Boulder, Coloorado U.S., Deptartment of Commerce, National Oceanic and Atmospheric Administration, National Environmental Satellite, Data, and Information Service, National Geophysical Data Center, Marine Geology and Geophysics Division, https://purl.fdlp.gov/GPO/gpo441 (last access: 15 February 2017), 2009.

Bangs, N. L., Morgan, J., Tréhu, A., Contreras-Reyes, E., Arnulf, A., Han, S., Olsen, K., and Zhang, E.: Basal accretion along the south central Chilean margin and its relationship to great earthquakes, J. Geophys. Res.-Sol. Ea., 125, e2020JB019861, https://doi.org/10.1029/2020JB019861, 2020.

Bassett, D. and Watts, A. B.: Gravity anomalies, crustal structure, and seismicity at subduction zones: 2. Interrelationships between fore-arc structure and seismogenic behavior, Geochem. Geophy. Geosy., 16, 1541–1576, 2015.

Béjar-Pizarro, M., Socquet, A., Armijo, R., Carrizo, D., Genrich, J., and Simons, M.: Andean structural control on interseismic coupling in the North Chile subduction zone, Nat. Geosci., 6, 462–467, 2013.

Bletery, Q., Thomas, A. M., Rempel, A. W., Karlstrom, L., Sladen, A., and De Barros, L.: Mega-earthquakes rupture flat megathrusts, Science, 354, 1027–1031, 2016.

Bonnet, G., Agard, P., Angiboust, S., Fournier, M., and Omrani, J.: No large earthquakes in fully exposed subducted seamount, Geology, 47, 407–410, 2019.

Byerlee, J.: Friction of rocks, in: Rock friction and earthquake prediction, Springer, Birkhäuser, Basel, 615–626, https://doi.org/10.1007/978-3-0348-7182-2_4, 1978.

Chlieh, M., De Chabalier, J., Ruegg, J., Armijo, R., Dmowska, R., Campos, J., and Feigl, K.: Crustal deformation and fault slip during the seismic cycle in the North Chile subduction zone, from GPS and InSAR observations, Geophys. J. Int., 158, 695–711, 2004.

Clarke, A. P., Vannucchi, P., and Morgan, J.: Seamount chain–subduction zone interactions: Implications for accretionary and erosive subduction zone behavior, Geology, 46, 367–370, 2018.

Clift, P. and Vannucchi, P.: Controls on tectonic accretion versus erosion in subduction zones: Implications for the origin and recycling of the continental crust, Rev. Geophys., 42, RG2001, https://doi.org/10.1029/2003RG000127, 2004.

Clift, P. D. and Hartley, A. J.: Slow rates of subduction erosion and coastal underplating along the Andean margin of Chile and Peru, Geology, 35, 503–506, 2007.

Collot, J.-Y., Agudelo, W., Ribodetti, A., and Marcaillou, B.: Origin of a crustal splay fault and its relation to the seismogenic zone and underplating at the erosional north Ecuador–south Colombia oceanic margin, J. Geophys. Res.-Sol. Ea., 113, 3286–3305, https://doi.org/10.1002/2016JB013849, 2008.

Collot, J.-Y., Sanclemente, E., Nocquet, J.-M., Leprêtre, A., Ribodetti, A., Jarrin, P., Chlieh, M., Graindorge, D., and Charvis, P.: Subducted oceanic relief locks the shallow megathrust in central Ecuador, J. Geophys. Res.-Sol. Ea., 122, 3286–3305, 2017.

Cubas, N., Avouac, J.-P., Souloumiac, P., and Leroy, Y.: Megathrust friction determined from mechanical analysis of the forearc in the Maule earthquake area, Earth Planet. Sc. Lett., 381, 92–103, 2013.

Dahlen, F.: Noncohesive critical Coulomb wedges: An exact solution, J. Geophys. Res.-Sol. Ea., 89, 10125–10133, 1984.

Davis, D., Suppe, J., and Dahlen, F.: Mechanics of fold-and-thrust belts and accretionary wedges, J. Geophys. Res.-Sol. Ea., 88, 1153–1172, 1983.

Delouis, B., Philip, H., Dorbath, L., and Cisternas, A.: Recent crustal deformation in the Antofagasta region (northern Chile) and the subduction process, Geophys. J. Int., 132, 302–338, 1998.

Dominguez, S., Lallemand, S., Malavieille, J., and von Huene, R.: Upper plate deformation associated with seamount subduction, Tectonophysics, 293, 207–224, 1998.

Duputel, Z., Jiang, J., Jolivet, R., Simons, M., Rivera, L., Ampuero, J.-P., Riel, B., Owen, S. E., Moore, A. W., Samsonov, S. V., Duputel, Z., Jiang, J., Jolivet, R., Simons, M., Rivera, L., Ampuero, J.-P., Riel, B., Owen, S. E., Moore, A. W., Samsonov, S. V., Ortega Culaciati, F., and Minson, S. E.: The Iquique earthquake sequence of April 2014: Bayesian modeling accounting for prediction uncertainty, Geophys. Res. Lett., 42, 7949–7957, 2015.

Fagereng, Å. and Sibson, R. H.: Melange rheology and seismic style, Geology, 38, 751–754, 2010.

Fulton, P., Brodsky, E. E., Kano, Y., Mori, J., Chester, F., Ishikawa, T., Harris, R., Lin, W., Eguchi, N., Toczko, S., Expedition 343, 343T, and KR13-08 Scientists: Low coseismic friction on the Tohoku-Oki fault determined from temperature measurements, Science, 342, 1214–1217, 2013.

Gao, X. and Wang, K.: Strength of stick-slip and creeping subduction megathrusts from heat flow observations, Science, 345, 1038–1041, 2014.

Geersen, J., Ranero, C. R., Barckhausen, U., and Reichert, C.: Subducting seamounts control interplate coupling and seismic rupture in the 2014 Iquique earthquake area, Nat. Commun., 6, 1–6, 2015.

Hayes, G. P., Herman, M. W., Barnhart, W. D., Furlong, K. P., Riquelme, S., Benz, H. M., Bergman, E., Barrientos, S., Earle, P. S., and Samsonov, S.: Continuing megathrust earthquake potential in Chile after the 2014 Iquique earthquake, Nature, 512, 295–298, 2014.

Hayes, G. P., Moore, G. L., Portner, D. E., Hearne, M., Flamme, H., Furtney, M., and Smoczyk, G. M.: Slab2, a comprehensive subduction zone geometry model, Science, 362, 58–61, 2018.

Kaneko, Y., Avouac, J.-P., and Lapusta, N.: Towards inferring earthquake patterns from geodetic observations of interseismic coupling, Nat. Geosci., 3, 363–369, 2010.

Kato, A., Obara, K., Igarashi, T., Tsuruoka, H., Nakagawa, S., and Hirata, N.: Propagation of slow slip leading up to the 2011 M_{W} 9.0 Tohoku-Oki earthquake, Science, 335, 705–708, 2012.

Kimura, G., Kitamura, Y., Hashimoto, Y., Yamaguchi, A., Shibata, T., Ujiie, K., and Okamoto, S.: Transition of accretionary wedge structures around the up-dip limit of the seismogenic subduction zone, Earth Planet. Sc. Lett., 255, 471–484, 2007.

Kimura, H., Takeda, T., Obara, K., and Kasahara, K.: Seismic evidence for active underplating below the megathrust earthquake zone in Japan, Science, 329, 210–212, 2010.

Klein, E., Metois, M., Meneses, G., Vigny, C., and Delorme, A.: Bridging the gap between North and Central Chile: insight from new GPS data on coupling complexities and the Andean sliver motion, Geophys. J. Int., 213, 1924–1933, 2018.

Kodaira, S., Takahashi, N., Nakanishi, A., Miura, S., and Kaneda, Y.: Subducted seamount imaged in the rupture zone of the 1946 Nankaido earthquake, Science, 289, 104–106, 2000.

Konca, A. O., Avouac, J.-P., Sladen, A., Meltzner, A. J., Sieh, K., Fang, P., Li, Z., Galetzka, J., Genrich, J., Chlieh, M., Natawidjaja, D. H., Bock, Y., Fielding, E. J., Ji, C., and Helmberger, D. V.: Partial rupture of a locked patch of the Sumatra megathrust during the 2007 earthquake sequence, Nature, 456, 631–635, 2008.

Lallemand, S., Peyret, M., van Rijsingen, E., Arcay, D., and Heuret, A.: Roughness Characteristics of Oceanic Seafloor Prior to Subduction in Relation to the Seismogenic Potential of Subduction Zones, Geochem. Geophy. Geosy., 19, 2121–2146, https://doi.org/10.1029/2018GC007434, 2018.

Lay, T., Kanamori, H., Ammon, C. J., Koper, K. D., Hutko, A. R., Ye, L., Yue, H., and Rushing, T. M.: Depth-varying rupture properties of subduction zone megathrust faults, J. Geophys. Res.-Sol. Ea., 117, B04311, https://doi.org/10.1029/2011JB009133, 2012.

Lin, Y.-n. N., Sladen, A., Ortega-Culaciati, F., Simons, M., Avouac, J.-P., Fielding, E. J., Brooks, B. A., Bevis, M., Genrich, J., Rietbrock, A., Vigny, C., Smalley, R., and Socquet, A.: Coseismic and postseismic slip associated with the 2010 Maule Earthquake, Chile: Characterizing the Arauco Peninsula barrier effect, J. Geophys. Res.-Sol. Ea., 118, 3142–3159, 2013.

Liu, Y. and Rice, J. R.: Spontaneous and triggered aseismic deformation transients in a subduction fault model, J. Geophys. Res.-Sol. Ea., 112, B09404, https://doi.org/10.1029/2007JB004930, 2007.

Loveless, J. P. and Meade, B. J.: Spatial correlation of interseismic coupling and coseismic rupture extent of the 2011 M_w = 9.0 Tohoku-oki earthquake, Geophys. Res. Lett., 38, L17306, https://doi.org/10.1029/2011GL048561 , 2011.

Maksymowicz, A., Tréhu, A. M., Contreras-Reyes, E., and Ruiz, S.: Density-depth model of the continental wedge at the maximum slip segment of the Maule M_w 8.8 megathrust earthquake, Earth Planet. Sc. Lett., 409, 265–277, 2015.

Melnick, D.: Rise of the central Andean coast by earthquakes straddling the Moho, Nat. Geosci., 9, 401–407, 2016.

Menant, A., Angiboust, S., Gerya, T., Lacassin, R., Simoes, M., and Grandin, R.: Transient stripping of subducting slabs controls periodic forearc uplift, Nat. Commun., 11, 1–10, 2020.

Meng, L., Huang, H., Bürgmann, R., Ampuero, J. P., and Strader, A.: Dual megathrust slip behaviors of the 2014 Iquique earthquake sequence, Earth Planet. Sc. Lett., 411, 177–187, 2015.

Meng, L., Bao, H., Huang, H., Zhang, A., Bloore, A., and Liu, Z.: Double pincer movement: Encircling rupture splitting during the 2015 M_w 8.3 Illapel earthquake, Earth Planet. Sc. Lett., 495, 164–173, 2018.

Metois, M., Vigny, C., and Socquet, A.: Interseismic coupling, megathrust earthquakes and seismic swarms along the Chilean subduction zone (38–18° S), Pure Appl. Geophys., 173, 1431–1449, 2016.

Moreno, M., Rosenau, M., and Oncken, O.: 2010 Maule earthquake slip correlates with pre-seismic locking of Andean subduction zone, Nature, 467, 198–202, 2010.

Moreno, M., Haberland, C., Oncken, O., Rietbrock, A., Angiboust, S., and Heidbach, O.: Locking of the Chile subduction zone controlled by fluid pressure before the 2010 earthquake, Nat. Geosci., 7, 292–296, 2014.

Noda, H. and Lapusta, N.: Stable creeping fault segments can become destructive as a result of dynamic weakening, Nature, 493, 518, https://doi.org/10.1038/nature11703, 2013.

Olsen, K. M., Bangs, N. L., Tréhu, A. M., Han, S., Arnulf, A., and Contreras-Reyes, E.: Thick, strong sediment subduction along south-central Chile and its role in great earthquakes, Earth Planet. Sc. Lett., 538, 116195, https://doi.org/10.1016/j.epsl.2020.116195, 2020.

Perfettini, H., Avouac, J.-P., Tavera, H., Kositsky, A., Nocquet, J.-M., Bondoux, F., Chlieh, M., Sladen, A., Audin, L., Farber, D. L., and Soler, P.: Seismic and aseismic slip on the Central Peru megathrust, Nature, 465, 78–81, 2010.

Plunder, A., Agard, P., Dubacq, B., Chopin, C., and Bellanger, M.: How continuous and precise is the record of P-T paths? Insights from combined thermobarometry and thermodynamic modelling into subduction dynamics (Schistes Lustrés, W. Alps), J. Metamorph. Geol., 30, 323–346, 2012.

Plunder, A., Agard, P., Chopin, C., and Okay, A. I.: Geodynamics of the Tavşanlı zone, western Turkey: Insights into subduction/obduction processes, Tectonophysics, 608, 884–903, 2013.

Pritchard, M. and Simons, M.: An aseismic slip pulse in northern Chile and along-strike variations in seismogenic behavior, J. Geophys. Res.-Sol. Ea., 111, B08405, https://doi.org/10.1029/2006JB004258, 2006.

Radiguet, M., Perfettini, H., Cotte, N., Gualandi, A., Valette, B., Kostoglodov, V., Lhomme, T., Walpersdorf, A., Cano, E. C., and Campillo, M.: Triggering of the 2014 M_w 7.3 Papanoa earthquake by a slow slip event in Guerrero, Mexico, Nat. Geosci., 9, 829–833, 2016.

Ranero, C. R. and von Huene, R.: Subduction erosion along the Middle America convergent margin, Nature, 404, 748–752, 2000.

Rowe, C. D., Moore, J. C., Remitti, F., and Scientists, I. E. T.: The thickness of subduction plate boundary faults from the seafloor into the seismogenic zone, Geology, 41, 991–994, 2013.

Ruh, J. B., Sallarès, V., Ranero, C. R., and Gerya, T.: Crustal deformation dynamics and stress evolution during seamount subduction: High-resolution 3-D numerical modeling, J. Geophys. Res.-Sol. Ea., 121, 6880–6902, 2016.

Ruiz, S., Metois, M., Fuenzalida, A., Ruiz, J., Leyton, F., Grandin, R., Vigny, C., Madariaga, R., and Campos, J.: Intense foreshocks and a slow slip event preceded the 2014 Iquique M_w 8.1 earthquake, Science, 345, 1165–1169, https://doi.org/10.1126/science.1256074, 2014a.

Ruiz, S., Metois, M., Fuenzalida, A., Ruiz, J., Leyton, F., Grandin, R., Vigny, C., Madariaga, R., and Campos, J.: Intense foreshocks and a slow slip event preceded the 2014 Iquique M_w 8.1 earthquake, Science, 345, 1165–1169, 2014b.

Saillard, M., Audin, L., Rousset, B., Avouac, J.-P., Chlieh, M., Hall, S. R., Husson, L., and Farber, D.: From the seismic cycle to long-term deformation: linking seismic coupling and Quaternary coastal geomorphology along the Andean megathrust, Tectonics, 36, 241–256, 2017.

Santibáñez, I., Cembrano, J., García-Pérez, T., Costa, C., Yáñez, G., Marquardt, C., Arancibia, G., and González, G.: Crustal faults in the Chilean Andes: geological constraints and seismic potential, Andean Geol., 46, 32–65, 2018.

Schurr, B., Asch, G., Rosenau, M., Wang, R., Oncken, O., Barrientos, S., Salazar, P., and Vilotte, J.-P.: The 2007 M 7.7 Tocopilla northern Chile earthquake sequence: Implications for along-strike and downdip rupture segmentation and megathrust frictional behavior, J. Geophys. Res.-Sol. Ea., 117, B05305, https://doi.org/10.1029/2011JB009030, 2012.

Schurr, B., Moreno, M., Tréhu, A. M., Bedford, J., Kummerow, J., Li, S., and Oncken, O.: Forming a Mogi doughnut in the years prior to and immediately before the 2014 M 8.1 Iquique, northern Chile, earthquake, Geophys. Res. Lett., 47, e2020GL088351, https://doi.org/10.1029/2020GL088351, 2020.

Sippl, C., Schurr, B., Asch, G., and Kummerow, J.: Seismicity structure of the northern Chile forearc from > 100 000 double-difference relocated hypocenters, J. Geophys. Res.-Sol. Ea., 123, 4063–4087, 2018.

Socquet, A., Valdes, J. P., Jara, J., Cotton, F., Walpersdorf, A., Cotte, N., Specht, S., Ortega-Culaciati, F., Carrizo, D., and Norabuena, E.: An 8 month slow slip event triggers progressive nucleation of the 2014 Chile megathrust, Geophys. Res. Lett., 44, 4046–4053, 2017.

Song, T.-R. A. and Simons, M.: Large trench-parallel gravity variations predict seismogenic behavior in subduction zones, Science, 301, 630–633, 2003.

Tassara, A. and Echaurren, A.: Anatomy of the Andean subduction zone: three-dimensional density model upgraded and com-

pared against global-scale models, Geophys. J. Int., 189, 161–168, 2012.

Tilmann, F., Zhang, Y., Moreno, M., Saul, J., Eckelmann, F., Palo, M., Deng, Z., Babeyko, A., Chen, K., Baez, J., Schurr, B., Wang, R., and Dahm, T.: The 2015 Illapel earthquake, central Chile: A type case for a characteristic earthquake?, Geophys. Res. Lett., 43, 574–583, 2016.

Tréhu, A. M., Hass, B., de Moor, A., Maksymowicz, A., Contreras-Reyes, E., Vera, E., and Tryon, M. D.: Geologic controls on up-dip and along-strike propagation of slip during subduction zone earthquakes from a high-resolution seismic reflection survey across the northern limit of slip during the 2010 M_w 8.8 Maule earthquake, offshore Chile, Geosphere, 15, 1751–1773, 2019.

Vannucchi, P., Sage, F., Phipps Morgan, J., Remitti, F., and Collot, J.-Y.: Toward a dynamic concept of the subduction channel at erosive convergent margins with implications for interplate material transfer, Geochem. Geophy. Geosy., 13, Q02003, https://doi.org/10.1029/2011GC003846, 2012.

Vigny, C., Socquet, A., Peyrat, S., Ruegg, J.-C., Métois, M., Madariaga, R., Morvan, S., Lancieri, M., Lacassin, R., Campos, J., Carrizo, D., Bejar-Pizarro, M., Barrientos, S., Armijo, R., Aranda, C., Valderas-Bermejo, M.-C., Ortega, I., Bondoux, F., Baize, S., Lyon-Caen, H., Pavez, A., Vilotte, J. P., Bevis, M., Brooks, B., Smalley, R., Parra, H., Baez, J.-C., Blanco, M., Cimbaro, S., and Kendrick, E.: The 2010 M_w 8.8 Maule megathrust earthquake of central Chile, monitored by GPS, Science, 332, 1417–1421, 2011.

von Huene, R. and Ranero, C. R.: Subduction erosion and basal friction along the sediment-starved convergent margin off Antofagasta, Chile, J. Geophys. Res.-Sol. Ea., 108, 108, 2079, https://doi.org/10.1029/2001JB001569, 2003.

von Huene, R., Ranero, C. R., and Vannucchi, P.: Generic model of subduction erosion, Geology, 32, 913–916, 2004.

Wang, D. and Mori, J.: Frequency-dependent energy radiation and fault coupling for the 2010 M_w 8.8 Maule, Chile, and 2011 M_w 9.0 Tohoku, Japan, earthquakes, Geophys. Res. Lett., 38, L22308, https://doi.org/10.1029/2011GL049652, 2011.

Wang, K. and Bilek, S. L.: Invited review paper: Fault creep caused by subduction of rough seafloor relief, Tectonophysics, 610, 1–24, 2014.

Wang, K., He, J., and Hu, Y.: A note on pore fluid pressure ratios in the Coulomb wedge theory, Geophys. Res. Lett., 33, L19310, https://doi.org/10.1029/2006GL027233, 2006.

Wesnousky, S. G.: Predicting the endpoints of earthquake ruptures, Nature, 444, 358–360, 2006.

The topographic signature of temperature-controlled rheological transitions in an accretionary prism [Pajang et al., 2022b]

During her PhD, Sepideh Pajang used thermo-mechanical models accounting for temperature evolution and its feedback on rheology. She studied how dehydration reactions within the décollement and how the brittle-viscous transition could impact the deformation and topography of an accretionary wedge. She explored the effect of basal heat flow, shear heating, thermal blanketing by sediments, and of incoming sediments thickness.

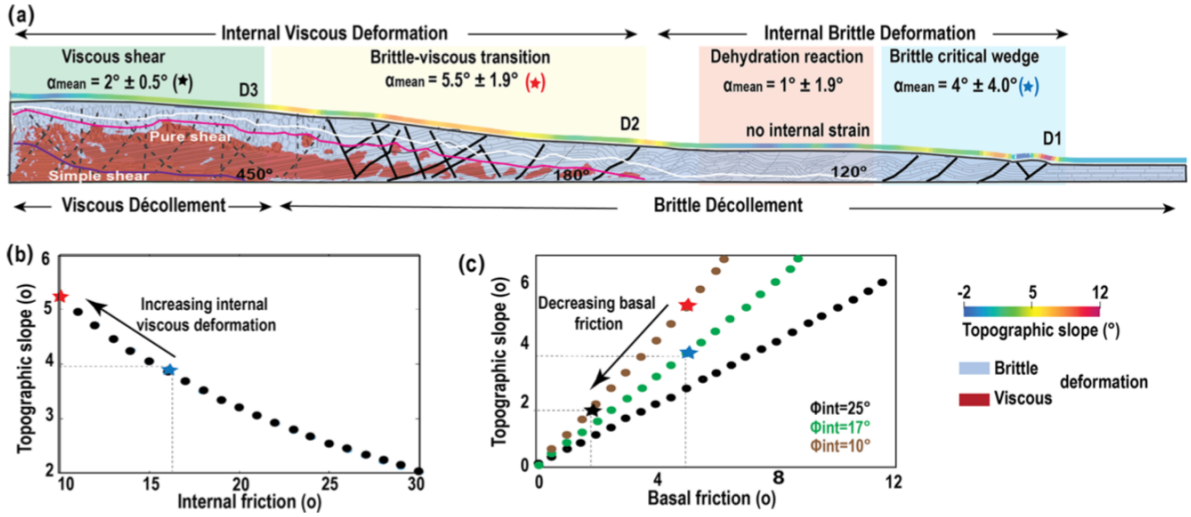

FIGURE 3.25 – (a.) Proposed model for the mature brittle–ductile wedge which forms three distinct segments ; pure brittle wedge with a rather constant slope predicted by the CTT at the front (blue star), low but non-zero topographic slope close to the backstop corresponds to viscous deformation (black star), and larger topographic slope in between these segments as a result of the brittle–ductile transition (red star and yellow rectangle). (b) Topographic slope versus internal friction for $\mu_{basal} = 5^o$. (c) Basal friction versus topographic slope for μ_{int} = 10, 17, and 25^o. Extracted from Pajang et al. [2022b]

According to the models, a mature wedge will end up forming three to four structural segments (figure 3.25) :

— the frontal brittle part of the wedge is characterized by an imbricated zone with active in-sequence thrusts faults ahead (figure 3.25a, blue box). The décollement and the above sequence behave plastically. The topographic slope created in this section is controlled by the basal and average internal friction and is consistent with the CTT predictions (figure 3.25b, c blue star).

— The presence of a smectite–illite transition (dehydration reaction) leads to a segment characterized by a flat topographic slope and little internal deformation, in between the frontal brittle wedge and the brittle–ductile transition (figure 3.25a, red box). If this dehydration reaction corresponds to the up-dip limit of the seismogenic zone, then this could explain the correlation between the rupture extent of large megathrust earthquakes with shelf-terraces or forearc basins marked by local gravity lows [Wells et al., 2003, Song and Simons, 2003].

— The brittle–viscous transition zone is characterized by out- of-sequence thrusts and backthrusts with high internal deformation (figure 3.25a, yellow box). This part forms a steeper topographic slope than the brittle-only one. A careful examination of the behaviour of this segment reveals that the décollement remains brittle, but the above sequence has entered the viscous phase. By plotting the surface slope on the critical taper diagram, we notice that this part is consistent with a critical taper of a lower internal friction angle (figure 3.25 b, red star). This internal deformation could cause an apparent decrease

of the geodetic coupling without implying any modification in the interface frictional properties or deformation mode.

— The viscous part presents an approximate flat zone without effective internal deformation. The décollement and the above sequence deform viscously (figure 3.25a, green box). The topographic slope is again consistent with the critical taper theory, considering that a viscous décollement is equivalent to a brittle décollement with extremely low friction (figure 3.25b, black star).

The morphologic resemblances of the brittle–ductile and ductile segments with fore-arc high and forearc basins of accretionary active margins, respectively, led us to propose an alternative metamorphic origin of the forearc crust in this context.

The distinct morphologic signature of underplating and seamounts in accretionary prisms, insights from thermomechanical modeling applied to Coastal Iranian Makran [Pajang et al., 2022a]

In a third paper, Sepideh Pajang used again thermo-mechanical models to produce onshore-offshore cross-sections of the Iranian Makran accretionary prism. To do so, she explored (1) the effect of underplating on the topography and on distribution of the brittle and viscous deformation, and (2) the conditions necessary to produce the large coastal normal faults.

She found that underplating can result from the onset of the brittle/viscous transition of the sediments located beneath the brittle décollement : viscous deformation occurs along the deeper décollement and in the duplexes while the shallow décollement keeps its frictional behaviour (figures 3.26 and 3.27). This could again explain the occurrence of earthquakes in apparently low coupling zones. As with a single décollement, the brittle-ductile transition and the dehydration reaction produce a four slope segment accretionary prism, as observed in Makran (figures 3.26 and 3.27) : the frontal segment corresponds to the regular accretionary prism, the flat segment marks the smectite-illite transition, a topographic rise is located above the zone where the tegument reaches its temperature-controlled brittle-ductile transition causing underplating, and a second flat marks the viscous décollement.

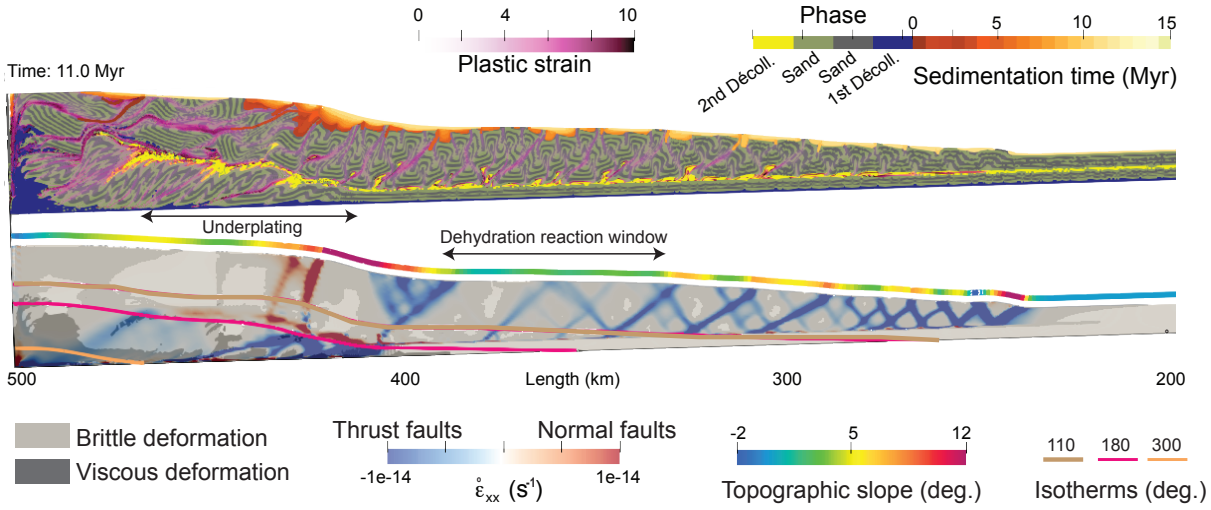

FIGURE 3.26 – Finite strain and Current strain rate of a simulation considering temperature dependent transitions (smectite-illite dehydration reaction and brittle-viscous transition). The yellowish-brown color illustrates syn-tectonic sedimentation in the form of piggyback basins, and represents a given age corresponding to the deposition time. Where the material is yielding plastically is in light grey or deforms viscously is in dark grey. The local topographic slope with a color code shown at the top of the slice is affected by temperature and frictional properties, 1 :1 scale. Extracted from Pajang et al. [2022a]

She also showed that neither the decrease in friction associated with dehydration nor the onset of underplating are sufficient to produce the normal faults observed along coastal Makran in a self-consistent manner. Large normal faults only emerged in simulations including the subduction of a large seamount. However, their position would vary with time. If not related to seamount subduction, these large normal faults may result from elastic deformation associated to the seismic cycle not taken into account in this visco-plastic model.

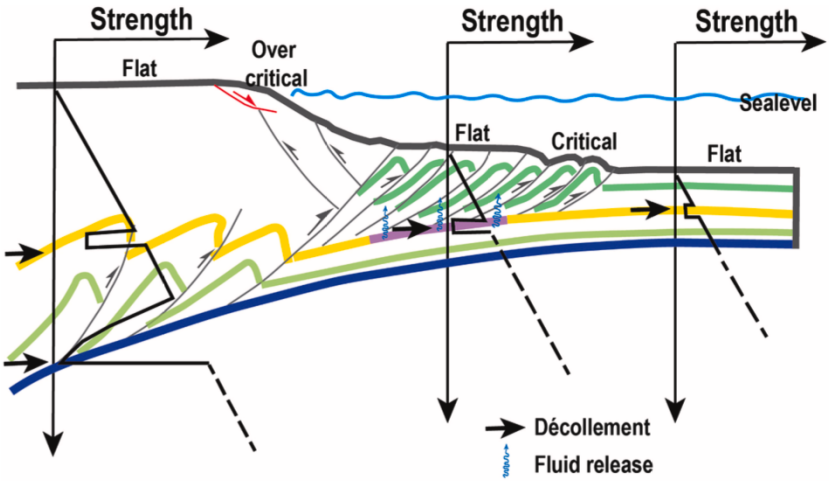

FIGURE 3.27 – Plot of the strength distribution (yield strength envelope) at the loading axis with depth along the first 30 km of a wedge, resulting from thermo-mechanical modelling interpretation. The purple segment marks the dehydration reaction window along the shallow décollement. Extracted from Pajang et al. [2022a]

3.5 Projet - Towards a mechanical understanding of the megathrust behaviour

3.5.1 ANR MechaThrust

As discussed in the last section, megathrust cannot be considered as formed of a unique plane, with a single composition and a single depth-dependent rheology. Megathrust can neither be considered as a unique fault plane embedded in an homogeneous nor purely elastic medium. To improve our capacity to assess seismic hazard, it is crucial to develop a true physical understanding of the megathrust behaviour and of the slip deficit patterns in their long-term tectonic environment.
In Pajang et al. [2022b], we have shown that long-term tectonics thermo-mechanical models at forearc scale, incorporating temperature evolution and its feedback on rock rheology, are capable of capturing how the complexity of the brittle-ductile transition in a wedge affects differently the rocks deforming in the wedge and the megathrust. Our main finding is that the brittle/ductile transition leads to a topographic slope increase related to the onset of internal distributed viscous deformation in between brittle structures above a brittle megathrust. This internal deformation would be interpreted as an apparent decrease of coupling by geodetic models, although no modification of frictional properties or deformation mode would affect the megathrust. The wedge morphology thus provides information on the distribution of the deformation that geodesy is unable to capture. In a following paper [Pajang et al., 2022a], we have also shown that a subducted seamount, hardly resolvable by geophysical means, can be captured from the long-term tectonic deformation style and the general shape of the forearc.

Yet, these papers focus on the Makran wedge, and neither the flexural response of the lower plate nor elasticity were incorporated in the model, impeding to capture the distribution of the deformation and the relationships between the megathrust, the internal faults and the bulk at an earthquake cycle scale. Emergence of dynamic thermo-mechanical simulations, at the whole subduction scale, incorporating equivalent rate-and-state friction laws, in which deformation and material properties evolve in response to tectonic stresses, temperatures, and pressures [e.g., Van Dinther et al., 2013] permit to produce a lot of the complexity mentioned above. However, the results of these large-scale models are so complex that they miss to convince part of the earthquake community. Very recent studies have focused on earthquake sequences along a planar megathrust governed by rate-and-state friction laws embedded in a visco-elasto-plastic wedge [Dal Zilio et al., 2022]. However, they did not yet consider the complexities acquired from the long-term evolution.

To summarize, to understand the controlling parameters of the seismogenic behaviour of a megathrust and to enhance the seismic hazard assessment, we need numerical modelling taking into account :

- the temperature evolution and its feedback on rock rheology to capture the effect of dehydration reactions and brittle/ductile competitions,
- complex geometries and sedimentary layering to capture the effect of bathymetric features subduction and underplating,
- elasticity, to capture the relationships between the deformation at the seismic cycle scale with the self-consistent long-term structure of the forearc.

I have thus proposed in the MechaThrust ANR, to :

1. Develop a **dynamic thermo-mechanical model at forearc scale** incorporating visco-elasto-plastic behaviour and temperature evolution, **able to drop the time steps at key**

geological moments of the simulations to capture slow motion of earthquake cycle conditioned by loading and structures that are self-consistent with long-term deformation. Our objectives are :

- To understand the **main parameters controlling the megathrust behaviour** and how they differ according to initial conditions (thermal state, accretionary - non-accretionary wedge, sediment thickness, rheology and mineralogy transitions of incoming material, plate roughness - subduction of bathymetric features, erosional rate, ...)
- To identify **how these different properties impact the overriding plate and the morphology of the wedge**
- To understand the **interactions between the long- and short-term (seismic cycle scale) deformation**.

2. Confront our results to **well-instrumented forearcs** such as the Northern, Central and Southern Chile, Nankai, Ecuador, known to host major earthquakes, a variety of seismic behaviours, to transition from erosive to accretionary and to be affected by seamounts subduction and underplating. Our objectives are :
   - To reproduce these forearcs, and by confronting our results to the short-term records, provide a mechanical understanding of the megathrust behaviour for each selected zone.
   - To study their expected behaviour at the seismic cycle scale to improve their seismic hazard assessment.
3. Finally, thanks to our understanding of how the megathrust behaviour impact the distribution of the deformation and the forearc morphology, we will **constrain the seismic potential of weakly constrained subduction zones**, such as Makran, the Antilles, or the Mediterranean ridge.

Two technical barriers have to be lifted. The first one relates to the incorporation of the elasticity and the time stepping algorithm. However, I will work with Laëtitia Le Pourhiet who has already carried such work and has working prototypes **[Le Pourhiet, 2013, Duretz et al., 2019, 2020]**. The second relates to the incorporation of the rate-and-state laws to reproduce the whole seismic cycle steps. However, the objective of this stage is to capture how the long-term loading affects the rupture dynamics. If we do not succeed, first, this will not impede us to study the main parameters controlling the megathrust mechanical behaviour, main goal of the project, and second, in that case, we will export the long-term stress obtained in our simulations as starting stress (initial condition) in an existing rupture propagation code, developed by my collaborator M. Thomas.

3.5.2 Targets

Nankai

I will start with the Nankai Trough, a booktype accretionary prism. Numerous 2D and 3D seismic reflection and ocean bottom seismometer wide-angle seismic surveys have been conducted [e.g., Aoki et al., 1982, Moore et al., 1990, Nakanishi et al., 2002, Park et al., 2002, Kodaira et al., 2006], some calibrated with Integrated Ocean Drilling Program (IODP) core and log data of the Nankai Trough Seismogenic Zone Experiment drillling program (NanTroSEIZE). Heat flow surveys have also been conducted [e.g., Ashi et al., 2002]. The megasplay fault in the rupture area of the 1944 Tonankai Mw 8.1 has been intensively studied [e.g., Park et al., 2002, Moore et al., 2007, Kimura et al., 2011]. Two Mw 8 have occurred in 1944 and 1946 [e.g., Baba and Cummins, 2005], and the subduction is suspected to host Mw 9 [Yokota et al.,

2016]. The subduction shows along-dip and along-strike variations of slip behaviours. Along-dip, the megathrust is characterized by stable sliding at the front, followed by a low frequency and very low frequency earthquakes zone, then the classic seismogenic zone hosting megathrust earthquakes, followed by a zone of long-term SSE (lasting years), and then short-term SSE (lasting days) with deep low frequency tremors [Obara and Kato, 2016]. The along-strike coupling segmentation is related to bathymetric features, two seamounts and a ridge, highlighted by very low frequency earthquakes [Kodaira et al., 2000, Park et al., 2004, Yamamoto et al., 2013, Yokota et al., 2016]. Nankai hence presents the advantage to have a rich variety of mechanical behaviours to investigate.

Chili

I will follow with the Chilean subduction zone, possibly in the context of a PRCI proposal named BEES (PIs : Romain Jolivet, ENS, and Claudio Faccena, GFZ). Numerous seismic campaigns have been conducted along the Chilean subduction zone [e.g., Contreras-Reyes et al., 2008, 2010, 2015, 2021, Maksymowicz et al., 2018, Olsen et al., 2020, Bangs et al., 2020, Storch et al., 2021]. From these works, the margin is known to transition from erosive to the North to accretionary to the South. Along the erosive part, seamounts have been imaged around the 2014 Iquique rupture [Geersen et al., 2015]. The sediment thickness increases from North to South, where part of the sediments is accreted and part subducted [Olsen et al., 2020, Bangs et al., 2020]. Heat flows have been published [Gao and Wang, 2014]. Five major earthquakes have occurred over the last 25 years, and an abundant literature published [e.g., Cubas et al., 2022]. Several coupling models have been proposed showing important along-strike variations [e.g., Metois et al., 2016, Klein et al., 2018]. Splay faults have been imaged [Melnick et al., 2012, Farías et al., 2011]. An along-dip segmentation has also been proposed from the location of past earthquakes, of unknown mechanical origin [Lay et al., 2012]. The Chilean margin hence offers the possibility to study effects of varying sediment thickness, of bathymetric features and underplated sediments. Furthermore, I will take advantage of several strong constraints acquired in the framework of the ANR PRCI proposal BEES, such as : active faults mapping, P-T-t paths, short- and long-term vertical movements, and relocated seismicity.

Ecuador - ANR PRC FLUID2SLIP

I will then pursue with the Ecuadorian subduction zone, in the framework of the ANR FLUID2SLIP (PI Audrey Galve, Géoazur). The region, as the former two, host major earthquakes, shows along-strike and along-dip variations of slip behaviours [Nocquet et al., 2014, Rolandone et al., 2018], host SSEs [Rolandone et al., 2018, Vaca et al., 2018], some related to a seamount subduction [Collot et al., 2017]. Splay faults have been imaged [Collot et al., 2008], heat flow constrained [Marcaillou et al., 2008], and a recent seismic campain conducted (HIPER).

Predicting the seismic potential of weakly constrained forearcs

I will finally apply our models along less constrained subduction zones to improve their seismic hazard assessment. We plan to start with Makran. Our previous numerical investigation were unable to reproduce the large coastal normal faults at their present day location. We suspect that these features are related to the seismic behaviour of the megathrust, and will investigate this option to provide extent of potential seismic asperities. We could continue with the Antilles, also poorly constrained by geodesy due to the distance and sparcity of the stations, and along which the seismogenic potential of the megathrust is strongly debated [Van Rijsingen et al.,

2021, Philibosian et al., 2022]. The mediterranean Ridge and its unknow seismic risk could also be an important target.

Annexe - Selection de publications

S. Pajang, Le Pourhiet, L., and **N. Cubas** (2022), The topographic signature of temperature-controlled rheological transitions in an accretionary prism, **Solid Earth**, 13, 535–551, https://doi.org/10.5194/se-13-535-2022

N. Cubas, P. Souloumiac, S. Singh (2016), Relationship link between landward vergence in accretionary prisms and tsunami generation, **Geology**, https://doi.org/10.1130/G38019.1.

N. Cubas, N. Lapusta, J. P. Avouac, H. Perfettini (2015), Numerical modeling of long-term earthquake sequences on the NE Japan megathrust : Comparison with observations and implications for fault friction, **Earth and Planetary Science Letters**, 419, p.187-198, https://doi.org/10.1016/j.epsl.2015.03.002.

N. Cubas, J. P. Avouac, P. Souloumiac, Y. Leroy (2013)c, Megathrust friction determined from mechanical analysis of the forearc in the Maule Earthquake area, **Earth and Planetary Science Letters**, 381,p.92-103, https://doi.org/10.1016/j.epsl.2013.07.037.

Solid Earth, 13, 535–551, 2022
https://doi.org/10.5194/se-13-535-2022

Solid Earth Open Access EGU

The topographic signature of temperature-controlled rheological transitions in an accretionary prism

Sepideh Pajang[1,2], **Laetitia Le Pourhiet**[1], **and Nadaya Cubas**[1]

[1]Institut des Sciences de la Terre Paris, ISTeP UMR 7193, Sorbonne Universite, CNRS-INSU, 75005 Paris, France
[2]Geoscience department, University of Birjand, Birjand, Iran

Correspondence: Sepideh Pajang (sepideh.pajang@sorbonne-universite.fr)

Received: 26 October 2021 – Discussion started: 4 November 2021
Revised: 3 February 2022 – Accepted: 8 February 2022 – Published: 15 March 2022

Abstract. The local topographic slope of the accretionary prism is often used together with the critical taper theory to determine the effective friction on subduction megathrust. In this context, extremely small topographic slopes associated with extremely low effective basal friction ($\mu \leq 0.05$) can be interpreted either as seismically locked portions of megathrust, which deforms episodically at dynamic slip rates or as a viscously creeping décollement. Existing mechanical models of the long-term evolution of accretionary prism, sandbox models, and numerical simulations alike, generally do not account for heat conservation nor for temperature-dependent rheological transitions. Here, we solve for advection–diffusion of heat with imposed constant heat flow at the base of the model domain. This allows the temperature to increase with burial and therefore to capture how the brittle–ductile transition and dehydration reactions within the décollement affect the dynamic of the accretionary prism and its topography. We investigate the effect of basal heat flow, shear heating, thermal blanketing by sediments, and the thickness of the incoming sediments. We find that while reduction of the friction during dewatering reactions results as expected in a flat segment often in the forearc, the brittle–ductile transition results unexpectedly in a local increase of topographic slope by decreasing internal friction. We show that this counterintuitive backproduct of the numerical simulation can be explained by the onset of internal ductile deformation in between the active thrusts. Our models, therefore, imply significant viscous deformation of sediments above a brittle décollement, at geological rates, and we discuss its consequences in terms of interpretation of coupling ratios at subduction megathrust. We also find that, with increasing burial and ductile deformation, the internal brittle deformation tends to be accommodated by backthrusts until the basal temperature becomes sufficient to form a viscous channel, parallel to the décollement, which serves as the root to a major splay fault and its backthrust and delimits a region with a small topographic slope. Morphologic resemblances of the brittle–ductile and ductile segments with forearc high and forearc basins of accretionary active margins, respectively, allow us to propose an alternative metamorphic origin of the forearc crust in this context.

1 Introduction

Several studies have suggested a link between the morphology of forearc wedges and the seismic behavior of megathrusts, showing a correlation between large subduction earthquakes and forearc basins or deep-sea terraces (Wells et al., 2003) or with negative free-air gravity anomalies (Song and Simons, 2003; Wells et al., 2003).

Forearc wedges are to the first order well described by the critical taper theory (CTT) (Davis et al., 1983; Dahlen et al., 1984). This theory assumes that wedges are built by accretion of material equivalent to sand pushed by a moving bulldozer over a frictional basal décollement. This theory has been very successful in describing the equilibrium morphology of wedges in response to accretion and as a function of its effective internal and basal frictional strength (Davis et al., 1983; Dahlen et al., 1984).

The relationship between the forearc wedge morphology and the seismogenic behavior has been attributed to spatial variations of basal shear strength (Song and Simons, 2003) and forearc basins are generally associated with an extremely

low effective friction within the seismogenic zone ($\mu \leq 0.05$) (Cubas et al., 2013; Pajang et al., 2021a), which is also supported by heat flow measurements and thermal modeling (Gao and Wang, 2014).

The effective friction $\mu_{\text{eff}} = \tau^*/(\sigma_{\text{n}})$ is the ratio of the effective shear stress τ^* to the normal stress σ_{n} acting on a specific plane. Effective shear stress is the shear stress τ corrected from isotropic fluid pressure contribution P_{f} following $\tau^* = \tau - P_{\text{f}}$ (Terzaghi, 1925). Effective friction differs from the internal friction of rocks $\mu = \tau/\sigma_{\text{n}}$, which is constant for most geological material except mineralogical clays (Byerlee, 1978). Clay minerals are phyllosilicate hydrated and their stability field is mainly controlled by temperature. Prograde metamorphic reactions that affect clay minerals release water in the system, which is suspected to raise fluid pressure and diminish effective friction. Clay contents, their nature, and their evolution during accretion may therefore affect the effective friction of the décollement as a function of temperature history.

Several studies have related the depth dependence of subduction megathrust seismicity to the diagenetic transformation of smectite to illite, two clay minerals (Vrolijk, 1990; Hyndman et al., 1995; Oleskevich et al., 1999; Moore and Saffer, 2001).

This transition appears at $\sim$ 2.5–5 km depth or 100–150 °C temperature threshold in clay-rich accretionary complexes (Pytte and Reynolds, 1988; Hyndman et al., 1995; Oleskevich et al., 1999) and could account for up to 80 % of the excess in pore fluid pressure (Bekins et al., 1994; Lanson et al., 2009) necessary to explain the low topographic slope of forearc basins according to CTT. This transition is found to roughly correlate with the up-dip limit of the seismogenic zone (Oleskevich et al., 1999). Yet, the relationships between forearc basins and seismogenic zones do not work along all subduction zones (Song and Simons, 2003; Wells et al., 2003).

An alternative explanation for the flat slope of forearc basins could be the presence of a weak viscous décollement. This hypothesis is supported by rock records in exhumed large accretionary complexes (Raimbourg et al., 2014; Chen et al., 2018), which show that the increase in temperature with burial permits to reach the brittle–ductile transition. Yet, this transition from solid (rate-independent or rate-weakening) versus fluid (rate-hardening) friction is hard to parametrize within the CTT as it produces rate-dependent effective friction and rate dependence is absent of CTT. Long-term models which include the tectonic and thermal structure inherited from building the forearc wedge are thus needed to explore alternative or reconciling explanations.

The evolution and distribution of long-term internal deformation of forearc wedges has been intensively studied by numerical models in two (Burbidge and Braun, 2002; Strayer et al., 2001; Buiter et al., 2016; Stockmal et al., 2007; Miyakawa et al., 2010; Simpson, 2011; Ruh et al., 2012; Ruh, 2020) and three dimensions (Braun and Yamato, 2010; Ruh et al., 2013; Ruh, 2016) complementing analogue models (see Graveleau et al., 2012, for a review). These models have covered the influence of many parameters such as the geometry (e.g., Dahlen et al., 1984; Davis et al., 1983; Smit et al., 2003; Ruh et al., 2016), basal friction (e.g., Colletta et al., 1991; Nieuwland et al., 2000; Burbidge and Braun, 2002; Ruh et al., 2012; Cubas et al., 2008), surface processes (e.g., Storti and McClay, 1995; Mary et al., 2013; Willett, 1999; Bonnet et al., 2007; Fillon et al., 2013; Simpson, 2006), and the presence of viscous material along the décollement (e.g., Costa and Vendeville, 2002; Smit et al., 2003; Pichot and Nalpas, 2009; Simpson et al., 2010; Ruh et al., 2012; Borderie et al., 2018). Despite the large number of published studies, none of them included the dependence of effective basal friction on temperature due to metamorphic reaction or brittle–ductile transition.

Here, we study how the introduction of temperature evolution and its feedback on rock rheology generates deviations from CTT. For that purpose, we use a typical CTT setup (Fig. 1), and we solve for the heat equation on the same domain with a constant heat flow boundary condition at the base, which corresponds to plate age, to allow the temperature to increase with burial. As this contribution focuses on the thermal effect, we also include shear heating and thermal blanketing of sediments. We present different series of 2-D thermomechanical simulations which assess how the brittle–ductile and the smectite–illite transitions affect the topographic slope of an accretionary prism and its internal deformation. We briefly discuss the internal deformation and the morphology of the wedge and also its potential seismic behavior. We therefore retrieve the spatial and temporal variation of the morphologies and deformation patterns and discuss their implications in terms of the forearc basin and forearc high genesis and nature.

2 Modeling approach

2.1 Method

In order to model the long-term behavior of the accretionary prism, we use pTatin2d (May et al., 2014, 2015), a code based on finite element method that employs an arbitrary Lagrangian–Eulerian (ALE) discretization together with the material point method to solve the conservation of momentum (Eq. 1), mass (Eq. 2), and energy (Eq. 3) for an incompressible fluid. It allows solving thermomechanical problems. It has been widely used to model lithospheric-scale long-term tectonic problems coupled to surface processes (Jourdon et al., 2018; Perron et al., 2021) and benchmarked with sandbox experiments (Buiter et al., 2016).

The code solves for velocity v and pressure P assuming conservation of momentum:

$$\nabla \cdot (2\eta \dot{\boldsymbol{\varepsilon}}) - \nabla P = \rho \boldsymbol{g}, \quad (1)$$

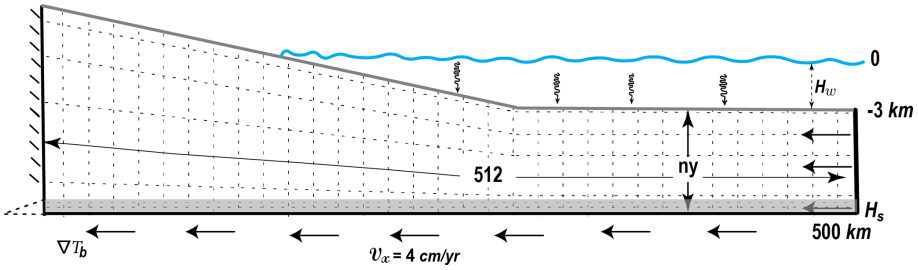

Figure 1. Model setup. Mechanical boundary conditions are a non-deformable backstop on the left side, a constant velocity in the horizontal direction of 4 cm yr^{-1}; the top boundary behaves as a free surface above sea level, while the weight of the water column is prescribed as stress normal to the deformed boundary below sea level. Temperature is fixed at the surface; the thermal gradient is prescribed across all other boundaries with the value of zero on vertical ones and value of ∇T_b at the bottom boundary. The mesh consists of $512 \times n_y$ Q2P1 elements which deform to adapt to the deforming top boundary. Parameters are defined in Table 1.

in an incompressible fluid assuming

$$\nabla \cdot \mathbf{v} = 0, \tag{2}$$

of nonlinear effective viscosity η and constant density ρ. $\dot{\boldsymbol{\varepsilon}}$ is the strain rate tensor and $\boldsymbol{g}$ the gravity acceleration. Evolution of temperature T is obtained by solving the time-dependent, t, conservation of heat:

$$\frac{\partial T}{\partial t} = \nabla \cdot (\kappa \nabla T) - v \nabla T + \frac{H}{\rho C_p}. \tag{3}$$

The coefficients of Eq. (3) are κ the thermal diffusivity, C_p the heat capacity, and H the heat production. We do not include radiogenic heat production in our simulation, and

$$H = \tau_{ij} \dot{\varepsilon}_{ij} = 2\eta(\dot{\varepsilon}_{xx}^2 + 2\dot{\varepsilon}_{xy}^2 + \dot{\varepsilon}_{yy}^2) \tag{4}$$

corresponds to the sole shear heating. The Stokes problem (Eqs. 1 and 2) is solved using high-order stable elements ($Q_2 - P_1$), while the heat equation (Eq. 3) is discretized on Q_1 elements. Physical properties of rocks are computed on Lagrangian markers and projected to gauss points using constant value per element. Averaging of marker-defined coefficients within element is geometric for viscosity and algebraic for other properties. At every time step, the surface of the models, h, is smoothed according to the Culling diffusive erosion law:

$$\frac{\partial h}{\partial t} = -\nabla \cdot (k \nabla h), \tag{5}$$

with a diffusion coefficient k. Details on implementation of the surface process model in pTatin2d are to be found in Jourdon et al. (2018).

2.2 Rheological model

We use temperature- and pressure-dependent nonlinear rheologies. Effective viscosity is evaluated on material points using first the Arrhenius flow law for dislocation creep:

$$\eta_{\text{vis}} = A^{-\frac{1}{n}} \left(\dot{\varepsilon}^{\text{II}}\right)^{\frac{1}{n-1}} \exp\left(\frac{Q + PV}{nRT}\right), \tag{6}$$

written in term of the second invariant of the strain rate tensor $\dot{\varepsilon}^{\text{II}}$. The activation volume is set to $V = 8 \times 10^{-6}$ m^3 mol^{-1} for all the lithologies; the other constants (A, n, Q) are listed for each lithology in Table 1. If the prediction of the second invariant of stress for a viscous rheology

$$\sigma^{\text{II}} = 2\eta_{\text{vis}} \dot{\varepsilon}^{\text{II}} \tag{7}$$

exceeds the Drucker–Prager frictional plastic yield criterion,

$$\sigma_Y = \sin\phi P + C\cos\phi, \tag{8}$$

which depends on ϕ the internal friction angle and C the cohesion, the effective viscosity of the marker is corrected in order to return to the yield envelop with

$$\eta_p = \frac{\sigma_Y}{2\dot{\varepsilon}^{\text{II}}}. \tag{9}$$

Finally, the friction angle ϕ and cohesion C decrease linearly with accumulation of strain in the brittle regime ε_p from an initial friction ϕ_0 to a final friction ϕ_∞ (C_0 and C_∞ for cohesion, respectively):

$$\phi = \phi_0 - \frac{\varepsilon_p - \varepsilon_{\min}}{\varepsilon_{\max} - \varepsilon_{\min}} (\phi_0 - \phi_\infty), \tag{10}$$

over a range of accumulated plastic strain varying from $\varepsilon_{\min} = 0$ to $\varepsilon_{\max} = 0.5$. This drop of friction and cohesion permits former faults to remain brittle where undeformed rocks creep viscously. The décollement is exempt from softening both to facilitate the comparison with CTT and because it is considered originally frictionally weak. Frictional parameters are listed together with viscous parameters, density, and thermal diffusivity in Table 1. As all Stokes solvers, pTatin2d also applies cut-off values on effective viscosity in order to maintain a reasonably well-conditioned system of equations. These are set to a minimum value $\eta_{\min} = 10^{16}$ Pa s and a maximum value $\eta_{\max} = 10^{25}$ Pa s. We made sure that the minimum is never reached to ensure that the frictional properties of the décollement reflect its extremely low friction.

Table 1. Variable rheological parameters and coefficients for the different lithologies; creep parameters [a] from Ranalli and Murphy (1987) and [b] from Shea and Kronenberg (1992). [c] In models **M13** to **M15** the friction in the shale is temperature dependent.

Parameter	Name	Unit	Sandstone/quartz[a]	Shale[b]	Sediment/quartz[a]
A	Pre-exponential factor	$\mathrm{MPa}^{-n}\,\mathrm{s}^{-1}$	6.8×10^{-6}	1.3×10^{-67}	6.8×10^{-6}
n	Exponential stress	–	3	31	3
Q	Activation energy	kJ	156	98	156
C_0	Initial cohesion	MPa	2	0.1	2
C_∞	Final cohesion	MPa	1	0.1	1
ϕ_0	Initial friction	degrees	25	5	25
ϕ_∞	Final friction	degrees	10	5[c]	10
κ	Heat diffusivity	$\mathrm{m}^2\,\mathrm{s}^{-1}$	10^{-6}	10^{-6}	10^{-7}
ρ	Density	$\mathrm{kg\,m}^{-3}$	2400	2400	2000

2.3 Initial and boundary conditions

The model domain is 500 km long and its initial thickness is either 4 or 7.5 km (Fig. 1). It is constituted of two layers, a 500 m thick décollement modeled by shale, while the rest is modeled by sandstone/quartz. The domain is discretized with a mesh of 512×16 and 512×24 Q2 elements, for 4 and 7.5 km thickness, respectively. In the y direction, two mesh elements are aligned with the initial décollement layer to better capture its interface and friction at small strain. The décollement material is considered as part of the domain, as such, we allow shale to be dragged in the rest of the model domain contrarily to frictional boundary conditions adopted to benchmark the code with sandbox experiments (Buiter et al., 2016). The shortening of the model is driven by a constant horizontal velocity $v_x = 4\,\mathrm{cm\,yr}^{-1}$, applied both at the right and bottom boundaries. Above the décollement level, the left side of the domain is rigid. Within the two mesh elements of the left boundary which belongs to the décollement, a vertical velocity gradient is applied to ensure the continuity with the bottom boundary. The surface of the domain is modeled with a free surface above sea level (located 3 km above the top of the mechanical model, Fig. 1); below sea level, additional normal stress:

$$\sigma_\mathrm{n} = H_\mathrm{w} \rho_\mathrm{w} g, \tag{11}$$

is applied on the deformed surface to mimic the weight of water, yet shear stress is zero like above sea level.

The thermal boundary conditions assign the temperature $T_0 = 0\,^\circ\mathrm{C}$ at the surface, a constant thermal gradient $\nabla T_\mathrm{b} = \left.\frac{\partial T}{\partial y}\right|_{y=y_\mathrm{b}}$ at the base and no horizontal gradient (insulating boundary) on the vertical walls of the domain. As we assume no radiogenic heat production, the initial temperature in the domain is fixed to

$$T = T_0 - \nabla T_\mathrm{b} y, \tag{12}$$

consistently with the boundary conditions.

2.4 Post-processing

Models are named by a number within a bullet on the right of the panels. This number refers to Table 2 which contains all the specific parameters used for this realization of the model. For each simulation, we show the finite brittle strain in the rocks and the strain rate of the current state. The total strain (brittle and viscous) can be deduced from the geometry of the incoming sediments (gray and black originally horizontal).

The finite strain figure displays the lithologies of rocks and the accumulated plastic strain on markers with a linear color map. Markers with values of plastic strain ε_p larger than 2 or 3 can be interpreted as being part of a fault. In order to better show the deformation, sandstone sequences have been colored with thin layers that have no physical existence. Sediment markers deposited by surface processes are colored by the time of deposition from brown to yellow colors. As the color palette for brittle strain would not show well in the sediments produced by the surface process model (SPM), we actually do not plot the brittle strain on top of erosional products. However, they do deform in a brittle manner from the strain rate and as for incoming sedimentary rocks. The brittle/localized deformation in the sediments is outlined by the deformation of their bedding.

The current state figure displays whether the material is yielding plastically (blue) or deforms viscously (red). It is overlaid by green shades of the second invariant of strain rate to outline structures that are currently active by comparison to finite strain. A cut-off range from $5 \times 10^{-16}\,\mathrm{s}^{-1}$ to $2 \times 10^{-14}\,\mathrm{s}^{-1}$ is used for the post-processing. The actual values span a larger range. We also represent three isotherms (180, 300, and 450 °C) which have been chosen to correspond to the onset of viscous deformation in low strain islands, brittle–ductile transition for quartz at average strain rate and completely ductile behavior. In the simulation with dehydration reactions, the 120 °C isotherm is added to locate the onset of the dehydration reaction. Finally, we represent the local slope with a color code at the top of the slice.

Table 2. Variable parameters. H_s indicates domain thickness, n_y indicates the number of vertical element, ∇T_b indicates the basal thermal gradient, k indicates coefficient of diffusion for surface process model, SH indicates shear heating, DR indicates dehydration reaction followed by values for temperature-dependent internal friction angle in degrees.

Model	H_s (km)	n_y	∇T_b (° km^{-1})	k	SH	DR
M0	4	16	–	10^{-6}	off	off
M1	4	16	15	10^{-6}	on	off
M2	4	16	15	10^{-6}	off	off
M3	4	16	15	10^{-5}	on	off
M4	4	16	15	10^{-5}	off	off
M5	7.5	24	15	10^{-6}	off	off
M6	7.5	24	15	10^{-5}	off	off
M7	7.5	24	15	10^{-6}	on	off
M8	7.5	24	15	10^{-5}	on	off
M9	4	16	25	10^{-6}	on	off
M10	4	16	25	10^{-5}	on	off
M11	7.5	24	25	10^{-6}	on	off
M12	7.5	24	25	10^{-5}	on	off
M13	4	16	15	10^{-6}	off	on 5–0.1–10
M14	4	16	15	10^{-6}	on	on 5–0.1–10
M15	4	16	15	10^{-6}	on	on 5–0.1–5

2.5 Experimental plan

Our aim is to provide the community with a first assessment of the topographic expression of the change in thermorheological regime with burial in an accretionary prism. We, therefore, have chosen a simple reference model which produces well defined thrust and backthrust, with a moderate amount of sedimentation. The effects of softening, basal friction, and basal slope on accretion have already been thoroughly studied (e.g., Graveleau et al., 2012; Buiter et al., 2016; Ruh et al., 2012, 2014).

Hence, we here concentrate on parameters that are known to affect the geotherm: basal heat flow (represented by basal thermal gradient ∇T_b), initial burial (H_s), coefficient of diffusion of the topography (erosion and sedimentation) (κ), and shear heating (SH) following the plan listed in Table 2. In all the experiments, thermal blanketing (Jeffreys, 1931; Wangen, 1994) is very roughly simulated by using a lower thermal diffusivity for sediments produced by the surface process model (see Table 1). As we do not simulate the compaction of sediments with burial, thermal insulation is probably overestimated but it allows testing potential effects of sedimentation on the thermal state of the accretionary wedges.

3 Main results

3.1 Effect of brittle–ductile transition at one glance

In Fig. 2, we first compare the results of our reference model (**M1**), with a 4 km thick pile of sediments affected by moderate erosion sedimentation, shear heating, and a thermal gradient of 15° km^{-1} which corresponds to a plate age of 65 Ma, with the same model run without thermal coupling (**M0**).

While the frontal parts are not significantly different, with similar tapers and ramp spacing, as soon as the thickness of the wedge doubles (close to sea level at x of approximately 300 km), the backthrusts are more active in the purely brittle wedge than in the thermally controlled wedge for these brittle parameters. This results in the deactivation of one ramp over two, which leads to the formation of the distinct twinned-slice patterns observed between $x = 430$ km and $x = 300$ km in **M0**. In **M1**, the twinning of slice by backthrust occurs only once the temperature at the base of the model reaches 300 °C.

Looking at the internal part of the two accretionary prisms, the differences become of course more striking. In the case without thermal coupling (**M0**), deformation continues by pairing together more and more slices within sequences of thrust and backthrust which root deeper and deeper as the accretionary prism thickens. The prolonged activity of these out-of-sequence thrusts and backthrust is best measured by the small out-of-sequence basins that form at their top, discordant on the older sediments. Very little exhumation occurs close to the backstop. In the case of thermal coupling, as soon as the 450 °C isotherm is reached, deformation becomes highly partitioned vertically. A thick layer at the base accommodates the simple shear and branches on main frontal thrusts which root at the brittle–ductile transition. The ductile material is exhumed along a normal fault that roots on the backstop. In between, the deformation in the brittle part is either very distributed or almost nonexistent as the strain rate remains below our visualization threshold.

In the end, zooming out of these details and looking at the topographic slope, we can see that a brittle accretionary wedge displays a rather constant 4° slope, as predicted by the CTT taking into account the softening parameter (Ruh et al., 2014). A mature brittle–ductile wedge forms three distinct segments that can be distinguished based on topographic slope. The back segment, close to the backstop where the décollement is viscous displays a rather low but non-zero topographic slope. The third segment, at the toe where the wedge is purely brittle, displays a CTT predicted slope. In between, where both brittle and ductile deformation coexist within the wedge, while the décollement is still brittle, a central segment displays a distinctively larger topographic slope than predicted by CTT. We refer to that segment as the brittle–ductile transition segment of the wedge.

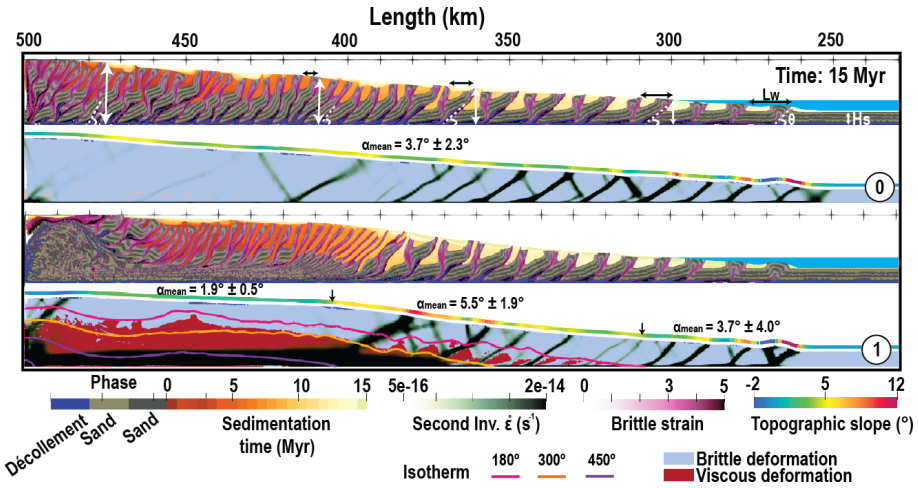

Figure 2. Model **M0**: without temperature compared to model **M1**: the same experiment with temperature-dependent rheologies, both after 15 Myr evolution. The finite strain and the current state and strain rate are shown for basal frictional angle ($\phi_b = 5°$) and internal friction angle dropping from 25 to 10° with strain. The yellowish-brown color illustrates syn-tectonic sedimentation in the form of piggyback basins which represent a given age that corresponds to the time of deposition. Where the material is yielding plastically is in blue or where it deforms viscously is in red with the onset of 180, 300, and 450 °C isotherms. Black arrows display decreasing thrust space towards the backstop and white arrows show increasing sequence thickness and inclination angle θ. The local topographic slope with a color code shown at the top of the slice is affected by temperature and frictional properties, 1 : 1 scale.

3.2 Time evolution of reference model

Figure 3 shows the structural evolution of the reference simulation **M1** through time. The wedge grows horizontally by in-sequence thrusting and vertically by reactivation of thrusts within the wedge. Most of the horizontal shortening is accommodated by the active frontal thrust. As the wedge evolves, the surface slope also changes and we detail here its evolution in time.

After 1 Ma, accumulated plastic strain shows that the deformation is strongly localized along the frontal part and on the décollement. Brittle shear bands initially occurred in conjugate sets; with ongoing shortening, landward dipping brittle shear bands are preferred and backthrusts are almost abandoned. The wedge is trying to reach a critical state by creating a topographic slope. Due to internal frictional softening, the brittle wedge present a slope $\overline{\alpha}$, which corresponds to the slope predicted by CTT for basal friction ϕ_b and internal friction of 17°, i.e., the average of $\phi_\infty = 10°$ and $\phi_0 = 25°$.

At 5 Ma, some patches of viscous deformation appear in between the main faults at $x = 413$ km once the base of the model reaches 180 °C. From that point, landward plastic strain and the second invariant of the strain rate indicate the activity of out-of-sequence thrusts and steep backthrusts which dissect the former slices and tend to flatten horizontally the sequences as the former ramps become more and more vertical. This phenomena induces vertical thickening that correlates with the occurrence of internal viscous deformation at depth and with an increase in local slope $\overline{\alpha}$ independently of basal friction which remains constant. This increase in slope causes an increase in sedimentation rate at the front where piggyback basins tend to be more starved than in the initial phase favoring the activity of thrusts, and a lengthening of the slices as predicted by other studies like Storti and McClay (1995) using sandbox experiments or Simpson et al. (2010) using numerical simulations.

As the shortening goes on, the temperature continues increasing at the back of the wedge due to burial. Between 5 and 10 Ma, the strain rate shows that the thickness of the décollement increases to reach 2 km. A normal fault forms near the backstop (which could be probably an inevitable boundary effect) and starts accommodating the exhumation of high metamorphic grade rocks, which deforms in a ductile manner. At the front of this wide ductile horizontal shear zone, which terminates right at the 300 °C isotherm, roots a system of low-angle thrusts and high-angle backthrusts which separates the warm distributed part of the wedge from the thrust dominated section of the wedge.

From 10 to 15 Ma, the warm part of the wedge grows in length and its topography flattens. The vertical partitioning between simple shear at the base and pure shear at the top becomes evident. At the front of this ductile wedge, the transition zone, where thrusts and their backthrust roots directly in the ductile décollement near the 300 °C isotherm, develops giving rise to a distinctively larger slope than predicted by CTT. At the toe of the wedge, the slope remains constant and CTT compatible.

At 20 Ma, the overall architecture of the accretionary prism has not changed; the whole wedge is just shifted towards the right as the ductile part of the wedge has grown wider. One could state that the brittle–ductile wedge has

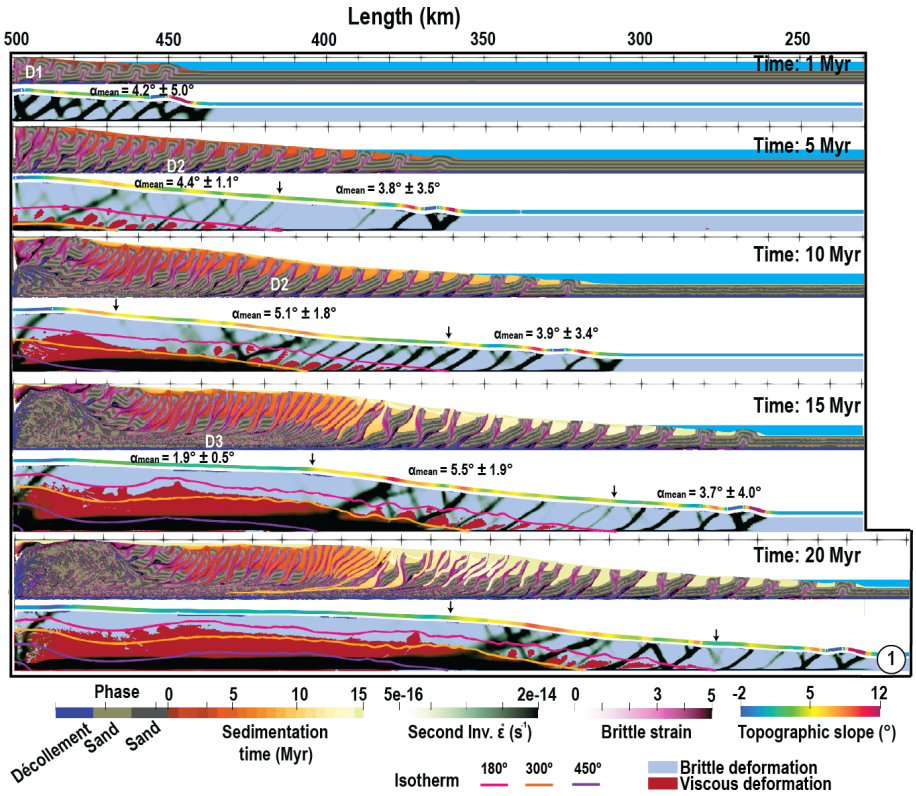

Figure 3. Temporal evolution of the reference model (**M1**) from beginning to 20 Myr of shortening, 1 : 1 scale.

reached some sort of steady state between 15 and 20 Ma. Rocks that are incorporated in the wedge start by rotating along with brittle thrust and maybe deforming in a pure brittle manner within the slice. In a second semi-brittle phase, internal viscous–ductile deformation affects the whole tectonic slices separated by brittle thrusts. This phase of deformation corresponds to the moment at which the incoming sediments are incorporated to the second segment of the wedge where the topographic slope is larger than CTT predictions. Finally, depending on whether rocks were incorporated in the ramp or not, they go through passive rotation by distributed pure shear thickening associated with low temperature or intense ductile simple shear before being exhumed by the higher temperature.

In conclusion, the large slope segment which corresponds to the brittle–ductile transition is acquired as soon as some viscous internal deformation occurs in between faults. The brittle–ductile wedge reaches a steady state when ductile deformation becomes predominant on the décollement that is for temperature greater than 450 °C.

3.3 Sensitivity to shear heating, erosion, and thickness of incoming sediments

Depending on the chosen thermal parameters, the three segments described above are more or less developed in our simulations. A major player in the development of the ductile flat part of the wedge associated with high-grade metamorphic rock exhumation and formation of a forearc basin is the occurrence of shear heating.

Shear heating might be largely reduced by several factors and noteworthy enough the presence of water which reduces the ductile strength of the material or by thermal pressurization during earthquakes (Sibson, 1973; Lachenbruch and Sass, 1980; Mase and Smith, 1984, 1987; Segall and Rice, 2006). Gao and Wang (2014) actually showed that megathrusts that produce great earthquakes tend to dissipate less heat than megathrusts that slip mainly by creep. Hence, our shear heating models give a maximum bound for the heat that could be produced in the system. In order to study the other bound, we run some model with shear heating off which would correspond to a system where most slip is accommodated by earthquakes.

Results are clear; all models with shear heating (Fig. 4) develop a large flat area because the shear at depth helps the temperature to rise above the 450 °C isotherm, which correlates with the formation of the topographic plateau where high-grade metamorphic rocks are exhumed. Models with no shear heating hardly develop a plateau and a normal fault to exhume high-grade material at the back (Fig. 5).

Actually, exhumation is reached under two conditions in our models, with large erosion coefficients, i.e., **M4** and **M6**, and in presence of shear heating. The peak metamorphic tem-

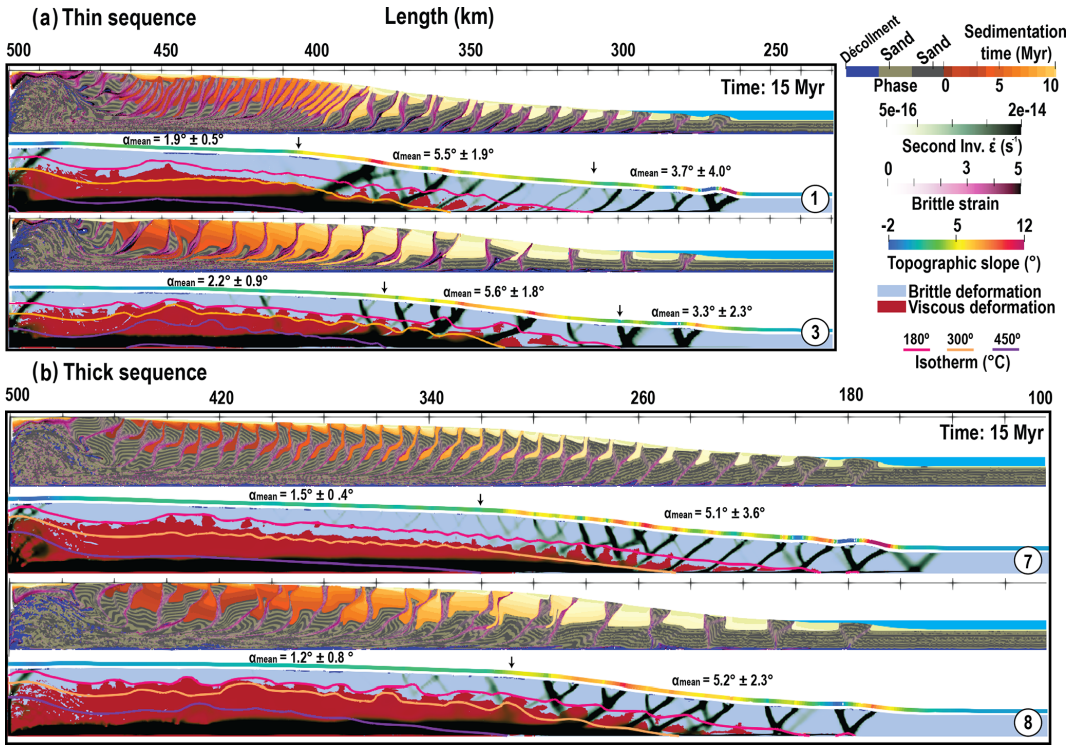

Figure 4. Models with shear heating on after 15 Myr of shortening. **(a)** Thin and **(b)** thick sequence pile models. **M1**, **M3** and **M7**, **M8** are the same experiment with normal and high surface diffusion rates, respectively. Experiment parameters are given in Tables 1 and 2, and color code for markers is given in Fig. 2, 1 : 1 scale.

perature of rocks exhumed at the backstop is compatible with thermochronometry studies in stationary accretionary prism like Taiwan (Suppe, 1981; Willett and Brandon, 2002). Its samples are exhumed to the surface by rock uplift to compensate for the mass lost via erosion (Fuller et al., 2006) and they have experienced temperatures in excess of 300–365 °C but below 440 °C (e.g., Lo and Onstott, 1995; Fuller et al., 2006).

Models with larger sedimentation rate (models **M3**, **M4**, **M6**, **M8**, **M10**, **M12**) produce, as expected from former studies (Storti and McClay, 1995; Simpson et al., 2010), a smaller number of thrusts and a larger spacing between them. Erosion and sedimentation also participate at reducing the slope at every step, thus favoring out-of-sequence activity (Fig. 5 **M2** from $x = 260$ to 380 km and **M4** from $x = 290$ to 320 km). In our models, sediments also affect the thermal regime because they are attributed a lower thermal diffusivity; thick sediment sequences act therefore as a blanket isolating the heat flux coming from below. As a result, temperature rises faster at depth when a large sedimentary basin forms. This explains why, in absence of shear heating (Fig. 5), only models with large sedimentation rate develop a ductile flat at the back (Fig. 5 **M4** and **M6**).

Thermal blanketing also affects the geotherm at a smaller scale as shown by the distinctive wiggles in the isotherms. For small basins, these wiggles are limited to the 180 °C isotherm (Fig. 5 **M2** and **M5**), but for large basins the 300 °C isotherm is affected at larger wavelength and potentially feeds back on the rheology (Fig. 5 **M4** and **M6**).

In absence of heat production and large vertical advective terms, the temperature is more or less proportional to the depth and thermal gradient in the models. Therefore, in experiments with thick sequences (**M5** and **M6** in Fig. 5 and **M7** and **M8** in Fig. 4) or in models with larger imposed basal gradient (**M9, M10, M11, M12** in Fig. 6), the brittle–ductile transition is reached earlier. As a result, the completely brittle part of the accretionary prism, located at the toe of the wedge, is less developed in models with a larger pile of incoming sediments and in models with a larger thermal gradient. The local slope in these models is always larger than the CTT-predicted one and backthrust appear earlier in the history of deformation.

3.4 Effect of dehydration reactions

We now report some models which intend to tackle the effect of fluid over pressure due to dehydration of shale materials which potentially corresponds to smectite–illite transition. In clay-rich accretionary complexes, this transition appears at ∼ 2.5–5 km depth corresponding approximately to 100–150 °C (Pytte and Reynolds, 1988; Hyndman et al., 1995; Oleskevich et al., 1999). Smectite and illite clays are fric-

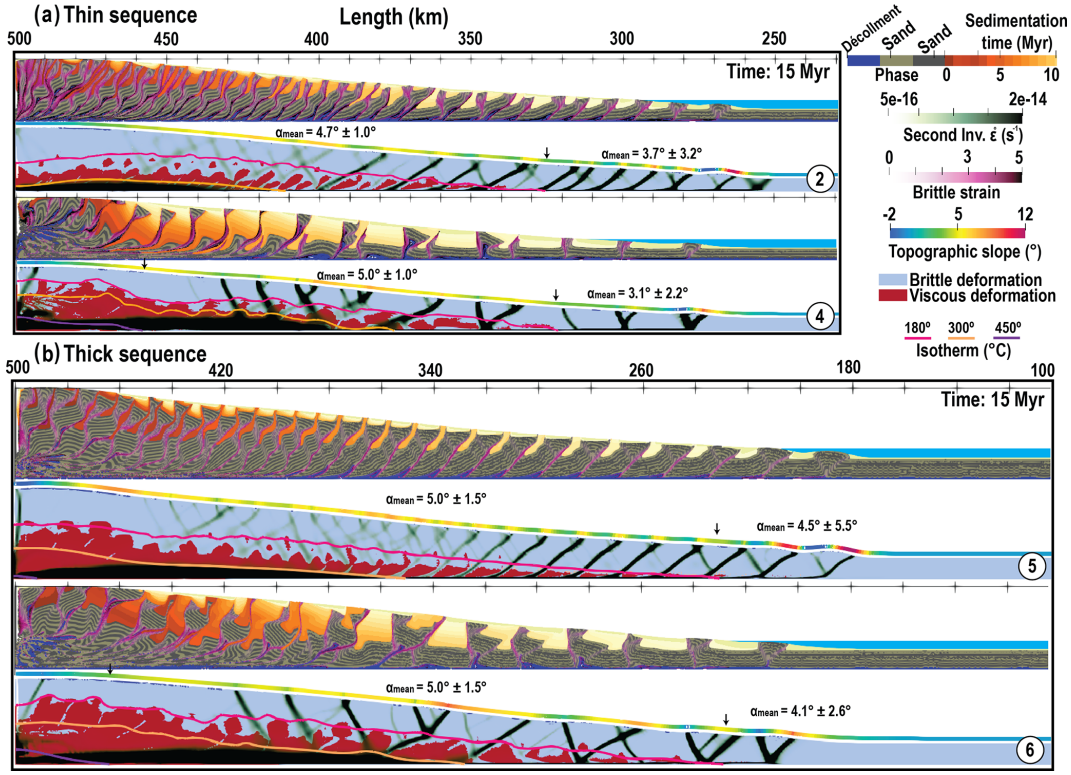

Figure 5. Models with no shear heating after 15 Myr of shortening for **(a)** thin and **(b)** thick sequence pile models. Normal sedimentation rate use in **M2** and **M5**, and high erosion rate in **M4** and **M6**. Refer to Fig. 2 for color codes and Tables 1 and 2 for experiment parameters, 1 : 1 scale.

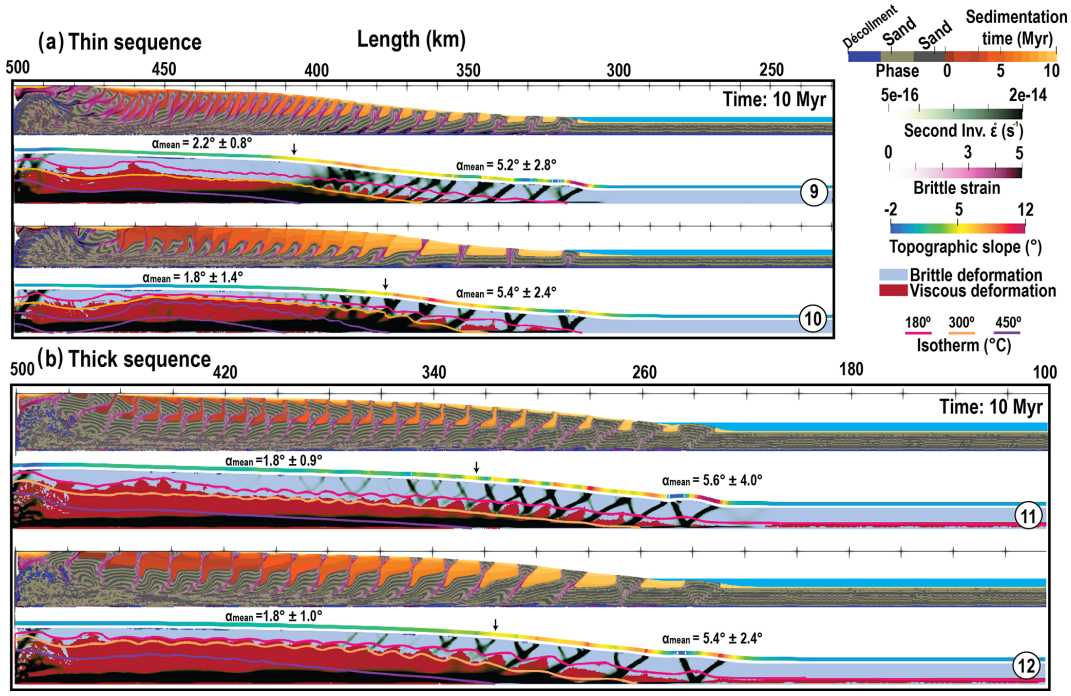

Figure 6. High temperature gradient (25 °C km^{-1}) after 10 Myr for **(a)** thin sequence and **(b)** thick sequence. **M9** and **M11** are with normal erosion and sedimentation rate whereas **M10** and **M12** indicate high sedimentation rate. Color codes and experiment parameters are given in Fig. 2 and Tables 1 and 2, 1 : 1 scale.

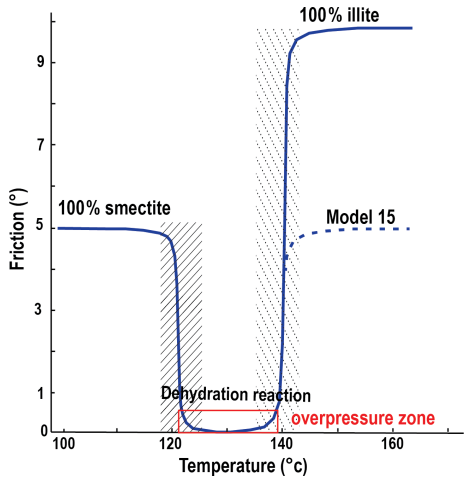

Figure 7. Evolution of friction with temperature with our parameterization of smectite–illite transition. The dashed line is for the evolution of friction in simulation **M15** which serves as comparison with **M1** at the brittle–ductile transition zone.

tionally weak but illite is slightly stronger (Morrow et al., 1982; Saffer and Marone, 2003). We therefore consider that our clay-rich décollement is initially smectite rich with an internal friction angle of 5°. Once dehydration reaction is terminated the same décollement is considered illite rich and affected a friction angle of 10°. We do not have a kinetic reaction included in the code but we assume that the reaction is occurring at fast rate in the 120–140 °C window. This is slightly smaller than the 100–150 °C reported in the literature and it is aimed at roughly accounting for a slow kinetic at lower temperatures and the lack of reactant (smectite) left at higher temperatures. During this phase of fast reaction, fluids are released in the clay-rich décollement of low permeability permitting to build strong local fluid over pressure (Bekins et al., 1994; Lanson et al., 2009). The code does not explicitly include fluids, but these overpressures are reflected by an effective friction angle of 0.1° within the reaction temperature window. The evolution of friction with temperature in the décollement layer is reported in Fig. 7.

Figure 8 shows the structural evolution of simulation **M14**, identical to the reference model **M1** but accounting for the smectite–illite transition.

After 1 Ma, by the formation of conjugate shear bands, the wedge tries to reach its critical state in accordance with basal friction of $\phi_b = 5°$. Since the base quickly reaches 120 °C, the frontal wedge is extremely narrow and followed by a flat area induced by the drop of friction ($\phi_b = 0.1°$), as expected from CTT.

At 3.8 Ma, the flat area is highly extended ($x = 380$–470 km). The onset of this transition serves as the root to a shallow splay fault accompanied by a backthrust.

At 6.3 Ma, as the shortening goes on, the temperature rises due to burial. Once the décollement reaches 140 °C, the basal friction increases to 10°, leading to the onset of a larger topographic slope. Once the décollement reaches 180 °C, some patches of viscous deformation appear in between active thrusts (at $x = 440$ km). As observed in model **M1**, a segment of the high topographic slope, formed by a low-angle thrust and its backthrusts, separates the flat segment from the warmer distributed part of the wedge.

At 10 Ma, the wedge is characterized by four distinct segments: a narrow frontal critical taper, a weakly deformed zone with a flat topographic slope associated with the smectite–illite transition (120 to 140 °C), a high topographic slope corresponding to the brittle–ductile transition formed by a low-angle thrust and its backthrusts rooting on the ductile décollement, and, finally, a second flat segment corresponding to the ductile wedge once the décollement reaches a temperature of 450 °C. The brittle–ductile transition segment shows a larger topographic slope than the reference model **M1** (Fig. 3), because of the higher basal friction reached once the dehydration reaction finishes ($\phi_b = 10°$). From 10 to 15 Ma, the warm and flat part of the ductile wedge grows in length like in model **M1**.

Figure 8b illustrates that shear heating tends to increase the extent of the flat dehydration segment by reducing both the size of the critical taper corresponding to the smectite décollement located at the toe of the wedge and the lateral extent of the steep segment located at the brittle–ductile transition. Figure 8c demonstrates that the increase of slope of the brittle–ductile segment in model **M14** as compared to model **M1** is indeed related to the increase in basal friction up to 10° after the dehydration reaction. As described above, without shear heating, the flat plateau above the viscous décollement hardly develops.

4 Discussion

4.1 Slopes and modes of deformation

The thermomechanical model provides an opportunity to investigate the specific variations of topographic slope of an accretionary prism, supported by the CTT analysis (Davis et al., 1983). Our results show that very simple models of accretionary prism lead to the formation of four different structural zones which corresponds to three different type phases of deformation related to transitions in the rheology.

The frontal brittle part of the wedge is characterized by an imbricated zone and active in-sequence thrusts faults ahead. The décollement and the above sequence behave plastically (Fig. 9a). The topographic slope created in this section is controlled by the basal and average internal friction and is consistent with the CTT predictions (Fig. 9b and c, blue star).

The presence of a smectite–illite transition (dehydration reaction) leads to a segment characterized by a flat topographic slope and little internal deformation, in between the frontal brittle wedge and the brittle–ductile transition

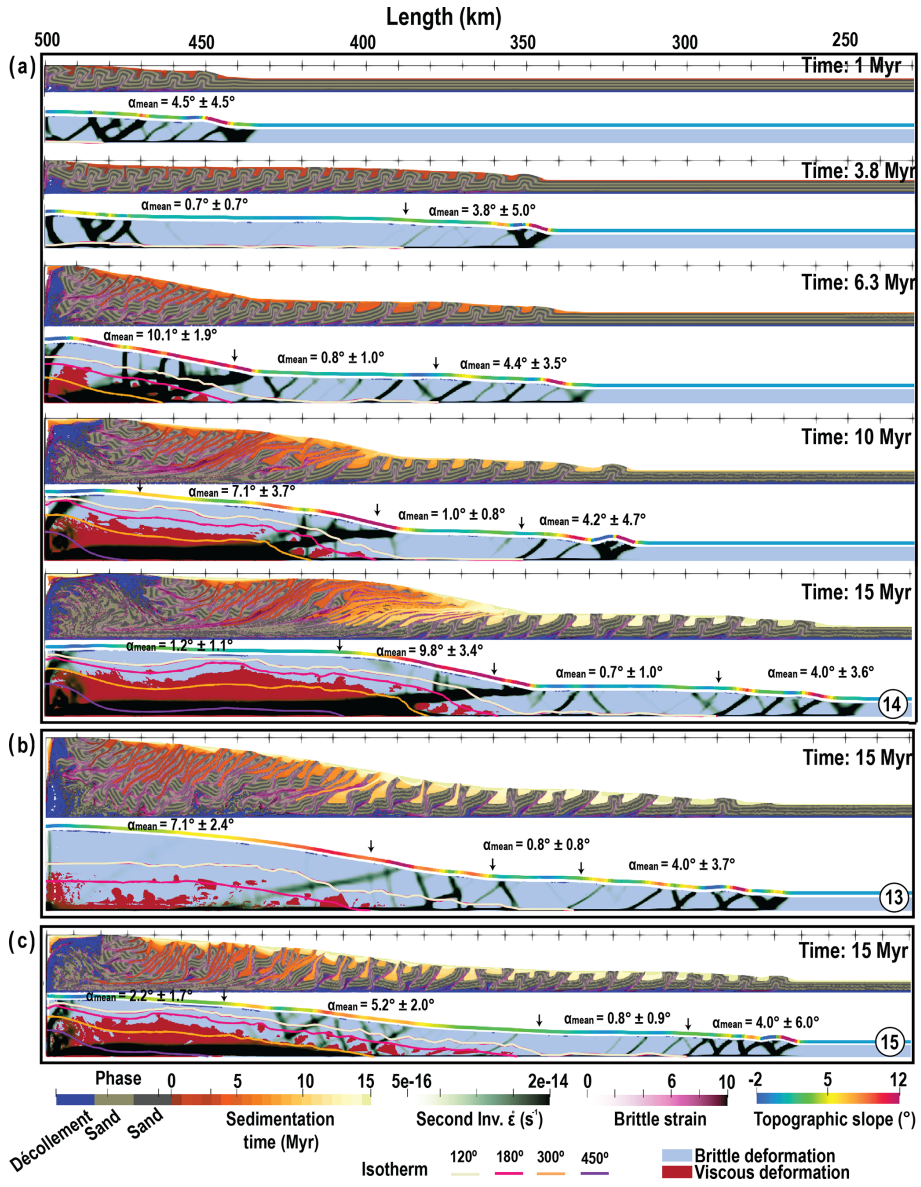

Figure 8. **(a)** 15 Myr of time evolution of simulation **M14** with dehydration reaction and shear heating. **(b)** Model at 15 Ma for similar simulation without shear heating **M13**. **(c)** Model at 15 Ma for similar simulation **M15** with 5° friction instead of 10° friction after the end of dehydration reaction, 1 : 1 scale.

(Fig. 9a). This flat segment appears during the early stage of the accretionary prism formation.

The brittle–viscous transition zone is characterized by out-of-sequence thrusts and backthrusts with high internal deformation (Fig. 9a). This part forms a steeper topography slope than the brittle-only part. A careful examination of the behavior of this segment reveals that the décollement remains brittle, but the above sequence has entered the viscous phase (Fig. 9a). By plotting the surface slope on the critical taper diagram, we notice that this part is consistent with a critical taper of a lower internal friction angle (Fig. 9b, red star).

The viscous part presents an approximate flat zone without effective internal deformation. Décollement and above sequence deform viscously. The topographic slope is again consistent with the critical taper theory, considering that a viscous décollement is equivalent to a brittle décollement of extremely low friction. Therefore, the increase of the topographic slope between the brittle and viscous segments results from an equivalent decrease of internal friction rather than an increase of basal friction. Since we run simulations with basal slope $\beta = 0$, according to CTT the simulated topographic slope might be overestimated compared with natural examples. We thus run the reference simulation with a

basal slope of 2°. We found the same segmentation but with slightly lower topographic slopes as expected from the CTT (Movie M16, please see Sect. "Video supplement" for further information).

4.2 Comparison with exhumed accretionary prism

Based on the models, we can interpret that the rocks exhumed at the back of the models have been through three main phases of deformation through time. The first phase (D1) is purely brittle and corresponds to the onset of accretion at the toe of the accretionary prism. The passive transport through the dehydration flat segment does not cause important deformation. The D1 is therefore overprinted by the phase D2, which is the start of a low grade metamorphic foliation as a result of penetrative horizontal shortening. As temperature increases with burial, material behavior in between faults which deforms with lower strain rates changes from brittle to ductile decreasing the effective friction coefficient of the bulk. This in turns causes the steepening of the slope which favors the activation of brittle backthrusts, that scrap off the frontal wedge rather than forethrusts that would have to uplift a lot of material. In an accretionary prism with large basal heat flow, or thick incoming sediments, sequence D2 appears closer to the toe of the prism and might replace D1. Warmer models then develop a phase in which deformation is partitioned between ductile simple shear at depth (D3) and distributed shortening at the surface (more penetrative version of D2). Once the horizontal ductile shear zone corresponding to D3 has formed, it branches on a shallow dipping splay fault accompanied by a vertical backthrust. The three phases of deformation recorded by the rocks exhumed at the back of the models along a normal fault correspond to the different phases recorded in exhumed accretionary prism like the Shimanto belt (Raimbourg et al., 2014), although this paper would classify our D1 and D2 as more or less localized deformation related to frontal accretion and in our case the high-grade ductile foliation D3 would show a more marked asymmetry. In the Lesser Antilles arc, Verati et al. (2018) have documented distributed deformation by pressure solution occurring at 300 °C/4–5 km depth conditions, in volcanics reworked within the brittle accretionary prism which could correspond to exhumed remnants of D2, although our models are too simplistic to account for incorporation of arc material into the tectonic wedge.

4.3 Forearc basins

Every phase of deformation is accompanied by different types of sedimentary basins. Indeed, while phase D1 is accompanied by piggyback basins which length depends on the sedimentation rate (e.g., Fig. 4), D2 is accompanied with the formation of trench slope basins discordant on the early piggyback basins, and the onset of D3 pinpoints the start of activity of the splay fault and its backthrust. These structures isolate the ductile part of the prism, where forearc sediments can accumulate within small basins in discordance on the sediments accreted during D1 and D2, from the brittle part of the prism. The splay fault and its conjugate high-angle backthrust serve as a current backstop for the brittle part before being incorporated into the ductile forearc part of the prism as accretion continues.

Backthrusting between the imbricated segment and forearc basins has been described along various accretionary margins of high sedimentation rate (Silver and Reed, 1988). Along the Sumatra subduction zone, well known for its high sedimentation rate and high thermal gradient (Chlieh et al., 2008), the slope break predicted by our model is visible on seismic images of northern (Chauhan et al., 2009) and southwestern (Singh et al., 2010) Sumatra, and a clear backthrust has been imaged down to 7 s (TWT) (15 km) (Chauhan et al., 2009). Backthrusts have also been imaged along the Antilles subduction zone, in particular along the Barbados region, again known for its high sedimentation rate (Silver and Reed, 1988; Laigle et al., 2013). A backthrust is also well documented in New Zealand (Barnes and Nicol, 2004) but has been interpreted as resulting from a change in basal friction. Noda (2016) reviews a number of other compressive accretionary margins which all seem to develop an active backthrust at the edge of the forearc basin like in our models.

However, most of these seismic studies place the splay fault and its backthrust at the limit of the continental crust which posits, in a way, a stable position through time, at least relative to the upper plate. In our simulations, the splay fault roots at the location of the 450 °C isotherm along the décollement (Fig. 10a). This isotherm at 15 km depth corresponds to greenschist facies metamorphic conditions. Using typical sediments composition, perplex software yields typical continental crust seismic attributes with $5.5 > V_p > 5\,\mathrm{km\,s^{-1}}$ and $V_s \sim 2.5\,\mathrm{km\,s^{-1}}$. With volcanoclastic sediments, larger velocities are expected for similar metamorphic conditions. As a result, seismic refraction investigation of active margin would definitely identify this part of the models as a continental crust or former arc crust. Using the location of the splay fault in warm, compressional accretionary contexts like South Sumatra (Fig. 10b) and Lesser Antilles (Fig. 10c), we propose that what is typically interpreted as attenuated continental or arc crust with $V_p >= 5$ could also well mark the location of the brittle–ductile transition According to our models, along with accretionary prisms of little seismic activity, the forearc basin should correlate with the fully viscous domain at least along high sedimentation rate and high thermal gradient compressive accretionary margins (Fig. 9a).

4.4 Up- and down-dip end of the seismogenic zone

We here confirm that the smectite–illite transition produces a flat segment that can explain, for young or cold accretionary complexes, the observed correlation between deep-sea terraces or forearc basins with large subduction earth-

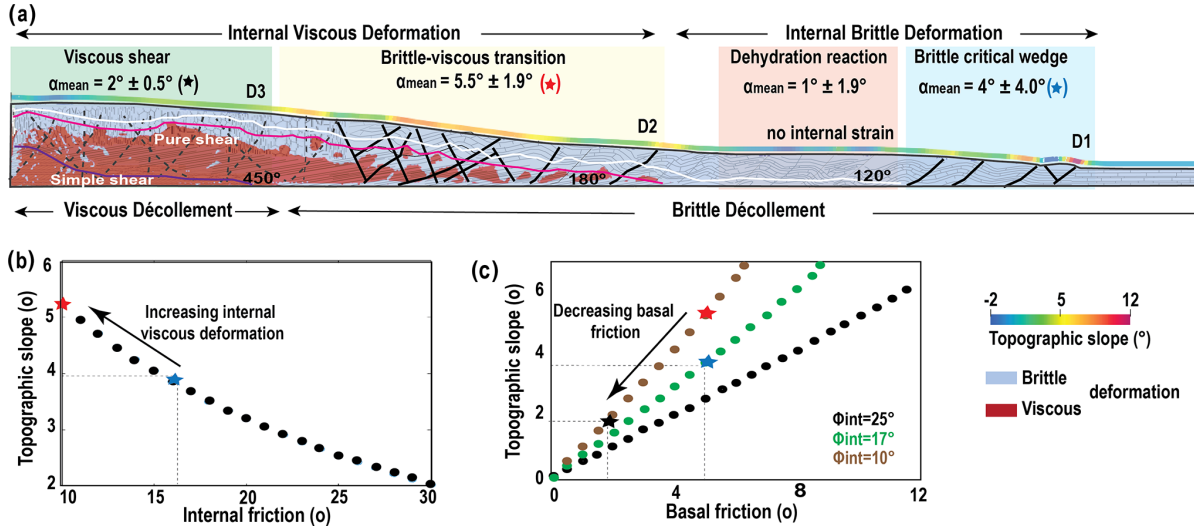

Figure 9. **(a)** Proposed model for the mature brittle–ductile wedge which forms three distinct segments; pure brittle wedge with a rather constant slope predicted by the CTT at the front (blue star), low but non-zero topographic slope close to the backstop corresponds to viscous deformation (black star), and larger topographic slope in between these segments as a result of the brittle–ductile transition (red star and yellow rectangle). **(b)** Topographic slope versus internal friction for $\phi_{basal} = 5°$. **(c)** Basal friction versus topographic slope for ϕ_{int} of 10, 17, and 25°.

quakes (Song and Simons, 2003; Wells et al., 2003). In such specific contexts, the flat segment would thus underline the up-dip limit of the seismogenic zone (part of the megathrust geodetically coupled, i.e., locked during the interseismic period). Along seismically active accretionary prisms, an increase of topographic slope and decrease in apparent geodetic coupling are interpreted as the down-dip limit of the seismogenic zone (Cubas et al., 2013). In the first case, the rise in topographic slope indicates an increase of effective basal friction which corresponds to the down-dip end of dominant seismic slip (Cubas et al., 2013; Pajang et al., 2021a). In the second case, geodetic deformation at velocities that differs from subducting plate velocities is generally interpreted as a lack of coupling on the plate interface based on elastic models (Perfettini et al., 2010; Chlieh et al., 2008). Here, we show that the brittle–ductile transition corresponds to the onset of internal distributed viscous deformation in between brittle structures in the accretionary prism above a brittle décollement. Internal deformation causes a decreased geodetic coupling and an increased apparent basal friction but does not imply any modification in the interface frictional properties or deformation mode. This questions both the search for field analogs of the down-dip end of the seismogenic zone and the interpretation of seismic coupling in terms of locked/creeping décollement.

4.5 Limitations and perspectives

Our simple models permit us to understand first-order mechanisms in forearc formation, but improvements are still needed to better understand how the brittle–ductile transition affects the formation of splay faults providing an alternative model to the formation of forearc basins as well as an alternative origin for the forearc crust. We find that the drop in friction between the ductile and brittle part of the accretionary prism and smectite to illite dehydration reaction is not sufficient to explain the normal faults observed along some accretionary margins like Chile or Makran Cubas et al. (2013); Pajang et al. (2021a). This result leads us to conclude that the normal faults arise from phenomena we neglected in our simplified approach. This includes

- the effect of heterogeneities in the subducting plate,
- the effect of elastic deformation during the seismic cycle, and/or
- the oversimplification of the bottom boundary conditions which does not allow an increase in taper angle with burial like in Beaumont et al. (1992) and Ruh (2020).

We plan on testing these other hypotheses in the future and posit that improving the bottom mechanical boundary conditions will also permit performing more accurate simulations of the sedimentation in the forearc basins by keeping them below sea level.

5 Conclusions

Despite the simplicity and limitations of our simulations, their results are sufficient to propose a new model for the

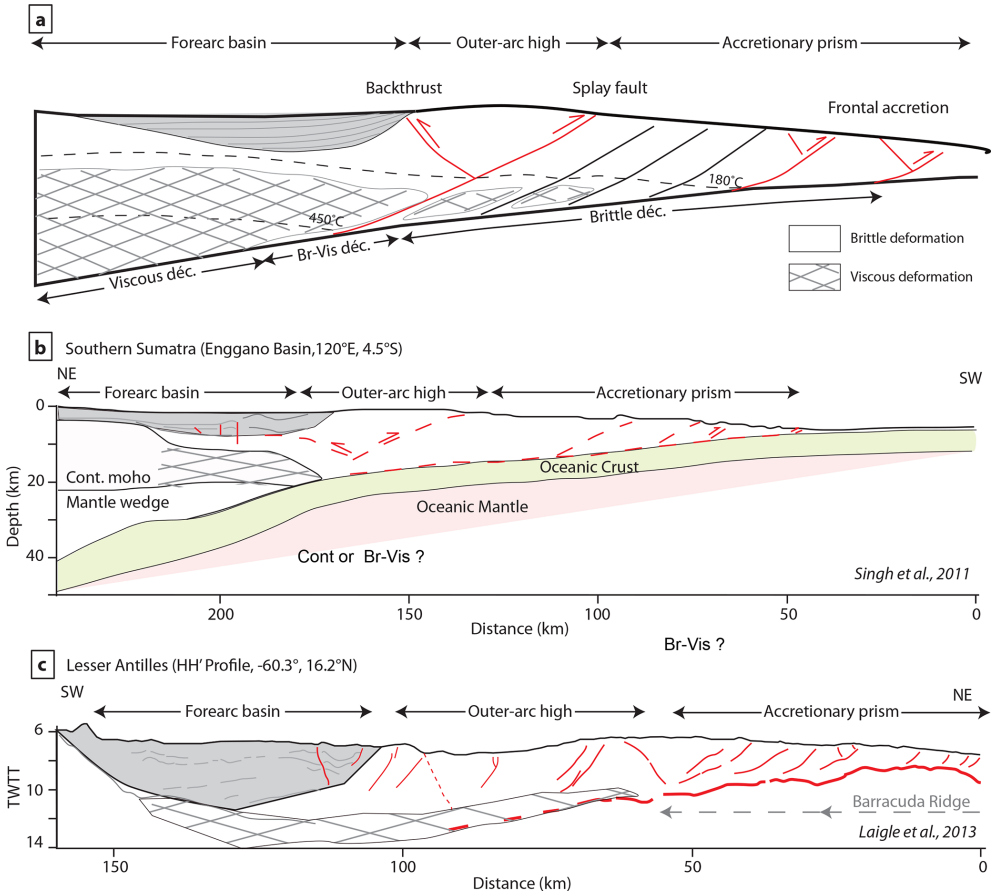

Figure 10. (a) Structure of accretionary wedge and forearc basin modified from Noda (2016) based on our modeling results for the geometry of isotherms and the distribution of brittle and viscous strain. Schematic cross sections of **(b)** South Sumatra based on Singh et al. (2011). **(c)** Lesser Antilles based on Laigle et al. (2013) with indication of the possible location of the brittle–ductile transition based on our model and the observed geometry of faults.

interpretation of changes in topographic slope at compressive accretionary margins, at least, warm margins with large sedimentary supply. Using only the topographic gradient, our model distinguished four segments, which correspond to three modes of deformations observed in exhumed accretionary complexes:

- brittle décollement and internal deformation at the toe where the topographic slope respects the CTT;
- a flat area with little internal deformation in young accretionary prisms, if a dehydration reaction is considered;
- brittle décollement and viscous internal deformation of fault-bounded blocks, where the topographic slope is in excess compared to the CTT and these large slopes should not be interpreted as the down-dip limit of the seismogenic zone;
- viscous décollement and backthrust-bounded blocks in the most internal part where the topographic slope is close to zero.

The most important finding is that the onset of internal viscous deformation in fault-bounded blocks increases the topographic slope of the accretionary complex independently of the basal friction.

Comparing the simulations results with natural cases, we show that this anomalous topography related to the brittle–ductile transition is analogue to the forearc high in a compressional accretionary prism. It is indeed the location of an active backthrust and splay fault system rooting on the viscous channel that forms in the internal part where the basal temperature reaches 450 °C. The location of this viscous channel, which is active in greenschist facies conditions, corresponds to portions of seismic sections that are often interpreted as an attenuated continental crust or former arc crust. Our model provides, we believe, a valid alternative interpretation which has the advantage to explain why the forearc crust is always thinner than the continental crust

on seismic sections but also why the warm subduction segments are representative of our mature stage simulation, such as South Sumatra or the Lesser Antilles are considered aseismic.

Code availability. The version of pTatin2d and the input files used in this contribution are archived following the FAIR principle at https://doi.org/10.5281/zenodo.4911354 (May and Le Pourhiet, 2021). Input files are located in published_inputs/Pajang2021_SE.

Data availability. Data are available at https://zenodo.org/record/4911354/preview/ptatin2d.zip#tree_item354 (May and Le Pourhiet, 2021).

Video supplement. All simulations are available as movies archived at https://doi.org/10.5281/zenodo.5599365 (Pajang et al., 2021b).

Author contributions. SP designed the simulation, ran the simulation prepared the figure and wrote the paper, LLP implemented the heat flow boundary condition, LLP and NC participated in the interpretation of the simulation, application to natural cases and writing of the paper.

Competing interests. The contact author has declared that neither they nor their co-authors have any competing interests.

Disclaimer. Publisher's note: Copernicus Publications remains neutral with regard to jurisdictional claims in published maps and institutional affiliations.

Acknowledgements. The authors thank Tiphaine Larvet for computing seismic velocity with PerpleX.

Financial support. This research has been supported by the Centre National de la Recherche Scientifique (IRN trigger).

Review statement. This paper was edited by Patrice Rey and reviewed by Guillaume Duclaux and one anonymous referee.

References

Barnes, P. M. and Nicol, A.: Formation of an active thrust triangle zone associated with structural inversion in a subduction setting, eastern New Zealand, Tectonics, 23, TC1015, https://doi.org/10.1029/2002TC001449, 2004.

Beaumont, C., Fullsack, P., and Hamilton, J.: Erosional control of active compressional orogens, in: Thrust tectonics, edited by: McClay, K. R., 1–18, Chapman and Hall, New York, Springer, Dordrecht, https://doi.org/10.1007/978-94-011-3066-0_1, 1992.

Bekins, B., McCaffrey, A. M., and Dreiss, S. J.: Influence of kinetics on the smectite to illite transition in the Barbados accretionary prism, J. Geophys. Res.-Sol. Ea., 99, 18147–18158, 1994.

Bonnet, C., Malavieille, J., and Mosar, J.: Interactions between tectonics, erosion, and sedimentation during the recent evolution of the Alpine orogen: Analogue modeling insights, Tectonics, 26, TC6016, https://doi.org/10.1029/2006TC002048, 2007.

Borderie, S., Graveleau, F., Witt, C., and Vendeville, B. C.: Impact of an interbedded viscous décollement on the structural and kinematic coupling in fold-and-thrust belts: Insights from analogue modeling, Tectonophysics, 722, 118–137, 2018.

Braun, J. and Yamato, P.: Structural evolution of a three-dimensional, finite-width crustal wedge, Tectonophysics, 484, 181–192, 2010.

Buiter, S. J., Schreurs, G., Albertz, M., Gerya, T. V., Kaus, B., Landry, W., Le Pourhiet, L., Mishin, Y., Egholm, D. L., Cooke, M., Maillot B., Thieulot, C., Crook, T., May, D., Souloumiac, P., and Beaumont, C.: Benchmarking numerical models of brittle thrust wedges, J. Struct. Geol., 92, 140–177, 2016.

Burbidge, D. R. and Braun, J.: Numerical models of the evolution of accretionary wedges and fold-and-thrust belts using the distinct-element method, Geophys. J. Int., 148, 542–561, 2002.

Byerlee, J.: Friction of rocks, in: Rock friction and earthquake prediction, 615–626, Springer, 1978.

Chauhan, A. P., Singh, S. C., Hananto, N. D., Carton, H., Klingelhoefer, F., Dessa, J.-X., Permana, H., White, N., Graindorge, D., and SumatraOBS Scientific Team: Seismic imaging of forearc backthrusts at northern Sumatra subduction zone, Geophys. J. Int., 179, 1772–1780, 2009.

Chen, C.-T., Chan, Y.-C., Lo, C.-H., Malavieille, J., Lu, C.-Y., Tang, J.-T., and Lee, Y.-H.: Basal accretion, a major mechanism for mountain building in Taiwan revealed in rock thermal history, J. Asian Earth Sci., 152, 80–90, 2018.

Chlieh, M., Avouac, J.-P., Sieh, K., Natawidjaja, D. H., and Galetzka, J.: Heterogeneous coupling of the Sumatran megathrust constrained by geodetic and paleogeodetic measurements, J. Geophys. Res.-Sol. Ea., 113, B05305, https://doi.org/10.1029/2007JB004981, 2008.

Colletta, B., Letouzey, J., Pinedo, R., Ballard, J. F., and Balé, P.: Computerized X-ray tomography analysis of sandbox models: Examples of thin-skinned thrust systems, Geology, 19, 1063–1067, 1991.

Costa, E. and Vendeville, B.: Experimental insights on the geometry and kinematics of fold-and-thrust belts above weak, viscous evaporitic décollement, J. Struct. Geol., 24, 1729–1739, 2002.

Cubas, N., Leroy, Y., and Maillot, B.: Prediction of thrusting sequences in accretionary wedges, J. Geophys. Res.-Sol. Ea., 113, B12412, https://doi.org/10.1029/2008JB005717, 2008.

Cubas, N., Avouac, J.-P., Souloumiac, P., and Leroy, Y.: Megathrust friction determined from mechanical analysis of the forearc in the Maule earthquake area, Earth Planet. Sc. Lett., 381, 92–103, 2013.

Dahlen, F., Suppe, J., and Davis, D.: Mechanics of fold-and-thrust belts and accretionary wedges: Cohesive Coulomb theory, J. Geophys. Res.-Sol. Ea., 89, 10087–10101, 1984.

Davis, D., Suppe, J., and Dahlen, F.: Mechanics of fold-and-thrust belts and accretionary wedges, J. Geophys. Res.-Sol. Ea., 88, 1153–1172, 1983.

Fillon, C., Huismans, R. S., and van der Beek, P.: Syntectonic sedimentation effects on the growth of fold-and-thrust belts, Geology, 41, 83–86, 2013.

Fuller, C., Willett, S., Fisher, D., and Lu, C.: A thermomechanical wedge model of Taiwan constrained by fission-track thermochronometry, Tectonophysics, 425, 1–24, 2006.

Gao, X. and Wang, K.: Strength of stick-slip and creeping subduction megathrusts from heat flow observations, Science, 345, 1038–1041, 2014.

Graveleau, F., Malavieille, J., and Dominguez, S.: Experimental modelling of orogenic wedges: A review, Tectonophysics, 538, 1–66, 2012.

Hyndman, R., Wang, K., and Yamano, M.: Thermal constraints on the seismogenic portion of the southwestern Japan subduction thrust, J. Geophys. Res.-Sol. Ea., 100, 15373–15392, 1995.

Jeffreys, H.: The Thermal Effects of Blanketing by Sediments, Geophys. J. Int., 2, 323–329, 1931.

Jourdon, A., Le Pourhiet, L., Petit, C., and Rolland, Y.: Impact of range-parallel sediment transport on 2D thermo-mechanical models of mountain belts: Application to the Kyrgyz Tien Shan, Terra Nova, 30, 279–288, 2018.

Lachenbruch, A. H. and Sass, J.: Heat flow and energetics of the San Andreas fault zone, J. Geophys. Res.-Sol. Ea., 85, 6185–6222, 1980.

Laigle, M., Becel, A., De Voogd, B., Sachpazi, M., Bayrakci, G., Lebrun, J.-F., Evain, M., Daignières, M., Gailler, A., Gesret, A., Hirn, A., Klaeschen, D., Kopp, H., Marthelot, J.-M., Mazabraux, Y., Roux, E., and Weinzierl, W.: Along-arc segmentation and interaction of subducting ridges with the Lesser Antilles Subduction forearc crust revealed by MCS imaging, Tectonophysics, 603, 32–54, 2013.

Lanson, B., Sakharov, B. A., Claret, F., and Drits, V. A.: Diagenetic smectite-to-illite transition in clay-rich sediments: A reappraisal of X-ray diffraction results using the multi-specimen method, Am. J. Sci., 309, 476–516, 2009.

Lo, C.-H. and Onstott, T. C.: Rejuvenation of KAr systems for minerals in the Taiwan Mountain Belt, Earth Planet. Sc. Lett., 131, 71–98, 1995.

Mary, B. C., Maillot, B., and Leroy, Y. M.: Predicting orogenic wedge styles as a function of analogue erosion law and material softening, Geochem. Geophy. Geosy., 14, 4523–4543, 2013.

Mase, C. W. and Smith, L.: Pore-fluid pressures and frictional heating on a fault surface, Pure Appl. Geophys., 122, 583–607, 1984.

Mase, C. W. and Smith, L.: Effects of frictional heating on the thermal, hydrologic, and mechanical response of a fault, J. Geophys. Res.-Sol. Ea., 92, 6249–6272, 1987.

May, D. A. and Le Pourhiet, L.: pTatin2d (https://bitbucket.org/ptatin/ptatin2d/commits/991118fb4cdae93cf75859a9b1b96ba43e9bc999?at=restart, last access: 8 June 2021), Zenodo [code, data set], https://doi.org/10.5281/zenodo.4911354, 2021.

May, D. A., Brown, J., and Le Pourhiet, L.: pTatin3D: High-performance methods for long-term lithospheric dynamics, in: SC'14: Proceedings of the International Conference for High Performance Computing, Networking, Storage and Analysis, 274–284, IEEE, 2014.

May, D. A., Brown, J., and Le Pourhiet, L.: A scalable, matrix-free multigrid preconditioner for finite element discretizations of heterogeneous Stokes flow, Comput. Method. Appl. M., 290, 496–523, 2015.

Miyakawa, A., Yamada, Y., and Matsuoka, T.: Effect of increased shear stress along a plate boundary fault on the formation of an out-of-sequence thrust and a break in surface slope within an accretionary wedge, based on numerical simulations, Tectonophysics, 484, 127–138, 2010.

Moore, J. C. and Saffer, D.: Updip limit of the seismogenic zone beneath the accretionary prism of southwest Japan: An effect of diagenetic to low-grade metamorphic processes and increasing effective stress, Geology, 29, 183–186, 2001.

Morrow, C., Shi, L., and Byerlee, J.: Strain hardening and strength of clay-rich fault gouges, J. Geophys. Res.-Sol. Ea., 87, 6771–6780, 1982.

Nieuwland, D., Leutscher, J., and Gast, J.: Wedge equilibrium in fold-and-thrust belts: prediction of out-of-sequence thrusting based on sandbox experiments and natural examples, Neth. J. Geosci., 79, 81–91, 2000.

Noda, A.: Forearc basins: Types, geometries, and relationships to subduction zone dynamics, Bulletin, 128, 879–895, 2016.

Oleskevich, D., Hyndman, R., and Wang, K.: The updip and downdip limits to great subduction earthquakes: Thermal and structural models of Cascadia, south Alaska, SW Japan, and Chile, J. Geophys. Res.-Sol. Ea., 104, 14965–14991, 1999.

Pajang, S., Cubas, N., Letouzey, J., Le Pourhiet, L., Seyedali, S., Fournier, M., Agard, P., Khatib, M. M., Heyhat, M., and Mokhtari, M.: Seismic hazard of the western Makran subduction zone: insight from mechanical modelling and inferred frictional properties, Earth Planet. Sc. Lett., 562, 116789, https://doi.org/10.1016/j.epsl.2021.116789, 2021a.

Pajang, S., Le Pourhiet, L., and Cubas, N.: The topographic signature of temperature controlled rheological transitions in accretionary prism, Zenodo [video], https://doi.org/10.5281/zenodo.5599365, 2021b.

Perfettini, H., Avouac, J.-P., Tavera, H., Kositsky, A., Nocquet, J.-M., Bondoux, F., Chlieh, M., Sladen, A., Audin, L., Farber, D. L., and Soler, P.: Seismic and aseismic slip on the Central Peru megathrust, Nature, 465, 78–81, 2010.

Perron, P., Le Pourhiet, L., Guiraud, M., Vennin, E., Moretti, I., Portier, É., and Konaté, M.: Control of inherited accreted lithospheric heterogeneity on the architecture and the low, long-term subsidence rate of intracratonic basins, BSGF-Earth Sciences Bulletin, 192, 15, https://doi.org/10.1051/bsgf/2020038, 2021.

Pichot, T. and Nalpas, T.: Influence of synkinematic sedimentation in a thrust system with two decollement levels; analogue modelling, Tectonophysics, 473, 466–475, 2009.

Pytte, A. and Reynolds, R.: The thermal transformation of smectite to illite, in: Thermal History of Sedimentary Basins, edited by: Naeser, N. D. and McCulloh, T. H., Springer, 133–140, https://doi.org/10.1007/978-1-4612-3492-0_8, 1988.

Raimbourg, H., Augier, R., Famin, V., Gadenne, L., Palazzin, G., Yamaguchi, A., and Kimura, G.: Long-term evolution of an accretionary prism: The case study of the Shimanto Belt, Kyushu, Japan, Tectonics, 33, 936–959, 2014.

Ranalli, G. and Murphy, D. C.: Rheological stratification of the lithosphere, Tectonophysics, 132, 281–295, 1987.

Ruh, J. B.: Submarine landslides caused by seamounts entering accretionary wedge systems, Terra Nova, 28, 163–170, 2016.

Ruh, J. B.: Numerical modeling of tectonic underplating in accretionary wedge systems, Geosphere, 16, 1385–1407, 2020.

Ruh, J. B., Kaus, B. J., and Burg, J.-P.: Numerical investigation of deformation mechanics in fold-and-thrust belts: Influence of rheology of single and multiple décollements, Tectonics, 31, TC3005, https://doi.org/10.1029/2011TC003047, 2012.

Ruh, J. B., Gerya, T., and Burg, J.-P.: High-resolution 3D numerical modeling of thrust wedges: Influence of décollement strength on transfer zones, Geochem. Geophy. Geosy., 14, 1131–1155, 2013.

Ruh, J. B., Gerya, T., and Burg, J.-P.: 3D effects of strain vs. velocity weakening on deformation patterns in accretionary wedges, Tectonophysics, 615, 122–141, 2014.

Ruh, J. B., Sallarès, V., Ranero, C. R., and Gerya, T.: Crustal deformation dynamics and stress evolution during seamount subduction: High-resolution 3-D numerical modeling, J. Geophys. Res.-Sol. Ea., 121, 6880–6902, 2016.

Saffer, D. M. and Marone, C.: Comparison of smectite-and illite-rich gouge frictional properties: application to the updip limit of the seismogenic zone along subduction megathrusts, Earth Planet. Sc. Lett., 215, 219–235, 2003.

Segall, P. and Rice, J. R.: Does shear heating of pore fluid contribute to earthquake nucleation?, J. Geophys. Res.-Sol. Ea., 111, B09316, https://doi.org/10.1029/2005JB004129, 2006.

Shea, W. T. and Kronenberg, A. K.: Rheology and deformation mechanisms of an isotropic mica schist, J. Geophys. Res.-Sol. Ea., 97, 15201–15237, 1992.

Sibson, R.: Interactions between temperature and pore-fluid pressure during earthquake faulting and a mechanism for partial or total stress relief, Nature Physical Science, 243, 66–68, 1973.

Silver, E. A. and Reed, D. L.: Backthrusting in accretionary wedges, J. Geophys. Res.-Sol. Ea., 93, 3116–3126, 1988.

Simpson, G.: Mechanics of non-critical fold–thrust belts based on finite element models, Tectonophysics, 499, 142–155, 2011.

Simpson, G.: Modelling interactions between fold–thrust belt deformation, foreland flexure and surface mass transport, Basin Res., 18, 125–143, 2006.

Simpson, M. J., Landman, K. A., and Hughes, B. D.: Cell invasion with proliferation mechanisms motivated by time-lapse data, Physica A, 389, 3779–3790, 2010.

Singh, S. C., Hananto, N. D., Chauhan, A. P., Permana, H., Denolle, M., Hendriyana, A., and Natawidjaja, D.: Evidence of active backthrusting at the NE Margin of Mentawai Islands, SW Sumatra, Geophys. J. Int., 180, 703–714, 2010.

Singh, S. C., Hananto, N., Mukti, M., Robinson, D. P., Das, S., Chauhan, A., Carton, H., Gratacos, B., Midnet, S., Djajadihardja, Y., and Harjono, H.: Aseismic zone and earthquake segmentation associated with a deep subducted seamount in Sumatra, Nat. Geosci., 4, 308–311, 2011.

Smit, J., Brun, J., and Sokoutis, D.: Deformation of brittle-ductile thrust wedges in experiments and nature, J. Geophys. Res.-Sol. Ea., 108, 2480, https://doi.org/10.1029/2002JB002190, 2003.

Song, T.-R. A. and Simons, M.: Large trench-parallel gravity variations predict seismogenic behavior in subduction zones, Science, 301, 630–633, 2003.

Stockmal, G. S., Beaumont, C., Nguyen, M., Lee, B., and Sears, J.: Mechanics of thin-skinned fold-and-thrust belts: Insights from numerical models, Geol. S. Am. S., 433, 63, https://doi.org/10.1130/2007.2433(04), 2007.

Storti, F. and McClay, K.: Influence of syntectonic sedimentation on thrust wedges in analogue models, Geology, 23, 999–1002, 1995.

Strayer, L. M., Hudleston, P. J., and Lorig, L. J.: A numerical model of deformation and fluid-flow in an evolving thrust wedge, Tectonophysics, 335, 121–145, 2001.

Suppe, J.: Mechanics of mountain building and metamorphism in Taiwan, Mem. Geol. Soc. China, 4, 67–89, 1981.

Terzaghi, K.: Erdbaumechanik auf bodenphysikalischer Grundlage, Leipzig u. Wien, Franz Deuticke, 399 pp., 1925.

Verati, C., Lardeaux, J.-M., Favier, A., Corsini, M., Philippon, M., and Legendre, L.: Arc-related metamorphism in the Guadeloupe archipelago (Lesser Antilles active island arc): First report and consequences, Lithos, 320, 592–598, 2018.

Vrolijk, P.: On the mechanical role of smectite in subduction zones, Geology, 18, 703–707, 1990.

Wangen, M.: The blanketing effect in sedimentary basins, Basin Res., 7, 283–298, 1994.

Wells, R. E., Blakely, R. J., Sugiyama, Y., Scholl, D. W., and Dinterman, P. A.: Basin-centered asperities in great subduction zone earthquakes: A link between slip, subsidence, and subduction erosion?, J. Geophys. Res.-Sol. Ea., 108, 2507, https://doi.org/10.1029/2002JB002072, 2003.

Willett, S. D.: Rheological dependence of extension in wedge models of convergent orogens, Tectonophysics, 305, 419–435, 1999.

Willett, S. D. and Brandon, M. T.: On steady states in mountain belts, Geology, 30, 175–178, 2002.

THE GEOLOGICAL SOCIETY OF AMERICA®

Relationship link between landward vergence in accretionary prisms and tsunami generation

Nadaya Cubas[1,2], Pauline Souloumiac[3], and Satish C. Singh[2]
[1]ISTeP (Institut des Sciences de la Terre de Paris), Université Pierre et Marie Curie, 4 place Jussieu, 75005 Paris, France
[2]Marine Geosciences Laboratory, Institut de Physique du Globe, 1 rue Jussieu, 75005 Paris, France
[3]Département Géosciences et Environnement, Université de Cergy-Pontoise, Neuville-sur-Oise, 5 mail Gay Lussac, 95031 Cergy-Pontoise cedex, France

ABSTRACT

The very large slip up to the subduction front of the 2011 Tohoku-Oki (Japan) earthquake has challenged our classic view of the megathrust undergoing only aseismic slip at shallow depth. Furthermore, the enhancement of tsunamis during frontal rupturing has increased concern about tsunami risks. Recent seismic reflection images from the Sumatra subduction zone show frontal landward-vergent thrusts in the accretionary prism in the area of supposed shallow ruptures and enhanced tsunamis. Using mechanical analysis, we here show that sudden and successive decreases of the effective friction along the megathrust are required to form landward-vergent frontal thrusts. These decreases are most likely caused by dynamic weakening mechanisms, such as thermal pressurization of the pore fluids related to the propagation of earthquakes to the seafloor. Therefore, landward vergence in accretionary prisms is indicative of past seafloor frontal ruptures and consequent tsunamis. The presence of landward-verging structures in the Cascadia and Sumatra accretionary prisms might indicate future frontal rupture of the shallowest portion of the megathrust, resulting in large tsunamis.

INTRODUCTION

The Tohoku-Oki (Japan) earthquake produced a devastating tsunami because of the shallow propagation of the rupture. This earthquake surprised the earth science community because the upper portion of the megathrust was commonly thought to slip aseismically (Scholz, 1998) and because interseismic strain accumulation models were showing creep at shallow depth (Loveless and Meade, 2011). However, the shallow creep was essentially due to the assumed initial conditions and the inability to resolve, on onshore geodetic data, megathrust behavior near the trench (Loveless and Meade, 2011). From the Tohoku-Oki event, we have also learned that shallow megathrusts have the potential to creep at a slow slip rate and to have very large coseismic slip due to efficient weakening by thermal pressurization of pore fluids (Noda and Lapusta, 2013). As a consequence, assessing the potential for shallow propagation of earthquakes along subduction zones worldwide has become a new challenge.

Recent seismic reflection studies have indicated a possible correlation between landward-vergent thrusts and shallow propagation of earthquakes along the Sumatra subduction zone (Gulick et al., 2011; Moeremans et al., 2014). Several landward-vergent thrusts are observed at the front of the accretionary wedge where the 2004 M_w 9.2 Sumatra-Andaman earthquake seems to have reached the seafloor (Chlieh et al., 2007; Singh et al., 2008; Gulick et al., 2011) (Figs. 1A and 1C). Furthermore, the shallow 2010 M_w 7.8 Mentawai Islands (Sumatra) tsunami earthquake (Lay et al., 2011) also occurred in the frontal landward-vergent accretionary prism region (Moeremans et al., 2014) (Figs. DR2a and DR2b in the GSA Data Repository[1]). Both of these events produced large tsunamis. The seismic gap along the Sumatra subduction zone also shows frontal landward-vergent structures (Kuncoro et al., 2015; Cook et al., 2014). In this region, the 1797 M_w ~8.7 event generated a very large tsunami with run-up heights of ~10 m in Padang (Newcomb and McCann, 1987), suggesting that the locked patch offshore Sumatra (Konca et al., 2008) could produce a large tsunami. No landward-vergent thrusts have been reported along the Nias segment where the 2005 M_w 8.7 earthquake was limited to the deep seismogenic zone (Cook et al., 2014; Konca et al., 2008).

Normal sequences of landward-vergent thrusts have also been reported along the Cascadia subduction zone offshore the Oregon-Washington (USA) margin (Figs. 1B–1D) (MacKay, 1995; Adam et al., 2004) and north of the Mendocino triple junction (Fig. 1D) (Gulick et al., 1998). This subduction zone is also known to generate M_w ~9 earthquakes every 300–500 yr with consequent tsunamis across the Pacific (Satake et al., 1996; Atwater and Griggs, 2012). In this region, the extent of the landward vergence in accretionary prism matches well with the location of high slip patches of the 1700 earthquake (Wang et al., 2013; Fig. 1D). Therefore, understanding the mechanical requirements for landward vergence and the possible link with frontal propagation of earthquakes is of fundamental importance for seismic and tsunamigenic risk assessment for Sumatra and Cascadia.

To date, the most recurrent explanation for landward vergence has been a low megathrust friction due to high pore pressure along the megathrust (Seely, 1977; MacKay, 1995; Adam et al., 2004; Moeremans et al., 2014). This hypothesis is mainly based on the observed low taper (MacKay, 1995; Gulick et al., 1998), the presence of a high amplitude–negative polarity (HA-NP) reflector above the oceanic basement in northern Cascadia (Cochrane et al., 1994) and Sumatra (Dean et al., 2010; Gulick et al., 2011; Moeremans et al., 2014), and comparison with sandbox experiments done at very low basal friction showing conjugate thrust systems with mixed vergence (Seely, 1977). Clear landward vergence in analogue models was only obtained with a viscous basal layer (Gutscher et al., 2001) or with strong lateral wall effects standing for lateral strike-slip faults (Zhou et al., 2015). However, the deformation style of the Cascadia megathrust is not in good accordance with a viscoelastic behavior (Adam et al., 2004) and strike-slip faults are not systematically observed. The high basal pore pressure has been linked to the compaction of a large amount of sediments (Moeremans et al., 2014; Adam et al., 2004). However, some accretionary prisms displaying both very large sediment thickness (>4 km) and high pore pressure, such as Barbados (Bangs et al., 1990) or Makran (Pakistan) (Kukowski et al., 2001), did not develop landward-vergent thrusts. On the contrary, a thin sedimentary layer (1.5 km) in the Mentawai segment contains landward-vergent

[1]GSA Data Repository item 2016258, methods, Figure DR1 (modeling stages), and Figure DR2 (landward vergence and frictional properties of the Mentawai Islands segment, Southern Sumatra), is available online at www.geosociety.org/pubs/ft2016.htm, or on request from editing@geosociety.org.

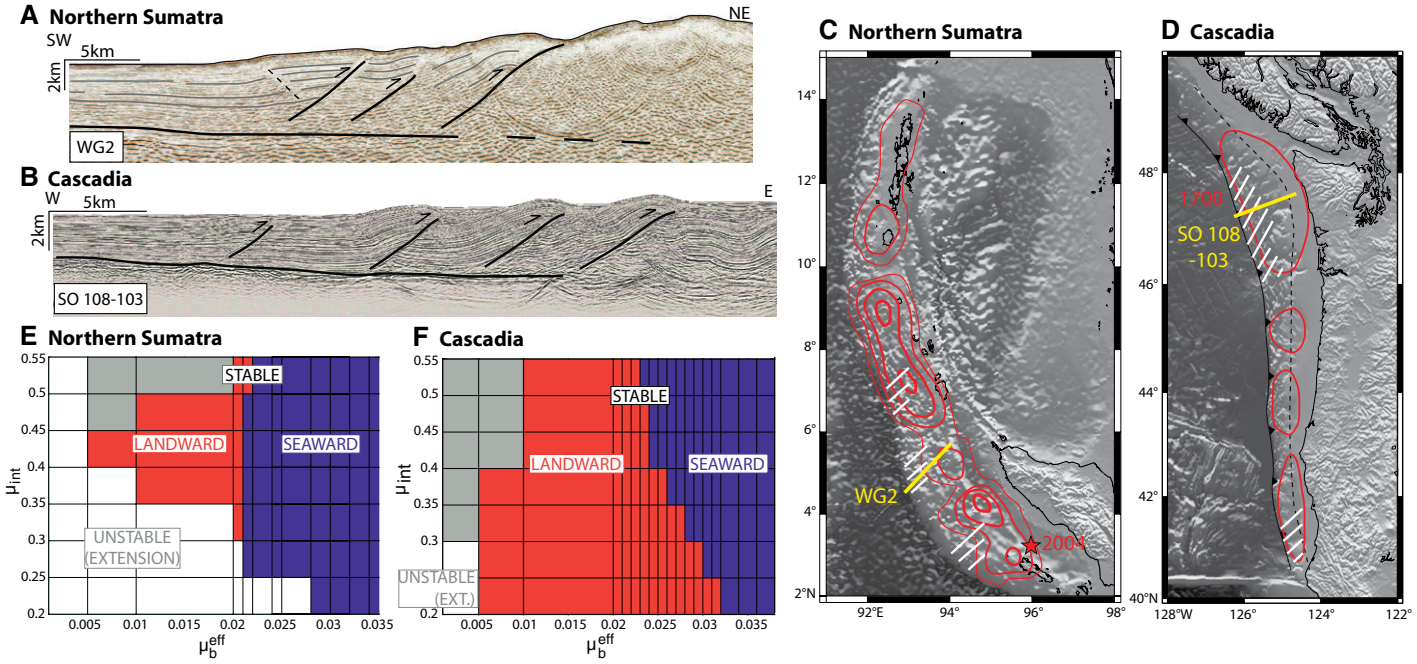

Figure 1. Landward-vergent accretionary prisms and frictional properties. A: Seismic profile WG2 in northern Sumatra (Moeremans et al., 2014). B: Seismic profile SO 108–03 in Cascadia (Adam et al., 2004). C: Comparison of the observed landward-vergent thrusts in northern Sumatra (hachured white lines; compilation from Dean et al., 2010; Gulick et al., 2011; Moeremans et al., 2014) with coseismic slip of the 2004 M_w 9.1 Sumatra-Andaman earthquake (slip contours in red every 5 m increment; Chlieh et al., 2007). D: Comparison of the observed landward-vergent thrusts in Cascadia (hachured white lines; compilation from MacKay, 1995, Gulick et al., 1998; Adam et al., 2004) with the estimated slip contours of the 1700 Cascadia earthquake considering a trench-breaking rupture scenario with a M_w 8.9 (Wang et al., 2013); the downdip end of the highly locked zone is shown by the black dotted line (Wang et al., 2013). E, F: Vergence is shown as a function of the internal friction (μ_{int}) and the megathrust effective friction (μ_b^{eff}) for northern Sumatra and Cascadia. In the studied frictional range, the prism can either be at stable state (the full megathrust is activated as well as a frontal thrust) or at extensional unstable state (white domain, corresponding to a gravitational collapse). At stable state, the frontal thrust can either be landward (red domain) or seaward (blue domain) vergent. The gray domain stands for the propagation of the deformation toward the tip of the wedge.

structures (Moeremans et al., 2014; Cook et al., 2014; Kuncoro et al., 2015) (Fig. DR2a). Therefore, high pore pressure and large sediment thickness might be important ingredients but not sufficient to control the vergence of thrusts. Here we investigate if landward-vergent thrust faults could result from specific frictional properties.

METHODS

We apply the two-dimensional mechanical model named Sequential Limit Analysis Method for Tectonics (SLAMTec; Mary et al., 2013) that allows predicting faults and their evolution in accretionary wedges. The method, accounting for mechanical equilibrium and based on the Coulomb criterion, is composed of two major steps (for a complete description, see the Data Repository). The first stage consists in computing the pushing tectonic force associated with any possible set of faults in the wedge. The fault system leading to the lowest tectonic pushing force is selected as the optimum. The second stage consists of a rigid translation along the predicted faults. In that stage, we compare the force that would require a translation along a landward-vergent thrust fault with the force required by a seaward-vergent thrust fault. We select the one leading to the lowest force. The location and evolution of faults are thus predicted from the frictional properties of the wedge ($\mu_{int} = \tan \phi_{int}$), the megathrust ($\mu_b = \tan \phi_b$), and the thrust faults ($\mu_f = \tan \phi_f$).

RESULTS

We first explore the role of the topographic slope (α) and the slab dip (β) on the vergence with a simple triangular wedge followed by a flat layer of sediments beyond the deformation front. The results are plotted in the α versus β envelope to compare with the mechanical states defined by the critical taper theory (Davis et al., 1983; Dahlen, 1984) (Figs. 2A and 2B). For a dry wedge, with megathrust frictions from μ_b 0.25 to 0.05, we find that landward vergence develops for large slab dips and is favored by very low basal frictions. The topographic slope only has a minor influence, in particular for the typical range of observed slab dip and topographic slope (gray box in Fig. 2B). Along the accretionary prism, because the maximum compressional principal stress plunges seaward (Hafner, 1951), landward-vergent thrusts always have larger dips than seaward-vergent thrusts. As a consequence, uplifting material above a seaward-vergent thrust requires less gravitational energy than along a landward-vergent thrust. For negligible basal shear stress and a strong wedge, conjugate faults tend to have the same dip, and both can be active in forming pop-up structures (Hafner, 1951). However, when the seaward-vergent thrust is the active fault, some additional material coming from the tip of the wedge also needs to be uplifted, whereas the landward-verging kinematics requires uplifting only the frontal horizontal pack of sediments (Figs. DR1b and DR1c). For very low basal friction, the frictional force decreases compared to the gravitational force. Therefore, for a large slab dip, the increase of the gravitational force due to the additional material coming from the tip of the wedge becomes important and allows for the jump from seaward to landward vergence (Fig. 2B).

We also investigate the effect of the frictional properties on the vergence (Fig. 2C). We set $\alpha = \beta = 5°$ to be consistent with a real case scenario. We vary the internal friction and the megathrust friction that we consider as effective to take into account the megathrust pore pressure effect. We find that, in addition to the very low megathrust effective friction ($\mu_b^{eff} \leq 0.04$), landward vergence is favored by a low strength ratio between the megathrust and the wedge. Moreover, the landward vergence develops in the upper part of the stable domain of the α-β plot (or in the left part of the friction graph) close to the extensional critical limit.

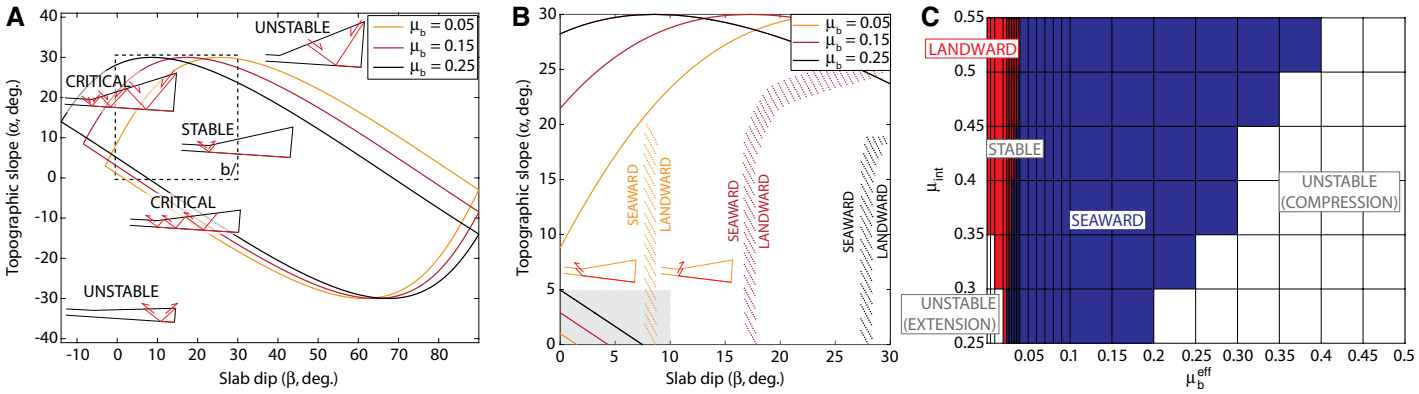

Figure 2. Thrust vergence compared with critical taper envelops. A: Mechanical states of a wedge defined by the critical taper theory (Davis et al., 1983, Dahlen, 1984). B: Transitions from landward to seaward vergence for three different megathrust frictions with a standard internal friction μ_{int} = 0.57. Gray rectangles: typical range of topographic slope α and slab dip β for accretionary prisms. Landward vergence develops in the stable domain. C: Kinematics as a function of internal friction (μ_{int}) and effective basal friction (μ_b^{eff}) for α = β = 5°. Landward vergence develops close the extensional critical limit.

We now consider three accretionary prisms characterized by different sediment thickness: northern Sumatra (4.5 km), southern Sumatra (1.5 km), and Cascadia (2–3 km); we take into account the real topography and assume a single slab dip for the megathrust (β = 2.1°, 5.8°, and 1.1°, respectively). For the Cascadia example, landward vergence is obtained for effective megathrust friction lower than 0.032 (Fig. 1F). For high internal friction, a landward thrust fault tends to appear seaward of the incipient fault. For the northern Sumatra case, the range of internal and basal frictions allowing for landward-vergent fault is very narrow, and the effective megathrust friction has to be ≤0.02 (Fig. 1E). The range of frictional parameters for southern Sumatra (Fig. DR2c) is larger, although the effective megathrust friction is still low ($\mu_b^{eff} \leq 0.13$). The larger range is probably due to the high topographic slope and slab dip and the triangular shape of the sedimentary pile at the front of the wedge.

DISCUSSION

The very low effective friction necessary to develop landward-vergent thrusts could be due to long-term pore pressure or dynamic weakening mechanisms such as thermal pressurization of pore fluids (Di Toro et al., 2011). In the long-term pore pressure case, deformation would thus be aseismic and take place during the interseismic and/or postseismic period. In the dynamic case, the high pore pressure would be related to the shallow propagation of earthquake. Deformation would then take place during the coseismic or very early postseismic period. From these mechanical results, it is clear that landward vergence develops for tapers far from the compressional critical limit. However, a wedge will always tend to stay close to the compressional critical state, because it requires a lower tectonic pushing force. Only two conditions can lead a wedge to move away from this limit: (1) a very high sedimentation rate impeding the wedge to recover the compressional critical state (Fig. 3A), or (2) sudden and successive decreases of the effective megathrust friction (Fig. 3B).

However, in the typical range of topographic slope and slab dip of an accretionary prism, we have shown that an increase of the topographic slope does not imply a change in the vergence; landward vergence is favored by large differences of pore pressure between the sedimentary pile and the megathrust, and no high sedimentation rates have been reported for the southern Cascadia (MacKay, 1995) and the Sumatra margins. As a consequence, we favor the dynamic hypothesis.

Therefore, the deformation style of accretionary prisms could provide strong insights on past seafloor ruptures and the tsunamigenic potential of subduction zones (Fig. 3C). Accretionary prisms with seaward-vergent faults (c1 in Fig. 3C), close to critical state and characterized by megathrust frictions >0.1, such as that for central Chile, are probably only deformed aseismically (Gao and Wang, 2014; Cubas et al., 2013b). No conclusion can be drawn for seaward-vergent prisms at stable state with very low effective friction. However, accretionary prisms showing two styles of deformation, seaward- and landward-vergent thrusts (c2) such as southern Sumatra or thrust and normal faults (c3) as the Tohoku-Oki prism, could undergo both aseismic and seismic slip. At a slow slip rate, the wedge is at compressional critical state, characterized

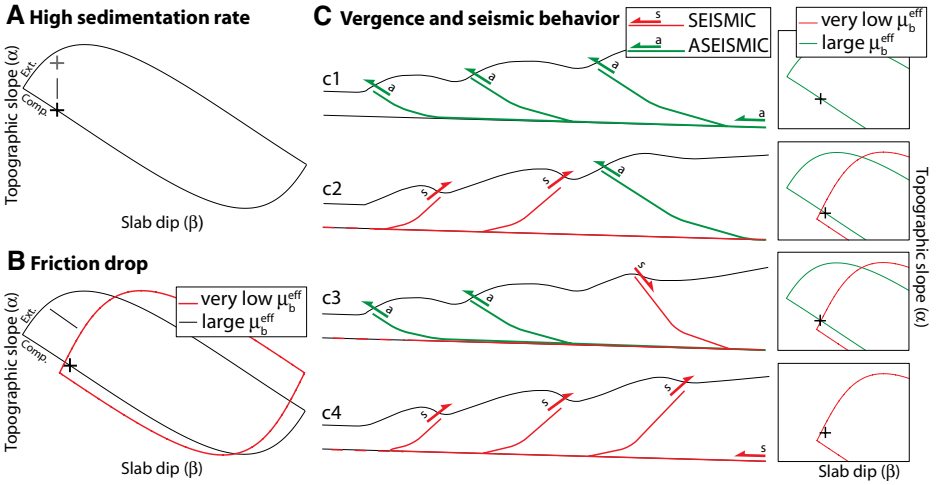

Figure 3. Mechanical explanations for landward vergence in accretionary prisms. A: A strong sedimentation rate can increase the topographic slope, transferring the prism from the compressional (comp) critical state (black cross) to the landward domain (gray cross). ext.—extension. B: A sudden decrease of the effective megathrust friction can bring the prism (black cross) from the compressional critical state associated with a relatively high megathrust effective friction to the stable landward domain of a low effective megathrust friction envelope (μ_b^{eff}—effective basal friction). C: Relations between thrusting, normal faulting, and vergence with the seismic behavior. Seaward-vergent thrust faults of a prism at compressional critical state are expected to be aseismic. Landward-vergent thrust faults and normal faults can be related to a dynamic decrease of the effective megathrust friction.

by friction >0.1, but during frontal propagation of an earthquake, the dynamic decrease of the effective friction would displace the wedge either in the landward domain or at the extensional critical limit, as inferred for the Tohoku-Oki prism (Cubas et al., 2013a). Accretionary prisms with only landward-vergent thrusts such as Cascadia and some portions of Sumatra (c4) are probably mainly deformed during or shortly after the frontal propagation of earthquakes.

As shown by the Tohoku-Oki earthquake, tsunami assessment is currently strongly limited by the fact that geodetic models based on onshore GPS stations cannot resolve the slip behavior near the trench. Here we have shown that the deformation of accretionary prisms can help us apprehend seismic and tsunami risks. In particular, we need to pay particular attention to the presence of frontal landward-vergent thrust faults, markers of past seafloor coseismic ruptures leading to very large tsunamis. For these areas, such as the Mentawai section of Sumatra or Cascadia, appropriate measures should be taken to mitigate these risks.

ACKNOWLEDGMENTS

We thank Bertrand Maillot and Yves Leroy for constructive discussions. This project has been funded by French National Research Agency (ANR) grant SEAFRONTTERA ANR-13-PDOC-0013–01.

REFERENCES CITED

Adam, J., Klaeschen, D., Kukowski, N., and Flueh, E., 2004, Upward delamination of Cascadia Basin sediment infill with landward frontal accretion thrusting caused by rapid glacial age material flux: Tectonics, v. 23, TC3009, doi:10.1029/2002TC001475.

Atwater, B.F., and Griggs, G.B., 2012, Deep-sea turbidites as guides to Holocene earthquake history at the Cascadia subduction zone—Alternative views for a seismic-hazard workshop: U.S. Geological Survey Open-File Report 2012-1043, 58 p.

Bangs, N.L.B., Westbrook, G.K., Ladd, J.W., and Buhl, P., 1990, Seismic velocities from the Barbados Ridge complex: Indicators of high pore fluid pressures in an accretionary complex: Journal of Geophysical Research, v. 95, p. 8767–8782, doi:10.1029/JB095iB06p08767.

Chlieh, M., et al., 2007, Coseismic slip and afterslip of the great M_w 9.15 Sumatra–Andaman earthquake of 2004: Seismological Society of America Bulletin, v. 97, p. S152–S173, doi:10.1785/0120050631.

Cochrane, G.R., MacKay, M.E., Moore, G.F., and Moore, J.C., 1994, Consolidation and deformation of sediments at the toe of the Central Oregon accretionary prism from multichannel seismic data, *in* Westbrook, G.K., et al., eds., Proceedings of the Ocean Drilling Program, Initial reports, Volume 146: College Station, Texas, Ocean Drilling Program, p. 421–426, doi:10.2973/odp.proc.ir.146-1.003.1994.

Cook, B.J., Henstock, T.J., McNeill, L.C., and Bull, J.M., 2014, Controls on spatial and temporal evolution of prism faulting and relationships to plate boundary slip offshore north-central Sumatra: Journal of Geophysical Research, v. 119, p. 5594–5612, doi:10.1002/2013JB010834.

Cubas, N., Avouac, J.P., Souloumiac, P., and Leroy, Y., 2013a, Megathrust friction determined from mechanical analysis of the forearc in the Maule earthquake area: Earth and Planetary Science Letters, v. 381, p. 92–103, doi:10.1016/j.epsl.2013.07.037.

Cubas, N., Avouac, J.P., Leroy, Y.M., and Pons, A., 2013b, Low friction along the high slip patch of the 2011 Mw 9.0 Tohoku-Oki earthquake required from the wedge structure and extensional splay faults: Geophysical Research Letters, v. 40, p. 4231–4237, doi:10.1002/grl.50682.

Dahlen, F.A., 1984, Noncohesive critical coulomb wedges: An exact solution: Journal of Geophysical Research, v. 89, p. 10,125–10,133, doi:10.1029/JB089iB12p10125.

Davis, D.M., Suppe, J., and Dahlen, F.A., 1983, Mechanics of fold-and-thrust belts and accretionary wedges: Journal of Geophysical Research, v. 88, p. 1153–1172, doi:10.1029/JB088iB02p01153.

Dean, S.M., McNeill, L.C., Henstock, T.J., Bull, J.M., Gulick, S.P.S., Austin, J.A., Jr., Bangs, N.L.B., Djajadihardja, Y.S., and Permana, H., 2010, Contrasting décollement and prism properties over the Sumatra 2004–2005 earthquake rupture boundary: Science, v. 329, p. 207–210, doi:10.1126/science.1189373.

Di Toro, G.D., Han, R., Hirose, T., Paola, N.D., Nielsen, S., Mizoguchi, K., Ferri, F., Cocco, M., and Shimamoto, T., 2011, Fault lubrication during earthquakes: Nature, v. 471, p. 494–498, doi:10.1038/nature09838.

Gao, X., and Wang, K., 2014, Strength of stick-slip and creeping subduction megathrusts from heat flow observations: Science, v. 345, p. 1038–1041, doi:10.1126/science.1255487.

Gulick, S.P.S., Meltzer, A.M., and Clarke, S.H., Jr., 1998, Seismic structure of the southern Cascadia subduction zone and accretionary prism north of the Mendocino triple junction: Journal of Geophysical Research, v. 103, p. 27,207–27,222, doi:10.1029/98JB02526.

Gulick, S.P.S., Austin, J.A., Jr., McNeill, L.C., Bangs, N.L.B., Martin, K.M., Henstock, T.J., Bull, J.M., Dean, S., Djajadihardja, Y., and Permana, H., 2011, Updip rupture of the 2004 Sumatra earthquake extended by thick indurated sediments: Nature Geoscience, v. 4, p. 453–456, doi:10.1038/ngeo1176.

Gutscher, M.A., Klaeschen, D., Flueh, E., and Malavieille, J., 2001, Non-Coulomb wedges, wrong-way thrusting, and natural hazards in Cascadia: Geology, v. 29, p. 379–382, doi:10.1130/0091-7613(2001)029<0379:NCWWWT>2.0.CO;2.

Hafner, W., 1951, Stress distributions and faulting: Seismological Society of America Bulletin, v. 62, p. 373–398, doi:10.1130/0016-7606(1951)62[373:SDAF]2.0.CO;2.

Konca, A.O., et al., 2008, Partial rupture of the locked patch of the Sumatra megathrust during the 2007 earthquake sequence: Nature, v. 456, p. 631–635, doi:10.1038/nature07572.

Kukowski, N., Schillhorn, T., Huhn, K., Von Rad, U., Husen, S., and Flueh, E.R., 2001, Morphotectonics and mechanics of the central Makran accretionary wedge off Pakistan: Marine Geology, v. 173, p. 1–19, doi:10.1016/S0025-3227(00)00167-5.

Kuncoro, A.K., Cubas, N., Singh, S.C., Etchebes, M., and Tapponnier, P., 2015, Tsunamigenic potential due to frontal rupturing in the Sumatra locked zone: Earth and Planetary Science Letters, v. 432, p. 311–322, doi:10.1016/j.epsl.2015.10.007.

Lay, T., Ammon, C.J., Kanamori, H., Yamazaki, Y., Cheung, K.F., and Hutko, A.R., 2011, The 25 October 2010 Mentawai tsunami earthquake (M_w 7.8) and the tsunami hazard presented by shallow megathrust ruptures: Geophysical Research Letters, v. 38, L06302, doi:10.1029/2010GL046552.

Loveless, J.P., and Meade, B.J., 2011, Spatial correlation of interseismic coupling and coseismic rupture extent of the 2011 M_w 9.0 Tohoku-oki earthquake: Geophysical Research Letters, v. 38, L17306, doi:10.1029/2011GL048561.

MacKay, M.E., 1995, Structural variation and landward vergence at the toe of the Oregon accretionary prism: Tectonics, v. 14, p. 1309–1320, doi:10.1029/95TC02320.

Mary, B.C.L., Maillot, B., and Leroy, Y.M., 2013, Predicting orogenic wedge styles as a function of analogue erosion law and material softening: Geochemistry, Geophysics, Geosystems, v. 14, p. 4523–4543, doi:10.1002/ggge.20262.

Moeremans, R., Singh, S.C., Mukti, M., McArdle, J., and Johansen, K., 2014, Seismic images of structural variations along the deformation front of the Andaman-Sumatra subduction zone: Implications for rupture propagation and tsunamigenesis: Earth and Planetary Science Letters, v. 386, p. 75–85, doi:10.1016/j.epsl.2013.11.003.

Newcomb, K.R., and McCann, W.R., 1987, Seismic history and seismotectonics of the Sunda Arc: Journal of Geophysical Research, v. 92, p. 421–439, doi:10.1029/JB092iB01p00421.

Noda, H., and Lapusta, N., 2013, Stable creeping fault segments can become destructive as a result of dynamic weakening: Nature, v. 493, p. 518–521, doi:10.1038/nature11703.

Satake, K., Shimazaki, K., Tsuji, Y., and Ueda, K., 1996, Time and size of a giant earthquake in Cascadia inferred from Japanese tsunami records of January 1700: Nature, v. 379, p. 246–249, doi:10.1038/379246a0.

Scholz, C.H., 1998, Earthquakes and friction laws: Nature, v. 391, p. 37–42, doi:10.1038/34097.

Seely, D.R., 1977, The significance of landward vergence and oblique structural trends on the trench inner slopes, *in* Talwanim M., and Pitman, W.C., eds., Island arcs, deep sea trenches and back-arc basins: American Geophysical Union Maurice Ewing Series Volume 1, p. 187–198, doi:10.1029/ME001p0187.

Singh, S.C., et al., 2008, Seismic evidence for broken oceanic crust in the 2004 Sumatra earthquake epicentral region: Nature Geoscience, v. 1, p. 777–781, doi:10.1038/ngeo336.

Wang, P.-L., Engelhart, S.E., Wang, K., Hawkes, A.D., Horton, B.P., Nelson, A.R., and Witter, R.C., 2013, Heterogeneous rupture in the great Cascadia earthquake of 1700 inferred from coastal subsidence estimates: Journal of Geophysical Research, v. 118, p. 2460–2473, doi:10.1002/jgrb.50101.

Zhou, J., Zhang, B., and Xu, Q., 2015, Effects of lateral friction on the structural evolution of fold-and-thrust belts: Insights from sandbox experiments with implications for the origin of landward-vergent thrust wedges in Cascadia: Geological Society of America Bulletin, v. 128, p. 669–683, doi:10.1130/B31320.1.

Manuscript received 22 April 2016
Revised manuscript received 8 July 2016
Manuscript accepted 11 July 2016

Printed in USA

Earth and Planetary Science Letters 419 (2015) 187–198

Contents lists available at ScienceDirect

Earth and Planetary Science Letters

www.elsevier.com/locate/epsl

Numerical modeling of long-term earthquake sequences on the NE Japan megathrust: Comparison with observations and implications for fault friction

Nadaya Cubas [a,*,1], Nadia Lapusta [a,b], Jean-Philippe Avouac [a], Hugo Perfettini [c]

[a] Division of Geological and Planetary Sciences, California Institute of Technology, 1200 E. California Blvd, Pasadena, CA 91125, USA
[b] Division of Engineering and Applied Science, California Institute of Technology, 1200 E. California Blvd, Pasadena, CA 91125, USA
[c] Institut de Recherche pour le Développement, ISTerre, Grenoble, France

ARTICLE INFO

Article history:
Received 20 November 2014
Received in revised form 28 February 2015
Accepted 3 March 2015
Available online 20 March 2015
Editor: P. Shearer

Keywords:
Tohoku-Oki earthquake
thermal pressurization
shallow propagation
2D dynamic simulations of earthquake cycle

ABSTRACT

We use numerical modeling to investigate fault properties that explain key features of the 2011 Mw 9.0 Tohoku-Oki earthquake as well as the overall regional behavior of the NE Japan megathrust. In particular, we study the possibility that slip near the trench resulted from thermal pressurization on a shallow patch of the megathrust, and investigate whether low-velocity friction on that patch is rate-strengthening or rate-weakening. Our models also contain a deeper rate-weakening patch, not prone to efficient thermal pressurization, to account for the moderate-sized interplate seismicity. We produce earthquake sequences and aseismic slip in our models using 2D dynamic simulations that incorporate shear-induced temperature variations and the associated change in pore fluid pressure to capture thermal pressurization. We find that all our models can reproduce more frequent deeper moderate (Mw 7.5) events and less frequent larger events with substantial slip at shallow depth, as observed along the Fukushima–Miyagi segment of the Japan megathrust. However, only the scenario with a sufficiently rate-strengthening patch can match the thousand-year recurrence time of Tohoku-Oki-like earthquakes suggested by the historical and geological record, due to co-existence of seismic and aseismic slip at the shallow depths. This scenario also reproduces other characteristics of the Tohoku-Oki earthquake: the trenchward-skewed distribution of slip, the backward re-rupture of the deeper patch, as well as the weaker radiation at high frequency of the shallower portion of the rupture in spite of its larger slip.

1. Introduction

The 2011 Mw 9.0 Tohoku-Oki earthquake produced exceptionally large shallow slip, at depth between 10 and 20 km, generating a major tsunami (Yamagiwa et al., 2015; Bletery et al., 2014; Wei et al., 2012; Ozawa et al., 2011; Ide et al., 2011; Simons et al., 2011; Ito et al., 2011) (Fig. 1a). The rupture propagated all the way to the trench, with the shallow-portion displacement of 15 to 40 m as attested from the displacement of ocean-bottom pressure gages (Ito et al., 2011) and comparison of bathymetric profiles measured in 1999 and after the earthquake in March 2011 (Fujiwara et al., 2011).

This large shallow slip is most surprising since (1) the upper portion of the megathrust is commonly thought to slip aseismically (e.g., Byrne et al., 1992; Oleskevich et al., 1999), (2) previous magnitude 7.5 earthquakes had only been instrumentally recorded along the deeper portion of the megathrust (Fig. 1b), and (3) interseismic strain accumulation models were not showing any evidence for locking of the megathrust at shallow depth (Hashimoto et al., 2009; Loveless and Meade, 2011). It should be noted, however, that the creep at shallow depth inferred from the interseismic models (Hashimoto et al., 2009; Loveless and Meade, 2011) was essentially due to the assumed initial condition and lack of resolution near the trench of the onshore geodetic data used in these inversions (Loveless and Meade, 2011).

Fig. 1a shows the co-seismic and afterslip models of Yamagiwa et al. (2015) derived from the modeling of on-shore and seafloor displacements. The co-seismic model is similar to the models obtained by other groups incorporating seismological and tsunami waveforms (e.g., Bletery et al., 2014), which all show that the rupture propagated close to the trench. The deeper patch of afterslip

* Corresponding author.
E-mail address: nadaya.cubas@upmc.fr (N. Cubas).
[1] Now at Institut des Sciences de la Terre, Université Pierre et Marie Curie, UMR 7193, 4 Place Jussieu, 75005 Paris, France.

http://dx.doi.org/10.1016/j.epsl.2015.03.002
0012-821X/

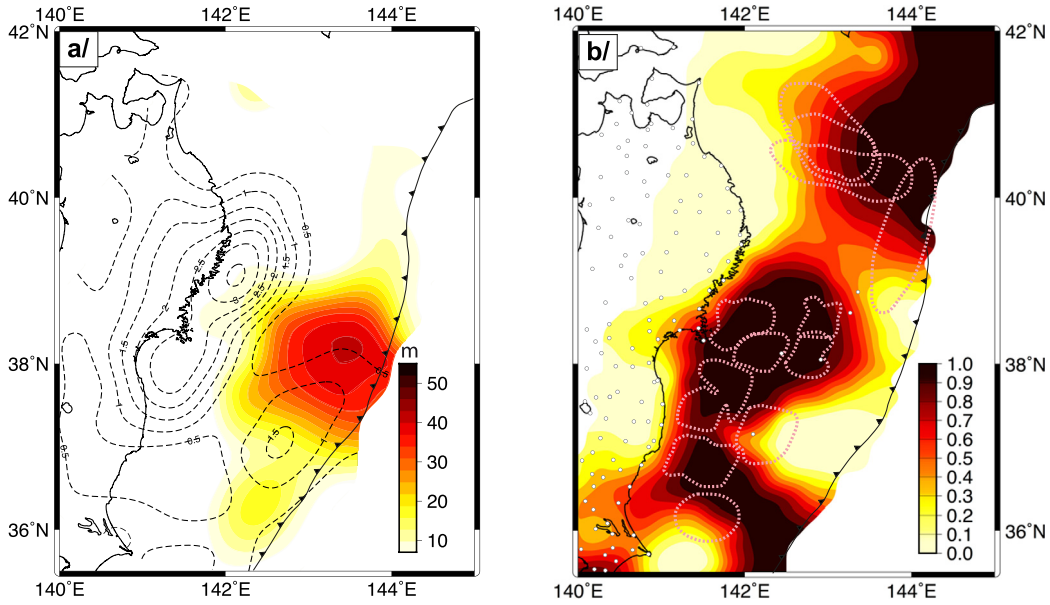

Fig. 1. (a) Coseismic (colors) and postseismic (black dashed lines) slip from Yamagiwa et al. (2015) derived from the modeling of on-shore and seafloor displacements. (b) Interseismic coupling ratio (colors) from an updated inversion of onshore and offshore geodetic measurements based on Perfettini and Avouac (2014) but including the interseismic seafloor displacements of Sato et al. (2013). Comparison of the observed and predicted displacements is given in the supplementary figure. The dotted pink contour lines show the estimated location of rupture areas of smaller (~M7.5) historical earthquakes (Yamanaka and Kikuchi, 2004; Shibazaki et al., 2011; Johnson et al., 2012). (For interpretation of the references to color in this figure legend, the reader is referred to the web version of this article.)

outlines the downdip end of the co-seismic rupture as observed by previous studies (Ozawa et al., 2012; Johnson et al., 2012; Sun et al., 2014; Hu et al., 2014). There is some degree of uncertainty regarding the exact amount of slip that occurred near the trench due to the fact that the postseismic seafloor measurements were acquired weeks after the mainshock. Eastward displacement and subsidence at station FUKU, south of the rupture area, clearly indicate shallow afterslip there. In contrast, the postseismic seafloor displacements are mostly westward above the rupture area and indicate a predominantly viscoelastic relaxation process there, over the time period covered by these measurements, from one month to three years after the mainshock (Sun et al., 2014; Watanabe et al., 2014; Hu et al., 2014). The data does not rule out the possibility of shallow afterslip but the afterslip would need to be small enough to be obscured by the viscoelastic response over this time period. As suggested by Perfettini and Avouac (2014) (see their Section 6.3 and Appendix A1), some significant shallow afterslip could have occurred over the first month. The afterslip model of Yamagiwa et al. (2015) shows both deep and shallow afterslip mostly complementary to the co-seismic rupture area. It should be noted that this afterslip model, similarly to others (e.g., Ozawa et al., 2012), assumes no slip at the trench as a boundary condition in the inversion. Shallow afterslip could be underestimated as a result of this boundary condition and of the Laplacian regularization.

An interseismic coupling model before the Tohoku-Oki event is shown in Fig. 1b. It is a revised version of the model given in Fig. 11 of Perfettini and Avouac (2014). In this revised version, the interseismic seafloor displacements of Matsumuto et al. (2008) were replaced by the more recent measurements of Sato et al. (2013). These measurements, initially given relative to the North American plate, are referenced to NE Honshu assuming the NUVEL-1A plate motion of North America relative to Eurasia and the block motion of NE Honshu relative to Eurasia of Loveless and Meade (2011). We have considered two boundary conditions: one for which back-slip is prohibited near the trench (corresponding to a creeping trench at the long term slip rate prior to the mainshock, dabbed CT in the following), and another one for which back-slip rate at the trench is unconstrained (corresponding to a partially to fully locked trench prior to the mainshock, dabbed LT in the following). The two resulting inverted models yield nearly identical coupling maps, with the corresponding reduced chi-square values being 9.82 and 9.76, respectively; the LT model is shown in Fig. 1b. The LT model matches the data slightly better than the CT model because it has more degrees of freedom. The comparison of observed and predicted displacements and residuals are shown in the supplementary material.

Therefore, the seafloor measurements as reported in Sato et al. (2013) require some amount of interseismic creep near the trench. This implies that the locked patches below are apparently not screening the interseismic loading as would be expected from the stress shadow effect (Bürgmann et al., 2005; Hetland and Simons, 2010). Note that the historical ruptures are all located in the highly coupled area, with the exception of the 1896 Sanriku tsunami earthquake (Fig. 1b). It thus seems that the shallow portion of the Japan megathrust could creep aseismically, e.g. as afterslip and interseismically, as well as accumulate substantial slip during large tsunamigenic earthquakes.

The Tohoku-Oki earthquake is remarkable in two other ways. The large shallow slip area did not radiate much seismic energy at high frequencies compared to the deeper portion of the megathrust which experienced less slip (Ide et al., 2011; Simons et al., 2011; Meng et al., 2011; Wei et al., 2012). A complex propagation was also observed, with a small initial phase of deep rupture up to 40 s, followed by extensive shallow rupture at 60–70 s, and a continuing deep rupture lasting over 100 s (Ide et al., 2011). Finally, from tsunami records (Sawai et al., 2012), the last earthquake in the area with comparable tsunami deposits occurred in AD 869 and hence the recurrence time of the Tohoku-Oki-like events is probably ~1000 years, unless the recurrence interval is quite irregular.

To reconcile these observations, Noda and Lapusta (2013) have suggested that the shallow megathrust could undergo aseismic slip at low slip rates, due to its rate-strengthening properties, as well as substantial coseismic slip due to efficient weakening by thermal pressurization of pore fluids (Sibson, 1973; Lachenbruch, 1980; Mase and Smith, 1985, 1987; Rice, 2006). From model parameters based on lab experiments (Tanikawa and Shimamoto, 2009), they were able to reproduce the larger slip of the shallow

(rate-strengthening) patch, the difference of the frequency content of seismic radiation, and the re-rupture of the deeper (rate-weakening) patch. This dual behavior, rate-strengthening at low slip rates and strong weakening at seismic slip rates, was also observed from lab experiments on wet clays characteristic of shallow megathrust, and also attributed to thermal pressurization at high slip rates (Faulkner et al., 2011). We also note that the post-earthquake temperature measurements in the shallow part of the megathrust imply a co-seismic friction coefficient of 0.08 (Fulton et al., 2013), which supports substantial co-seismic weakening during the Tohoku-Oki earthquake.

However, thermal pressurization can explain the large co-seismic slip regardless of the rate-strengthening or rate-weakening behavior of the shallow zone. Since it is uncertain that the megathrust was fully locked up to the trench before the Tohoku-Oki event (Loveless and Meade, 2011), the properties of the interface can be rate-weakening at low slip rates. This hypothesis has been considered in dynamic simulations, which attributed the large shallow slip to either enhanced weakening at high slip rate by strong slip-weakening (Shibazaki et al., 2011), or thermal pressurization (Mitsu et al., 2012), or the effect of the free surface (Kozdon and Dunham, 2013).

Determining if the observed behavior of the megathrust that hosted the 2011 Tohoku-Oki event is due to an unusual rate-weakening shallow patch or to co-seismic weakening of an otherwise rate-strengthening shallow portion of the fault is of fundamental importance for future seismic and tsunamigenic risk assessment.

In this study, we follow up on the study of Noda and Lapusta (2013) and investigate several possible scenarios of the megathrust properties, some with a shallow rate-weakening patch and others with a shallow rate-strengthening patch. All models include a deeper seismogenic zone where magnitude ~7.5 earthquakes occur. In all scenarios, the shallow zones can undergo coseismic weakening by thermal pressurization. The model set-up and results are presented in the next two sections. To determine the most likely scenario, simulations results are compared to the observed slip accumulation of the last 300 years along the Fukushima–Miyagi segment. The approach is conceptually similar to the modeling of the Parkfield segment of the San Andreas Fault in Barbot et al. (2012) but under a two-dimensional approximation and incorporating the effect of thermal pressurization. Note that our models do not incorporate a free surface. The interaction of the earthquake-generated stress field with a free surface can promote large slip at shallow depth during thrust event (Oglesby et al., 1998) and this effect may have been at play during the Tohoku-Oki earthquake (Kozdon and Dunham, 2013). We take into account this discrepancy in our comparison.

2. Dynamic simulation of fault slip

2.1. Model

We use the 2D modeling approach of Noda and Lapusta (2010), which builds on earlier work by Lapusta et al. (2000) and Lapusta and Liu (2009). The approach allows to simulate slow fault slip as well as self-driven rupture propagation with all inertial effects under slow tectonic-type loading in a mode II configuration while accounting for shear heating and pore pressure changes. Our model consists of a planar fault embedded in a homogeneous elastic medium and governed by the ageing form of the rate-and-state friction law (Dieterich, 1979; Rice and Ruina, 1983; Ruina, 1983):

$$\tau = (\sigma - p)\left(\mu_o + a \ln \frac{V}{V_o} + b \ln \frac{V_o \theta}{L}\right), \tag{1}$$

$$\dot{\theta} = 1 - \frac{V\theta}{L}, \tag{2}$$

where σ is the elastodynamic normal stress, p is the pore pressure, $\sigma - p = \sigma^{eff}$ is the effective normal stress, μ_o and V_o are the reference friction coefficient and slip rate, V the slip rate, $a > 0$ and $b > 0$ are rate and state parameters, θ is a state variable which can be interpreted as the average age of the population of contacts between two surfaces, and L is the characteristic slip for state evolution (e.g. Dieterich, 1979; Rice and Ruina, 1983; Ruina, 1983). At constant slip rate, the shear stress τ evolves towards steady state:

$$\tau_{ss} = (\sigma - p)\left(\mu_o + (a-b) \ln \frac{V}{V_o}\right). \tag{3}$$

If $a - b < 0$, the friction is rate-weakening leading to a stick-slip behavior on large enough fault patches, whereas for $a - b > 0$, the friction is rate-strengthening allowing for stable sliding. Note, however, that rate-strengthening areas can also be locked, for example, after they experience seismic slip that drops their shear stress levels (Noda and Lapusta, 2013).

To capture thermal pressurization leading to efficient coseismic weakening, the model incorporates shear-induced temperature variations on the fault and the associated evolution of pore fluid pressure, in the form (e.g., Lachenbruch, 1980):

$$\frac{\delta T(x,y,z,t)}{\delta t} = \alpha_{th} \frac{\delta^2 T(x,y,z,t)}{\delta y^2} + \frac{\omega(x,y,z,t)}{\rho c}, \tag{4}$$

$$\frac{\delta p(x,y,z,t)}{\delta t} = \alpha_{hy} \frac{\delta^2 p(x,y,z,t)}{\delta y^2} + \Lambda \frac{\delta T(x,y,z,t)}{\delta t}, \tag{5}$$

where $T(x,y,z,t)$ is the temperature, $p(x,y,z,t)$ is the pore fluid pressure, $\omega(x,y,z,t)$ is the shear heating source, α_{th} is the thermal diffusivity, α_{hy} is the hydraulic diffusivity, ρc is the specific heat capacity, and Λ is the pore pressure change per unit temperature under undrained conditions. The shear heating source is due to fault slip:

$$\omega = \tau\, V \frac{\exp(-y^2/2h_w^2)}{\sqrt{2\pi}\, h_w} \tag{6}$$

where h_w is the half width of the shear zone.

2.2. Model set-up

Based on coseismic slip and afterslip models of the Tohoku-Oki earthquake (Wei et al., 2012; Perfettini and Avouac, 2014; Bletery et al., 2014; Yamagiwa et al., 2015) as well as on the rupture areas of previous more moderate earthquakes and interseismic coupling models (Fig. 1b), the fault is divided into 4 patches (Fig. 2):

1. A deeper rate-strengthening zone, below the seismogenic zone, at down-dip distance larger than 160 km from the trench (or depth larger than 40 km);
2. A seismogenic zone located at 80 to 160 km from the trench (15 to 40 km depth) where historical Mw 7.5 earthquakes have occurred;
3. A shallower patch prone to thermal pressurization to get enhanced slip in which we will explore the dependency on the rate and state parameter $(a - b)$; and
4. An updip rate-strengthening patch where coseismic slip tapers off and postseismic slip is observed.

The models do not account for the free surface. We extend the up-dip and down-dip rate-strengthening zones by 40 km, to avoid edge effects on the cumulated slip.

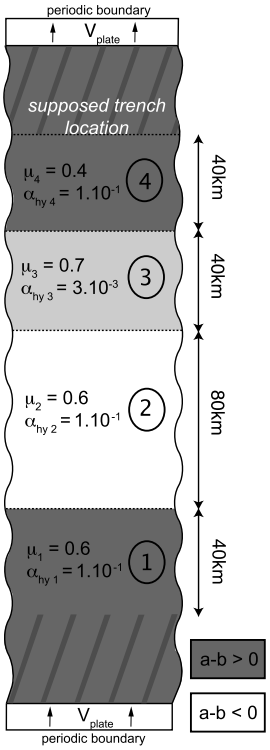

Fig. 2. Model set-up. Patch 3 has a higher reference friction coefficient consistent with the study of Cubas et al. (2013) and lower hydraulic diffusivity to get efficient thermal pressurization and enhanced slip. Different values of parameter $(a-b)$ are explored along this patch.

From a mechanical analysis of the forearc deformation, Cubas et al. (2013) found an increase of the static friction coefficient from the inner wedge corresponding to the deeper seismogenic zone to the outer wedge where the maximum of slip occurred. We therefore increase the reference friction coefficient from $\mu_1 = \mu_2 = 0.6$ in patches 1 and 2 to $\mu_3 = 0.7$ in patch 3. The friction coefficient is then decreased to $\mu_4 = 0.4$ approaching the trench to simulate under-consolidated clay-rich sediments along the plate interface (Table 1). The effective normal stress can be written as:

$$\sigma^{eff} = (1-\lambda)\sigma_n \tag{7}$$

where λ is the ratio between the fluid pore pressure and the lithostatic stress. This fluid pore pressure ratio has been shown to be larger than 0.8 along the frontal part of the forearc (Cubas et al., 2013). Assuming a λ of 0.84, we thus set $\sigma^{eff} = 15$ MPa at the trench location, and increase it linearly with depth to 40 MPa at the distance of 50 km from the trench (Suppe, 2014).

Obtaining rare Tohoku-Oki-like earthquakes requires avoiding the systematic propagation of Mw 7.5 earthquakes to the seafloor. To accomplish that, we explore models that have efficient thermal pressurization only in the relatively shallow patch 3, and not in patch 2 designed to host the observed Mw 7.5 earthquakes. The efficiency of thermal pressurization can be estimated through the characteristic slip L^* (Rice, 2006):

$$L^* = \frac{4}{\mu_0^2}\left(\frac{\rho_c}{\Lambda}\right)^2 \frac{(\sqrt{\alpha}_{hy} + \sqrt{\alpha}_{th})^2}{V}\,. \tag{8}$$

Slip comparable to L^* induces substantial thermal pressurization, and hence substantial weakening, in a model where slip is confined to a mathematical plane. In this study, following Noda and Lapusta (2010), we distribute the slip over a narrow but finite shear zone while computing the temperature evolution (Eqs. (4)–(6)), and hence L^* is an approximation useful in the order-of-magnitude sense. Since hydraulic diffusivity α_{hy} is typically much larger than the thermal diffusivity α_{th}, L^* is approximately proportional to α_{hy}, which varies by orders of magnitude in laboratory studies of fault samples (Tanikawa and Shimamoto, 2009). To get thermal pressurization only in patch 3, we use relatively small hydraulic diffusivity there (Table 1) and larger values elsewhere, with all values within laboratory measurements of Tanikawa and Shimamoto (2009). In the shallowest patch 4, the larger hydraulic diffusivity simulates unconsolidated clays close to the trench. Even in patch 3, the chosen parameters lead to $L^* = 18$ m, enabling only relatively large slips of the order of 10 m to activate efficient weakening.

Table 1
Mechanical and hydraulic properties used in dynamic simulations.

	Symbol	Value
Shear modulus	G	30 GPa
Poisson's ratio	ν	0.25
Shear wave speed	c_s	3 km/s
Plate velocity	V_{plate}	8.5 cm/yr
Reference slip rate	V_0	10^{-6} m/s
Characteristic slip distance	L	0.004 m
Parameter a	a	0.01
Static friction, patches 1 and 2	μ_1, μ_2	0.6
Static friction, patch 3	μ_3	0.7
Static friction, patch 4	μ_4	0.4
Specific heat	ρ_c	2.7 MPa/K
Hydraulic diffusivity, patches 1, 2 and 4	$\alpha_{hy\,1}$, $\alpha_{hy\,2}$, $\alpha_{hy\,4}$	10^{-1} m^2/s
Hydraulic diffusivity, patch 3	$\alpha_{hy\,3}$	3.10^{-3} m^2/s
Thermal diffusivity	α_{th}	10^{-6} m^2/s
Undrained $\Delta p/\Delta T$	Λ	0.1 MPa/K
Half width of shear zone	h_w	10^{-2} m

All other parameters are constrained to their commonly used values (Noda and Lapusta, 2010, 2013; Table 1). We simulate fault slip over thousands of years using the spectral boundary integral approach (Lapusta et al., 2000; Lapusta and Liu, 2009; Noda and Lapusta, 2010). Following the criteria described in Lapusta and Liu (2009), the 280-km-long megathrust is discretized into 40-m cells.

3. Results

3.1. Dependence of the model behavior on parameter $(a-b)$

We explore the dependence of the model behavior on the value of $(a-b)$ of patch 3 (Table 2), considering several typical rate-strengthening values, from 0.004 to 0.011 (Models A1–A4), the rate-neutral case ($a-b=0.0$; Model B) and finally a rate-weakening value ($a-b=-0.004$; Model C1).

All models reproduce some of the Fukushima–Miyagi segment characteristics (Figs. 3 and 4): the alternation between deeper moderate events and much larger events with large slip along patch 3, as well as the shallow postseismic slip. We refer to these much larger events as 'large' events in the following. Since the simulations are 2D, we cannot determine the exact magnitude of these earthquakes. According to their slip (typically of the order of meters) and the along-dip extent of the ruptures (about 80 km), the moderate earthquakes correspond to a magnitude ranging from 7 to 8.

There are, however, important differences between the response of the models. The first one is in the recurrence time of large events. In Models A1–A4 and, to some extent, in Model B, interseismic slip takes place up-dip, including in patch 3 which is rate-strengthening at low slip rates, increasing the recurrence time of large events. Since no interseismic slip can occur along most of the shallow rate-weakening patch 3 in model C1 ($a-b=-0.004$), the recurrence time of large events in that model is de-

Table 2
Rate and state parameters and hydraulic diffusivity along patch 3.

	Parameter a	Parameter b	Coefficient $a-b$	Hydraulic diffusivity α_{hy} (m^2/s)	Parameter L (m)
Model A1	0.01	0.001	0.009	3.10^{-3}	0.004
Model A2	0.012	0.001	0.011	3.10^{-3}	0.004
Model A3	0.01	0.003	0.007	3.10^{-3}	0.004
Model A4	0.01	0.006	0.004	3.10^{-3}	0.004
Model B	0.01	0.01	0.0	3.10^{-3}	0.004
Models C1, C4	0.01	0.014	−0.004	3.10^{-3}	0.004
Model C2	0.01	0.014	−0.004	3.10^{-4}	0.004
Model C3	0.01	0.014	−0.004	3.10^{-3}	0.1
Model C5	0.01	0.014	−0.004	3.10^{-3}	10

termined by the amount of co-seismic slip. In the presented example, the recurrence time is relatively short, ranging between 200 and 250 years. The smaller recurrence time of larger events leads to smaller number of moderate events. Some of them rupture patch 3, in contradiction with the observed historical seismicity along the Fukushima–Miyagi segment which is confined to patch 2. As expected, the recurrence time increases with larger, rate-strengthening $(a-b)$ (Figs. 3–4): from three hundred years in Model A4 $(a-b=0.004)$ to about four hundred years in Model A3 $(a-b=0.007)$, to a thousand years in Model A1 $(a-b=0.009)$, and more than two thousand years in Model A2 $(a-b=0.011)$. As a consequence, the number of Mw-7.5-like earthquakes observed between large events as well as their magnitude increase with larger recurrence time.

So, clearly, making patch 3 more rate-strengthening increases the recurrence time of large events, allowing the model to match the inferred recurrence time of about a thousand years for the Japan megathrust. Another way to increase the recurrence time for a model with a rate-weakening patch, such as Model C1, is to have larger co-seismic slip in patch 3. This larger co-seismic slip can be achieved with a more efficient shear-induced weakening along patch 3. To explore this avenue, we decrease the hydraulic diffusivity in patch 3 of Model C1 by one order of magnitude (Model C2, $\alpha_{hy}=3.10^{-4}$ m^2/s; Fig. 5a). This change leads to the decrease of L^* from 18 m to 2 m, facilitating more slip during large events. Indeed, the recurrence time increases from 200 years to 300 years (Fig. 5a). To increase the recurrence time in a model with rate-weakening patch 3 to a thousand years, a much larger co-seismic slip in patch 3, of 80 to 90 m would be required throughout patch 3; however, such large co-seismic slip over a large fault area is inconsistent with observations.

Yet another way to increase the recurrence time of large events would be to increase the nucleation size of earthquakes over patch 3. This can be achieved either by decreasing the effective normal stress or by increasing parameter L. The increase of nucleation size could also lead to transient slow slip events. However, the decrease of the effective normal stress would result in a small shear stress drop and would not produce large shallow slip. We thus test the effect of an increase of parameter L.

3.2. Effect of an increase of the nucleation size

Earthquakes can develop in a rate-weakening patch only if the size of the patch exceeds the nucleation size (e.g., Rice and Ruina, 1983; Rice, 1993; Rubin and Ampuero, 2005). One theoretical estimate of the earthquake nucleation size, h^*_{RR}, was derived by Rice and Ruina (1983) using the linear stability analysis of steady sliding:

$$h^*_{RR}=\frac{\pi}{4}\frac{G/(1-\nu)\,L}{(b-a)\,\sigma}. \tag{9}$$

Another one is from Rubin and Ampuero (2005), h^*_{RA}, derived for the parameter regime $(a/b)>0.5$ using the energy balance for a quasi-statically extending crack:

$$h^*_{RA}=\frac{2}{\pi}\frac{G/(1-\nu)\,b\,L}{(b-a)^2\,\sigma}. \tag{10}$$

For Model C3 (Table 2), we choose $L=0.1$ m in order to get a nucleation size comparable to the size of patch 3 ($h^*_{RR}=24.5$ km, $h^*_{RA}=69.6$ km). We observe the same alternation between deeper moderate events and large events with large slip along patch 3, as well as the shallow postseismic slip (Fig. 6a). After large events, patch 3 is first locked and then creeps aseismically. The recurrence time of large earthquakes is increased in comparison to Model C1, to about 430 years. Larger values of L lead to more interseismic creep in patch 3 between large events and a longer recurrence interval, about 545 years for $L=10$ m (Fig. 6b). This is understandable, since increasing values of L lead to increasingly stable slip on the patch; if L were infinite, the patch would behave as a velocity-strengthening one with the effective $(a-b)$ given by a (0.01 in this model). Note that even $L=10$ m does not allow us to match the thousand-year recurrence times as observed, and such large values of L do not have any experimental support.

3.3. Effect of a rate-strengthening barrier between two rate-weakening patches

To potentially avoid moderate events rupturing both patches 2 and 3 as well as decrease the number of large events of Model C1, we also explore the effect of a rate-strengthening barrier between patches 2 and 3 (Fig. 5b). In Model C4, a 10 km barrier has been added with the same reference friction coefficient and hydraulic diffusivity as in patch 2 and $(a-b)=0.009$. A similar recurrence time for large events is obtained (in comparison with Model C1), although moderate events extending over both patches 2 and 3 become more limited. However, all large earthquakes nucleate in the shallow rate-weakening patch, which also hosts some small events. This is because it is easier to propagate through the barrier from patch 3, which has much larger slip due to dynamic weakening, than from patch 2. In Model C4, once the event nucleates close to the middle of the fault in patch 3, it readily propagates up because of dynamic weakening but its propagation down is delayed by the presence of the barrier. We do not observe backward propagation. The same conclusion should hold for stronger barriers (the ones with either larger values of the velocity-strengthening parameter $(a-b)$ or large sizes), and hence simulations with stronger barriers would also have largest events that start in patch 3 and propagate into patch 2, contrary to the observations of Ide et al. (2011). For strong enough patches, the events that span both patches 2 and 3 will disappear altogether. On the contrary, weaker barriers (the ones with either less velocity strengthening or smaller sizes) would induce more events over patches 2 and 3.

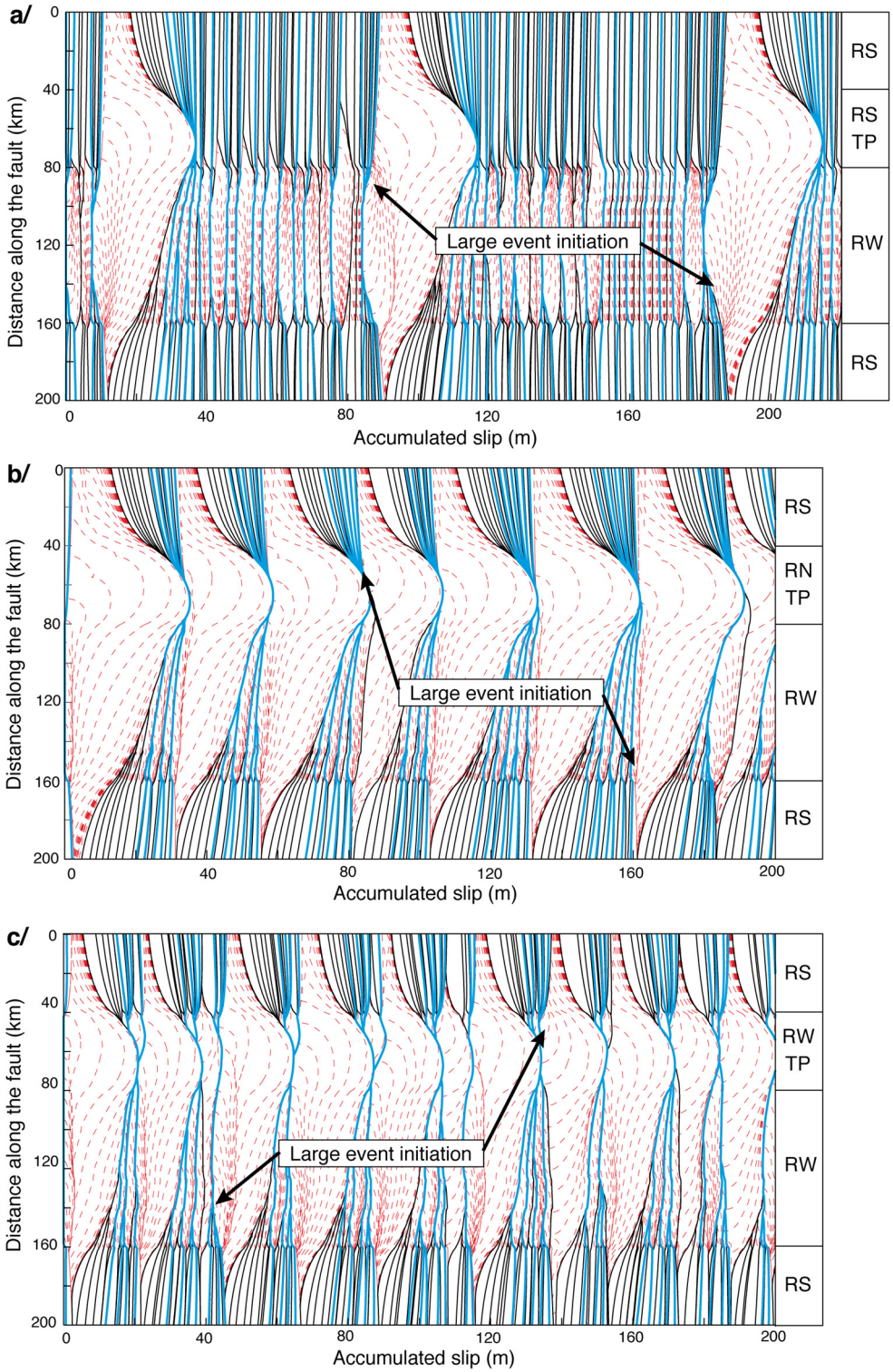

Fig. 3. Accumulated slip as a function of the distance along the fault, for (a) Model A1, rate-strengthening patch 3 ($a - b = 0.009$); (b) Model B, rate-neutral patch 3 ($a - b = 0.0$); (c) Model C1, rate-weakening patch 3 ($a - b = -0.004$). Dashed red lines show coseismic slip every 4 seconds, thick blue lines indicate interseismic slip every 50 years, thin black lines signify the end of each earthquake. Here and in similar figures, zero slip corresponds to fault slip after several tens of simulated earthquakes, to focus on the long-term response of the model. (For interpretation of the references to color in this figure legend, the reader is referred to the web version of this article.)

3.4. Large events characteristics

We now compare characteristics of large events in models with a velocity-strengthening (Model A1) and velocity-weakening (Model C4) patch 3 with the 2011 Tohoku-Oki earthquake. First, the slip distribution with depth is approximately reproduced in both models. An exact comparison of the slip values is not useful since our models are 2D and hence approximate. Furthermore, the simulated values can be somewhat adjusted by adjustments of the model parameters such as friction coefficient values, hydraulic diffusivity etc.

Next, we examine the frequency content (Fig. 7a). For both models, we observe more high frequency radiation along the deeper patch and more low frequency radiation along the shal-

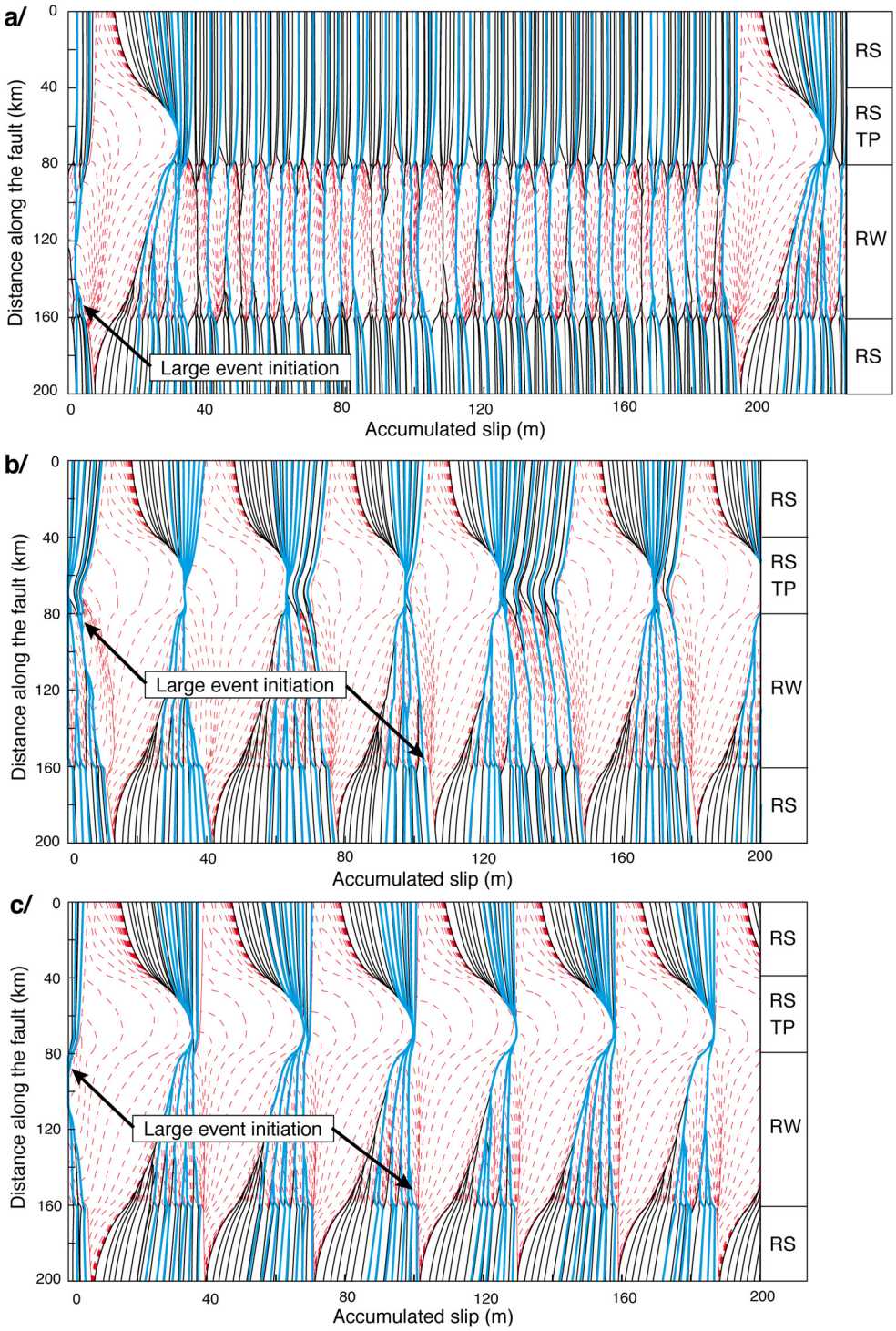

Fig. 4. Accumulated slip as a function of the distance along the fault with rate-strengthening patch 3 for different $a-b$ values: (a) Model A2 ($a-b=0.011$); (b) Model A3 ($a-b=0.007$); (c) Model A4 ($a-b=0.004$). Dashed red lines show coseismic slip every 4 seconds, thick blue lines indicate interseismic slip every 50 years, thin black lines signify the end of each earthquake. (For interpretation of the references to color in this figure legend, the reader is referred to the web version of this article.)

lower patch. This difference is due to the difference in thermal pressurization efficiency as already reported by Noda and Lapusta (2013). The difference is larger with Model A1, probably because of the enhanced thermal pressurization, and perhaps also due to the initial rate-strengthening response in patch 3 for Model A1. Still, both models reproduce the observation that high frequency waves during the Tohoku-Oki earthquake were dominantly generated by the deeper part of the rupture (Ide et al., 2011; Meng et al., 2011; Wei et al., 2012).

Note that nucleation in the middle of the fault is required to reproduce the rupture pattern of the 2011 Tohoku-Oki earthquake as determined by Ide et al. (2011). The rupture went down first, then up, then down again, re-rupturing the bottom patch (Fig. 7b). This pattern occasionally occurs in Models A1, C1, C2 and C3 but never in Model C4 with a barrier. In Model A1, earthquakes cannot nucleate in the rate-strengthening patch 3, and hence all events nucleate in the deeper rate-weakening patch 2. Once in a while, an event penetrates into the rate-strengthening patch 3 energet-

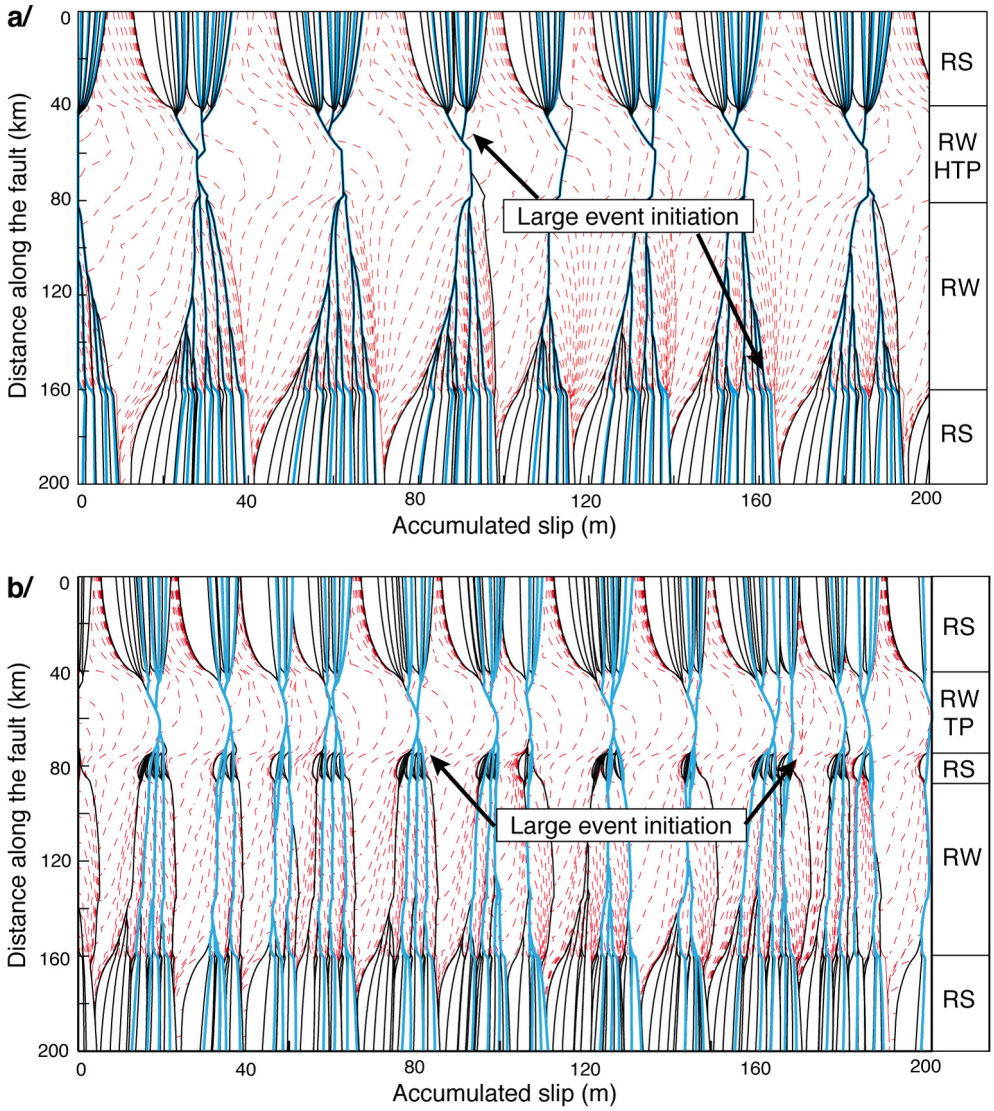

Fig. 5. Accumulated slip as a function of the distance along the fault for (a) Model C2, with rate-weakening patch 3 prone to more efficient shear-heating-induced weakening than Model C1 and (b) Model C4 with a rate-strengthening barrier of 10 km between patch 2 and 3. The rate-strengthening barrier has the same static friction μ and hydraulic diffusivity α_{hy} as patch 2. Dashed red lines show coseismic slip every 4 seconds, thick blue lines indicate interseismic slip every 50 years, thin black lines signify the end of each earthquake. (For interpretation of the references to color in this figure legend, the reader is referred to the web version of this article.)

ically enough to activate shear-heating-induced weakening there through pore fluid pressurization, in which case a large event results. If a large event nucleates at the transition between the shallow rate-strengthening and rate-weakening patches, the timing of the rupture propagation observed during the Tohoku-Oki earthquake is quite well reproduced in Model A1 (Fig. 7c). The rupture first propagates for 38 s downdip, then exhibits extensive shallow slip between 40 and 75 s, and then re-ruptures the downdip megathrust up to 100 s, very similar to what has been observed by Ide et al. (2011) for the Tohoku-Oki event.

Another intriguing particularity is observed with Model A1: supershear speeds are reached by the rupture front along the shallow rate-strengthening patch. Such behavior was also observed by Kaneko and Lapusta (2010) for a model with linear slip-weakening friction close to the free surface. In both cases, the behavior is likely due to low effective normal and shear stresses close to the free surface, which make the stress perturbations coming with waves from the deeper portions of the fault significant enough to transition the rupture to supershear.

Note that high, above-melting temperatures are reached at the deeper rate-weakening patch in our models during large events. The models can be improved by either incorporating the effects of melting, which could involve a combination of weakening and strengthening of the fault (Tsutsumi and Shimamoto, 1997; Di Toro et al., 2006), or modifying the friction properties so that the melting temperatures are not reached. In the latter case, the reference friction coefficient or the effective normal stress need to be reduced. Co-seismic weakening, e.g. efficient thermal pressurization, can also be incorporated in that region, although, without other changes, that would lead to larger slips there, potentially contrary to observation, especially during the re-rupturing of those portions of the fault.

4. Discussion – conclusion

This study shows that fault models with rate-and-state friction that incorporate enhanced co-seismic weakening due to thermal pressurization at a distance of 40 to 80 km from the trench reproduce several inferred features of the 2011 Tohoku-Oki earthquake as well as the overall fault behavior in the region. Such models reproduce an observed alternation between several deeper moderate (M $\sim$ 7.5) events and much larger (M $\sim$ 9) events that accumu-

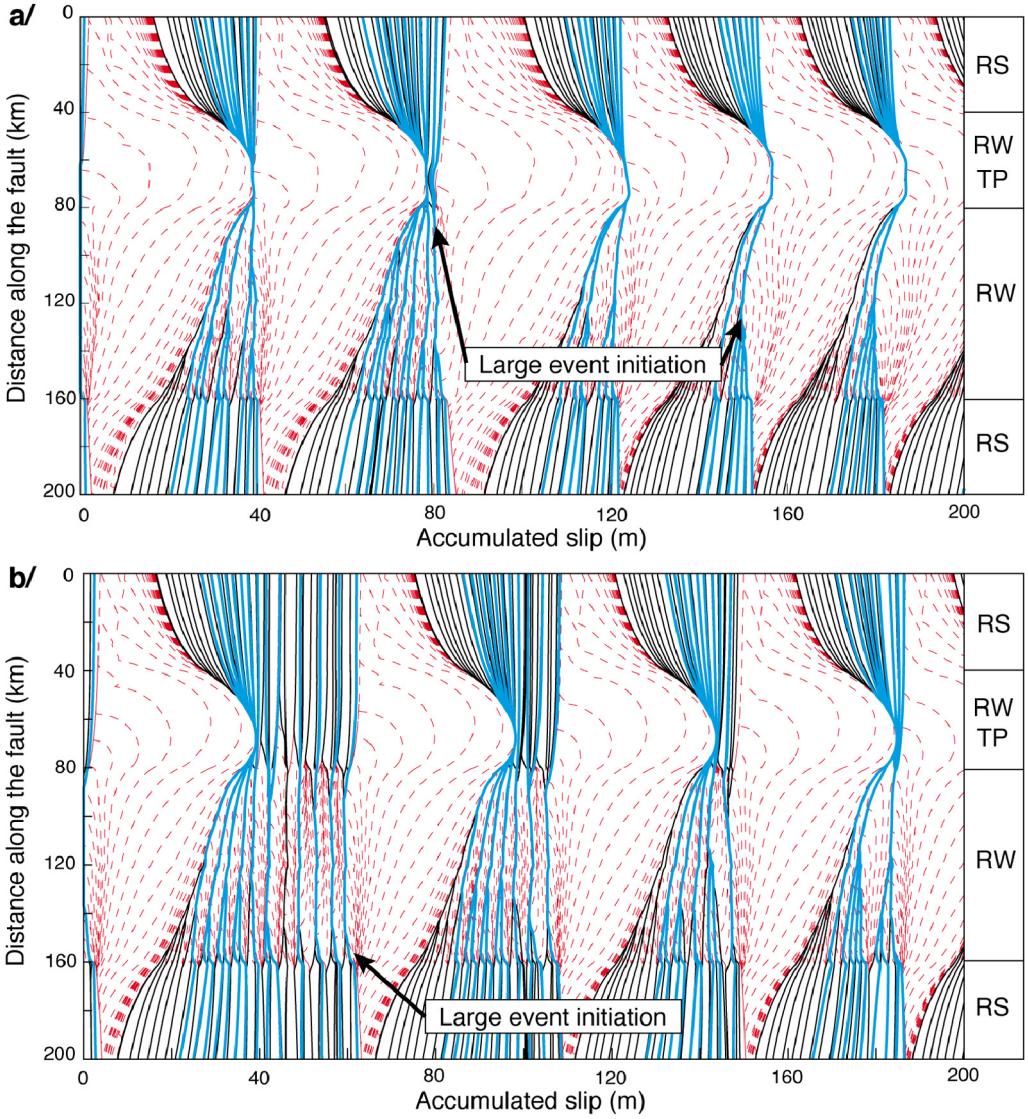

Fig. 6. Accumulated slip as a function of the distance along the fault for (a) Model C3, with rate-weakening patch 3 with a larger value of L (0.1 m) resulting in the nucleation size larger than patch, and (b) even larger $L = 10$ m. Dashed red lines show coseismic slip every 4 seconds, thick blue lines indicate interseismic slip every 50 years, thin black lines signify the end of each earthquake.

late significant slip close to the trench. The models also reproduce dominant high-frequency radiation from the deeper portions of the fault as well as the complex up- and down-dip rupture propagation inferred for the 2011 event. These features are reproduced regardless of whether the shallower portions of the fault (between 40 and 80 km in our models) have rate-strengthening or rate-weakening friction properties at low slip rates.

The comparison of our models with the inferred ~1000-year recurrence of the largest events as well as the seismic behavior over the last 300 years favors a rate-strengthening friction of the shallower patch at low slip rates. The rate-strengthening properties result in interseismic creep in addition to occasional significant co-seismic slip, allowing the model to reproduce the inferred recurrence times of the order of 1000 years. We are not able to reproduce such a long recurrence time in any other model, including ones with a barrier. The rate-strengthening properties near the trench also explain the lack of smaller seismicity near the trench in the last 300 years (except for the rare large events), as observed along the Japan megathrust as well as along most subduction megathrusts worldwide (Byrne et al., 1992).

With a rate-weakening shallow patch, (1) the recurrence time of large events is smaller than the one inferred from tsunami records and (2) moderate events could rupture both patches 2 and 3, in contradiction with the observed location of Mw 7 to 8 earthquakes along the Fukushima–Miyagi segment. A barrier between the two rate-weakening patches results in nucleation from the shallow patch for large events, in contradiction with the observations. A more efficient thermal pressurization or a larger value of L can increase the recurrence time but without reaching the 1000 years deduced from tsunami records. Models with large values of parameter L (such as C3) produce more shallow slip, variation of coupling during the interseismic period as proposed by Sato et al. (2013), and possible slow slip events. However, the model does not reproduce the observed recurrence time for the values of L as high as 10 m, and such large values do not have much laboratory or theoretical support.

The efficient thermal pressurization is obtained along the shallow portion of the megathrust by a local increase of static friction and decrease of the hydraulic diffusivity. The increase of static friction is consistent with values retrieved by Cubas et al. (2013). In addition, the work of Cubas et al. (2013) found a long-term low effective friction as well as a dynamic increase of the pore pressure along the high slip patch, both consistent with a locally low permeability leading to more efficient thermal pressurization. This

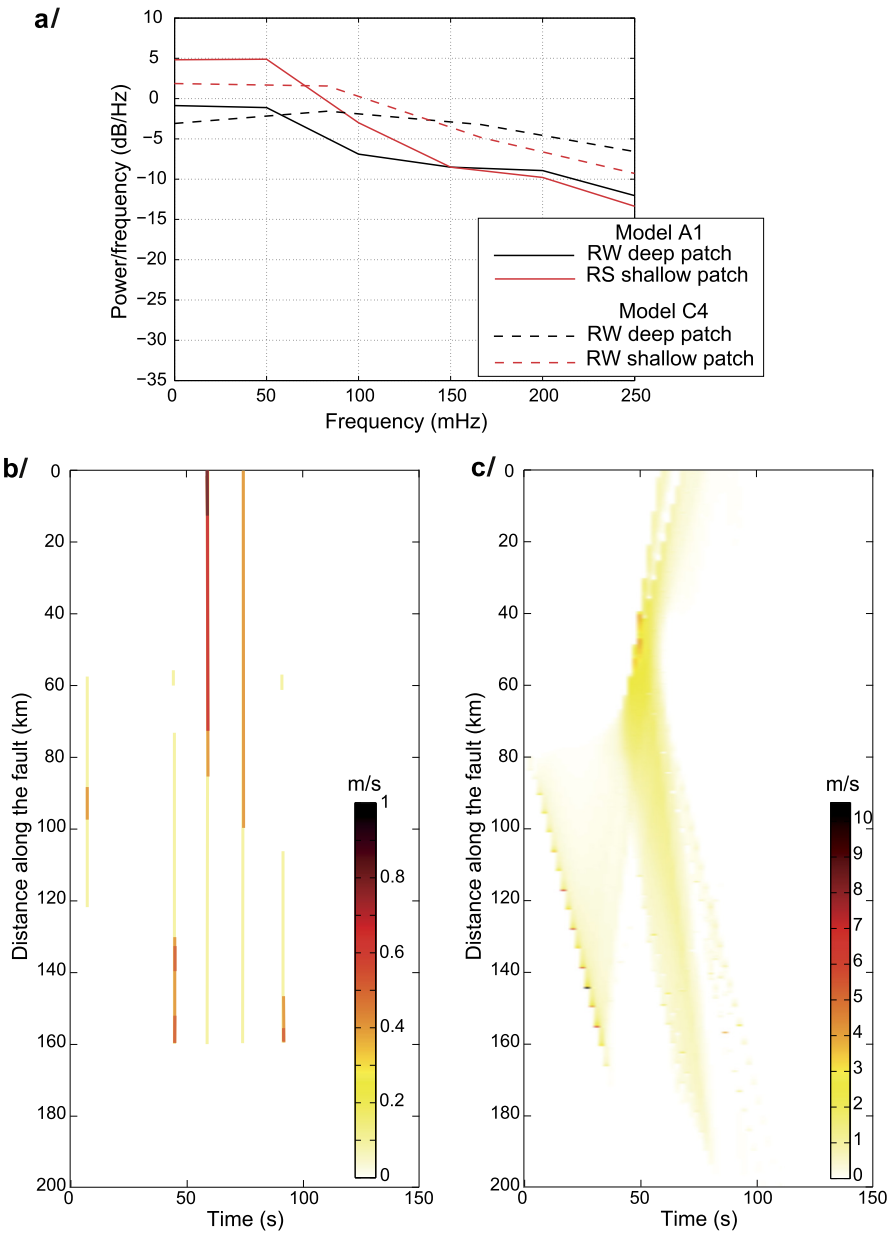

Fig. 7. (a) Comparison of Welch Power Spectral Density Estimate (Welch, 1967) of the slip rate for the deeper and shallower patches of models C4 and A1 for a representative large event. Slip rate as a function of time and distance from the trench (b) from the work of Ide et al. (2011) for the 2011 Tohoku-Oki event, (c) from model A1, when a large earthquake nucleates at the rate-strengthening/rate-weakening transition as in Fig. 3a (slip rate is plotted every 2 s).

local variation in permeability could be related to the low incoming sediment thickness or the disrupted oceanic crust by horst and grabben.

The main limitation of our models is their much simplified geometry. First, our models do not truly account for the free surface, although they do incorporate an increase of the stresses with depth which is one of the features due to the free surface. The true free surface would further promote slip along the high slip patch and at the surface (e.g., Kozdon and Dunham, 2013). Since the shallow coseismic and postseismic slips produced by our simulations are lower than those retrieved from the observations, such enhanced slip at the surface would actually bring our simulations closer to the observations. Second, our model considers a planar 1-D fault embedded into a 2-D elastic medium, whereas the megathrust has a complex 3D shape and, in particular, it is curved next to the trench. The important advantage of our simulations is their ability to consider long slip histories and faithfully reproduce the interaction of seismic and aseismic slip. It would be important to verify the conclusions of this study in fully 3D simulations of a non-planar megathrust with a true free surface, although we anticipate that the results would be qualitatively similar. However, such simulations of long slip histories are not feasible at present.

Overall, our study shows that the features of the great 2011 Tohoku-Oki earthquake as well as historic observations in the area are consistent with the traditional picture of rate-strengthening (and mostly aseismic) shallow portions of megathrusts, with the caveat of their potential co-seismic weakening during extreme events. When such ‘stable’ areas do weaken co-seismically, they have the potential to accumulate large seismic slips due to nearly complete stress drops. Hence it is important to assess the potential and consequences of such rare but catastrophic events on other fault segments that are currently considered to be stable (i.e., creeping or decoupled).

Acknowledgements

We thanks Olivier Lengliné for helpfull discussion. We thank our two reviewers, Roland Bürgmann and Sylvain Barbot, for their constructive comments. This project was supported by the National Science Foundation through EAR grants 1118239 and 1142183 and by the Gordon and Betty Moore Foundation through grant GBMF #423.01 to the Caltech Tectonics Observatory. This is Tectonics Observatory contribution #280.

Appendix A. Supplementary material

Supplementary material related to this article can be found online at http://dx.doi.org/10.1016/j.epsl.2015.03.002.

References

Barbot, Sylvain, Lapusta, N., Avouac, J.P., 2012. Under the hood of the earthquake machine: toward predictive modeling of the seismic cycle. Science 336, 707–710. http://dx.doi.org/10.1126/science.1218796.

Bletery, Q., Sladen, A., Delouis, B., Vallé, M., Nocquet, J.-M., Rolland, L., Jiang, J., 2014. A detailed source model for the Mw 9.0 Tohoku-Oki earthquake reconciling geodesy, seismology, and tsunami records. J. Geophys. Res. 119. http://dx.doi.org/10.1002/2014JB011261.

Bürgmann, R., Kogan, M.G., Steblov, G.M., Hilley, G., Levin, V.E., Apel, E., 2005. Interseismic coupling and asperity distribution along the Kamchatka subduction zone. J. Geophys. Res. 110, B07405. http://dx.doi.org/10.1029/2005JB003648.

Byrne, D.E., Sykes, L.R., Davis, D.M., 1992. Great thrust earthquakes and aseismic slip along the plate boundary of the Makran subduction zone. J. Geophys. Res. 97 (B1), 449–478. http://dx.doi.org/10.1029/91JB02165.

Cubas, N., Avouac, J.P., Leroy, Y.M., Pons, A., 2013. Low friction along the high slip patch of the 2011 Mw 9.0 Tohoku-Oki earthquake required from the wedge structure and extensional splay faults. Geophys. Res. Lett. 40. http://dx.doi.org/10.1002/grl.50682.

Dieterich, J.H., 1979. Modelling of rock friction: 1. Experimental results and constitutive equations. J. Geophys. Res. 84, 2161–2168. http://dx.doi.org/10.1029/JB084iB05p02161.

Di Toro, G., Hirose, T., Nielsen, S., Pennacchioni, G., Shimamoto, T., 2006. Natural and experimental evidence of melt lubrication of faults during earthquakes. Science 311 (5761), 647–649. http://dx.doi.org/10.1126/science.1121012.

Faulkner, D.R., Mitchell, T.M., Behnsen, J., Hirose, T., Shimamoto, T., 2011. Stuck in the mud? Earthquake nucleation and propagation through accretionary forearcs. Geophys. Res. Lett. 38, L18303. http://dx.doi.org/10.1029/2011GL048552.

Fujiwara, T., Kodaira, S., No, T., Kaiho, Y., Takahashi, N., Kaneda, Y., 2011. The 2011 Tohoku-Oki earthquake: displacement reaching the trench axis. Science 334, 1240. http://dx.doi.org/10.1126/science.1211554.

Fulton, P.M., Brodsky, E.E., Kano, Y., Mori, J.J., Chester, F.M., Ishikawa, T., Harris, R.N., Lin, W., Egnuchi, N., Toczko, S., Expedition 343, 343T and KR13-08 Scientists, 2013. Low coseismic friction on the Tohoku-Oki fault determined from temperature measurements. Science. http://dx.doi.org/10.1126/science.1243641.

Hashimoto, C., Noda, A., Sagiya, T., Matsu'ura, M., 2009. Interplate seismogenic zones along the Kuril–Japan trench inferred from GPS data inversion. Nat. Geosci. 2, 141–144. http://dx.doi.org/10.1038/ngeo421.

Hetland, E.A., Simons, M., 2010. Postseismic and interseismic deformation due to fault creep II: transient creep and interseismic stress shadows on megathrusts. Geophys. J. Int. 181, 99–112. http://dx.doi.org/10.1111/j.1365-246X.2009.04482.x.

Hu, Y., Bürgmann, R., Freymueller, J.T., Banerjee, P., Wang, K., 2014. Contributions of poroelastic rebound and a weak volcanic arc to the postseismic deformation of the 2011 Tohoku earthquake. Earth Planets Space 66, 106. http://dx.doi.org/10.1186/1880-5981-66-106.

Ide, S., Baltay, A., Beroza, G.C., 2011. Shallow dynamic overshoot and energetic deep rupture in the 2011 Mw 9.0 Tohoku-Oki earthquake. Science 332, 1426–1429. http://dx.doi.org/10.1126/science.1207020.

Ito, Y., Tsuji, T., Osada, Y., Kido, M., Inazu, D., Hayashi, Y., Tsushima, H., Hino, R., Fujimoto, H., 2011. Frontal wedge deformation near the source region of the 2011 Tohoku-Oki earthquake. Geophys. Res. Lett. 38. http://dx.doi.org/10.1029/2011GL048355.

Johnson, K.M., Fukuda, J., Segall, P., 2012. Challenging the rate-state asperity model: afterslip following the 2011 M9 Tohoku-Oki, Japan, earthquake. Geophys. Res. Lett. 39. http://dx.doi.org/10.1029/2012GL052901.

Kaneko, Y., Lapusta, N., 2010. Supershear transition due to a free surface in 3-D simulations of spontaneous dynamic rupture on vertical strike-slip faults. Tectonophysics. http://dx.doi.org/10.1016/j.tecto.2010.06.015.

Kozdon, J.E., Dunham, E.M., 2013. Rupture to the trench: dynamic rupture simulations of the 11 March 2011 Tohoku earthquake. Bull. Seismol. Soc. Am. 103 (2B), 1275–1289. http://dx.doi.org/10.1785/0120120136.

Lachenbruch, A.H., 1980. Frictional heating, fluid pressure, and the resistance to fault motion. J. Geophys. Res. 85, 6097–6112. http://dx.doi.org/10.1029/JB085iB11p06097.

Lapusta, N., Rice, J.R., Ben-Zion, Y., Zheng, G., 2000. Elastodynamic analysis for slow tectonic loading with spontaneous rupture episodes on faults with rate- and state-dependent friction. J. Geophys. Res. 105, 23765–23789. http://dx.doi.org/10.1029/2000JB900250.

Lapusta, N., Liu, Y., 2009. Three-dimensional boundary integral modeling of spontaneous earthquake sequences and aseismic slip. J. Geophys. Res. 114, B09303. http://dx.doi.org/10.1029/2008JB005934.

Loveless, J.P., Meade, B.J., 2011. Spatial correlation of interseismic coupling and coseismic rupture extent of the 2011 Mw 9.0 Tohoku-Oki earthquake. Geophys. Res. Lett. 38, L17306. http://dx.doi.org/10.1029/2011GL048561.

Mase, C.W., Smith, L., 1985. Pore-fluid pressures and frictional heating on a fault surface. Pure Appl. Geophys. 122, 583–607. http://dx.doi.org/10.1007/BF00874618.

Mase, C.W., Smith, L., 1987. Effects of frictional heating on the thermal, hydrologic, and mechanical response of a fault. J. Geophys. Res. 92 (B7), 6249–6272. http://dx.doi.org/10.1029/JB092iB07p06249.

Matsumoto, Y., Ishikawa, T., Fujita, M., Sato, M., Saito, H., Mochizuki, M., Yabuki, T., Asada, A., 2008. Weak interplate coupling beneath the subduction zone of Fukushima, NE Japan, inferred from GPS/acoustic seaoor geodetic observation. Earth Planets Space 60.

Meng, L., Inbal, A., Ampuero, J.-P., 2011. A window into the complexity of the dynamic rupture of the 2011 Mw 9 Tohoku-Oki earthquake. Geophys. Res. Lett. 38, L00G07. http://dx.doi.org/10.1029/2011GL048118.

Mitsu, Y., Iio, Y., Fukahata, Y., 2012. A scenario for the generation process of the 2011 Tohoku earthquake based on dynamic rupture simulation: role of stress concentration and thermal fluid pressurization. Earth Planets Space 64, 1177–1187. http://dx.doi.org/10.5047/eps.2012.05.016.

Noda, H., Lapusta, N., 2010. Three-dimensional earthquake sequence simulations with evolving temperature and pore pressure due to shear heating: effect of heterogeneous hydraulic diffusivity. J. Geophys. Res. 115, B12314. http://dx.doi.org/10.1029/2010JB007780.

Noda, H., Lapusta, N., 2013. Stable creeping fault segments can become destructive as a result of dynamic weakening. Nature 493, 518–521. http://dx.doi.org/10.1038/nature11703.

Oglesby, D.D., Archuleta, R.J., Nielsen, S.B., 1998. Earthquakes on dipping faults: the effects of broken symmetry. Science 280 (5366), 1055–1059. http://dx.doi.org/10.1126/science.280.5366.1055.

Oleskevich, D.A., Hyndman, R.D., Wang, K., 1999. The updip and downdip limits to great subduction earthquakes: thermal and structural models of Cascadia, south Alaska, SW Japan, and Chile. J. Geophys. Res. 104, 14965–14991. http://dx.doi.org/10.1029/1999JB900060.

Ozawa, S., Nishimura, T., Suito, H., Kobayashi, T., Tobita, M., Imakiire, T., 2011. Coseismic and postseismic slip of the 2011 magnitude 9 Tohoku-Oki earthquake. Nature 117, 373–376. http://dx.doi.org/10.1038/nature10227.

Ozawa, S., Nishimura, T., Munekata, H., Suito, H., Kobayashi, T., Tobita, M., Imakiire, T., 2012. Preceding, coseismic, and postseismic slips of the 2011 Tohoku earthquake. J. Geophys. Res. 117. http://dx.doi.org/10.1029/2011JB009120.

Perfettini, H., Avouac, J.P., 2014. The seismic cycle in the area of the 2011 Mw9:0 Tohoku-Oki earthquake. J. Geophys. Res. 119. http://dx.doi.org/10.1002/2013JB010697.

Rice, J.R., 1993. Spatio-temporal complexity of slip on a fault. J. Geophys. Res. 98, 9885–9907. http://dx.doi.org/10.1029/93JB00191.

Rice, J.R., 2006. Heating and weakening of faults during earthquake slip. J. Geophys. Res. 111, B05311. http://dx.doi.org/10.1029/2005JB004006.

Rice, J.R., Ruina, A.L., 1983. Stability of steady frictional slipping. J. Appl. Mech. 50, 343–349.

Rubin, A.M., Ampuero, J.-P., 2005. Earthquake nucleation on (aging) rate and state faults. J. Geophys. Res. 110, B11312. http://dx.doi.org/10.1029/2005JB003686.

Ruina, A.L., 1983. Slip instabilities and state variable friction laws. J. Geophys. Res. 88, 10359–10370. http://dx.doi.org/10.1029/JB088iB12p10359.

Sato, M., Fujita, M., Matsumoto, Y., Ishikawa, T., Saito, H., Mochizuki, M., Asada, A., 2013. Interplate coupling off northeastern Japan before the 2011 Tohoku-oki earthquake, inferred from seafloor geodetic data. J. Geophys. Res. Solid Earth 118, 3860–3869. http://dx.doi.org/10.1002/jgrb.50275.

Sawai, Y., Namegaya, Y., Okamura, Y., Satake, K., Shishikura, M., 2012. Challenges of anticipating the 2011 Tohoku earthquake and tsunami using coastal geology. Geophys. Res. Lett. 39, L21309. http://dx.doi.org/10.1029/2012GL053692.

Shibazaki, B., Matsuzawa, T., Tsutsumi, A., Ujiie, K., Hasegawa, A., Ito, Y., 2011. 3D modeling of the cycle of a great Tohoku-Oki earthquake, considering frictional behavior at low to high slip velocities. Geophys. Res. Lett. 38, L21305. http://dx.doi.org/10.1029/2011GL049308.

Sibson, R.H., 1973. Interaction between temperature and pore-fluid pressure during earthquake faulting – a mechanism for partial or total stress relief. Nature 243, 66–68.

Simons, M., Minson, S.E., Sladen, A., Ortega, F., Jiang, J.L., Owen, S.E., Meng, L.S., Ampuero, J.P., Wei, S.J., Chu, R.S., Helmberger, D.V., Kanamori, H., Hetland, E., Moore, A.W., Webb, F.H., 2011. The 2011 magnitude 9.0 Tohoku-Oki earthquake: mosaicking the megathrust from seconds to centuries. Science 332, 1421–1425. http://dx.doi.org/10.1126/science.1206731.

Sun, T., Wang, K., Iinuma, T., Hino, R., He, J., Fujimoto, H., Kido, M., Osada, Y., Satoshi, M., Ohta, Y., Hu, Y., 2014. Prevalence of viscoelastic relaxation after the 2011 Tohoku-Oki earthquake. Nature 514, 84–87. http://dx.doi.org/10.1038/nature13778.

Suppe, J., 2014. Fluid overpressures and strength of the sedimentary upper crust. J. Struct. Geol. 69, 481–492. http://dx.doi.org/10.1016/j.jsg.2014.07.009.

Tanikawa, W., Shimamoto, T., 2009. Frictional and transport properties of the Chelungpu fault from shallow borehole data and their correlation with seismic behavior during the 1999 Chi–Chi earthquake. J. Geophys. Res. 114, B01502. http://dx.doi.org/10.1029/2008JB005750.

Tsutsumi, A., Shimamoto, T., 1997. High-velocity frictional properties of gabbro. Geophys. Res. Lett. 24 (6), 699–702. http://dx.doi.org/10.1029/97GL00503.

Yamanaka, Y., Kikuchi, M., 2004. Asperity map along the subduction zone in northeastern Japan inferred from regional seismic data. J. Geophys. Res. 109, B07307. http://dx.doi.org/10.1029/2003JB002683.

Yamagiwa, S., Miyazaki, S., Hirahara, K., Fukahata, Y., 2015. Afterslip and viscoelastic relaxation following the 2011 Tohoku-Oki earthquake (Mw9.0) inferred from inland GPS and seafloor GPS/Acoustic data. Geophys. Res. Lett. 42. http://dx.doi.org/10.1002/2014GL061735.

Watanabe, S., Sato, M., Fujita, M., Ishikawa, T., Yokota, Y., Ujihara, N., Asada, A., 2014. Evidence of viscoelastic deformation following the 2011 Tohoku-Oki earthquake revealed from seafloor geodetic observation. Geophys. Res. Lett. 41, 5789–5796. http://dx.doi.org/10.1002/2014GL061134.

Wei, S., Graves, R., Helmberger, D., Avouac, J.P., Jiang, J., 2012. Sources of shaking and flooding during the Tohoku-Oki earthquake: a mixture of rupture styles. Earth Planet. Sci. Lett. 333–334, 91–100. http://dx.doi.org/10.1016/j.epsl.2012.04.006.

Welch, P.D., 1967. The use of fast Fourier transform for the estimation of power spectra: a method based on time averaging over short, modified periodogram. IEEE Trans. Audio Electroacoust. 15, 70–73.

Earth and Planetary Science Letters 381 (2013) 92–103

Contents lists available at ScienceDirect

Earth and Planetary Science Letters

www.elsevier.com/locate/epsl

Megathrust friction determined from mechanical analysis of the forearc in the Maule earthquake area

Nadaya Cubas [a,*], Jean-Philippe Avouac [a], Pauline Souloumiac [b], Yves Leroy [c]

[a] Tectonics Observatory, Division of Geological and Planetary Sciences, California Institute of Technology, 1200 E. California Blvd, Pasadena, CA 91125, USA
[b] Département Géosciences et Environnement, Université de Cergy-Pontoise, Neuville-sur-Oise, 5 mail Gay Lussac, 95031 Cergy-Pontoise cedex, France
[c] Laboratoire de Géologie, Ecole Normale Supérieure, 24 rue Lhomond, 75231 Paris Cedex 05, France

ARTICLE INFO

Article history:
Received 8 March 2013
Received in revised form 25 July 2013
Accepted 29 July 2013
Available online xxxx
Editor: P. Shearer

Keywords:
Maule earthquake
frictional properties
dynamic weakening
critical wedge

ABSTRACT

The seismogenic potential of a given fault depends essentially on its frictional properties and on the mechanical properties of the medium. Determining the spatio-temporal variations of frictional properties is therefore a key issue in seismotectonics. This study aims to characterize the friction on the South America megathrust in the 2010 Mw 8.8 Maule earthquake area from mechanical analysis of the forearc structure and morphology. Based on the critical taper theory, we first show that the rupture area of the Maule earthquake, also shown to be locked in the interseismic period, coincides with the stable part of the wedge. In the surrounding area, the wedge is critical, a finding consistent with various evidence for active deformation there. This is in particular true for the Arauco Peninsula area which seems to have arrested the Maule earthquake's rupture to the South. This observation lends support to the view that the seismic rupture is inhibited when propagating beneath a critical area. The geometry of the critical portion of the wedge suggests a standard internal friction ($\mu_{int} = 0.7 \pm 0.13$) and a hydrostatic pore pressure within the wedge. The effective friction beneath the critical outer wedge is estimated to be $\mu_b^{eff} = 0.27 \pm 0.03$. This could be related to intrinsically low friction minerals (clay) or high pore pressure along the megathrust. We next use the limit analysis approach to constrain the variation of the effective friction along the megathrust based on the location and geometry of internal faulting within the forearc. A low effective friction is found within the rupture area ($\mu_b^{eff} \leqslant 0.14$) to explain the reactivation of thrust fault such as the Santa Maria, updip of the coseismic rupture, or the activation of normal splay faults downdip of the rupture area. The low effective friction found there could reflect strong dynamic weakening.

1. Introduction

The determination of the mechanical properties of subduction megathrusts and forearcs is an important goal of seismotectonics for a number of reasons. First, these properties determine the mechanical coupling across the subduction zone and, as such, are thought to influence state of stress, elevation and deformation style of the continental margin (e.g., Hassani et al., 1997; Bonnardot et al., 2008; Lamb and Davis, 2003). Second, the factors that determine the seismic potential of a subduction megathrust remain poorly understood and there are hints that the structure and mechanical state of the forearc might provide some insight. In particular, the shallower, presumably rate-strengthening portion of the megathrust is thought to possibly coincide with the extent of the outer accretionary prism, the most frontal part of the forearc formed of imbricated thrust sheets of accreted sediments, which is considered to deform internally (Byrne et al., 1987; Ruff and Tichelaar, 1996; Fuller et al., 2006; Wang and Hu, 2006). The limit between the deforming wedge and the more internal stable part of the wedge would then mark the updip portion of the seismogenic zone as suggested from the correlation between the rupture extent of large megathrust earthquakes with shelf-terraces or forearc basins marked by local gravity lows (Song and Simons, 2003; Wells et al., 2003). Splay faults are commonly observed at the backstop of the deforming wedge and their location seem to mark the updip limit of megathrust ruptures (Collot et al., 2008). The fact that splay faults form at the transition between aseismic and seismic patches has also been observed in analog experiments (Rosenau and Oncken, 2009). As the morphology of the deforming accretionary prism naturally evolves toward a critical geometry determined by the friction along the megathrust and the wedge strength (Davis et al., 1983), the frictional properties could then control both the seismogenic behavior and the forearc morphology.

In this study, we analyze the forearc structure and morphology in the area of the 27th February 2010 Mw 8.8 Maule earthquake

* Corresponding author.
E-mail address: cubas@caltech.edu (N. Cubas).

0012-821X/$ – see front matter
http://dx.doi.org/10.1016/j.epsl.2013.07.037

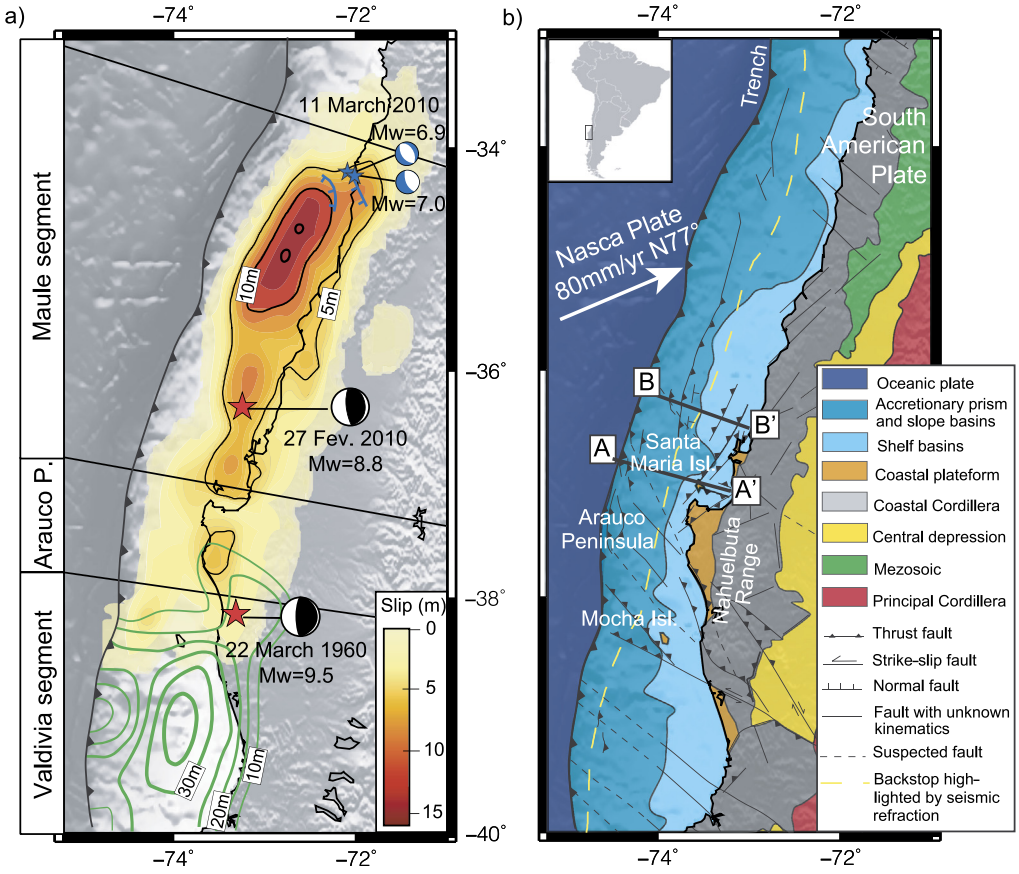

Fig. 1. (a) Coseismic slip model of the 2010 Mw 8.8 Maule earthquake obtained by Lin et al. (2013) from inversion of geodetic, seismic and tsunami data, and slip model for the northern rupture of the 1960 Mw 9.5 Valdivia earthquake from Moreno et al. (2010) in green. Large red stars: locations of hypocenters, small blue stars: Pichilemu normal aftershocks. Surface evidence of the Pichilemu sequence are reported in blue. (b) Morpho-structural map of South Central Chile (based on Melnick and Echtler, 2010; Melnick et al., 2006, 2009; Geersen et al., 2011; Farías et al., 2011; Schobbenhaus and Bellizzia, 2001). (For interpretation of the references to color in this figure legend, the reader is referred to the web version of this article.)

to place constraints on the frictional properties of the megathrust. In the following section, we review the characteristics and the seismotectonic setting of the study area. We assess next a possible correlation between the spatial variations of the frictional properties and the mode of slip along the megathrust. To constrain the frictional properties, two different approaches are used. The first one, presented in Section 3, relies on the critical taper theory (Davis et al., 1983; Dahlen, 1984). The second approach, applied to the deeper locked section is presented in Section 4 and relies on the limit analysis theory (Salençon, 2002; Maillot and Leroy, 2006). It is used to retrieve spatial variations of effective basal friction required to explain the location of some documented splays faults.

2. Seismotectonic setting and characteristics of Maule earthquake

The Maule earthquake ruptured the Concepción segment (33°S–38°S) of the South America megathrust which accommodates the 65–85 mm/a convergence between the Nazca and South America plates (DeMets et al., 1994; Angermann et al., 1999) (Fig. 1). Prior to 2010, it had last ruptured in 1835 and therefore had been identified as a seismic gap (Campos et al., 2002; Ruegg et al., 2009; Madariaga et al., 2010). A number of coseismic slip models of the Mw 8.8 Maule earthquake have been derived (Lin et al., 2013; Delouis et al., 2010; Lorito et al., 2011; Vigny et al., 2011). Although they vary regarding the details, most of them are quite similar to first order. In this study, we refer to the particular coseismic model of Lin et al. (2013) which was derived from seismological, GPS, inSAR and tsunami data (Fig. 1a). Geodetic strain measured before the earthquake shows that the 80 km × 350 km rupture area coincides with a portion of the plate interface that had remained strongly locked (Moreno et al., 2010; Métois et al., 2012). As indicated from the relatively modest tsunami, the rupture didn't reach the trench (Lorito et al., 2011; Lin et al., 2013). The down-dip extent of the rupture follows the coastline as often observed for large megathrust earthquakes along the South America subduction zones (Ruff and Tichelaar, 1996; Sladen et al., 2010). The southern end of the rupture coincides with the Arauco Peninsula (Fig. 1b), an anomalous trench-coast distance and relief feature, which is known to have also acted as a barrier for past earthquakes (Lomnitz, 1970; Kaizuka et al., 1973; Melnick et al., 2009; Contreras-Reyes and Carrizo, 2011).

The mainshock induced aftershocks including a number of events with a thrust mechanism on the plate interface in the area surrounding and adjacent to the coseismic rupture (Rietbrock et al., 2012). Evidence for activation of forearc structures was also observed. These include normal faults near the town of Pichilemu which produced a major sequence of shallow aftershocks with two major events of magnitude Mw = 6.9 and 7.0 (Ryder et al., 2012; Farías et al., 2011) (Fig. 1a). The seismicity delineates an NW trend, consistent with the location and orientation of secondary surface cracks (Farías et al., 2011), and shows an SW dip between 40 and 83° from the surface down to the interplate (Fig. 1a). Evidence of activation of thrust faulting within the forearc was found on the Santa Maria island (Fig. 1b). The elevated topography of the island itself was formed as a result of thrusting along a 72°W dipping backthrust fault which most probably roots at depth into the

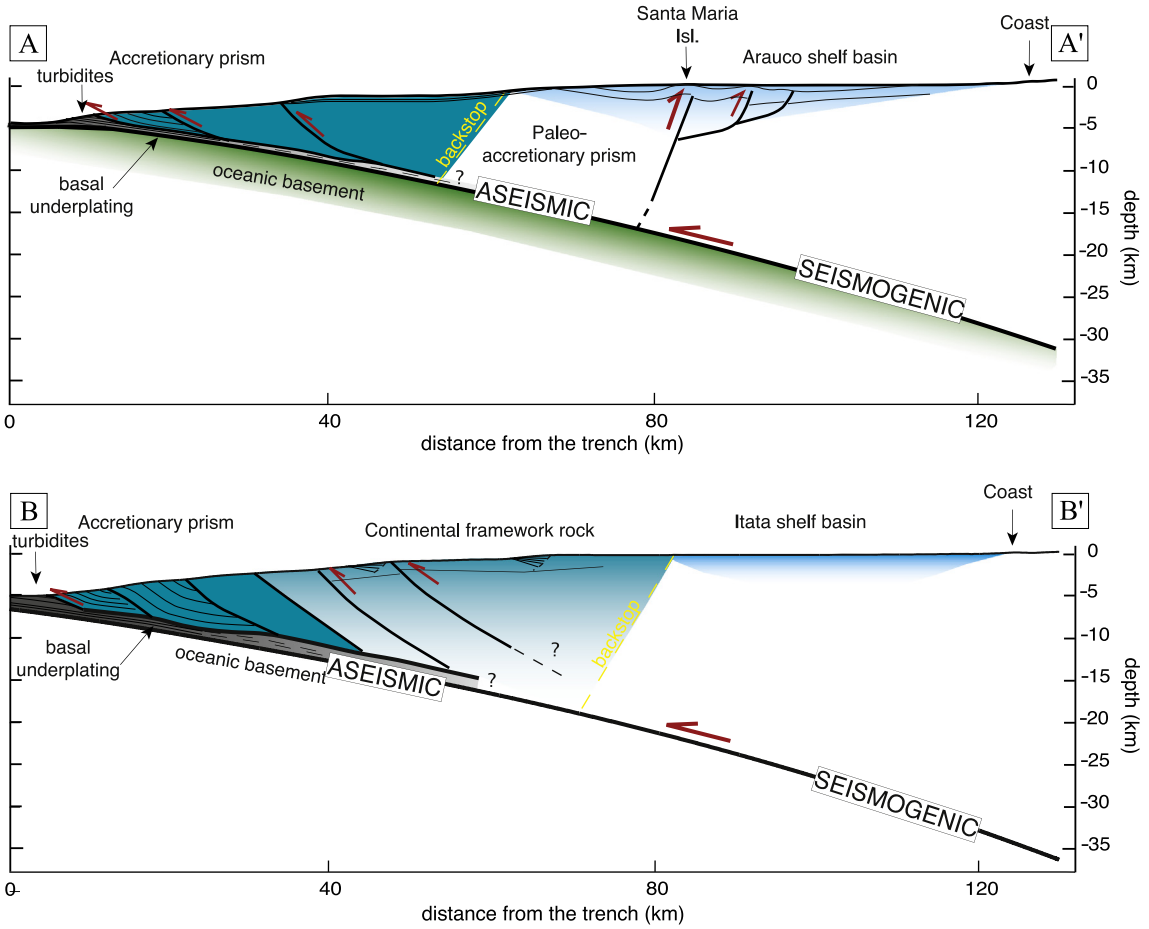

Fig. 2. Structural profiles from cross-sections AA′ and BB′ of Fig. 1b, modified from Melnick et al. (2006) and Geersen et al. (2011).

megathrust (Fig. 2, top) as highlighted by the seismicity recorded before the 2010 earthquake (Melnick et al., 2006). This backthrust fault has been interpreted as an inverted Early Pliocene normal fault related to the rift structure of the Arauco shelf basin (Melnick et al., 2006). The island has been the focus of previous studies because of repeated earthquake-related uplift. Melnick et al. (2012) reported a 1.6 m uplift during the 2010 earthquake, Darwin (1851) measured 2.4 m to 3 m of uplift two and six weeks after the 1835 $M > 8$ earthquake (Lomnitz, 1970), while Melnick et al. (2006) estimated a 6 m uplift related to the 1751 $M > 8$ event. The island is located close to the updip limit of the coseismic rupture (Fig. 1a). The splay fault may have been activated during or after the mainshock.

There is additional geological evidence for active deformation of the forearc at various other places offshore and onshore. Some splay faults are documented from geophysical investigations within the accretionary prism (Melnick et al., 2006, 2009; Geersen et al., 2011). These thrust faults are clear indication that the outer wedge is in critical state in the sense of the critical taper theory (Fig. 2). Both the Nahuelbuta range and the Arauco Peninsula are actively deforming as suggested from their relief and uplift documented from raised shorelines and thermochronology (Melnick et al., 2009). The relief of the Nahuelbuta Range is twice the relief of the coastal cordillera, and its exhumation rate has been estimated to be 0.03–0.04 mm/a until 4 ± 1.2 Ma, with an increase to <0.2 mm/a since that time (Glodny et al., 2008). At the Arauco Peninsula, the maximum uplift rate obtained is 1.8 ± 0.4 mm/a over the past 50 ka (Melnick et al., 2006) and 2.3 ± 0.2 mm/a over the past 3 ka (Bookhagen et al., 2006). In the following section we use the information on the morphology, structure and deformation of the forearc to constrain its mechanical state and friction along the megathrust. We assume that the state of stress of the forearc wedge above the megathrust is limited by its brittle strength and analyze the implications for the stress level along the megathrust. The analyzed domain extends from the trench to the Nahuelbuta range. The analysis provides an estimate of the quasistatic stresses within the wedge and along the megathrust needed to bring the wedge to the verge of brittle failure. Deformation in the deeper area, where the megathrust reaches a depth of about 50 km, might in fact be ductile. The analysis still provides some insight but the inferred basal friction might then be seen as an effective basal friction, a proxy for viscous stress. However we believe that this area is still dominantly in the brittle domain based on the relatively low temperature estimated from thermokinematic modeling (less than 400 °C according to Völker et al., 2011), the distribution of aftershocks (Rietbrock et al., 2012) and the time-evolution of afterslip which suggests a brittle creep mechanism (Lin et al., 2013).

3. Constraints derived based on the critical taper theory

The Coulomb wedge theory considers the mechanics of an accretionary wedge as analogous to sand pushed by a moving bulldozer along a frictional décollement (Davis et al., 1983). The wedge evolves into a critical geometry, corresponding to a point of internal state of stress for which the whole wedge including the basal décollement is on the verge of Coulomb failure. If the décollement is planar and material properties are homogeneous, the critical wedge is triangular for a cohesionless wedge. The conditions for stress equilibrium, Coulomb yielding of the wedge and frictional sliding along its base have an analytical solution. In fact

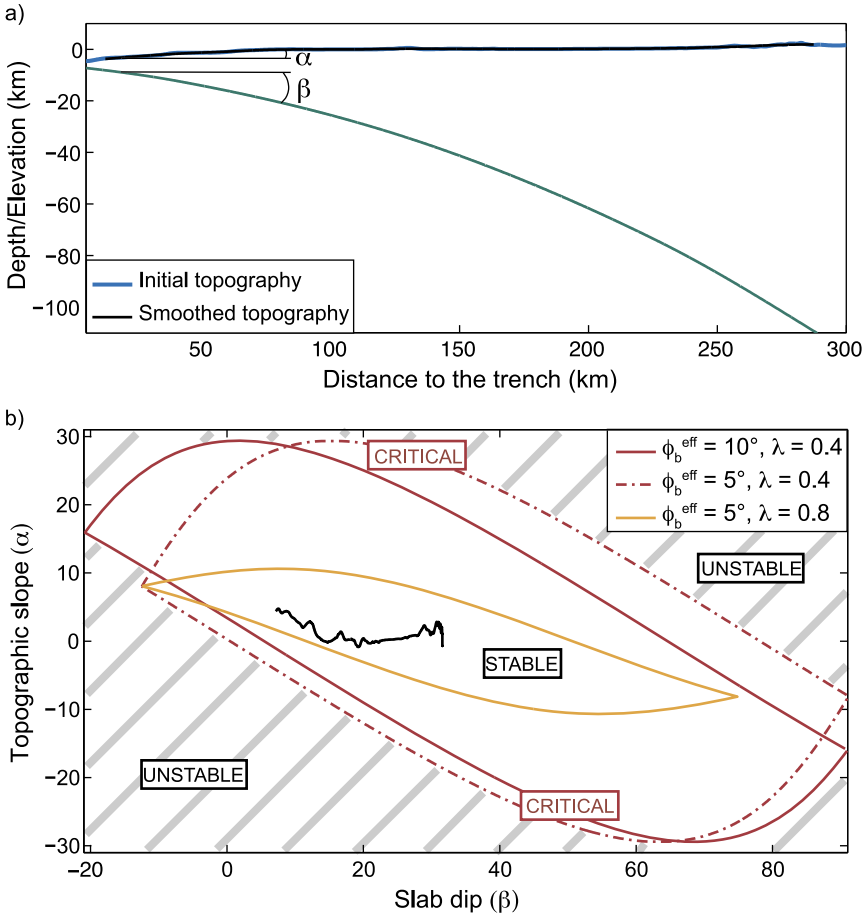

Fig. 3. (a) Initial and smoothed topography and slab morphology of the AA′ cross-section of Fig. 1b. (b) Topographic slope and slab dip of the cross-section AA′ compared to 3 different critical envelopes for an internal angle of friction of 30°, two different pore pressure, one hydrostatic ($\lambda = 0.4$), one high ($\lambda = 0.8$) and two different angles of effective basal friction (5° and 10°).

two critical states can be defined: one in which the wedge is on the verge of failure in horizontal compression and another in which the wedge is on the verge of failure in horizontal extension. In this study, we use the solution for a cohesionless wedge established by Dahlen (1984) and generalized with a Mohr's construction by Lehner (1986). The critical taper angle is a function of the angle Ψ_B formed by the maximum principal stress $\sigma 1$ and the base of the wedge, and the angle Ψ_0 formed by $\sigma 1$ and the top of the wedge. The solution corresponding to the compressional branch is:

$$(\alpha + \beta)_c = \Psi_B - \Psi_0, \tag{1}$$

where the subscript c means critical and the two angles Ψ_B and Ψ_0 are

$$\Psi_B = \frac{1}{2}\arcsin\left(\frac{\sin\phi_b'}{\sin\phi_b}\right) - \frac{1}{2}\phi_b', \tag{2}$$

$$\Psi_0 = \frac{1}{2}\arcsin\left(\frac{\sin\alpha'}{\sin\phi_{int}}\right) - \frac{1}{2}\alpha'. \tag{3}$$

The angles ϕ_{int} and ϕ_b are the internal and basal angles of friction. They are defined as:

$$\mu_{int} = \tan\phi_{int},$$

$$\mu_b = \tan\phi_b.$$

The two angles ϕ_b' and α' introduced in (2) and (3) are such that

$$\tan\phi_b' = \left(\frac{1-\lambda_b}{1-\lambda}\right)\tan\phi_b, \tag{4}$$

$$\alpha' = \arctan\left[\left(\frac{1-\rho_w/\rho}{1-\lambda}\right)\tan\alpha\right]. \tag{5}$$

They account for the pore fluid pressure through the generalized internal and basal Hubbert–Rubbey fluid pressure ratios λ and λ_b:

$$\lambda = \frac{P + \rho_w g D}{|\sigma_z| + \rho_w g D},$$

$$\lambda_b = \frac{P_b + \rho_w g D}{|\sigma_z| + \rho_w g D}, \tag{6}$$

with ρ and ρ_w being the densities of the wedge material and pore fluid (water), D the water depth and σ_z the vertical stress. As shown by Wang et al. (2006), the solution is exact if $\lambda = \lambda_b$, otherwise it is a valid approximation if a small taper is assumed. The reader is referred to Lehner (1986) for the full equations. For the sake of clarity, we define an effective basal friction as $\mu_b^{eff} = \tan\phi_b^{eff} = (1-\lambda_b)\tan\phi_b$.

The theoretical relation (1) between α and β forms a critical envelope defining three different mechanical states (Fig. 3b):

(1) a critical state, the wedge is on the verge of failure everywhere, in horizontal compression along the lower branch and in horizontal tension along the upper branch of the envelope.
(2) a stable state, if the taper angle lies in between the envelope limits. The wedge is mechanically stable and can slide along the décollement without any internal deformation.

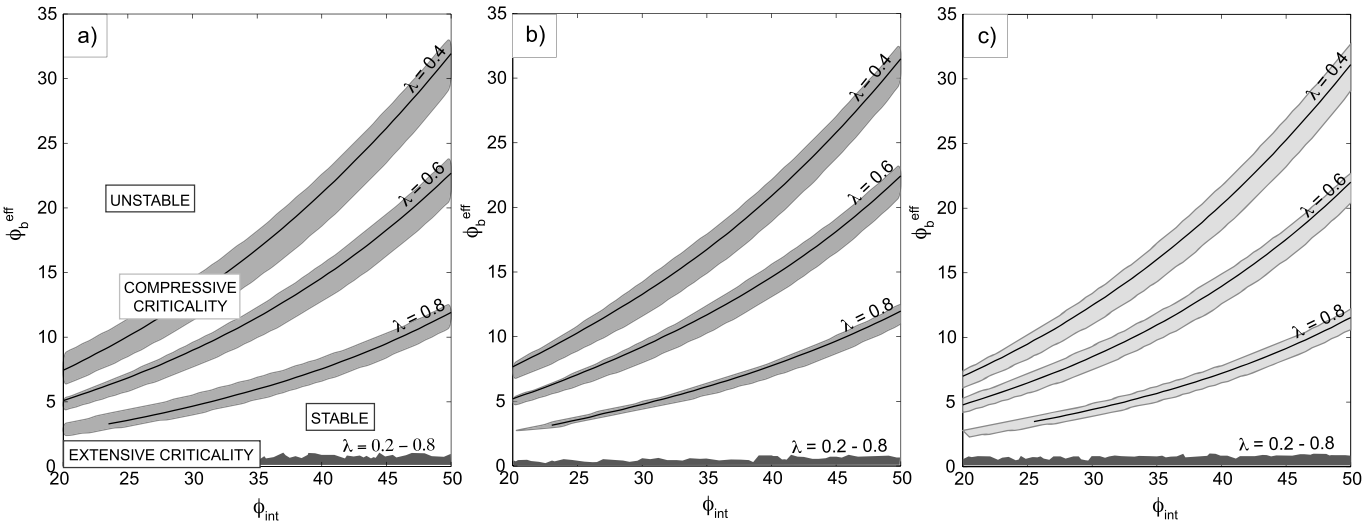

Fig. 4. Upper and lower bound of acceptable effective basal friction, as a function of the internal friction for different Hubbert and Rubbey parameter λ (Fig. 4) for the Maule segment (a), the Arauco Peninsula (b) and the Northern Valdivía segment (c). Cross-sections variability is represented in light gray for the upper bound, in dark gray for the lower bound. The thick black lines are the means.

(3) unstable state, if the taper lies outside the envelope. The Coulomb yielding limit on the strength of the wedge implies that the taper angle of a wedge in quasistatic equilibrium cannot be lower than the critical taper in compression nor higher than the critical taper in extension; a wedge lying in the area outside the envelope is therefore unstable.

As shown in the appendix, the critical taper theory holds for a curved megathrust as long as its radius of curvature is large compared to the wedge thickness.

The observed topographic slope and dip angle of the megathrust are consequently used to place constraints on the model parameters. The α–β curve describing the geometry of the forearc must lie within the area defined by the critical envelope as in the cross-section AA′ (Fig. 1b) in Fig. 3. A given portion of the forearc can either be in the stable domain or in a critical state, in which case some evidence for internal deformation of the wedge would be expected. The topographic slope and the slab dip along sections across the south central Chilean forearc are thus used to determine the range of possible values of the model parameters so that the wedge is everywhere stable or in a critical state. We analyzed 300 km long profiles. To determine the topographic slope α, we used ETOPO1 (Amante and Eakins, 2009, resolution 1′). To filter out the high-frequency content, the topographic profiles were smoothed using a sliding window. Different smoothing functions (triangular and rectangular) and width (10, 25 and 40 km) were tested. The reader is referred to the appendix for the discussion of the details and presentation of these tests. Only the results obtained with the topography smoothed by a 25 km wide rectangular window are shown here. The slab geometry is extracted from the slab 1.0 model of Hayes et al. (2012) which is based on a large compilation of data from active source, passive seismology and position of trenches (resolution 0.02°).

We distinguish three different areas: the northern one corresponds to the 2010 Mw 8.8 Maule earthquake rupture, the central one to the Arauco Peninsula area, and the southern one to the northern part of the 1960 Mw 9.5 Valdivía earthquake rupture (Fig. 1a). For each area, the upper (compression) and lower (extension) bound of acceptable effective basal friction angles as a function of the internal friction angle assuming different internal pore pressure ratios are determined (Fig. 4).

The three areas show a similar range of acceptable parameters. For an angle of internal friction of $\phi_{int} = 35°$ ($\mu_{int} = 0.7$) and a hydrostatic fluid pore pressure ratio ($\lambda = 0.4$), the angle of effective basal friction has to be $1° \leqslant \phi_b^{eff} \leqslant 16°$ ($0.017 \leqslant \mu_b^{eff} \leqslant 0.286$). For a very high internal pore pressure ratio ($\lambda > 0.8$), the acceptable range narrows down to: $1° \leqslant \phi_b^{eff} \leqslant 5°$ ($0.017 \leqslant \mu_b^{eff} \leqslant 0.08$). This analysis shows that the basal effective friction must be relatively low, less than about 17° ($\mu_b^{eff} < 0.3$) if a standard value of the internal friction angle (30–40°) and a hydrostatic pore pressure ratio are assumed ($\lambda = 0.4$).

Tighter constraints can be determined from the measured taper angle on those areas which are known to be in a critical state based on evidence of forearc deformation reviewed in the previous section. For this analysis, we considered five domains including three covering the rupture area of the Maule earthquake to capture the major lateral variations of the morphology of the forearc (Fig. 5). We computed an average swath profile for each domain (individual profiles are shown in the supplementary material, Fig. S1). Inspection of profiles show that some portions seem to follow the approximately linear relationship between α and β defining the critical state (Fig. 5b). This is particularly true for the outer wedge where there is evidence for internal thrust faulting (Fig. 2). In the Arauco Peninsula area, the wedge seems to follow the critical state envelope from the trench to the crest of the peninsula. Another portion of the profile, farther inland corresponding to the Nahuelbuta Range, also seems to follow a critical envelope that would then require a higher basal friction.

We then mapped the zones which are presumably critical by assessing the probability that a given portion of an individual profile follows a critical envelope. In practice, we evaluate this probability based on the local linearity of the α–β curve (see the appendix). The two critical zones in the Arauco Peninsula area appear to be separated by a relative narrow stable zone.

The Valdivía segment shows some significant variability along strike, but a critical section at the front nonetheless shows up in the swath profile. A limited zone inland is possibly at criticality at the southern edge of the study area. This zone would start at the coastline.

The southernmost profile in the Maule rupture area (Fig. 2, top), shows also that the outer wedge is critical from the trench up to the edge of the continental shelf. A second narrower critical area seems to show up further inland, starting also at the coastline. These critical zones lie in the continuity of those identified within the Arauco Peninsula area, though the intervening stable area is broader.

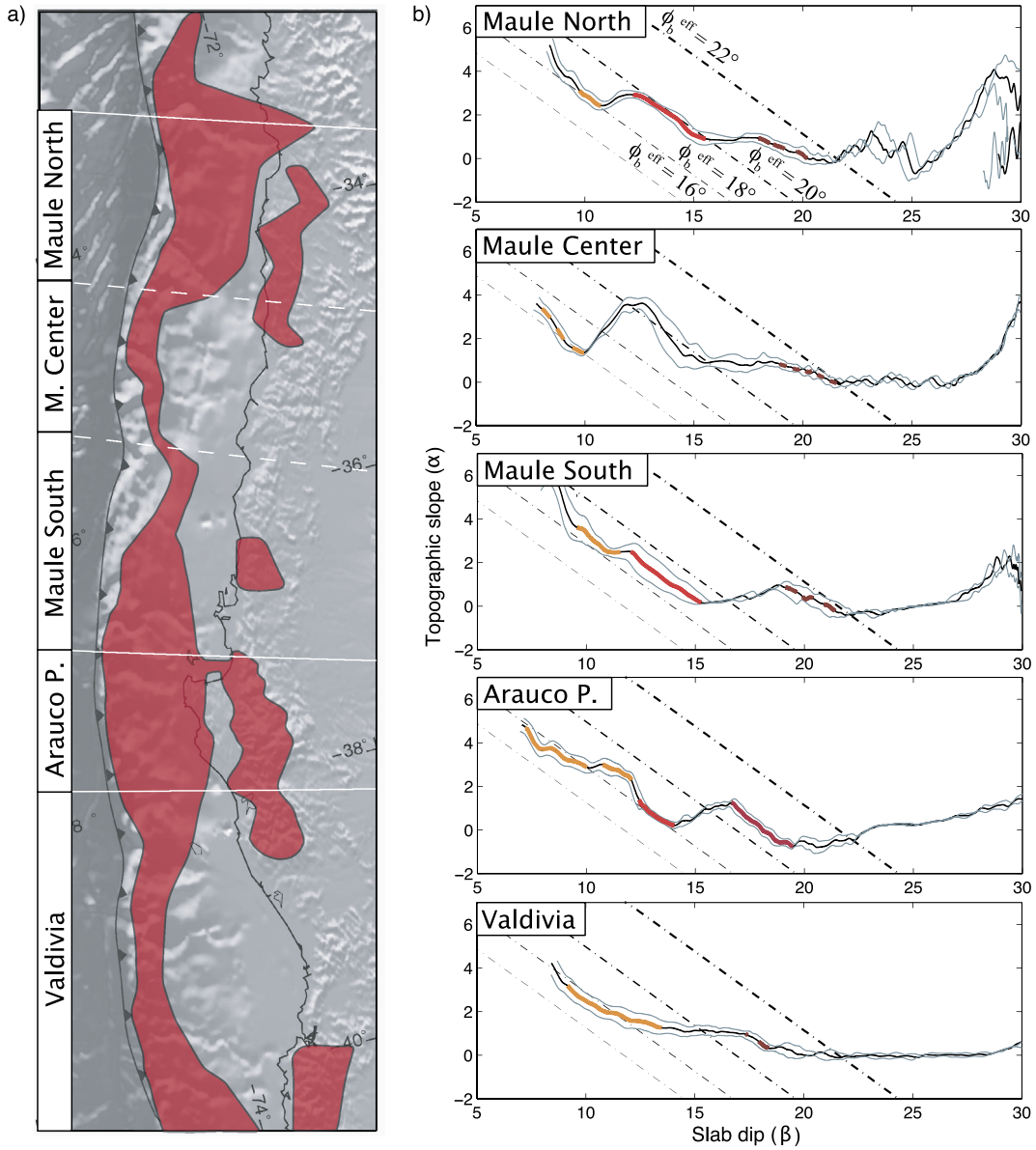

Fig. 5. (a) Areas at critical mechanical state are represented in red, the rest of the forearc is mechanically stable. (b) Tapers of each segment along the trench. Black: mean of the segment, gray: mean $\pm\,\sigma$. Critical sections are in orange for the accretionary prism, in red for the inner wedge, in dark red for the coastal cordillera. Dash-dotted lines are theoretical critical envelopes for increasing effective basal friction from $\phi_b^{eff} = 16$ to 22° ($\mu_b^{eff} = 0.28$–0.4) with an internal friction angle of 35° ($\mu = 0.7$) and a hydrostatic pore fluid pressure $\lambda = 0.4$. (For interpretation of the references to color in this figure legend, the reader is referred to the web version of this article.)

Two main critical regions are thus revealed by this analysis:

- one at the frontal part of the forearc mainly corresponding to the accretionary prism, with wider regions in the northern part of the Maule segment, and at the Arauco Peninsula,
- some portions of the Coastal Cordillera, such as the northern part of the Maule segment, the Arauco Peninsula and the Nahuelbuta range East of the peninsula, and the southern cordillera of the Valdivía segment.

All other areas are mechanically stable.

Now that the presumably critical areas are identified, we proceed to retrieve the corresponding best-fitting model parameters. To do so, we first computed a mean and standard deviation for each critical zone (Fig. 5b). We assume a density of 2800 kg/m^3 and calculate the predicted dip angle of the megathrust, β^{calc}, based on the critical taper theory given the observed topographic slope α. There are three model parameters: the internal friction angle ϕ_{int}, the effective basal friction angle ϕ_b^{eff} and the internal pore fluid ratio λ. We evaluate the merit of each set of model parameters by comparing the predicted, β^{calc} (Eq. (1)), and observed, β^{obs}, values of the taper angle with an L2 norm (assuming a Gaussian distribution of errors). The uncertainty on the taper angle is $\sigma = \sigma_{\beta_{obs}} + \sigma_\alpha$ including the contribution of the uncertainties on the topographic slope, $\sigma_{\alpha_{obs}}$ and dip angle $\sigma_{\beta_{obs}}$ on the predicted taper angle. The misfit M function calculated for each point of the sampling ($n\beta$) is then:

$$M_\beta = \frac{1}{n\beta + 1} \sum_{i=1}^{n\beta} \frac{1}{2} \frac{(\beta^{obs}(i) - \beta^{cal}(i))^2}{(\sigma(i))^2}. \tag{7}$$

The probability density distribution of the model parameters is computed based on the misfit, following Tarantola (2005):

$$P(\phi_{int}, \phi_b^{eff}, \lambda) = \frac{1}{K} e^{-M(\phi_{int}, \phi_b^{eff}, \lambda)}, \tag{8}$$

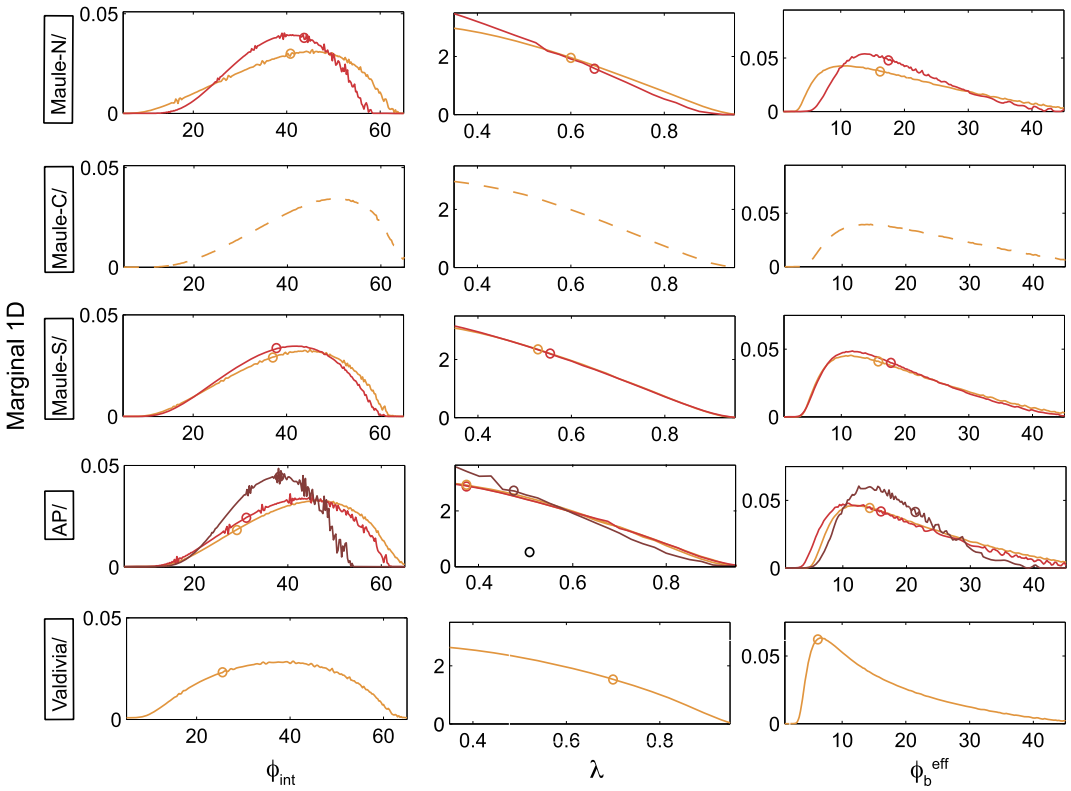

Fig. 6. Marginal 1D probability distributions for the three Maule segments (North, Central and South), the Arauco Peninsula (AP) segment and the Valdivía segment. ϕ_{int} the internal friction, λ the internal pore fluid ratio, ϕ_b^{eff} the effective basal friction. Results in orange for the accretionary prism, in red for the inner wedge and in dark red for the coastal cordillera. Best fits represented by circles. (For interpretation of the references to color in this figure legend, the reader is referred to the web version of this article.)

with K the constant normalization factor of the probability over the model space:

$$K = \int_{\phi_i nt} \int_{\phi_b^{eff}} \int_{\lambda} e^{-M(\phi_{int}, \phi_b^{eff}, \lambda)} \, d\phi_{int} \, d\phi_b^{eff} \, d\lambda. \tag{9}$$

Since the probability density has three dimensions, to visualize the results, 1D marginal probabilities are calculated from integrations over two model space parameters. These marginal probabilities provide the distributions of one parameter independently of others, also named 1D marginal probability density (Fig. 6), for instance for ϕ_{int}:

$$P(\phi_{int}) = \int_{\phi_b^{eff}} \int_{\lambda} P\left(\phi_{int}, \phi_b^{eff}, \lambda\right) d\phi_b^{eff} \, d\lambda. \tag{10}$$

The pore fluid pressure ratio is loosely constrained but consistently shows a most likely value close to hydrostatic ($\lambda = 0.4$). The probability distribution function of the internal friction peaks between 40 and 45° ($\mu_{int} = 0.83$ to 1), with 68% of probability of being in the range of 25 to 50° ($\mu_{int} = 0.44$ to 1.19) with slightly lower values below the Nahuelbuta range (35°, $\mu_{int} = 0.7$). For the Valdivía area, the effective basal friction of the accretionary prism shows low values with peaks at about 7 to 8° ($\mu_b^{eff} = 0.12$ to 0.14). The Arauco Peninsula accretionary wedge yields somewhat higher values (12°, $\mu_b^{eff} = 0.21$), and the effective basal friction increases again beneath the Nahuelbuta range (16°, $\mu_b^{eff} = 0.28$). For the Maule segment, the effective basal friction beneath the outer wedge peaks at 11–15°, $\mu_b^{eff} = 0.19$–0.26. The central Maule segment shows strong morphological variations, inversion results are thus poorly constrained. The same applies for the coastal cordillera of the Maule and Valdivía segments. Best fitting values are reported in Table 1. As the basal pore pressure is most likely equal or higher than the internal one, basal frictions were reported for the case $\lambda_b = \lambda$, providing a lower bound on the basal friction angle. The values of ϕ_{int} and λ obtained from this analysis are mostly reasonable. For comparison, laboratory measurements of internal friction angles for most common quartzo-feldspathic rocks are generally in the range of 0.6 to 0.85 (Byerlee, 1978). By contrast, the value of the effective basal friction is low and could point to either dominantly low friction minerals along the megathrust or high pore pressure.

In a second step, to limit the trade-off among the model parameters, we run partial inversion fixing either the internal friction to a standard value ($\phi_{int} = 35°$) or the internal pore pressure ratio parameter to hydrostatic ($\lambda = 0.4$) (Fig. 7). From the probability distribution as well as the best fit results reported in the supplementary material, Tables SM 2-1 and SM 2-2, the internal friction appears to be constrained to a narrower range, between 26 and 35°, and the pore pressure ratio is confirmed to be hydrostatic excepted along the accretionary prism of the Valdivía segment where larger values are required. In order to provide a view of the spatial variations of the frictional properties, the best fitting effective basal friction of each section has been reported in Fig. 9.

The effective basal friction is quite homogeneous in the accretionary prism of the Arauco and Maule segments with values ranging between 14 and 17.5° ($\mu_b^{eff} = 0.25$–0.31). It appears larger below the Nahuelbuta range at 21.25° ($\mu_b^{eff} = 0.39$) and lower in the accretionary prism along the Valdivía segment ($\phi_b^{eff} = 6°$, $\mu_b^{eff} = 0.1$). We show in the appendix that the analysis is robust despite the large uncertainty on the megathrust geometry.

Table 1
Best misfit for each segment.

Segment	λ	ϕ_{int} (°)	μ_{int}	ϕ_b^{eff} (°)	μ_b^{eff}	ϕ_b if $\lambda_b = \lambda$	μ_b if $\lambda_b = \lambda$
Maule North							
accretionary prism	0.60	40.75	0.86	16.25	0.29	36	0.72
inner wedge	0.65	43.75	0.95	17.5	0.31	41.5	0.88
Maule South							
accretionary prism	0.55	37.0	0.75	15.75	0.28	32.9	0.62
inner wedge	0.525	37.75	0.77	17.5	0.31	33	0.65
Arauco Peninsula							
accretionary prism	0.375	29.25	0.56	14.25	0.25	22	0.4
inner wedge	0.375	31.5	0.61	16.0	0.28	24	0.45
coastal cordillera	0.475	38.5	0.79	21.25	0.39	36.6	0.74
Valdivía							
accretionary prism	0.7	25.75	0.48	6.25	0.11	20	0.36

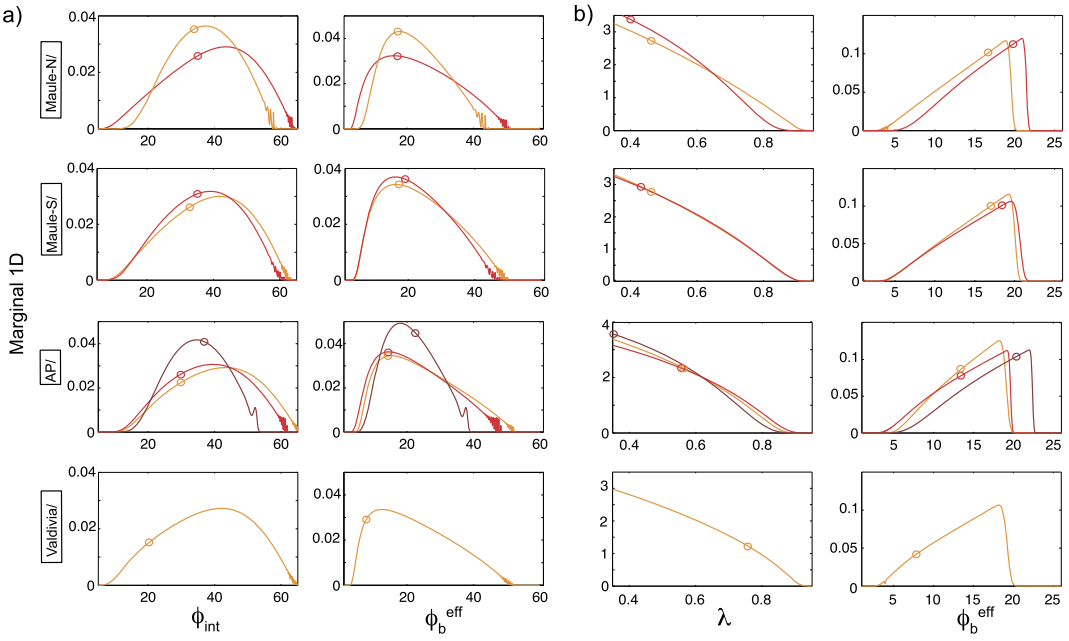

Fig. 7. Marginal 1D probability distributions of (a) ϕ_{int} and ϕ_b^{eff} with $\lambda = 0.4$, (b) ϕ_b^{eff} and λ with $\phi_{int} = 35°$. Results in orange for the accretionary prism, in red for the inner wedge and in dark red for the coastal cordillera. (For interpretation of the references to color in this figure legend, the reader is referred to the web version of this article.)

4. Spatial variations of frictional properties deduced from the limit analysis

Here we use the information available on the geometry and location of some splay faults to bring additional constraints on the frictional properties along the megathrust. To do so, we now apply the limit analysis approach (Chandrasekharaiah and Debnath, 1994; Salençon, 2002). This approach is based on the principle of virtual powers and the theorem of maximum rock strength (Maillot and Leroy, 2006). In this study, the Coulomb criterion is used to define the maximum rock strength. The method investigates all possible collapse mechanisms as a function of the frictional properties and selects the optimal one leading to the least upper bound to the tectonic force. The advantages compared with the critical taper theory are that there is no need to assume homogeneous mechanical properties nor that the wedge be at critical state. This method has previously been applied to retrieve frictions along the Nankai accretionary prism (Cubas et al., 2008; Souloumiac et al., 2009; Pons et al., 2013) and validated by comparison with analogue sandbox experiments (Cubas et al., 2013). The analysis is analytical for simple geometries and numerical otherwise. The procedure presented by Souloumiac et al. (2010) is applied here.

As a test example meant to develop some intuition of the model prediction, we ran some simulations in which we assume a planar megathrust and a constant taper angle (Fig. 8 a to c). We assume three segments with different but uniform basal friction along each. We choose an initial geometry so that the wedge is stable but close to critical in horizontal compression. The explored kinematics correspond to sliding along the full length of a portion of the megathrust with or without internal faulting within the wedge. Fully activated megathrust implies the formation of splay faults at the transition between the segments of different frictions. In the case of an increase of friction towards the trench, a backthrust forms at the transition (Fig. 8a), whereas a decrease of friction leads to the formation of a forethrust (Fig. 8b). A strong decrease can even lead to the formation of a normal fault (Fig. 8c). Virtual velocities (Chandrasekharaiah and Debnath, 1994; Salençon, 2002) are provided in the supplementary material (Fig. S3). Pons and Leroy (2012) studied the same prototype with two distinct regions on the megathrust and confirmed by analytical means that transition of frictions could lead to the formation of splay faults.

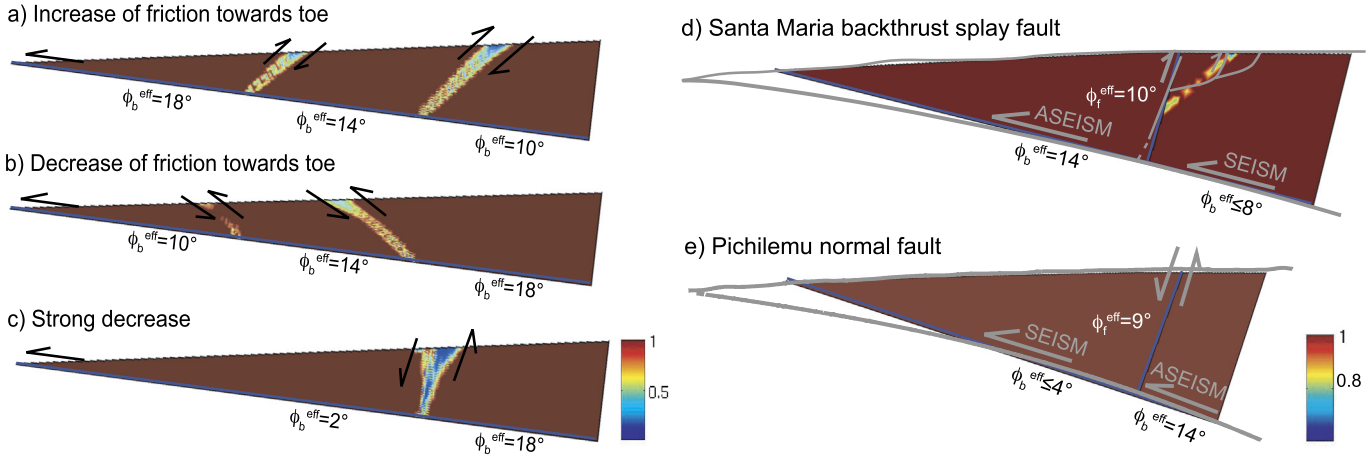

Fig. 8. Distance to the Coulomb criterion (red: far from the rupture, blue: at the rupture) for (a) an increase of effective basal friction towards the toe, (b) a decrease of basal friction towards the toe, (c) a very strong decrease, for a wedge of 200 km long, transitions at 60 and 120 km, with a topographic slope $\alpha = 3°$ and a décollement dip $\beta = 6°$, internal friction of 30°, (d) the Santa Maria backthrust set-up with $\phi_{int}^{eff} = 21°$, (e) the Pichilemu normal fault with $\phi_{int}^{eff} = 18.5°$. (For interpretation of the references to color in this figure legend, the reader is referred to the web version of this article.)

We start with the modeling of the Santa Maria backthrust splay fault (Fig. 8d). Since the fault is thought to be a pre-existing re-activated normal fault, the fault geometry is prescribed based on the geometry derived from structural and geophysical observations (Melnick et al., 2006). Since the variations of the topographic and basal slopes are small compared to the wedge thickness, we simplify the geometry by assuming a constant megathrust dip angle ($\beta = 13.5°$) and two different topographic slopes, one for the outer wedge ($\alpha_1 = 1.7°$) another for the Arauco shelf basin ($\alpha_2 = 0°$). The modeled megathrust is 104 km long.

The internal friction and updip basal friction are imposed to the values derived from the critical taper analysis. The effective internal friction is set at $\phi_{int}^{eff} = 21°$ ($\mu_{int}^{eff} = 0.383$, for $\phi_{int} = 31.5°$ and $\lambda = 0.375$). We then seek the effective basal friction within the seismogenic zone and the backthrust effective friction that will activate the fault. In order to activate the backthrust, the friction along this fault has to be equal or larger than $\phi_f^{eff} \geqslant 10°$ ($\mu_f^{eff} \geqslant 0.17$). Some secondary shear zone rooting into the backthrust are systematically observed. It is due to the fact that the backthrust is not optimally oriented, leading to secondary faults alike those featured in the structural section of Melnick et al. (2006). For $\phi_{aseis}^{eff} = 16°$ ($\mu_{aseis}^{eff} = 0.28$) along the updip aseismic portion of the megathrust found with the critical taper theory, activation of the splay fault requires the effective basal friction in the seismogenic zone to be lower or equal to $\phi_{seis}^{eff} = 12°$ ($\mu_{seis}^{eff} = 0.21$). For slightly lower $\phi_{aseis}^{eff} = 14°$, the geometry of the secondary backthrust matches better the observations. Activation of the splay fault then requires the effective basal friction in the seismogenic zone to be lower or equal to $\phi_{seis}^{eff} \leqslant 10°$ ($\mu_{seis}^{eff} \leqslant 0.17$). The limit analysis approach provides virtual velocities along each segment of faults. The ratio between the virtual velocities of two segments projected along their fault is assumed to be equal to the ratio of actual displacement between those segments. We find that to get about the right proportion between the vertical throw on the Santa Maria backthrust (1.6 m, Melnick et al., 2012) and the slip along the seismogenic zone below the island (6 m, Lin et al., 2013), for a $\phi_{aseis}^{eff} = 14°$ ($\mu_{aseis}^{eff} = 0.25$), the seismogenic effective friction has to be $\phi_{seis}^{eff} < 4°$ ($\mu_{seis}^{eff} < 0.07$).

The same analysis is now applied to the normal fault activated by the Pichilemu aftershock sequence which started two weeks after the Maule earthquake (Ryder et al., 2012; Farías et al., 2011). We consider a pre-existent fault striking 70°E (Fig. 8e). The décollement dip angle is set to $\beta = 19°$ and two different topographic slopes were considered, one for the coastal area ($\alpha_1 = 0°$) another for the shelf basin ($\alpha_2 = 1.5°$) along a 120 km long wedge.

Based on the critical taper results for the inner wedge, the effective internal friction is set to $\phi_{int}^{eff} = 18.5°$ ($\mu_{int}^{eff} = 0.344$, for $\phi_{int} = 43.75°$, $\lambda = 0.65$) and the down-dip basal friction is chosen so that the wedge is close to critical state in horizontal compression with $\phi_{aseis}^{eff} = 14°$ ($\mu_{aseis}^{eff} = 0.25$). To obtain normal motion on the fault, the seismogenic effective basal friction has to be lower or equal to $\phi_{seis}^{eff} \leqslant 8°$ (for $\phi_{aseis}^{eff} \leqslant 0.14$) and the friction along the fault $\phi_f{}^{eff} \leqslant 9°$. No associated deformation is observed.

This analysis is based on a quasistatic force balance and we do not take into account possible dynamic branching. The deformation of the Santa Maria backthrust fault is permanent and recurrent and the Pichilemu aftershock sequence occurs two weeks after the main event. Thus, activation of these splay faults has most probably resulted from a static stress change, justifying our static stress equilibrium analysis.

5. Discussion/conclusion

We now discuss how the mechanical state of the forearc and the inferred frictional properties compare with the coseismic rupture, afterslip and interseismic locking of the megathrust. We use the coseismic slip and afterslip models obtained by Lin et al. (2013), from the joint inversion of geodetic, seismic, and tsunamic data (Fig. 9a). We also refer to the coseismic slip of the 1960 Mw 9.5 Valdivía earthquake of Moreno et al. (2010) (Fig. 9a) and the interseismic strain accumulation model of Métois et al. (2012) (Fig. 9b).

A striking result is that the rupture area of the Maule earthquake, and possibly of the 1960 Valdivía earthquake coincides with stable areas of the forearc and is surrounded with critical areas. The updip limit of the 2010 rupture coincide well with the maximal extent of the critical outer wedge. The coseismic slip due to the 1960 rupture seems to taper down quite abruptly beneath the critical outer wedge. We also observe that most of the wedge forearc seems critical in the Arauco Peninsula which separates the 1960 and 2010 ruptures, and in the area just North of the 2010 rupture. The few critical patches along the coastal cordillera also delimit the down-dip extent of the coseismic slip. Similarly, we observe that the megathrust beneath the stable areas of the forearc wedge was mostly locked in the interseismic period (Fig. 9b).

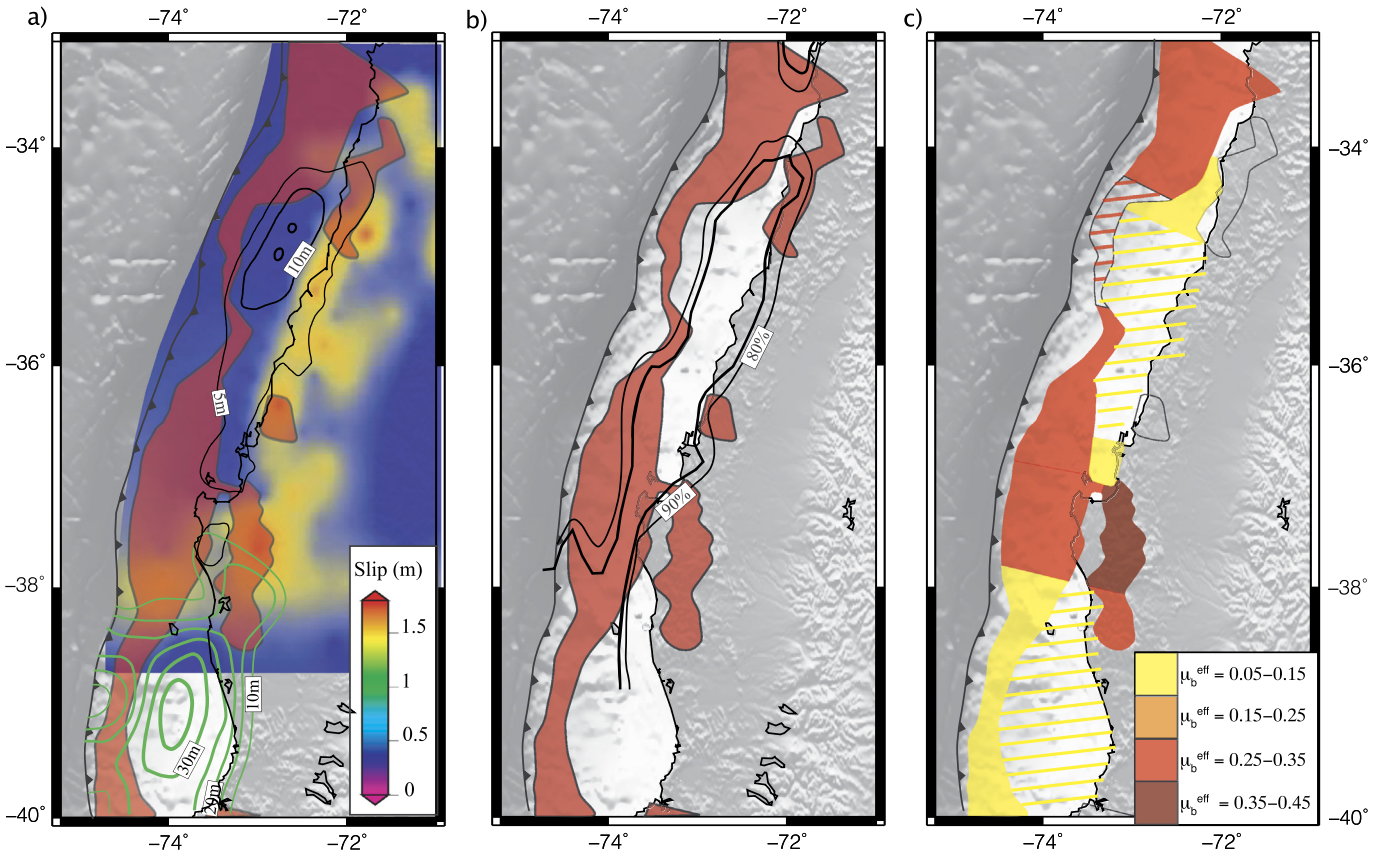

Fig. 9. Comparison of critical areas in red with (a) Maule earthquake coseismic and postseismic slip models from Lin et al. (2013) and Valdivía earthquake coseismic slip model from Moreno et al. (2010) with (b) interseismic strain accumulation model from Métois et al. (2012). (c) Effective basal friction map based on critical taper and limit analysis results, hatching: extrapolation of results. (For interpretation of the references to color in this figure legend, the reader is referred to the web version of this article.)

The comparison with the afterslip distribution is also instructing. Aseismic afterslip is observed downdip of the seismic rupture, below the Nahuelbuta range and seaward of the Arauco Peninsula (Lin et al., 2013). The critical areas appear thus to surround the seismic rupture and to be correlated with areas of postseismic sliding. These observations support the claim that the propagation of a megathrust seismic rupture is probably inhibited where the hanging wall is in critical mechanical state, in particular beneath the outer wedge and downdip of the rupture zone, beneath the coastal area. Furthermore, the observed correlations are consistent with the notion that the forearc is stable above the seismogenic portions of the megathrust, while the updip rate-strengthening portion of the megathrust is maintained in critical state as a result of the stress transfer operated by coseismic and postseismic deformation (Wang and Hu, 2006; Hu and Wang, 2008). The critical state of stress in the coastal area would rather be maintained by interseismic stress build up as aseismic creep proceeds downdip of the coseismic rupture. According to this model, all the deformation is accommodated along the megathrust in the seismogenic zone, no deformation being transferred to the upper plate. This model would explain the correlation between forearc basins or regions with negative gravity anomalies (Wells et al., 2003; Song and Simons, 2003) and seismic asperities. On the other hand, in the creeping areas, the forearc is at or close to critical state, and as a consequence, a small fraction of the convergence has to be accommodated by the upper plate leading to coastal uplift, active faulting in the accretionary prism and thrusting at the transition from the inner to the outer wedge (Fig. 2).

Since critical areas correlate well with aseismic zones, effective basal frictions along aseismic zones can thus be constrained thanks to the critical taper theory. Along the Arauco and Maule accretionary prism, according to the best fit results (Table 1 and Fig. 9c), the effective basal friction ranges between $\mu^{eff}_{aseis} = 0.25$ to 0.31 with a rather hydrostatic pore pressure ratio in the wedge. If the pore pressure along the megathrust is set equal to the pore pressure in the wedge, then the real static friction would range from $\mu_{aseis} = 0.4$ to 0.7, in good accordance with friction of clay deduced from laboratory experiments (Logan and Rauenzahn, 1987; Saffer and Marone, 2003; Moore and Lockner, 2004; Ikari et al., 2009). A similar range of effective basal friction values (0.2 to 0.28) has been previously found in other studies of the Nankai, Aleutians and Oregon accretionary prisms (Lallemand et al., 1994).

A stronger effective basal friction with hydrostatic pore pressure is found for the Arauco Peninsula and the Nahuelbuta Range ($\mu^{eff}_{aseis} = 0.4$), an area suspected to be a recurrent barrier to the propagation of earthquakes. If the internal pore pressure is set equivalent to the megathrust pore pressure, then the static friction along the aseismic megathrust portion downdip of the Maule rupture area would be $\mu_{aseis} = 0.7$. This larger value is consistent with the fact that at these depth and temperature conditions (typically 400 °C at 40 km depth, Völker et al., 2011) there is no reason to expect the kind of clay units that may well account for low friction of the upper portions of the megathrust. The rate-strengthening behavior deduced from the postseismic and interseismic models (Lin et al., 2013; Métois et al., 2012; Moreno et al., 2010) associated with the large static friction, low pore pressure and the heterogeneous deformation might explain why the peninsula is acting as a recurrent barrier (Kaneko et al., 2010).

If the frontal aseismic zone is rate-strengthening, then the effective basal frictions found in this study are most probably an average value of the higher friction most probably attained after

megathrust rupture as the outer wedge is then brought closer to failure (Wang and Hu, 2006). Along the seismogenic zone, lower effective basal frictions are deduced thanks to the modeling of splay faults with the limit analysis approach ($\mu^{eff}_{seis} \leqslant 0.14$). Since the Santa Maria backthrust has been activated during the main event, and if we consider the normal sequence of Pichilemu as a consequence of the main shock, the seismogenic friction found is most probably representative of the effective dynamic friction. Different possible explanations can be advanced for the low values determined in this study. An intrinsically low friction is a possibility in principle. This explanation seems improbable as the static friction retrieved for the surrounding aseismic zones is generally larger, and already at the lower end of the range that can be explained with low friction minerals, i.e. the clays of the accretionary prism.

The low effective basal friction in the seismogenic zone could alternatively reflect a high basal pore pressure, either permanent or due to a dynamic increase by thermal-pressurization. Dynamic modeling of earthquake cycles would be suitable to investigate this question.

Acknowledgements

This project was supported by the by the National Science Foundation through grant EAR-#1118239 and by the Gordon and Betty Moore Foundation through Grant GBMF #423.01 to the Caltech Tectonics Observatory. This is Tectonics Observatory contribution #236.

Appendix A. Tapers build up

The topography of individual profiles along the South Chilean forearc was first smoothed as shown in Fig. 3a to avoid high-frequency content. To prevent estimation errors on the mechanical interpretation linked to the smoothing, different smoothing window shapes (triangular and rectangular) and width (10, 25 and 40 km) were tested. For each smoothed profile, the topographic slope and the basal dip were calculated every 100 m. We then compared a profile with its different smoothing to theoretical envelopes (Supplementary Fig. S4). We evaluated the probability that a given portion of a profile follows a critical envelope based on the local linearity of the α–β curve. If the linearity appears obvious for all smoothing, we selected the portion of the profile supposed to be at critical state and reported it on the map in Fig. 5.

Swath profiles were then computed for each segment to obtain a mean and a standard deviation needed for the inversion. The same smoothing technique was applied. The inversion results are based on the profiles obtained with a rectangular 25 km width smoothing window. We also checked the consistency of the inversion results with a triangular window.

Appendix B. Effect of megathrust curvature

We ran numerical simulations with the limit analysis approach to validate the applicability of the critical taper theory derived for a triangular wedge, in the case of a curved megathrust. These simulations were run with the Optum-Geo software (2013) which turns out to be more convenient than our own tools due to its user friendly interface (Kristian Kranbbenhoft, personal communication). We consider a 100 km long wedge, and a megathrust with a constant radius of curvature of 100 km, close to the one observed for the megathrust in the Maule rupture area. We assume an internal friction of 30°, a basal friction of 15°, and compute the corresponding critical topographic slope α for the slab dip β from the relation for a cohesionless triangular wedge (Dahlen, 1984) with a point every 100 m as in our analysis (Supplementary Fig. S5a). We found that the criticality is observed for the same basal friction. In Supplementary Fig. S5b, the topographic slope exceeds by one degree the critical slope, the wedge is thus stable and the whole megathrust is activated. In Supplementary Fig. S5c, the topographic slope is lower by one degree than the critical slope, the wedge is thus unstable, only part of the megathrust is activated and a pop-up structure develops at the rear wall. The analytical solution is possible for a constant curvature and deserves some attention in the future.

Appendix C. Robustness of inversion results

Since the weakest parameter of this mechanical analysis is the megathrust dip β, we ran two simple tests in order to evaluate how a change on β could affect the results. In a first test, the megathrust dip β was changed by $\pm 5°$, and in a second test we applied a coefficient of $*1.5$ and $*0.66$, that we considered as reasonable errors (Supplementary Fig. S6). These changes only imply a horizontal translation of the taper and do not affect the critical state of the forearc. An error of 5° on β implies an error of about 3° on the effective basal friction, which is lower than the standard deviation of the probabilities. A coefficient error induces a change of dip of the critical envelope leading to a different couple of internal friction–internal pore fluid pressure. If the coefficient is lower than 1.5, the resulting error is again smaller than the standard deviation of the probability distribution.

Appendix D. Supplementary material

Supplementary material related to this article can be found online at http://dx.doi.org/10.1016/j.epsl.2013.07.037.

References

Amante, C., Eakins, B.W., 2009. ETOPO1 1 arc-minute global relief model: Procedures, data sources and analysis. NOAA Technical Memorandum NESDIS NGDC-24. 19 pp.

Angermann, D., Klotz, J., Reigber, C., 1999. Space-geodetic estimation of the Nazca–South America Euler vector. Earth Planet. Sci. Lett. 171, 329–334.

Bonnardot, M.A., Hassani, R., Tric, E., Ruellan, E., Régnier, M., 2008. Effect of margin curvature on plate deformation in a 3-D numerical model of subduction zones. Geophys. J. Int. 173, 1084–1094, http://dx.doi.org/10.1111/j.1365-246X.2008.03752.x.

Bookhagen, B., Echtler, H.P., Melnick, D., Strecker, M.R., Spencer, J.Q.G., 2006. Using uplifted Holocene beach berms for paleoseismic analysis on the Santa María Island, south-central Chile. Geophys. Res. Lett. 33, http://dx.doi.org/10.1029/2006GL026734.

Byerlee, J.D., 1978. Friction of rocks. Pure Appl. Geophys. 116, 615–626.

Byrne, D.E., Davis, D.M., Sykes, L.R., 1987. Loci and maximum size of thrust earthquakes and the mechanics of the shallow region of subduction zones. Tectonics 7, 833–857.

Campos, J., Hatzfeld, D., Madariaga, R., Kausel, E., Lopez, G., Zollo, A., Iannaconne, G., Barrientos, S., Lyon-Caen, H., 2002. A seismological study of the 1835 seismic gap in South Central Chile. Phys. Earth Planet. Inter. 132, 177–195, http://dx.doi.org/10.1016/s0031-9201(02)00051-1.

Chandrasekharaiah, D.S., Debnath, L., 1994. Continuum Mechanics. Academic Press, San Diego, California.

Collot, J.-Y., Agudelo, W., Ribodetti, A., Marcaillou, B., 2008. Origin of a crustal splay fault and its relation to the seismogenic zone and underplating at the erosional north Ecuador–south Colombia oceanic margin. J. Geophys. Res. 113, http://dx.doi.org/10.1029/2008JB005691.

Contreras-Reyes, E., Carrizo, D., 2011. Control of high oceanic features and subduction channel on earthquake ruptures along the Chile–Peru subduction zone. Phys. Earth Planet. Inter. 186 (1–2), 49–58, http://dx.doi.org/10.1016/j.pepi.2011.03.002.

Cubas, N., Leroy, Y.M., Maillot, B., 2008. Prediction of thrusting sequences in accretionary wedges. J. Geophys. Res. 113, http://dx.doi.org/10.1029/2008JB005717.

Cubas, N., Barnes, C., Maillot, B., 2013. Inverse method applied to a sand wedge: estimation of friction parameters and uncertainty analysis. J. Struct. Geol. 55, 101–113, hhttp://dx.doi.org/10.1016/j.jsg.2013.07.003.

Dahlen, F.A., 1984. Noncohesive critical coulomb wedges: An exact solution. J. Geophys. Res. 89, 10125–10133.

Darwin, C., 1851. Geological Observations of South America. Smith and Elder, London. 279 pp.
Davis, D.M., Suppe, J., Dahlen, F.A., 1983. Mechanics of fold-and-thrust belts and accretionary wedges. J. Geophys. Res. 88, 1153–1172.
Delouis, B., Nocquet, J.M., Vallee, M., 2010. Slip distribution of the February 27, 2010 Mw = 8.8 Maule earthquake, central Chile, from static and high-rate GPS, InSAR, and broadband teleseismic data. Geophys. Res. Lett. 37, http://dx.doi.org/10.1029/2010GL043899.
DeMets, C., Gordon, R.G., Argus, F., Stein, S., 1994. Effect of recent revisions of the geomagnetic timescale on estimates of current plate motions. Geophys. Res. Lett. 21, 2191–2194.
Farías, M., Comte, D., Roecker, S., Carrizo, D., Pardo, M., 2011. Crustal extensional faulting triggered by the 2010 Chilean earthquake: The Pichilemu seismic sequence. Tectonics 30, http://dx.doi.org/10.1029/2011TC002888.
Fuller, C.W., Willett, S.D., Brandon, M.T., 2006. Formation of forearc basins and their influence on subduction zone earthquakes. Geology 34 (2), 65–68, http://dx.doi.org/10.1130/G21828.1.
Geersen, J., Behrmann, J.H., Volker, D., Krastel, S., Ranero, C.R., Diaz-Naveas, J., Weinrebe, W., 2011. Active tectonics of the South Chilean marine forearc (35°S–40°S). Tectonics 30 (3), http://dx.doi.org/10.1029/2010TC002777.
Glodny, J., Gräfe, K., Echtler, H., Rosenau, M., 2008. Mesozoic to Quaternary continental margin dynamics in south-central Chile (36–42S), The apatite and zircon fission track perspective. Int. J. Earth Sci. 97, 1271–1291, http://dx.doi.org/10.1007/s00531-007-0203-1.
Hassani, R., Jongmans, D., Chéry, J., 1997. Study of plate deformation and stress in subduction processes using two-dimensional numerical models. J. Geophys. Res. 102, 17951–17965, http://dx.doi.org/10.1029/97JB01354.
Hayes, G.P., Wald, D.J., Johnson, R.L., 2012. Slab1.0: A three-dimensional model of global subduction zone geometries. J. Geophys. Res. 117, http://dx.doi.org/10.1029/2011JB008524.
Hu, Y., Wang, K., 2008. Coseismic strengthening of the shallow portion of the subduction fault and its effects on wedge taper. J. Geophys. Res. 113, http://dx.doi.org/10.1029/2008JB005724.
Ikari, M.J., Saffer, D.M., Marone, C., 2009. Frictional and hydrologic properties of clay-rich fault gouge. J. Geophys. Res. 114, B05409, http://dx.doi.org/10.1029/2008JB006089.
Kaizuka, S., Matsuda, T., Nogami, M., Yonekura, N., 1973. Quaternary tectonic and recent seismic crustal movements in the Arauco peninsula and its environs, central Chile. Geogr. Rep. Tokyo Metrop. Univ. 8, 1–49.
Kaneko, Y., Avouac, J.-P., Lapusta, N., 2010. Towards inferring earthquake patterns from geodetic observations of interseismic coupling. Nat. Geosci. 3 (5), 363–369, http://dx.doi.org/10.1038/NGEO843.
Lallemand, S., Schnürle, P., Malavieille, J., 1994. Coulomb theory applied to accretionary and non accretionary wedges: Possible causes for tectonic erosion and/or frontal accretion. J. Geophys. Res. 99, 12033–12055.
Lamb, S., Davis, P., 2003. Cenozoic climate change as a possible cause for the rise of the Andes. Nature 425, 792–797, http://dx.doi.org/10.1038/nature02049.
Lehner, F.K., 1986. Comments on "Noncohesive critical Coulomb wedges: An exact solution". J. Geophys. Res. 9, 793–796.
Lin, Y.N., Sladen, A., Ortega-Culaciati, F., Simons, M., Avouac, J.P., Fielding, E.J., Brooks, B.A., Bevis, M., Genrich, J., Rietbrock, A., Vigny, C., Smalley, R., Socquet, A., 2013. Coseismic and postseismic slip associated with the 2010 Maule earthquake, Chile: Characterizing the Arauco Peninsula barrier effect. J. Geophys. Res. 118, http://dx.doi.org/10.1002/jgrb.50207.
Logan, J.M., Rauenzahn, K.A., 1987. Frictional dependence of gouge mixtures of quartz and montmorillonite on velocity, composition and fabric. Tectonophysics 144, 87–108, http://dx.doi.org/10.1016/0040-1951(87)90010-2.
Lomnitz, C., 1970. Major earthquakes and tsunamis in Chile during the period 1535 to 1955. Geol. Rundsch. 59, 938–960, http://dx.doi.org/10.1007/BF02042278.
Lorito, S., Romano, F., Atzori, S., Tong, X., Avallone, A., McCloskey, J., Cocco, M., Boschi, E., Piatanesi, A., 2011. Limited overlap between the seismic gap and coseismic slip of the great 2010 Chile earthquake. Nat. Geosci. 4, 173–177, http://dx.doi.org/10.1038/ngeo1073.
Madariaga, R., Vigny, Ch., Métois, M., Campos, J., 2010. Central Chile finally breaks. Science 238, 181–182, http:dx.doi.org/10.1126/science.1189197.
Maillot, B., Leroy, Y.M., 2006. Kink-fold onset and development based on the maximum strength theorem. J. Mech. Phys. Solids 54, 2030–2059, http://dx.doi.org/10.1016/j.jmps.2006.04.004.
Melnick, D., Bookhagen, B., Echtler, H., Strecker, M., 2006. Coastal deformation and great subduction earthquakes, Isla Santa María, Chile (37°S). Geol. Soc. Am. Bull. 118, 1463–1480, http://dx.doi.org/10.1130/B25865.1.
Melnick, D., Bookhagen, B., Strecker, M., Echtler, H., 2009. Segmentation of megathrust rupture zones from fore arc deformation patterns over hundreds to millions of years, Arauco peninsula, Chile. J. Geophys. Res. 114, http://dx.doi.org/10.1029/2008JB005788.
Melnick, D., Echtler, H., 2010. Inversion of forearc basins in south-central Chile caused by rapid glacial age trench fill. Geology 34 (9), 709–712, http://dx.doi.org/10.1130/G22440.1.
Melnick, D., Moreno, M., Motagh, M., Cisternas, M., Wesson, R.L., 2012. Splay fault slip during the Mw 8.8 2010 Maule Chile earthquake. Geology 40 (3), 251–254, http://dx.doi.org/10.1130/G32712.1.
Métois, M., Socquet, A., Vigny, C., 2012. Interseismic coupling, segmentation and mechanical behavior of the Central Chile subduction zone. J. Geophys. Res. 117, http://dx.doi.org/10.1029/2011JB008736.
Moore, D.E., Lockner, D.A., 2004. Crystallographic controls on the frictional behavior of dry and water-saturated sheet structure minerals. J. Geophys. Res. 109, http://dx.doi.org/10.1029/2003JB002582.
Moreno, M., Rosenau, M., Oncken, O., 2010. Maule earthquake slip correlates with pre-seismic locking of Andean subduction zone. Nature 467, 198–202, http://dx.doi.org/10.1038/nature09349.
OptumGEo, 2013. Optum computational engineering. www.optumce.com.
Pons, A., Leroy, Y.M., 2012. Stability of accretionary wedges based on the maximum strength theorem for fluid-saturated porous media. J. Mech. Phys. Solids 60, 643–664, http://dx.doi.org/10.1016/j.jmps.2011.12.011.
Pons, A., Leroy, Y.M., Lallemant, S., 2013. Fluid pressure control on splay fault activation in accretionary prism based on the maximum strength theorem with application to the Nankai wedge. Earth Planet. Sci. Lett. 368, 4350, http://dx.doi.org/10.1016/j.epsl.2013.02.038.
Rietbrock, A., Ryder, I., Hayes, G., Haberland, C., Comte, D., Roecker, S., Lyon-Caen, H., 2012. Aftershock seismicity of the 2010 Maule Mw = 8.8, Chile, earthquake: Correlation between co-seismic slip models and aftershock distribution? Geophys. Res. Lett. 39, http://dx.doi.org/10.1029/2012GL051308.
Rosenau, M., Oncken, O., 2009. Fore-arc deformation controls frequency–size distribution of megathrust earthquakes in subduction zones. J. Geophys. Res. 114, http://dx.doi.org/10.1029/2009JB006359.
Ruegg, J.C., Rudloff, A., Vigny, C., Madariaga, R., de Chabalier, J.B., Campos, J., Kausel, E., Barrientos, S., Dimitrov, D., 2009. Interseismic strain accumulation measured by GPS in the seismic gap between Constitucion and Concepcion in Chile. Phys. Earth Planet. Inter. 175 (1–2), 78–85.
Ruff, L.J., Tichelaar, B.W., 1996. What controls the seismogenic plate interface in subduction zones? In: Bebout, E., et al. (Eds.), Subduction Top to Bottom. In: Geophys. Monogr., vol. 96. AGU, Washington, DC, pp. 105–111.
Ryder, I., Rietbrock, R., Kelson, K., Burgmann, R., 2012. Large extensional aftershocks in the continental forearc triggered by the 2010 Maule earthquake, Chile. Geophys. J. Int. 188 (3), http://dx.doi.org/10.1111/j.1365-246X.2011.0532.
Saffer, D.M., Marone, C., 2003. Comparison of smectite and illite rich gouge frictional properties: application to the updip limit of the seismogenic zone along subduction megathrusts. Earth Planet. Sci. Lett. 215 (1–2), 219–235, http://dx.doi.org/10.1016/S0012-821X(03)00424-2.
Salençon, J., 2002. De l'Elasto-Plasticité au Calcul à la Rupture. Ellipses, Paris. 264 pp.
Schobbenhaus, C., Bellizzia, A., 2001. Geological map of South America, 1:5000000. CGMW-CPRM-DNPM-UNESCO, Brasilia.
Sladen, A., Tavera, H., Simons, M., Avouac, J.P., Konca, A.O., Perfettini, H., Audin, L., Fielding, E.J., Ortega, F., Cavagnoud, R., 2010. Source model of the 2007 Mw 8.0 Pisco, Peru earthquake: Implications for seismogenic behavior of subduction megathrust s. J. Geophys. Res. 115, http://dx.doi.org/10.1029/2009JB006429.
Song, T.A., Simons, M., 2003. Large trench-parallel gravity variations predict seismogenic behavior in subduction zones. Science 301, 630–633, http://dx.doi.org/10.1126/science.1085557.
Souloumiac, P., Leroy, Y.M., Maillot, B., Krabbenhøft, K., 2009. Predicting stress distributions in fold-and-thrust belts and accretionary wedges by optimization. J. Geophys. Res. 114, http://dx.doi.org/10.1029/2008JB005986.
Souloumiac, P., Krabbenhøft, K., Leroy, Y.M., Maillot, B., 2010. Failure in accretionary wedges with the maximum strength theorem: numerical algorithm and 2D validation. Comput. Geosci. 14, 793–811, http://dx.doi.org/10.1007/s10596-010-9184-4.
Tarantola, A., 2005. Inverse Problem Theory and Model Parameter Estimation. SIAM, ISBN 978-0-89871-572-9.
Vigny, C., Socquet, A., Peyrat, S., Ruegg, J.-C., Métois, M., Madariaga, R., Morvan, S., Lancieri, M., Lacassin, R., Campos, J., Carrizo, D., Bejar-Pizarro, M., Barrientos, S., Armijo, R., the SSN team, the LIA-MdB team, the CAP team, 2011. The 2010 (Mw 8.8) Maule mega-thrust earthquake of Central Chile, monitored by GPS. Science 332 (6036), 1417–1421, http://dx.doi.org/10.1126/science.1204132.
Völker, D., Grevemeyer, I., Stipp, M., Wang, K., He, J., 2011. Thermal control of the seismogenic zone of southern central Chile. J. Geophys. Res. 116, http://dx.doi.org/10.1029/2011JB008247.
Wang, K., Hu, Y., 2006. Accretionary prisms in subduction earthquake cycles: The theory of dynamic Coulomb wedge. J. Geophys. Res. 111, http://dx.doi.org/10.1029/2005JB004094.
Wang, K., He, J., Hu, Y., 2006. A note on pore fluid pressure ratios in the Coulomb wedge theory. Geophys. Res. Lett. 33, L19310, http://dx.doi.org/10.1029/2006GL027233.
Wells, R.E., Blakely, R.J., Sugiyama, Y., Scholl, D.W., Dinterman, P.A., 2003. Basin-centered asperities in great subduction zone earthquakes: A link between slip, subsidence and subduction erosion? J. Geophys. Res. 108, 2507, http://dx.doi.org/10.1029/2002JB002072.

Bibliographie

J. Adam, D. Klaeschen, N. Kukowski, and E. Flueh. Upward delamination of cascadia basin sediment infill with landward frontal accretion thrusting caused by rapid glacial age material flux. *Tectonics*, 23(3), 2004.

K. L. Allison and E. M. Dunham. Earthquake cycle simulations with rate-and-state friction and power-law viscoelasticity. *Tectonophysics*, 733 :232–256, 2018.

N. Ambraseys and C. Melville. A history of persian earthquakes Ì§cambridge university press, 1982.

C. J. Ammon, C. Ji, H.-K. Thio, D. Robinson, S. Ni, V. Hjorleifsdottir, H. Kanamori, T. Lay, S. Das, D. Helmberger, et al. Rupture process of the 2004 sumatra-andaman earthquake. *science*, 308(5725) :1133–1139, 2005.

Y. Aoki, T. Tamano, and S. Kato. Detailed structure of the nankai trough from migrated seismic sections : Convergent margins : Field investigations of margin structure and stratigraphy. 1982.

Y. Asano, T. Saito, Y. Ito, K. Shiomi, H. Hirose, T. Matsumoto, S. Aoi, S. Hori, and S. Sekiguchi. Spatial distribution and focal mechanisms of aftershocks of the 2011 off the pacific coast of tohoku earthquake. *Earth, planets and space*, 63(7) :669–673, 2011.

J. Ashi, H. Tokuyama, and A. Taira. Distribution of methane hydrate bsrs and its implication for the prism growth in the nankai trough. *Marine Geology*, 187(1-2) :177–191, 2002.

B. F. Atwater and G. B. Griggs. *Deep-Sea Turbidites as Guides to Holocene Earthquake history at the Cascadia Subduction Zone : Alternative Views for a Seismic-Hazard Workshop*. US Department of the Interior, US Geological Survey, 2012.

P. Audet, M. G. Bostock, N. I. Christensen, and S. M. Peacock. Seismic evidence for over-pressured subducted oceanic crust and megathrust fault sealing. *Nature*, 457(7225) :76–78, 2009.

T. Baba and P. R. Cummins. Contiguous rupture areas of two nankai trough earthquakes revealed by high-resolution tsunami waveform inversion. *Geophysical Research Letters*, 32(8), 2005.

N. L. Bangs, G. K. Westbrook, J. W. Ladd, and P. Buhl. Seismic velocities from the barbados ridge complex : Indicators of high pore fluid pressures in an accretionary complex. *Journal of Geophysical Research : Solid Earth*, 95(B6) :8767–8782, 1990.

N. L. Bangs, S. P. Gulick, and T. H. Shipley. Seamount subduction erosion in the nankai trough and its potential impact on the seismogenic zone. *Geology*, 34(8) :701–704, 2006.

N. L. Bangs, J. Morgan, A. Tréhu, E. Contreras-Reyes, A. Arnulf, S. Han, K. Olsen, and E. Zhang. Basal accretion along the south central chilean margin and its relationship to great earthquakes. *Journal of Geophysical Research : Solid Earth*, 125(11) :e2020JB019861, 2020.

S. Barbot. Asthenosphere flow modulated by megathrust earthquake cycles. *Geophysical Research Letters*, 45(12) :6018–6031, 2018.

S. Barbot, N. Lapusta, and J.-P. Avouac. Under the hood of the earthquake machine : Toward predictive modeling of the seismic cycle. *Science*, 336(6082) :707–710, 2012.

D. Bassett and A. B. Watts. Gravity anomalies, crustal structure, and seismicity at subduction zones : 1. seafloor roughness and subducting relief. *Geochemistry, Geophysics, Geosystems*, 16(5) :1508–1540, 2015.

A. Bécel, D. J. Shillington, M. Delescluse, M. R. Nedimović, G. A. Abers, D. M. Saffer, S. C. Webb, K. M. Keranen, P.-H. Roche, J. Li, et al. Tsunamigenic structures in a creeping section of the alaska subduction zone. *Nature Geoscience*, 10(8) :609, 2017.

M. Béjar-Pizarro, A. Socquet, R. Armijo, D. Carrizo, J. Genrich, and M. Simons. Andean structural control on interseismic coupling in the north chile subduction zone. *Nature Geosc.*, 6(6) :462–467, 2013.

B. A. Bekins and S. J. Dreiss. A simplified analysis of parameters controlling dewatering in accretionary prisms. *Earth and Planetary Science Letters*, 109(3-4) :275–287, 1992.

R. Bell, R. Sutherland, D. H. Barker, S. Henrys, S. Bannister, L. Wallace, and J. Beavan. Seismic reflection character of the hikurangi subduction interface, new zealand, in the region of repeated gisborne slow slip events. *Geophysical Journal International*, 180(1) :34–48, 2010.

C. M. Bethke and S. P. Altaner. Layer-by-layer mechanism of smectite illitization and application to a new rate law. *Clays and Clay Minerals*, 34(2) :136–145, 1986.

M. Blanpied, D. Lockner, and J. Byerlee. Fault stability inferred from granite sliding experiments at hydrothermal conditions. *Geophysical Research Letters*, 18(4) :609–612, 1991.

M. L. Blanpied, D. A. Lockner, and J. D. Byerlee. Frictional slip of granite at hydrothermal conditions. *Journal of Geophysical Research : Solid Earth*, 100(B7) :13045–13064, 1995.

Q. Bletery, A. M. Thomas, A. W. Rempel, L. Karlstrom, A. Sladen, and L. De Barros. Mega-earthquakes rupture flat megathrusts. *Science*, 354(6315) :1027–1031, 2016.

M. Bonini. Deformation patterns and structural vergence in brittle–ductile thrust wedges : an additional analogue modelling perspective. *Journal of Structural Geology*, 29(1) :141–158, 2007.

C. Bonnet, J. Malavieille, and J. Mosar. Interactions between tectonics, erosion, and sedimentation during the recent evolution of the alpine orogen : Analogue modeling insights. *Tectonics*, 26(6), 2007.

S. Borderie, F. Graveleau, C. Witt, and B. C. Vendeville. Impact of an interbedded viscous décollement on the structural and kinematic coupling in fold-and-thrust belts : Insights from analogue modeling. *Tectonophysics*, 722 :118–137, 2018.

C. Bray and D. Karig. Porosity of sediments in accretionary prisms and some implications for dewatering processes. *Journal of Geophysical Research : Solid Earth*, 90(B1) :768–778, 1985.

S. J. Buiter. A review of brittle compressional wedge models. *Tectonophysics*, 530 :1–17, 2012.

S. J. Buiter, G. Schreurs, M. Albertz, T. V. Gerya, B. Kaus, W. Landry, L. Le Pourhiet, Y. Mishin, D. L. Egholm, M. Cooke, et al. Benchmarking numerical models of brittle thrust wedges. *Journal of Structural Geology*, 92 :140–177, 2016.

D. E. Byrne, D. M. Davis, and L. R. Sykes. Loci and maximum size of thrust earthquakes and the mechanics of the shallow region of subduction zones. *Tectonics*, 7(4) :833–857, 1988.

D. E. Byrne, L. R. Sykes, and D. M. Davis. Great thrust earthquakes and aseismic slip along the plate boundary of the makran subduction zone. *Journal of Geophysical Research : Solid Earth*, 97(B1) :449–478, 1992.

A. Calahorrano, V. Sallarès, J.-Y. Collot, F. Sage, and C. R. Ranero. Nonlinear variations of the physical properties along the southern ecuador subduction channel : Results from depth-migrated seismic data. *Earth and Planetary Science Letters*, 267(3-4) :453–467, 2008.

Y. Caniven and S. Dominguez. Validation of a multilayered analog model integrating crust-mantle visco-elastic coupling to investigate subduction megathrust earthquake cycle. *Journal of Geophysical Research : Solid Earth*, 126(2) :e2020JB020342, 2021.

J. Carreras. Zooming on northern cap de creus shear zones. *Journal of Structural Geology*, 23 (9) :1457–1486, 2001.

D. Chandrasekharaiah and L. Debnath. Continuum mechanics (new york : Academic). 1994.

M. Chlieh, J.-P. Avouac, V. Hjorleifsdottir, T.-R. A. Song, C. Ji, K. Sieh, A. Sladen, H. Hebert, L. Prawirodirdjo, Y. Bock, et al. Coseismic slip and afterslip of the great m w 9.15 sumatra–andaman earthquake of 2004. *Bulletin of the Seismological Society of America*, 97(1A) : S152–S173, 2007.

M. Chlieh, J.-P. Avouac, K. Sieh, D. H. Natawidjaja, and J. Galetzka. Heterogeneous coupling of the sumatran megathrust constrained by geodetic and paleogeodetic measurements. *Journal of Geophysical Research : Solid Earth*, 113(B5), 2008.

P. Clift and P. Vannucchi. Controls on tectonic accretion versus erosion in subduction zones : Implications for the origin and recycling of the continental crust. *Reviews of Geophysics*, 42 (2), 2004.

P. D. Clift, I. Pecher, N. Kukowski, and A. Hampel. Tectonic erosion of the peruvian forearc, lima basin, by subduction and nazca ridge collision. *Tectonics*, 22(3), 2003.

M. Cloos. Thrust-type subduction-zone earthquakes and seamount asperities : A physical model for seismic rupture. *Geology*, 20(7) :601–604, 1992.

B. Colletta, J. Letouzey, R. Pinedo, J. F. Ballard, and P. Balé. Computerized x-ray tomography analysis of sandbox models : Examples of thin-skinned thrust systems. *Geology*, 19(11) : 1063–1067, 1991.

J.-Y. Collot, W. Agudelo, A. Ribodetti, and B. Marcaillou. Origin of a crustal splay fault and its relation to the seismogenic zone and underplating at the erosional north ecuador–south colombia oceanic margin. *Journal of Geophysical Research : Solid Earth*, 113(B12), 2008.

J.-Y. Collot, A. Ribodetti, W. Agudelo, and F. Sage. The south ecuador subduction channel : Evidence for a dynamic mega-shear zone from 2d fine-scale seismic reflection imaging and implications for material transfer. *Journal of Geophysical Research : Solid Earth*, 116(B11), 2011.

J.-Y. Collot, E. Sanclemente, J.-M. Nocquet, A. Leprêtre, A. Ribodetti, P. Jarrin, M. Chlieh, D. Graindorge, and P. Charvis. Subducted oceanic relief locks the shallow megathrust in central ecuador. *JGR*, 122(5) :3286–3305, 2017.

E. Contreras-Reyes, I. Grevemeyer, E. R. Flueh, and C. Reichert. Upper lithospheric structure of the subduction zone offshore of southern arauco peninsula, chile, at 38 s. *Journal of Geophysical Research : Solid Earth*, 113(B7), 2008.

E. Contreras-Reyes, E. R. Flueh, and I. Grevemeyer. Tectonic control on sediment accretion and subduction off south central chile : Implications for coseismic rupture processes of the 1960 and 2010 megathrust earthquakes. *Tectonics*, 29(6), 2010.

E. Contreras-Reyes, J. A. Ruiz, J. Becerra, H. Kopp, C. Reichert, A. Maksymowicz, and C. Arriagada. Structure and tectonics of the central chilean margin (31°–33° s) : Implications for subduction erosion and shallow crustal seismicity. *Geophysical Journal International*, 203 (2) :776–791, 2015.

E. Contreras-Reyes, S. Obando-Orrego, J. Geersen, and J. P. Bello-González. Density structure, flexure, and tectonics of the iquique ridge, northern chile. *Journal of South American Earth Sciences*, 111 :103423, 2021.

B. J. Cook, T. J. Henstock, L. C. McNeill, and J. M. Bull. Controls on spatial and temporal evolution of prism faulting and relationships to plate boundary slip offshore north-central sumatra. *Journal of Geophysical Research : Solid Earth*, 119(7) :5594–5612, 2014.

F. Corbi, F. Funiciello, M. Moroni, Y. Van Dinther, P. M. Mai, L. Dalguer, and C. Faccenna. The seismic cycle at subduction thrusts : 1. insights from laboratory models. *Journal of Geophysical Research : Solid Earth*, 118(4) :1483–1501, 2013.

F. Corbi, R. Herrendörfer, F. Funiciello, and Y. Van Dinther. Controls of seismogenic zone width and subduction velocity on interplate seismicity : Insights from analog and numerical models. *Geophysical Research Letters*, 44(12) :6082–6091, 2017.

E. Costa and B. Vendeville. Experimental insights on the geometry and kinematics of fold-and-thrust belts above weak, viscous evaporitic décollement. *Journal of Structural Geology*, 24 (11) :1729–1739, 2002.

B. A. Couzens-Schultz, B. C. Vendeville, and D. V. Wiltschko. Duplex style and triangle zone formation : insights from physical modeling. *Journal of Structural Geology*, 25(10) :1623–1644, 2003.

N. Cubas, Y. Leroy, and B. Maillot. Prediction of thrusting sequences in accretionary wedges. *Journal of Geophysical Research : Solid Earth*, 113(B12), 2008.

N. Cubas, J.-P. Avouac, Y. M. Leroy, and A. Pons. Low friction along the high slip patch of the 2011 mw 9.0 tohoku-oki earthquake required from the wedge structure and extensional splay faults. *GRL*, 40(16) :4231–4237, 2013a.

N. Cubas, J.-P. Avouac, P. Souloumiac, and Y. Leroy. Megathrust friction determined from mechanical analysis of the forearc in the maule earthquake area. *EPSL*, 381 :92–103, 2013b.

N. Cubas, C. Barnes, and B. Maillot. Inverse method applied to a sand wedge : estimation of friction parameters and uncertainty analysis. *Journal of Structural Geology*, 55 :101–113, 2013c.

N. Cubas, N. Lapusta, J.-P. Avouac, and H. Perfettini. Numerical modeling of long-term earthquake sequences on the ne japan megathrust : Comparison with observations and implications for fault friction. *EPSL*, 419 :187–198, 2015.

N. Cubas, P. Souloumiac, and S. C. Singh. Relationship link between landward vergence in accretionary prisms and tsunami generation. *Geology*, 44(10) :787–790, 2016.

N. Cubas, P. Agard, and R. Tissandier. Earthquake ruptures and topography of the chilean margin controlled by plate interface deformation. *Solid Earth*, 13(3) :779–792, 2022.

P. R. Cummins and Y. Kaneda. Possible splay fault slip during the 1946 nankai earthquake. *Geophysical Research Letters*, 27(17) :2725–2728, 2000.

F. Dahlen, J. Suppe, and D. Davis. Mechanics of fold-and-thrust belts and accretionary wedges : Cohesive coulomb theory. *Journal of Geophysical Research : Solid Earth*, 89(B12) :10087–10101, 1984.

L. Dal Zilio, N. Lapusta, J.-P. Avouac, and T. Gerya. Subduction earthquake sequences in a non-linear visco-elasto-plastic megathrust. *Geophysical Journal International*, 229(2) : 1098–1121, 2022.

C. Darwin. *Geological observations on coral reefs, volcanic islands, and on South America : Being the geology of the voyage of the Beagle, under the command of Captain Fitzroy, RN, during the years 1832 to 1836*. Smith, Elder & Company, 1851.

D. Davis, J. Suppe, and F. Dahlen. Mechanics of fold-and-thrust belts and accretionary wedges. *Journal of Geophysical Research : Solid Earth*, 88(B2) :1153–1172, 1983.

S. M. Dean, L. C. McNeill, T. J. Henstock, J. M. Bull, S. P. Gulick, J. A. Austin Jr, N. L. Bangs, Y. S. Djajadihardja, and H. Permana. Contrasting décollement and prism properties over the sumatra 2004–2005 earthquake rupture boundary. *Science*, 329(5988) :207–210, 2010.

C. DeMets, R. G. Gordon, and D. F. Argus. Geologically current plate motions. *Geophysical Journal International*, 181(1) :1–80, 2010.

S. Den Hartog, A. Niemeijer, and C. J. Spiers. New constraints on megathrust slip stability under subduction zone p–t conditions. *Earth and Planetary Science Letters*, 353 :240–252, 2012.

S. Den Hartog, A. Niemeijer, and C. Spiers. Friction on subduction megathrust faults : Beyond the illite–muscovite transition. *Earth and Planetary Science Letters*, 373 :8–19, 2013.

J. H. Dieterich. Modeling of rock friction : 1. experimental results and constitutive equations. *Journal of Geophysical Research : Solid Earth*, 84(B5) :2161–2168, 1979.

S. Dominguez, S. Lallemand, J. Malavieille, and R. von Huene. Upper plate deformation associated with seamount subduction. *Tectonophys.*, 293(3-4) :207–224, 1998.

T. Duretz, R. de Borst, and L. Le Pourhiet. Finite thickness of shear bands in frictional viscoplasticity and implications for lithosphere dynamics. *G3*, 20(11) :5598–5616, 2019.

T. Duretz, R. de Borst, P. Yamato, and L. Le Pourhiet. Toward robust and predictive geodynamic modeling : The way forward in frictional plasticity. *GRL*, 47(5) :e2019GL086027, 2020.

B. A. Erickson, J. Jiang, M. Barall, N. Lapusta, E. M. Dunham, R. Harris, L. S. Abrahams, K. L. Allison, J.-P. Ampuero, S. Barbot, et al. The community code verification exercise for simulating sequences of earthquakes and aseismic slip (seas). *Seismological Research Letters*, 91(2A) :874–890, 2020.

Å. Fagereng and A. Beall. Is complex fault zone behaviour a reflection of rheological heterogeneity ? *Philosophical Transactions of the Royal Society A*, 379(2193) :20190421, 2021.

Å. Fagereng and R. H. Sibson. Melange rheology and seismic style. *Geology*, 38(8) :751–754, 2010.

M. Farías, D. Comte, S. Roecker, D. Carrizo, and M. Pardo. Crustal extensional faulting triggered by the 2010 chilean earthquake : The pichilemu seismic sequence. *Tectonics*, 30(6), 2011.

D. Faulkner, C. Jackson, R. Lunn, R. Schlische, Z. Shipton, C. Wibberley, and M. Withjack. A review of recent developments concerning the structure, mechanics and fluid flow properties of fault zones. *Journal of Structural Geology*, 32(11) :1557–1575, 2010.

D. Faulkner, T. Mitchell, J. Behnsen, T. Hirose, and T. Shimamoto. Stuck in the mud ? earthquake nucleation and propagation through accretionary forearcs. *Geophysical Research Letters*, 38(18), 2011.

E. Frohling and W. Szeliga. Gps constraints on interplate locking within the makran subduction zone. *Geophysical Supplements to the Monthly Notices of the Royal Astronomical Society*, 205(1) :67–76, 2016.

T. Fujiwara, S. Kodaira, T. No, Y. Kaiho, N. Takahashi, and Y. Kaneda. The 2011 tohoku-oki earthquake : Displacement reaching the trench axis. *Science*, 334(6060) :1240–1240, 2011.

C. W. Fuller, S. D. Willett, and M. T. Brandon. Formation of forearc basins and their influence on subduction zone earthquakes. *Geology*, 34(2) :65–68, 2006.

X. Gao and K. Wang. Strength of stick-slip and creeping subduction megathrusts from heat flow observations. *Science*, 345(6200) :1038–1041, 2014.

J. Geersen, C. R. Ranero, U. Barckhausen, and C. Reichert. Subducting seamounts control interplate coupling and seismic rupture in the 2014 iquique earthquake area. *Nature comm.*, 6(1) :1–6, 2015.

A. Goswami and S. Barbot. Slow-slip events in semi-brittle serpentinite fault zones. *Scientific reports*, 8(1) :6181, 2018.

F. Graveleau, J. Malavieille, and S. Dominguez. Experimental modelling of orogenic wedges : A review. *Tectonophysics*, 538 :1–66, 2012.

S. P. Gulick, A. M. Meltzer, and S. H. Clarke Jr. Seismic structure of the southern cascadia subduction zone and accretionary prism north of the mendocino triple junction. *Journal of Geophysical Research : Solid Earth*, 103(B11) :27207–27222, 1998.

S. P. Gulick, J. A. Austin Jr, L. C. McNeill, N. L. Bangs, K. M. Martin, T. J. Henstock, J. M. Bull, S. Dean, Y. S. Djajadihardja, and H. Permana. Updip rupture of the 2004 sumatra earthquake extended by thick indurated sediments. *Nature Geoscience*, 4(7) :453, 2011.

M.-A. Gutscher, N. Kukowski, J. Malavieille, and S. Lallemand. Episodic imbricate thrusting and underthrusting : Analog experiments and mechanical analysis applied to the alaskan accretionary wedge. *Journal of Geophysical Research : Solid Earth*, 103(B5) :10161–10176, 1998.

M.-A. Gutscher, D. Klaeschen, E. Flueh, and J. Malavieille. Non-coulomb wedges, wrong-way thrusting, and natural hazards in cascadia. *Geology*, 29(5) :379–382, 2001.

W. Hafner. Stress distributions and faulting. *Geological Society of America Bulletin*, 62(4) : 373–398, 1951.

S. Han, N. L. Bangs, S. M. Carbotte, D. M. Saffer, and J. C. Gibson. Links between sediment consolidation and cascadia megathrust slip behaviour. *Nature Geoscience*, 10(12) :954–959, 2017.

A. J. Hartley, G. May, G. Chong, P. Turner, S. J. Kape, and E. J. Jolley. Development of a continental forearc : A cenozoic example from the central andes, northern chile. *Geology*, 28 (4) :331–334, 2000.

C. Hashimoto, A. Noda, T. Sagiya, and M. Matsu'ura. Interplate seismogenic zones along the kuril–japan trench inferred from gps data inversion. *Nature Geoscience*, 2(2) :141–144, 2009.

A. Heuret, S. Lallemand, F. Funiciello, C. Piromallo, and C. Faccenna. Physical characteristics of subduction interface type seismogenic zones revisited. *Geochemistry, Geophysics, Geosystems*, 12(1), 2011.

A. Heuret, C. Conrad, F. Funiciello, S. Lallemand, and L. Sandri. Relation between subduction megathrust earthquakes, trench sediment thickness and upper plate strain. *Geophysical Research Letters*, 39(5), 2012.

T. W. Hilde. Sediment subduction versus accretion around the pacific. *Tectonophysics*, 99(2-4) : 381–397, 1983.

B. Hobbs, A. Ord, and C. Teyssier. Earthquakes in the ductile regime ? *Pure and Applied Geophysics*, 124 :309–336, 1986.

J. Hower, E. V. Eslinger, M. E. Hower, and E. A. Perry. Mechanism of burial metamorphism of argillaceous sediment : 1. mineralogical and chemical evidence. *Geological Society of America Bulletin*, 87(5) :725–737, 1976.

Y.-J. Hsu, M. Simons, J.-P. Avouac, J. Galetzka, K. Sieh, M. Chlieh, D. Natawidjaja, L. Prawirodirdjo, and Y. Bock. Frictional afterslip following the 2005 nias-simeulue earthquake, sumatra. *Science*, 312(5782) :1921–1926, 2006.

Y. Hu and K. Wang. Coseismic strengthening of the shallow portion of the subduction fault and its effects on wedge taper. *Journal of Geophysical Research : Solid Earth*, 113(B12), 2008.

R. D. Hyndman and S. M. Peacock. Serpentinization of the forearc mantle. *Earth and Planetary Science Letters*, 212(3-4) :417–432, 2003.

R. D. Hyndman, M. Yamano, and D. A. Oleskevich. The seismogenic zone of subduction thrust faults. *Island Arc*, 6(3) :244–260, 1997.

S. Ide, A. Baltay, and G. C. Beroza. Shallow dynamic overshoot and energetic deep rupture in the 2011 m w 9.0 tohoku-oki earthquake. *Science*, 332(6036) :1426–1429, 2011.

Y. Ito and K. Obara. Very low frequency earthquakes within accretionary prisms are very low stress-drop earthquakes. *Geophysical Research Letters*, 33(9), 2006.

Y. Ito, T. Tsuji, Y. Osada, M. Kido, D. Inazu, Y. Hayashi, H. Tsushima, R. Hino, and H. Fujimoto. Frontal wedge deformation near the source region of the 2011 tohoku-oki earthquake. *Geophysical Research Letters*, 38(7), 2011.

J. Jiang and N. Lapusta. Deeper penetration of large earthquakes on seismically quiescent faults. *Science*, 352(6291) :1293–1297, 2016.

J. Jiang, B. A. Erickson, V. R. Lambert, J.-P. Ampuero, R. Ando, S. D. Barbot, C. Cattania, L. D. Zilio, B. Duan, E. M. Dunham, et al. Community-driven code comparisons for three-dimensional dynamic modeling of sequences of earthquakes and aseismic slip. *Journal of Geophysical Research : Solid Earth*, 127(3) :e2021JB023519, 2022.

Y. Kaneko, J.-P. Avouac, and N. Lapusta. Towards inferring earthquake patterns from geodetic observations of interseismic coupling. *Nature Geosc.*, 3(5) :363–369, 2010.

A. M. Kassi, A. K. Kasi, J. McManus, and A. S. Khan. Lithostratigraphy, petrology and sedimentary facies of the late cretaceous-palaeocene ispikan group, southwestern makran, pakistan. *Journal of Himalayan Earth Science*, 46(2), 2013.

G. Kimura, G. F. Moore, M. Strasser, E. Screaton, D. Curewitz, C. Streiff, and H. Tobin. Spatial and temporal evolution of the megasplay fault in the nankai trough. *Geochemistry, Geophysics, Geosystems*, 12(3), 2011.

G. Kimura, A. Yamaguchi, M. Hojo, Y. Kitamura, J. Kameda, K. Ujiie, Y. Hamada, M. Hamahashi, and S. Hina. Tectonic mélange as fault rock of subduction plate boundary. *Tectonophysics*, 568 :25–38, 2012.

J. D. Kirkpatrick and C. D. Rowe. Disappearing ink : How pseudotachylytes are lost from the rock record. *Journal of Structural Geology*, 52 :183–198, 2013.

E. Klein, M. Metois, G. Meneses, C. Vigny, and A. Delorme. Bridging the gap between north and central chile : insight from new gps data on coupling complexities and the andean sliver motion. *Geophysical Journal International*, 213(3) :1924–1933, 2018.

S. Kodaira, N. Takahashi, A. Nakanishi, S. Miura, and Y. Kaneda. Subducted seamount imaged in the rupture zone of the 1946 nankaido earthquake. *Science*, 289(5476) :104–106, 2000.

S. Kodaira, T. Hori, A. Ito, S. Miura, G. Fujie, J.-O. Park, T. Baba, H. Sakaguchi, and Y. Kaneda. A cause of rupture segmentation and synchronization in the nankai trough revealed by seismic imaging and numerical simulation. *Journal of Geophysical Research : Solid Earth*, 111(B9), 2006.

A. O. Konca, J.-P. Avouac, A. Sladen, A. J. Meltzner, K. Sieh, P. Fang, Z. Li, J. Galetzka, J. Genrich, M. Chlieh, et al. Partial rupture of a locked patch of the sumatra megathrust during the 2007 earthquake sequence. *Nature*, 456(7222) :631–635, 2008.

E. Konstantinovskaya and J. Malavieille. Accretionary orogens : erosion and exhumation. *Geotectonics*, 39(1) :69–86, 2005.

E. Konstantinovskaya and J. Malavieille. Thrust wedges with décollement levels and syntectonic erosion : A view from analog models. *Tectonophysics*, 502(3-4) :336–350, 2011.

C. Kopp, J. Fruehn, E. Flueh, C. Reichert, N. Kukowski, J. Bialas, and D. Klaeschen. Structure of the makran subduction zone from wide-angle and reflection seismic data. *Tectonophysics*, 329(1-4) :171–191, 2000.

E. Kosari, M. Rosenau, T. Ziegenhagen, and O. Oncken. Upper plate response to a sequential elastic rebound and slab acceleration during laboratory-scale subduction megathrust earthquakes. *Journal of Geophysical Research : Solid Earth*, 127(9) :e2022JB024143, 2022.

H. A. Koyi and B. C. Vendeville. The effect of décollement dip on geometry and kinematics of model accretionary wedges. *Journal of Structural Geology*, 25(9) :1445–1450, 2003.

N. Kukowski, T. Schillhorn, K. Huhn, U. von Rad, S. Husen, and E. R. Flueh. Morphotectonics and mechanics of the central makran accretionary wedge off pakistan. *Marine Geology*, 173 (1-4) :1–19, 2001.

A. K. Kuncoro, N. Cubas, S. C. Singh, M. Etchebes, and P. Tapponnier. Tsunamigenic potential due to frontal rupturing in the sumatra locked zone. *Earth and Planetary Science Letters*, 432 :311–322, 2015.

A. H. Lachenbruch and J. Sass. Heat flow and energetics of the san andreas fault zone. *Journal of Geophysical Research : Solid Earth*, 85(B11) :6185–6222, 1980.

S. Lallemand, M. Peyret, E. van Rijsingen, D. Arcay, and A. Heuret. Roughness characteristics of oceanic seafloor prior to subduction in relation to the seismogenic potential of subduction zones. *Geochemistry, Geophysics, Geosystems*, 19(7) :2121–2146, 2018.

S. E. Lallemand, P. Schnürle, and J. Malavieille. Coulomb theory applied to accretionary and nonaccretionary wedges : Possible causes for tectonic erosion and/or frontal accretion. *Journal of Geophysical Research : Solid Earth*, 99(B6) :12033–12055, 1994.

S. Lamb. Shear stresses on megathrusts : Implications for mountain building behind subduction zones. *Journal of Geophysical Research : Solid Earth*, 111(B7), 2006.

S. Lamb and P. Davis. Cenozoic climate change as a possible cause for the rise of the andes. *Nature*, 425(6960) :792–797, 2003.

N. Lapusta, J. R. Rice, Y. Ben-Zion, and G. Zheng. Elastodynamic analysis for slow tectonic loading with spontaneous rupture episodes on faults with rate-and state-dependent friction. *Journal of Geophysical Research : Solid Earth*, 105(B10) :23765–23789, 2000.

L. L. Lavier, X. Tong, and J. Biemiller. The mechanics of creep, slow slip events, and earthquakes in mixed brittle-ductile fault zones. *Journal of Geophysical Research : Solid Earth*, 126(2) :e2020JB020325, 2021.

T. Lay. The surge of great earthquakes from 2004 to 2014. *Earth and Planetary Science Letters*, 409 :133–146, 2015.

T. Lay, H. Kanamori, C. J. Ammon, M. Nettles, S. N. Ward, R. C. Aster, S. L. Beck, S. L. Bilek, M. R. Brudzinski, R. Butler, et al. The great sumatra-andaman earthquake of 26 december 2004. *science*, 308(5725) :1127–1133, 2005.

T. Lay, C. J. Ammon, H. Kanamori, Y. Yamazaki, K. F. Cheung, and A. R. Hutko. The 25 october 2010 mentawai tsunami earthquake (mw 7.8) and the tsunami hazard presented by shallow megathrust ruptures. *Geophysical Research Letters*, 38(6), 2011.

T. Lay, H. Kanamori, C. J. Ammon, K. D. Koper, A. R. Hutko, L. Ye, H. Yue, and T. M. Rushing. Depth-varying rupture properties of subduction zone megathrust faults. *Journal of Geophysical Research : Solid Earth*, 117(B4), 2012.

L. Le Pourhiet. Strain localization due to structural softening during pressure sensitive rate independent yielding. *BSGF*, 184(4-5) :357–371, 2013.

F. Lehner. Comments on "noncohesive critical coulomb wedges : An exact solution" by fa dahlen. *Journal of Geophysical Research : Solid Earth*, 91(B1) :793–796, 1986.

P. Leturmy, J. Mugnier, P. Vinour, P. Baby, B. Colletta, and E. Chabron. Piggyback basin development above a thin-skinned thrust belt with two detachment levels as a function of interactions between tectonic and superficial mass transfer : the case of the subandean zone (bolivia). *Tectonophysics*, 320(1) :45–67, 2000.

A. Lin, T. Maruyama, S. Aaron, K. Michibayashi, A. Camacho, and K.-i. Kano. Propagation of seismic slip from brittle to ductile crust : Evidence from pseudotachylyte of the woodroffe thrust, central australia. *Tectonophysics*, 402(1-4) :21–35, 2005.

Y. Lin, R. Jolivet, M. Simons, P. Agram, H. R. Martens, Z. Li, and S. Lodi. High interseismic coupling in the eastern makran (pakistan) subduction zone. *Earth and Planetary Science Letters*, 420 :116–126, 2015.

Y.-n. N. Lin, A. Sladen, F. Ortega-Culaciati, M. Simons, J.-P. Avouac, E. J. Fielding, B. A. Brooks, M. Bevis, J. Genrich, A. Rietbrock, et al. Coseismic and postseismic slip associated with the 2010 maule earthquake, chile : Characterizing the arauco peninsula barrier effect. *Journal of Geophysical Research : Solid Earth*, 118(6) :3142–3159, 2013.

Y. Liu and J. R. Rice. Spontaneous and triggered aseismic deformation transients in a subduction fault model. *Journal of Geophysical Research : Solid Earth*, 112(B9), 2007.

C. Lomnitz. Major earthquakes and tsunamis in chile during the period 1535 to 1955. *Geologische Rundschau*, 59 :938–960, 1970.

J. P. Loveless and B. J. Meade. Spatial correlation of interseismic coupling and coseismic rupture extent of the 2011 mw= 9.0 tohoku-oki earthquake. *Geophysical Research Letters*, 38(17), 2011.

M. E. MacKay. Structural variation and landward vergence at the toe of the oregon accretionary prism. *Tectonics*, 14(6) :1309–1320, 1995.

E. H. Madden, T. Ulrich, and A.-A. Gabriel. The state of pore fluid pressure and 3-d megathrust earthquake dynamics. *Journal of Geophysical Research : Solid Earth*, 127(4) : e2021JB023382, 2022.

M. E. Magee and M. D. Zoback. Evidence for a weak interplate thrust fault along the northern japan subduction zone and implications for the mechanics of thrust faulting and fluid expulsion. *Geology*, 21(9) :809–812, 1993.

B. Maillot and Y. M. Leroy. Kink-fold onset and development based on the maximum strength theorem. *Journal of the Mechanics and Physics of Solids*, 54(10) :2030–2059, 2006.

A. Maksymowicz, J. Ruiz, E. Vera, E. Contreras-Reyes, S. Ruiz, C. Arraigada, S. Bonvalot, and S. Bascuñan. Heterogeneous structure of the northern chile marine forearc and its implications for megathrust earthquakes. *Geophysical Journal International*, 215(2) :1080–1097, 2018.

J. Malavieille. Modélisation expérimentale des chevauchements imbriqués : application aux chaînes de montagnes. *Bulletin de la Société géologique de France*, 26(1) :129–138, 1984.

B. Marcaillou, G. Spence, K. Wang, J.-Y. Collot, and A. Ribodetti. Thermal segmentation along the n. ecuador–s. colombia margin (1–4 n) : Prominent influence of sedimentation rate in the trench. *Earth and Planetary Science Letters*, 272(1-2) :296–308, 2008.

L. Marill, D. Marsan, A. Socquet, M. Radiguet, N. Cotte, and B. Rousset. Fourteen-year acceleration along the japan trench. *Journal of Geophysical Research : Solid Earth*, 126(11) : e2020JB021226, 2021.

B. C. Mary, B. Maillot, and Y. M. Leroy. Predicting orogenic wedge styles as a function of analogue erosion law and material softening. *Geochemistry, Geophysics, Geosystems*, 14 (10) :4523–4543, 2013.

C. W. Mase and L. Smith. Pore-fluid pressures and frictional heating on a fault surface. *Pure and Applied Geophysics*, 122(2) :583–607, 1984.

C. W. Mase and L. Smith. Effects of frictional heating on the thermal, hydrologic, and mechanical response of a fault. *Journal of Geophysical Research : Solid Earth*, 92(B7) :6249–6272, 1987.

F. Masson, M. Anvari, Y. Djamour, A. Walpersdorf, F. Tavakoli, M. Daignières, H. Nankali, and S. Van Gorp. Large-scale velocity field and strain tensor in iran inferred from gps measurements : new insight for the present-day deformation pattern within ne iran. *Geophysical Journal International*, 170(1) :436–440, 2007.

G. Mastella, F. Corbi, F. Funiciello, and M. Rosenau. Foamquake : a novel analog model mimicking megathrust seismic cycles. *Journal of Geophysical Research : Solid Earth*, 127 (3) :e2021JB022789, 2022.

A. P. Mavrommatis, P. Segall, and K. M. Johnson. A decadal-scale deformation transient prior to the 2011 mw 9.0 tohoku-oki earthquake. *Geophysical Research Letters*, 41(13) :4486–4494, 2014.

K. McIntosh, E. Silver, and T. Shipley. Evidence and mechanisms for forearc extension at the accretionary costa rica convergent margin. *Tectonics*, 12(6) :1380–1392, 1993.

D. McKenzie and J. Jackson. Tsunami earthquake generation by the release of gravitational potential energy. *Earth and Planetary Science Letters*, 345 :1–8, 2012.

D. Melnick, B. Bookhagen, H. P. Echtler, and M. R. Strecker. Coastal deformation and great subduction earthquakes, isla santa maría, chile (37 s). *Geological Society of America Bulletin*, 118(11-12) :1463–1480, 2006.

D. Melnick, M. Moreno, M. Motagh, M. Cisternas, and R. L. Wesson. Splay fault slip during the m w 8.8 2010 maule chile earthquake. *Geology*, 40(3) :251–254, 2012.

L. Meng, A. Inbal, and J.-P. Ampuero. A window into the complexity of the dynamic rupture of the 2011 mw 9 tohoku-oki earthquake. *Geophysical Research Letters*, 38(7), 2011.

M. Métois, A. Socquet, and C. Vigny. Interseismic coupling, segmentation and mechanical behavior of the central chile subduction zone. *Journal of Geophysical Research : Solid Earth*, 117(B3), 2012.

M. Metois, C. Vigny, and A. Socquet. Interseismic coupling, megathrust earthquakes and seismic swarms along the chilean subduction zone (38–18 s). *Pure and Applied Geophysics*, 173 (5) :1431–1449, 2016.

S. Michel, A. Gualandi, and J.-P. Avouac. Interseismic coupling and slow slip events on the cascadia megathrust. *Pure and Applied Geophysics*, 176(9) :3867–3891, 2019.

Y. Miyake and H. Noda. Fully dynamic earthquake sequence simulation of a fault in a viscoelastic medium using a spectral boundary integral equation method : does interseismic stress relaxation promote aseismic transients ? *Earth, Planets and Space*, 71(1) :1–12, 2019.

R. Moeremans, S. C. Singh, M. Mukti, J. McArdle, and K. Johansen. Seismic images of structural variations along the deformation front of the andaman–sumatra subduction zone : implications for rupture propagation and tsunamigenesis. *Earth and Planetary Science Letters*, 386 :75–85, 2014.

G. Moore, N. Bangs, A. Taira, S. Kuramoto, E. Pangborn, and H. Tobin. Three-dimensional splay fault geometry and implications for tsunami generation. *Science*, 318(5853) :1128–1131, 2007.

G. F. Moore, T. Shipley, P. Stoffa, D. Karig, A. Taira, S. Kuramoto, H. Tokuyama, and K. Suyehiro. Structure of the nankai trough accretionary zone from multichannel seismic reflection data. *Journal of Geophysical Research : Solid Earth*, 95(B6) :8753–8765, 1990.

M. Moreno, M. Rosenau, and O. Oncken. 2010 maule earthquake slip correlates with preseismic locking of andean subduction zone. *Nature*, 467(7312) :198–202, 2010.

M. Moreno, S. Li, D. Melnick, J. Bedford, J. Baez, M. Motagh, S. Metzger, S. Vajedian, C. Sippl, B. Gutknecht, et al. Chilean megathrust earthquake recurrence linked to frictional contrast at depth. *Nature Geoscience*, 11(4) :285–290, 2018.

M. S. Moreno, J. Bolte, J. Klotz, and D. Melnick. Impact of megathrust geometry on inversion of coseismic slip from geodetic data : Application to the 1960 chile earthquake. *Geophysical Research Letters*, 36(16), 2009.

I. A. Muldashev and S. V. Sobolev. What controls maximum magnitudes of giant subduction earthquakes ? *Geochemistry, Geophysics, Geosystems*, 21(9) :e2020GC009145, 2020.

G. Mulugeta. Modelling the geometry of coulomb thrust wedges. *Journal of Structural Geology*, 10(8) :847–859, 1988.

R. Musson. Subduction in the western makran : the historian's contribution. *Journal of the Geological Society*, 166(3) :387–391, 2009.

A. Nakanishi, N. Takahashi, J.-O. Park, S. Miura, S. Kodaira, Y. Kaneda, N. Hirata, T. Iwasaki, and M. Nakamura. Crustal structure across the coseismic rupture zone of the 1944 tonankai earthquake, the central nankai trough seismogenic zone. *Journal of Geophysical Research : Solid Earth*, 107(B1) :EPM–2, 2002.

K. Newcomb and W. McCann. Seismic history and seismotectonics of the sunda arc. *Journal of Geophysical Research : Solid Earth*, 92(B1) :421–439, 1987.

D. Nieuwland, J. Leutscher, and J. Gast. Wedge equilibrium in fold-and-thrust belts : prediction of out-of-sequence thrusting based on sandbox experiments and natural examples. *Netherlands Journal of Geosciences*, 79(1) :81–91, 2000.

J.-M. Nocquet, J. C. Villegas-Lanza, M. Chlieh, P. Mothes, F. Rolandone, P. Jarrin, D. Cisneros, A. Alvarado, L. Audin, F. Bondoux, et al. Motion of continental slivers and creeping subduction in the northern andes. *Nature Geoscience*, 7(4) :287–291, 2014.

J.-M. Nocquet, P. Jarrin, M. Vallée, P. A. Mothes, R. Grandin, F. Rolandone, B. Delouis, H. Yepes, Y. Font, D. Fuentes, et al. Supercycle at the ecuadorian subduction zone revealed after the 2016 pedernales earthquake. *Nature Geoscience*, 10(2) :145–149, 2017.

A. Noda. Forearc basins : Types, geometries, and relationships to subduction zone dynamics. *Bulletin*, 128(5-6) :879–895, 2016a.

H. Noda. Implementation into earthquake sequence simulations of a rate-and state-dependent friction law incorporating pressure solution creep. *Geophysical Journal International*, 205 (2) :1108–1125, 2016b.

H. Noda and N. Lapusta. Three-dimensional earthquake sequence simulations with evolving temperature and pore pressure due to shear heating : Effect of heterogeneous hydraulic diffusivity. *Journal of Geophysical Research : Solid Earth*, 115(B12), 2010.

H. Noda and N. Lapusta. Stable creeping fault segments can become destructive as a result of dynamic weakening. *Nature*, 493(7433) :518, 2013.

K. Obana and S. Kodaira. Low-frequency tremors associated with reverse faults in a shallow accretionary prism. *Earth and Planetary Science Letters*, 287(1-2) :168–174, 2009.

K. Obara and A. Kato. Connecting slow earthquakes to huge earthquakes. *Science*, 353(6296) : 253–257, 2016.

D. Oleskevich, R. Hyndman, and K. Wang. The updip and downdip limits to great subduction earthquakes : Thermal and structural models of cascadia, south alaska, sw japan, and chile. *Journal of Geophysical Research : Solid Earth*, 104(B7) :14965–14991, 1999.

K. M. Olsen, N. L. Bangs, A. M. Tréhu, S. Han, A. Arnulf, and E. Contreras-Reyes. Thick, strong sediment subduction along south-central chile and its role in great earthquakes. *Earth and Planetary Science Letters*, 538 :116195, 2020.

S. Ozawa, T. Nishimura, H. Suito, T. Kobayashi, M. Tobita, and T. Imakiire. Coseismic and postseismic slip of the 2011 magnitude-9 tohoku-oki earthquake. *Nature*, 475(7356) :373–376, 2011.

S. Pajang, N. Cubas, J. Letouzey, L. Le Pourhiet, and et al. Seismic hazard of the western makran subduction zone : insight from mechanical modelling and inferred frictional properties. *Earth and Planetary Science Letters*, 562 :116789, 2021.

S. Pajang, M. M. Khatib, M. Heyhat, N. Cubas, E. Bessiere, J. Letouzey, M. Mokhtari, and L. Le Pourhiet. The distinct morphologic signature of underplating and seamounts in accretionary prisms, insights from thermomechanical modeling applied to coastal iranian makran. *Tectonophysics*, 845 :229617, 2022a.

S. Pajang, L. Le Pourhiet, and N. Cubas. The topographic signature of temperature-controlled rheological transitions in an accretionary prism. *Solid Earth*, 13(3) :535–551, 2022b.

J.-O. Park, T. Tsuru, S. Kodaira, A. Nakanishi, S. Miura, Y. Kaneda, Y. Kono, and N. Takahashi. Out-of-sequence thrust faults developed in the coseismic slip zone of the 1946 nankai earthquake (mw= 8.2) off shikoku, southwest japan. *Geophysical Research Letters*, 27(7) : 1033–1036, 2000.

J.-O. Park, T. Tsuru, S. Kodaira, P. R. Cummins, and Y. Kaneda. Splay fault branching along the nankai subduction zone. *Science*, 297(5584) :1157–1160, 2002.

J.-O. Park, G. F. Moore, T. Tsuru, S. Kodaira, and Y. Kaneda. A subducted oceanic ridge influencing the nankai megathrust earthquake rupture. *Earth and Planetary Science Letters*, 217(1-2) :77–84, 2004.

C. Penney, F. Tavakoli, A. Saadat, H. R. Nankali, M. Sedighi, F. Khorrami, F. Sobouti, Z. Rafi, A. Copley, J. Jackson, et al. Megathrust and accretionary wedge properties and behaviour in the makran subduction zone. *Geophysical Journal International*, 209(3) :1800–1830, 2017.

H. Perfettini and J. Avouac. The seismic cycle in the area of the 2011 mw9. 0 tohoku-oki earthquake. *Journal of Geophysical Research : Solid Earth*, 119(5) :4469–4515, 2014.

H. Perfettini, J.-P. Avouac, H. Tavera, A. Kositsky, J.-M. Nocquet, F. Bondoux, M. Chlieh, A. Sladen, L. Audin, D. L. Farber, et al. Seismic and aseismic slip on the central peru megathrust. *Nature*, 465(7294) :78–81, 2010.

B. Philibosian, K. Sieh, J.-P. Avouac, D. H. Natawidjaja, H.-W. Chiang, C.-C. Wu, C.-C. Shen, M. R. Daryono, H. Perfettini, B. W. Suwargadi, et al. Earthquake supercycles on the mentawai segment of the sunda megathrust in the seventeenth century and earlier. *Journal of Geophysical Research : Solid Earth*, 122(1) :642–676, 2017.

B. Philibosian, N. Feuillet, J. Weil-Accardo, E. Jacques, A. Guihou, A.-S. Mériaux, A. Anglade, J.-M. Saurel, and S. Deroussi. 20th-century strain accumulation on the lesser antilles megathrust based on coral microatolls. *Earth and Planetary Science Letters*, 579 :117343, 2022.

T. Pichot and T. Nalpas. Influence of synkinematic sedimentation in a thrust system with two decollement levels ; analogue modelling. *Tectonophysics*, 473(3-4) :466–475, 2009.

G. Plafker and J. C. Savage. Mechanism of the chilean earthquakes of may 21 and 22, 1960. *Geological Society of America Bulletin*, 81(4) :1001–1030, 1970.

M. Radiguet, F. Cotton, M. Vergnolle, M. Campillo, A. Walpersdorf, N. Cotte, and V. Kostoglodov. Slow slip events and strain accumulation in the guerrero gap, mexico. *Journal of Geophysical Research : Solid Earth*, 117(B4), 2012.

C. R. Ranero and R. von Huene. Subduction erosion along the middle america convergent margin. *Nature*, 404(6779) :748–752, 2000.

C. R. Ranero, I. Grevemeyer, H. Sahling, U. Barckhausen, C. Hensen, K. Wallmann, W. Weinrebe, P. Vannucchi, R. Von Huene, and K. McIntosh. Hydrogeological system of erosional convergent margins and its influence on tectonics and interplate seismogenesis. *Geochemistry, Geophysics, Geosystems*, 9(3), 2008.

S. Rennie, Å. Fagereng, and J. Diener. Strain distribution within a km-scale, mid-crustal shear zone : the kuckaus mylonite zone, namibia. *Journal of Structural Geology*, 56 :57–69, 2013.

J. R. Rice. Heating and weakening of faults during earthquake slip. *Journal of Geophysical Research : Solid Earth*, 111(B5), 2006.

J. R. Rice and A. L. Ruina. Stability of steady frictional slipping. 1983.

F. Rolandone, J.-M. Nocquet, P. A. Mothes, P. Jarrin, M. Vallée, N. Cubas, S. Hernandez, M. Plain, S. Vaca, and Y. Font. Areas prone to slow slip events impede earthquake rupture propagation and promote afterslip. *Science adv.*, 4(1) :eaao6596, 2018.

P. Romanet, H. S. Bhat, R. Jolivet, and R. Madariaga. Fast and slow slip events emerge due to fault geometrical complexity. *Geophysical Research Letters*, 45(10) :4809–4819, 2018.

M. Rosenau and O. Oncken. Fore-arc deformation controls frequency-size distribution of megathrust earthquakes in subduction zones. *Journal of Geophysical Research : Solid Earth*, 114(B10), 2009.

M. Rosenau, J. Lohrmann, and O. Oncken. Shocks in a box : An analogue model of subduction earthquake cycles with application to seismotectonic forearc evolution. *Journal of Geophysical Research : Solid Earth*, 114(B1), 2009.

M. Rosenau, I. Horenko, F. Corbi, M. Rudolf, R. Kornhuber, and O. Oncken. Synchronization of great subduction megathrust earthquakes : Insights from scale model analysis. *Journal of Geophysical Research : Solid Earth*, 124(4) :3646–3661, 2019.

B. Rousset, C. Lasserre, N. Cubas, and G. al. Lateral variations of interplate coupling along the mexican subduction interface : Relationships with long-term morphology and fault zone mechanical properties. *Pure and Applied Geophysics*, 173(10-11) :3467–3486, 2016.

W. W. Rubey and M. King Hubbert. Role of fluid pressure in mechanics of overthrust faulting : Ii. overthrust belt in geosynclinal area of western wyoming in light of fluid-pressure hypothesis. *Geological Society of America Bulletin*, 70(2) :167–206, 1959.

L. J. Ruff and B. W. Tichelaar. What controls the seismogenic plate interface in subduction zones ? *Washington DC American Geophysical Union Geophysical Monograph Series*, 96 : 105–111, 1996.

J. B. Ruh. Numerical modeling of tectonic underplating in accretionary wedge systems. *Geosphere*, 16(6) :1385–1407, 2020.

J. B. Ruh, B. J. Kaus, and J.-P. Burg. Numerical investigation of deformation mechanics in fold-and-thrust belts : Influence of rheology of single and multiple décollements. *Tectonics*, 31(3), 2012.

J. B. Ruh, V. Sallarès, C. R. Ranero, and T. Gerya. Crustal deformation dynamics and stress evolution during seamount subduction : High-resolution 3-d numerical modeling. *Journal of Geophysical Research : Solid Earth*, 121(9) :6880–6902, 2016.

A. Ruina. Slip instability and state variable friction laws. *Journal of Geophysical Research : Solid Earth*, 88(B12) :10359–10370, 1983.

R. Rutland. Andean orogeny and ocean floor spreading. *Nature*, 233(5317) :252–255, 1971.

D. M. Saffer and B. A. Bekins. Hydrologic controls on the morphology and mechanics of accretionary wedges. *Geology*, 30(3) :271–274, 2002.

D. M. Saffer and H. J. Tobin. Hydrogeology and mechanics of subduction zone forearcs : Fluid flow and pore pressure. *Annual Review of Earth and Planetary Sciences*, 39 :157–186, 2011.

M. Saillard, L. Audin, B. Rousset, J.-P. Avouac, M. Chlieh, S. R. Hall, L. Husson, and D. Farber. From the seismic cycle to long-term deformation : linking seismic coupling and quaternary coastal geomorphology along the andean megathrust. *Tectonics*, 36(2) :241–256, 2017.

J. Salençon. *De l'élasto-plasticité au calcul à la rupture*. Editions Ecole Polytechnique, 2002.

K. Satake, K. Shimazaki, Y. Tsuji, and K. Ueda. Time and size of a giant earthquake in cascadia inferred from japanese tsunami records of january 1700. *Nature*, 379(6562) :246–249, 1996.

M. Sato, M. Fujita, Y. Matsumoto, T. Ishikawa, H. Saito, M. Mochizuki, and A. Asada. Interplate coupling off northeastern japan before the 2011 tohoku-oki earthquake, inferred from seafloor geodetic data. *Journal of Geophysical Research : Solid Earth*, 118(7) :3860–3869, 2013.

Y. Sawai, Y. Namegaya, Y. Okamura, K. Satake, and M. Shishikura. Challenges of anticipating the 2011 tohoku earthquake and tsunami using coastal geology. *Geophysical Research Letters*, 39(21), 2012.

D. W. Scholl and R. von Huene. Crustal recycling at modern subduction zones applied to the past—issues of growth and preservation of continental basement crust, mantle geochemistry, and supercontinent reconstruction. 2007.

C. H. Scholz. Earthquakes and friction laws. *Nature*, 391(6662) :37–42, 1998.

C. H. Scholz and C. Small. The effect of seamount subduction on seismic coupling. *Geology*, 25(6) :487–490, 1997.

D. Seely. The evolution of structural highs bordering major forearc basins : Convergent margins. 1979.

B. Shibazaki, T. Matsuzawa, A. Tsutsumi, K. Ujiie, A. Hasegawa, and Y. Ito. 3d modeling of the cycle of a great tohoku-oki earthquake, considering frictional behavior at low to high slip velocities. *Geophysical Research Letters*, 38(21), 2011.

T. Shimamoto. The origin of sc mylonites and a new fault-zone model. *Journal of Structural Geology*, 11(1-2) :51–64, 1989.

R. Sibson. Interactions between temperature and pore-fluid pressure during earthquake faulting and a mechanism for partial or total stress relief. *Nature Physical Science*, 243(126) :66–68, 1973.

R. Sibson. Transient discontinuities in ductile shear zones. *Journal of Structural Geology*, 2 (1-2) :165–171, 1980.

R. H. Sibson. Fault zone models, heat flow, and the depth distribution of earthquakes in the continental crust of the united states. *Bulletin of the Seismological Society of America*, 72 (1) :151–163, 1982.

K. Sieh, D. H. Natawidjaja, A. J. Meltzner, C.-C. Shen, H. Cheng, K.-S. Li, B. W. Suwargadi, J. Galetzka, B. Philibosian, and R. L. Edwards. Earthquake supercycles inferred from sea-level changes recorded in the corals of west sumatra. *Science*, 322(5908) :1674–1678, 2008.

M. Simons, S. E. Minson, A. Sladen, F. Ortega, J. Jiang, S. E. Owen, L. Meng, J.-P. Ampuero, S. Wei, R. Chu, et al. The 2011 magnitude 9.0 tohoku-oki earthquake : Mosaicking the megathrust from seconds to centuries. *science*, 332(6036) :1421–1425, 2011.

G. D. Simpson. Modelling interactions between fold–thrust belt deformation, foreland flexure and surface mass transport. *Basin Research*, 18(2) :125–143, 2006.

D. T. Small and D. Melgar. Geodetic coupling models as constraints on stochastic earthquake ruptures : An example application to ptha in cascadia. *Journal of Geophysical Research : Solid Earth*, 126(7) :e2020JB021149, 2021.

J. Smit, J. Brun, and D. Sokoutis. Deformation of brittle-ductile thrust wedges in experiments and nature. *Journal of Geophysical Research : Solid Earth*, 108(B10), 2003.

G. Smith, L. McNeill, T. J. Henstock, and J. Bull. The structure and fault activity of the makran accretionary prism. *Journal of Geophysical Research : Solid Earth*, 117(B7), 2012.

S. V. Sobolev and I. A. Muldashev. Modeling seismic cycles of great megathrust earthquakes across the scales with focus at postseismic phase. *Geochemistry, Geophysics, Geosystems*, 18(12) :4387–4408, 2017.

T.-R. A. Song and M. Simons. Large trench-parallel gravity variations predict seismogenic behavior in subduction zones. *Science*, 301(5633) :630–633, 2003.

G. S. Stockmal, C. Beaumont, M. Nguyen, B. Lee, and J. Sears. Mechanics of thin-skinned fold-and-thrust belts : Insights from numerical models. *SPECIAL PAPERS-GEOLOGICAL SOCIETY OF AMERICA*, 433 :63, 2007.

I. Storch, S. Buske, P. Victor, and O. Oncken. Seismic images of the northern chilean subduction zone at 19 40 s, prior to the 2014 iquique earthquake. *Geophysical Journal International*, 225 (2) :1048–1061, 2021.

F. Storti and K. McClay. Influence of syntectonic sedimentation on thrust wedges in analogue models. *Geology*, 23(11) :999–1002, 1995.

M. Strasser, G. F. Moore, G. Kimura, Y. Kitamura, A. J. Kopf, S. Lallemant, J.-O. Park, E. J. Screaton, X. Su, M. B. Underwood, et al. Origin and evolution of a splay fault in the nankai accretionary wedge. *Nature Geoscience*, 2(9) :648–652, 2009.

J. Suppe. Geometry and kinematics of fault-bend folding. *American Journal of science*, 283 (7) :684–721, 1983.

W. Tanikawa and T. Shimamoto. Comparison of klinkenberg-corrected gas permeability and water permeability in sedimentary rocks. *International Journal of Rock Mechanics and Mining Sciences*, 46(2) :229–238, 2009.

M. Y. Thomas and H. S. Bhat. Dynamic evolution of off-fault medium during an earthquake : a micromechanics based model. *Geophysical Journal International*, 214(2) :1267–1280, 2018.

M. Y. Thomas, N. Lapusta, H. Noda, and J.-P. Avouac. Quasi-dynamic versus fully dynamic simulations of earthquakes and aseismic slip with and without enhanced coseismic weakening. *Journal of Geophysical Research : Solid Earth*, 119(3) :1986–2004, 2014.

M. Y. Thomas, J.-P. Avouac, and N. Lapusta. Rate-and-state friction properties of the longitudinal valley fault from kinematic and dynamic modeling of seismic and aseismic slip. *JGR*, 122(4) :3115–3137, 2017.

R. Tissandier, J.-M. Nocquet, E. Klein, C. Vigny, J. Ojeda, and S. Ruiz. Afterslip of the mw 8.3 2015 illapel earthquake imaged through a time-dependent inversion of continuous and survey gnss data. *Journal of Geophysical Research : Solid Earth*, page e2022JB024778, 2023.

H. J. Tobin and D. M. Saffer. Elevated fluid pressure and extreme mechanical weakness of a plate boundary thrust, nankai trough subduction zone. *Geology*, 37(8) :679–682, 2009.

T. Tsuji, Y. Ito, M. Kido, Y. Osada, H. Fujimoto, J. Ashi, M. Kinoshita, and T. Matsuoka. Potential tsunamigenic faults of the 2011 off the pacific coast of tohoku earthquake. *Earth, planets and space*, 63(7) :58, 2011.

S. Vaca, M. Vallée, J.-M. Nocquet, J. Battaglia, and M. Régnier. Recurrent slow slip events as a barrier to the northward rupture propagation of the 2016 pedernales earthquake (central ecuador). *Tectonophysics*, 724 :80–92, 2018.

Y. Van Dinther, T. Gerya, L. Dalguer, P. M. Mai, G. Morra, and D. Giardini. The seismic cycle at subduction thrusts : Insights from seismo-thermo-mechanical models. *Journal of Geophysical Research : Solid Earth*, 118(12) :6183–6202, 2013.

E. van Rijsingen, S. Lallemand, M. Peyret, D. Arcay, A. Heuret, F. Funiciello, and F. Corbi. How subduction interface roughness influences the occurrence of large interplate earthquakes. *Geochemistry, Geophysics, Geosystems*, 19(8) :2342–2370, 2018.

E. Van Rijsingen, E. Calais, R. Jolivet, J.-B. De Chabalier, J. Jara, S. Symithe, R. Robertson, and G. A. Ryan. Inferring interseismic coupling along the lesser antilles arc : A bayesian approach. *Journal of Geophysical Research : Solid Earth*, 126(2) :e2020JB020677, 2021.

I. Van Zelst, S. Wollherr, A.-A. Gabriel, E. H. Madden, and Y. van Dinther. Modeling megathrust earthquakes across scales : One-way coupling from geodynamics and seismic cycles to dynamic rupture. *Journal of Geophysical Research : Solid Earth*, 124(11) :11414–11446, 2019.

P. Vannucchi, D. W. Scholl, M. Meschede, and K. McDougall-Reid. Tectonic erosion and consequent collapse of the pacific margin of costa rica : Combined implications from odp leg 170, seismic offshore data, and regional geology of the nicoya peninsula. *Tectonics*, 20(5) : 649–668, 2001.

P. Vannucchi, C. R. Ranero, S. Galeotti, S. M. Straub, D. W. Scholl, and K. McDougall-Ried. Fast rates of subduction erosion along the costa rica pacific margin : Implications for nonsteady rates of crustal recycling at subduction zones. *Journal of Geophysical Research : Solid Earth*, 108(B11), 2003.

P. Vannucchi, D. M. Fisher, S. Bier, and T. W. Gardner. From seamount accretion to tectonic erosion : Formation of osa mélange and the effects of cocos ridge subduction in southern costa rica. *Tectonics*, 25(2), 2006.

P. Vannucchi, F. Sage, J. Phipps Morgan, F. Remitti, and J.-Y. Collot. Toward a dynamic concept of the subduction channel at erosive convergent margins with implications for interplate material transfer. *Geochemistry, Geophysics, Geosystems*, 13(2), 2012.

R. von Huene and S. Lallemand. Tectonic erosion along the japan and peru convergent margins. *Geological Society of America Bulletin*, 102(6) :704–720, 1990.

R. von Huene and C. R. Ranero. Subduction erosion and basal friction along the sediment-starved convergent margin off antofagasta, chile. *Journal of Geophysical Research : Solid Earth*, 108(B2), 2003.

R. Von Huene and D. W. Scholl. Observations at convergent margins concerning sediment subduction, subduction erosion, and the growth of continental crust. *Reviews of Geophysics*, 29(3) :279–316, 1991.

R. von Huene, C. R. Ranero, and P. Vannucchi. Generic model of subduction erosion. *Geology*, 32(10) :913–916, 2004.

L. M. Wallace, S. C. Webb, Y. Ito, K. Mochizuki, R. Hino, S. Henrys, S. Y. Schwartz, and A. F. Sheehan. Slow slip near the trench at the hikurangi subduction zone, new zealand. *Science*, 352(6286) :701–704, 2016.

K. Wang and S. L. Bilek. Invited review paper : Fault creep caused by subduction of rough seafloor relief. *Tectonophys.*, 610 :1–24, 2014.

K. Wang and Y. Hu. Accretionary prisms in subduction earthquake cycles : The theory of dynamic coulomb wedge. *Journal of Geophysical Research : Solid Earth*, 111(B6), 2006.

K. Wang, R. Wells, S. Mazzotti, R. D. Hyndman, and T. Sagiya. A revised dislocation model of interseismic deformation of the cascadia subduction zone. *Journal of Geophysical Research : Solid Earth*, 108(B1), 2003.

K. Wang, J. He, and Y. Hu. A note on pore fluid pressure ratios in the coulomb wedge theory. *Geophysical research letters*, 33(19), 2006.

K. Wang, Y. Hu, and J. He. Deformation cycles of subduction earthquakes in a viscoelastic earth. *Nature*, 484(7394) :327–332, 2012.

P.-L. Wang, S. E. Engelhart, K. Wang, A. D. Hawkes, B. P. Horton, A. R. Nelson, and R. C. Witter. Heterogeneous rupture in the great cascadia earthquake of 1700 inferred from coastal subsidence estimates. *Journal of Geophysical Research : Solid Earth*, 118(5) :2460–2473, 2013.

S. Wei, R. Graves, D. Helmberger, J.-P. Avouac, and J. Jiang. Sources of shaking and flooding during the tohoku-oki earthquake : A mixture of rupture styles. *Earth and Planetary Science Letters*, 333 :91–100, 2012.

R. E. Wells, R. J. Blakely, Y. Sugiyama, D. W. Scholl, and P. A. Dinterman. Basin-centered asperities in great subduction zone earthquakes : A link between slip, subsidence, and subduction erosion ? *Journal of Geophysical Research : Solid Earth*, 108(B10), 2003.

J. C. White. Transient discontinuities revisited : pseudotachylyte, plastic instability and the influence of low pore fluid pressure on deformation processes in the mid-crust. *Journal of Structural Geology*, 18(12) :1471–1486, 1996.

S. D. Willett. Rheological dependence of extension in wedge models of convergent orogens. *Tectonophysics*, 305(4) :419–435, 1999.

Y. Yamamoto, K. Obana, T. Takahashi, A. Nakanishi, S. Kodaira, and Y. Kaneda. Imaging of the subducted kyushu-palau ridge in the hyuga-nada region, western nankai trough subduction zone. *Tectonophysics*, 589 :90–102, 2013.

Y. Yamanaka and M. Kikuchi. Asperity map along the subduction zone in northeastern japan inferred from regional seismic data. *Journal of Geophysical Research : Solid Earth*, 109(B7), 2004.

Y. Yokota, T. Ishikawa, S.-i. Watanabe, T. Tashiro, and A. Asada. Seafloor geodetic constraints on interplate coupling of the nankai trough megathrust zone. *Nature*, 534(7607) :374–377, 2016.

J. Zhou, B. Zhang, and Q. Xu. Effects of lateral friction on the structural evolution of fold-and-thrust belts : Insights from sandbox experiments with implications for the origin of landward-vergent thrust wedges in cascadia. *Bulletin*, 128(3-4) :669–683, 2016.

J. Zhu, J. P. Canales, S. Han, S. M. Carbotte, A. Arnulf, and M. R. Nedimović. Vp/vs ratio of incoming sediments off cascadia subduction zone from analysis of controlled-source multicomponent obs records. *Journal of Geophysical Research : Solid Earth*, 125(6) :e2019JB019239, 2020a.

W. Zhu, K. L. Allison, E. M. Dunham, and Y. Yang. Fault valving and pore pressure evolution in simulations of earthquake sequences and aseismic slip. *Nature communications*, 11(1) : 1–11, 2020b.